Rapidly solidified metallic glass alloys for antibacterial touching surfaces

Victor Manuel Villapun Puzas

PhD

A thesis submitted in partial fulfilment of the requirements of the University of Newcastle for the degree of Doctor of Philosophy

Research undertaken in the Faculty of Engineering and Environment

August 2018

I declare that no outputs submitted for this degree have been submitted for a research degree of any other institution. I also confirm that this work fully acknowledges opinions, ideas and contributions from the work of others.

Any ethical clearance for the research presented in this commentary has been approved by the Faculty Ethics Committee/ University Ethics Committee on 13/06/16

I declare that the word count is 44970 words

Name: Victor Manuel Villapun Puzas

Signature:

Date: 14/08/18

Abstract of the dissertation

The emergence of antibiotic resistant bacteria and healthcare-acquired infections are regarded among the greatest socioeconomic threats of our time, affecting up to two million patients annually, of whom about 90,000 die. Hospital surfaces are a reservoir of pathogens, which can be correlated to 20-40% of nosocomial infections due to hand to hand or surface to hand cross contamination. Pure copper and Cu-based alloys display outstanding antimicrobial activity (i.e. 7-8 $\log_{10}$ reduction per hour), but their relatively poor mechanical properties restrict their use. Cu-rich metallic glasses and metallic glass composites can bring together the high biocidal performance of copper and the exceptional physiochemical properties of amorphous materials. This work aimed to understand which parameters influence the antimicrobial and wear behaviour of Cu-rich metallic glasses metallic glasses.

Analysis of composition (i.e. increasingly copper content) and volume fraction of crystalline phases in Cu-Zr-Al bulk metallic glass composites revealed that increasing both parameters led to higher wear and antimicrobial performance, reaching scratch hardness between 3-2 GPa and antimicrobial activity as high as 2.5 $\log_{10}$ reduction after 4 hours. The main parameter influencing antimicrobial activity and wear resistance was the volume fraction of crystalline phases, optimal when the percolation threshold (~50%) was reached, but not overcome. Experiments developed on as-cast and oxidised samples of different roughness, 70-600 nm, showed that, while superficial changes had a limited influence on the contact killing properties, oxidation enhanced their antimicrobial properties, by at least 1 $\log_{10}$ reduction, due to the formation of a complex multi-layered Cu-rich structure.

Coating large surfaces with thin films is an attractive manufacturing option for antimicrobial surfaces; thus, Cu-Zr films were deposited by Magnetron sputtering using different chamber pressures, 0.1 to 0.5 Pa, and substrate temperatures, from room temperature to 403 K. Here, lowering compactness improved the antimicrobial activity (i.e. from 0.2 to 2.3 $\log_{10}$ reduction after 4 hours). At the same time, the authenticity of standard antimicrobial testing protocols for hospital touch surfaces is questionable. “Dry” applications of bacteria to surfaces is more authentic than the “wet” applications used in standards; here no substantial differences were found in

these experiments but dry applications resulted in more effective killing in the less compact films. A combination of careful bacterial recovery and imaging studies on both bulk and film samples suggested that contact killing occurs due to copper ion diffusion into the cell, rather than by extensive cell envelope degradation.

All aforementioned tests showed that it is possible to obtain tuneable materials with optimal antimicrobial and wear resistance for use in preventing bacterial transmission and healthcare-acquired infections.

Acknowledgments

First I will like to express my deepest gratitude to my main supervisor Dr. Sergio Gonzalez Sanchez , second supervisor Dr. Fawad Inam, third supervisor Dr. Lynn G. Dover as well as to Dr. Steve Bull for their guidance which made possible this work. I will like to express my gratitude to those researchers who have help in the development of the present work: H. Zhang, C. Howdeng, L. Cheung Chow, F. Esat, P. Pérez, J. Sort, J. Stach, S. Tardío, P. Cumpson, C.C. Lukose and M. Birkett I would like to state genuine gratitude to my family and Felipe Garcia Robles for their unconditional support. I would like to thank Dr. Juan Carlos del Real and Dr. Yolanda Ballesteros for introducing me to the research world. Finally, I would like to thank Northumbria University for their financial support.

Table of contents

Abstract of the dissertation ii
Acknowledgments iv
Table of contents v
List of abbreviations and symbols viii
List of Figures ix
List of Tables xvi
List of Equations xix
1 Introduction 1
1.1 Antimicrobial properties of metallic surfaces, metallic glasses and metallic glass composites 1
1.1.1 Why it is important to develop bactericidal surfaces? 1
1.1.2 Antimicrobial mechanisms of touch surfaces 8
1.1.3 Antimicrobial surfaces vs common disinfection methodologies 17
1.1.4 Antimicrobial standards for hard surfaces 25
1.1.5 Metallic glasses with bactericidal properties 30
1.2 Metallic glasses and their composites 35
1.2.1 Description of metallic glasses 35
1.2.2 Short history of metallic glasses 41
1.2.3 Glass forming ability 43
1.2.4 Mechanical behaviour of MGs and MGCs 49
1.2.5 Wear performance of metallic glasses 52
1.2.6 Cu-Zr-Al system and Cu-based BMG 59
1.3 Scope and objectives of the thesis 64
2 Materials and methods 66
2.1 Sample preparation 66
2.2 Suction casting 67
2.3 Magnetron sputtering 68
2.4 X-ray diffraction (XRD) 69
2.5 Scanning Electron Microscopy (SEM) 70
2.6 Profilometry and Atomic Force Microscopy (AFM) 71
2.7 Scratch tests 71

2.8 Nanoindentation 72
2.9 Sessile drop technique 72
2.10 Antimicrobial tests 72
2.11 X-ray photoelectron spectroscopy (XPS) 74
2.12 Inductively coupled plasma optical emission spectrometry (ICP-OES) 75
2.13 Transmission Electron Microscopy (TEM) 75
3 Influence of composition, cooling rate and annealing on the wear performance and antimicrobial behaviour of a Cu-Zr-Al metallic glass composite 77
3.1 Effect of composition in the wear and antimicrobial performance of a Cu-based BMG composite 77
3.1.1 Effect of the composition on the microstructure 77
3.1.2 Scratch tests 85
3.1.3 Antimicrobial and wettability tests 92
3.2 Influence of cooling rate and annealing in a Cu-rich metallic glass composite 96
3.2.1 Effect of changes in diameter and cooling temperature in the microstructure 96
3.2.2 Scratch test 102
3.2.3 Antimicrobial and wettability tests 108
3.3 Discussion 114
4 Impact of surface roughness and oxidation on the antimicrobial activity of a Cu-based BMGC 120
4.1 Oxidation and roughness analysis 121
4.1.1 Examination of the microstructure 121
4.1.2 Influence of oxidation in the roughness of the metallic glass composites 126
4.2 Analysis of the Cu ion impact in the recovery and morphology of *E. coli* cells 129
4.2.1 Antimicrobial tests 129
4.2.2 Cu ion diffusion 134
4.2.3 Minimum Inhibitory Concentration tests 135
4.2.4 Antimicrobial maps 137
4.3 Conclusions 139

5 Effect of magnetron sputtering pressure and temperature in the “wet” and “dry” antimicrobial properties of Cu-based thin films 141
5.1 Structure and physiochemical properties of the deposited thin films..... 142
5.1.1 Roughness and microstructure analysis..... 143
5.1.2 Wettability tests..... 149
5.2 Antimicrobial tests, “wet” vs “dry”, a first approach to real conditions..... 151
5.2.1 Influence of drying in the bacteria recovery..... 151
5.2.2 “Wet” and “dry” tests 155
5.2.3 Copper ion diffusion of Cu-Zr thin films 160
5.2.4 Influence of Cu-Zr thin film contact in the internal and external morphology of bacteria..... 161
5.2.5 Impact of bacteria deposition in the morphology of the films 164
5.3 Conclusions 166
6 Summary and future directions. 168
Presentations and publications 171
Publications..... 171
Presentations 171
References 173

List of abbreviations and symbols

Abbreviation	Meaning	Units
BMG	Bulk metallic glass	
BMGC	Bulk metallic glass composite	
CA	Contact angle	
CFU	Colony forming units	CFU/mL
CMC	Critical micelle concentration	
ΔH_{mix}^{AB}	Enthalpy of mixing between elements A and B	KJ/mol
ϕ_{crit}	Critical diameter	mm
E	Young's modulus/Elastic modulus	GPa
E_r	Reduced Young's modulus	GPa
GFA	Glass forming ability	
GN	Gram-negative bacteria	
GP	Gram-positive bacteria	
H	Nanoindentation hardness	Mpa
h_{max}	Maximum indentation depth	nm
H_S	Scratch Hardness	GPa
HAI	Hospital-associated infections/Hospital-acquired infections	
LB	Luria Bertani	
MG	Metallic glass	
MGC	Metallic glass composite	
MIC	Minimum inhibitory concentration test	
MRSA	Meticillin-resistant Staphylococcus aureus	
MscL	Mechanosensitive channel of large conductance	
MscS	Mechanosensitive channel of small conductance	
OD_{600}	Optical density measured at 600 nm	
R	Antimicrobial activity	
R_a	Arithmetic average of the roughness profile	nm
R_z	Average distance between the highest peak and lowest	nm
ROS	Reactive oxygen species	
STZ	Shear Transformation Zones	
SZM	Structural zone model (i.e. Thornton's)	
σ_y	Elastic limit	MPa
T_g	Glass transition temperature	°C or K
T_p	Peak temperature	°C or K
T_L	Liquidus temperature	°C or K
T_{rg}	Reduced glass temperature	°C or K
T_x	Onset temperature of crystallization	°C or K

List of Figures

Figure 1 Image showing surfaces susceptible of bacteria colonization (a) in a ward hospital and (b) number of bacteria per cm^2 recovered from bed rails (dark blue bars), call buttons and computer mice (red bars), arms of chairs (yellow bars), tray tables (light blue bars), data input devices and palm rest of laptop computer (purple bars) and IV poles (grey bars) over 23 months [30]. Red lines indicate the number of pathogens susceptible to cause an infection. 3

Figure 2 Example of a Gram staining result of a mixture between Staphylococci (GP) and *E. coli* (GN). Gram positive bacteria are stained violet, while Gram negative cells are pink stained [41]. 5

Figure 3 Cell membrane differences between Gram-positive and Gram-negative bacteria [44]. 6

Figure 4 Picture depicting the antimicrobial mechanisms of Cu ions diffused from a Cu-Zr-based bulk metallic glass (BMG) [66]. 11

Figure 5 *E. hirae* survivors against time for cultures treated with pure Cu. And copper oxides (CuO and Cu_2O) nanoparticles [68]. 12

Figure 6 Diagram showing the mechanism behind the photocatalytic disinfection of TiO_2 through the development of ROS (i.e. O_2^-) and Hydrogen Peroxide (H_2O_2) [95]. 15

Figure 7 Halo disinfection system making use of dry mist-generated hydrogen peroxide technology [134]. 20

Figure 8 Hand baton (a) before and (b) after two years of discontinuous hand contact used in Fredj's work [162]. 24

Figure 9 Images showing the (a) changes in turbidity between six MGs and an iron nail and (b) inhibition zone measurements for the same materials [187]. 32

Figure 10 Bright field TEM image of (a) a MGs [201] and (b) a crystalline material exhibiting typical interface between two crystalline phases [202]. 35

Figure 11 Sketch showing the differences between atomic rearrangement between monocrystalline, polycrystalline and amorphous materials. 36

Figure 12 Elastic limit (σ_y) versus Young's modulus (E) for several crystalline metallic alloys, composites and MGs [203]. 39

Figure 13 SEM images showing the lateral surfaces of compression BMGs samples. Note the serrated-flow behaviour and fracture mechanism is caused by multi-step shearing due to energy dissipation through shear banding [219]. 40

Figure 14 Design of Duwez's gun technique of splat quenching [241]. 42

Figure 15 Section of a Cu-based alloy casted in a wedge-shaped mould [247]. The increase in cross section lowered the cooling rate in the centre of the sample, causing the crystallization of the melt from completely crystalline (blue oval) to higher volume fractions (i.e. section A 10 % and section B 31 %). 44

Figure 16 Concentration vs radii plot of the constituent elements with concave downward shape [262]. 48

Figure 17 Deformation models for MGs (a) Spaepen and (b) Argon [278]. 50

Figure 18 Tensile test numerical simulation showing the increase in ductility caused by crystalline inclusions in BMGs (a and b) in contrast to the (c) brittle behaviour inherent to BMG. Lower panels display the shear band formation for a BMGC (a) v_f = 43 % ε_{xx} = 1.5 %, (b) v_f = 43 % ε_{xx} = 6.5 % and BMG (c) ε_{xx} = 1.5 % [288]. 52

Figure 19 CuZrAl bulk sample subjected to a scratch test showing the three common mechanisms of abrasive, adhesive and fatigue wear. 53

Figure 20 Stress components as a function of the maximum stress (q_0) and the ratio between the contact depth (z) and the radius of the circle of contact (b) [296]. 55

Figure 21 Image depicting the structural changes in a Cu-Zr-Al-Ni alloy due to the sliding contact of a pin-on-disc configuration as composition and load increased [293]. 57

Figure 22 Scratch test profile showing the total pile-up area (red) and the groove cross section area (green). 58

Figure 23 Cu-Zr phase diagram [326]. 60

Figure 24 Evaluated isothermal sections of the Al-Cu-Zr system for (a) liquidus [349] and (b) 800°C [354]. 63

Figure 25 Compact Arc Melter MAM-1 (a) equipment, (b) schematic 3D model of the chamber and (c) Cu-Zr-Al 2 mm rod. 68

Figure 26 Example of SEM images obtained for *E. coli* cells deposited on stainless steel after (a) 1 and (b) 7 days of incubation. 71

Figure 27 Schematic diagram showing the antimicrobial tests. 73

Figure 28 Example of inoculated and sealed samples: (a) BMGs and (b) stainless steel. 73

Figure 29 Example of LB agar plates of *E. coli* serial dilutions after 1 h of contact in (a) stainless steel and (b) Cu-based BMGC. Note that each colony (see red circles) corresponds to a single *E. coli* cell, which survived the antimicrobial tests. 74

Figure 30 XRD scans for samples (a) $Cu_{50}Zr_{44}Al_6$ (b) $Cu_{53}Zr_{41.4}Al_{5.6}$ and (c) $Cu_{56}Zr_{38.7}Al_{5.3}$ alloys [179]. 78

Figure 31 Backscattered SEM images taken from the middle radius for (a) $Cu_{50}Zr_{44}Al_6$, (b) $Cu_{53}Zr_{41.4}Al_{5.6}$ and (c) $Cu_{56}Zr_{38.7}Al_{5.3}$ alloys [179]. 80

Figure 32 Magnified backscattered SEM images taken from the middle radius for (a) $Cu_{50}Zr_{44}Al_6$, (b) $Cu_{53}Zr_{41.4}Al_{5.6}$ and (c) $Cu_{56}Zr_{38.7}Al_{5.3}$ alloys [179]. 82

Figure 33 Images showing the scratches at the middle radius of the samples (a) $Cu_{50}Zr_{44}Al_6$ (b) $Cu_{53}Zr_{41.4}Al_{5.6}$ and (c) $Cu_{56}Zr_{38.7}Al_{5.3}$ alloys [179]. 87

Figure 34 Average water contact angle on Cu-Zr-Al alloys (a, b and c) [179]. 93

Figure 35 Time-kill curve of *E. coli K12* and *B. subtilis 168* exposed to Cu-Zr-Al alloys for up to 250 min [179]. 95

Figure 36 XRD scans for $Cu_{52}Zr_{41}Al_7$ at. % alloy (a) CH 2 mm diameter, (b) NCH 2 mm diameter, (c) CH 3 mm diameter, (d) NCH 3 mm diameter and (e) 3 mm annealed at 850 °C for 48 h [13]. 97

Figure 37 Backscattered SEM images taken from the middle radius for $Cu_{52}Zr_{41}Al_7$ at. % alloy (a) CH 2 mm diameter, (b) NCH 2 mm diameter, (c) CH chilled 3 mm diameter, (d) NCH 3 mm diameter and (e) 3mm crystallized sample [13]. 99

Figure 38 Images showing the scratches at the middle radius of the samples (a) CH 2 mm diameter; (b) NCH 2 mm diameter; (c) CH3 mm diameter; (d) NCH 3 mm diameter; (e) 3 mm annealed at 850 °C for 48 h and (f) pure copper [13]. 103

Figure 39 Average water contact angle $Cu_{52}Zr_{41}Al_7$ at. % alloy (a) CH 2 mm diameter, (b) NCH 2 mm diameter, (c) CH 3 mm diameter, (d) NCH 3 mm diameter, (e)

Crystallized at 850 °C for 48 h, (f) 3 mm pure copper and (g) Stainless Steel [13]. 109

Figure 40 Recovery of *E. coli* exposed to indicated substrates. Each surface was inoculated with 1 µL of bacterial culture grown until OD_{600} = 0.3 [13]..... 110

Figure 41 Survival rate values for samples with highest difference in cooling rate (2 mm chiller and 3 mm no chiller) after 1, 2, 3 and 4 hours using the stainless steel CFU as 100% survival ratio [13]..... 111

Figure 42 Cu-Zr phase diagram [326] with the compositions analysed in this chapter. 115

Figure 43 Evaluated isothermal sections of the Al-Cu-Zr system for (a) liquidus [349] and (b) 800 °C [354] with the compositions analysed in this chapter..... 116

Figure 44 (a) XRD scans for the as-cast and oxidised $Cu_{55}Zr_{40}Al_5$ (at. %) BMGCs with the corresponding SEM backscattered images for the (b) as-cast and (c) oxidized samples. 121

Figure 45 (a) Secondary electron and (b) backscattered SEM images for the cross section of the 240 grit oxidized sample. (c) Compositional EDX mappings corresponding to Cu, Zr, O and Al. EDX spectra for all phases shown in the cross section backscattered image..... 123

Figure 46 XPS spectra of the oxidized $Cu_{55}Zr_{40}Al_5$ sample at 703 K for 5 h in the (a) untreated and (b) sputtered surface. In addition, Cu 2p, Zr 3d, Al 2s and O 1s core-level XPS spectra (c) from the oxidized sample without sputtering are shown. 125

Figure 47 Surface topography for all ground samples (240, 1200 and 4000) before and after oxidation. 127

Figure 48 Number of surviving *E. coli* cells deposited on steel and both as-cast and oxidized samples with different toughness for 1, 2.5 and 4 h of contact time. Morphology of the deposited *E. coli* bacteria on (a) 314SS, (b) 4000 as-cast and (c) 4000 oxidized samples after 4 h. 130

Figure 49 Mechanosensitive channels of (a) large and (b) small conductance [395]. 133

Figure 50 Minimum Inhibitory Concentration tests performed following the CLSI M07-A9 standard [413] and SEM images of *E. coli* treated with (a) 0.1 mM, (b) 3.5 mM and (c) 5.0 mM of $CuCl_2$ deposited on 314 stainless steel. 136

Figure 51 Sketch of an antimicrobial map for the current work: *E. coli* deposited on a BMGCs using LB broth as a growth medium. 138

Figure 52 X-ray diffraction scans for the thin films used in the present study (a) 1RT, (b) 3RT, (c) 5RT and (d) 3HT..... 144

Figure 53 SEM micrographs showing the cross-section and superficial morphology of the $Cu_{85}Zr_{15}$ coating. 146

Figure 54 Depiction of Thornton's Structural Zone Model (SZM) of sputtered coatings (T_m~1333 K) [326]. Adapted from [435]..... 147

Figure 55 Atomic Force Microscope scans of the thin films deposited on steel (a) 1RT, (b) 3RT, (c) 5RT and (d) 3HT. 148

Figure 56 Water contact angle images obtained for (a) 314 Stainless Steel, (b) 1RT, (c) 3RT, (d) 5RT and (e) 3HT..... 150

Figure 57 Number of *E. coli* and *S. aureus* Colony Forming Units per millilitre recovered from stainless steel in "dry" after 0, 15, 30 and 45 min of contact time. 152

Figure 58 SEM images of “wet” (a,b) and “dry” (c,d) *E. coli* and *S. aureus* cells deposited on stainless steel after 1 h. 153

Figure 59 SEM image showing the presence of NaCl crystals after the drying of LB broth. 155

Figure 60 Number of *E. coli* Colony Forming Units per mL (CFU/mL) recovered in “wet” conditions after 4 h of contact time. 156

Figure 61 Number of *S. aureus* Colony Forming Units per mL (CFU/mL) recovered in “wet” and “dry” tests after 1, 2.5 and 4 h of contact with stainless steel and the Cu-based thin films. 157

Figure 62 SEM images of *S. aureus* deposited for 4h on 1RT in a) “wet” and c) “dry” conditions and 5RT in b) “wet” and d) “dry” conditions. 162

Figure 63 TEM images of *E. coli* and *S. aureus* deposited for 4 h on Stainless Steel (a, b) and the 5RT thin film (c, d). 163

Figure 64 SEM images of the Cu-Zr thin films after 4 h of contact with the LB broth in “wet” and “dry” conditions. 165

List of Tables

Table 1 Factors that can facilitate transmission of HAI [38]. 4

Table 2 Usual composition of cleaning products [122]. 19

Table 3 Summary of antimicrobial testing standards. 26

Table 4 Advantages and drawbacks of MGs [203,216,217]. 38

Table 5 Some of the most common and accepted GFA criteria. 46

Table 6 Atomic radii (nm) and enthalpy of mixing (ΔH_{AB}^{mix}) for the elements discussed [331]. 61

Table 7 Elements used in the preparation of BMGCs and TFMGs. 66

Table 8 Crystalline phases detected in the analysis of all samples. 69

Table 9 Composition in at. % of the areas labelled on Figure 32 and phases to which they can be attributed. 83

Table 10 Summary of the pile-up height, groove deep at the centre and maximum, groove area over the pile-up area, track width, scratch hardness number, arithmetic average of the roughness profile and average distance between the highest peak and lowest valley for $Cu_{50+x}(Zr_{44}Al_6)_{50-x}$ (x = 0, x = 3 and x = 6). 88

Table 11 Summary of the mechanical properties of the $Cu_{50}Zr_{44}Al_6$, $Cu_{53}Zr_{41.4}Al_{5.6}$ and $Cu_{56}Zr_{38.7}Al_{5.3}$ alloys after nanoindentation using a maximum load of 300 mN. The values of hardness (H), reduced Young´s modulus (E_r, H/E_r, H^3/E_r^2) ratios and maximum indentation depth (h_{max}) are given in the table. 88

Table 12 Antimicrobial activity of samples. 93

Table 13 Codenames for the samples analysed in this section..... 96

Table 14 Composition in at. % of the areas labelled on Figure 37 and phases to which they can be attributed. 100

Table 15 Summary of the pile-up height, groove deep at the centre and maximum, groove area over the pille-up area, track width, scratch hardness number, arithmetic average of the roughness profile and average distance between the highest peak and lowest valley for the samples: CH 2 mm diameter, NCH 2 mm diameter, CH3mm diameter NCH 3 mm diameter, 3 mm annealed at 850 °C for 48 h and pure copper. 104

Table 16 Antimicrobial activity calculated using JIS Z 2801:2010 Antibacterial products -- Test for antibacterial activity and efficacy [171]. 113

Table 17 Reduction of bacteria percentage calculated using US EPA Protocol for the Evaluation of Bactericidal Activity of Hard, Non-porous Copper Containing Surface Products [173]. 114

Table 18 Summary of the arithmetic average of the roughness profile and average distance between the highest peak and lowest valley for several grit papers. 128

Table 19 Copper ion release (ppb) for the 4000 as-cast and 4000 oxidized samples. 135

Table 20 Summary of the deposition parameters used during the preparation of the Cu-Zr thin films. 142

Table 21 Compositional analysis and thickness measurements of the Cu-Zr thin films. 143

Table 22 arithmetic average of the roughness profile (R_a) and average distance between the highest peak and lowest valley (R_z) for the substrate and Cu-Zr thin films. 149

Table 23 Antimicrobial activity of the thin films obtained as stated in JIS Z 2801:2010 "*Antibacterial products—test for antibacterial activity and efficacy*" [171]. 158

Table 24 Percentage reduction of the thin films obtained as stated in U.S. EPA "*Protocol for the Evaluation of Bactericidal Activity of Hard, Non-Porous Copper-Containing Surface Products*" [173]. 159

Table 25 Copper ion release (ppb) for the 1RT and 5RT thin films 161

List of Equations

Equation 1 Antimicrobial activity (JIS Z2801:2010) 26

Equation 2 Reduction percentage (US EPA) 27

Equation 3 The λ parameter and the condition for crystal instability [261] 47

Equation 4 Contact temperature rise in a pin-on-disc configuration [312] 56

Equation 5 Scratch hardness number [314] 58

1 Introduction

1.1 Antimicrobial properties of metallic surfaces, metallic glasses and metallic glass composites

1.1.1 Why it is important to develop bactericidal surfaces?

The importance in developing new bactericidal materials can be summarized in two great hazards for public healthcare: increasing rates of nosocomial or hospital-acquired infections (HAI) and the emergence of antibiotic-resistant pathogens or "superbugs". Despite the efforts and economic resources invested in tackling nosocomial infections, the number of diseases acquired during in-patient hospital stay remain significant. The number of HAI in European hospitals was around 3.2 million in 2011-2012 [1-5], while in America 2 million patients are infected annually, of whom about 90,000 die [6], leading to an estimation of 5-10 % hospitalizations in Europe or North America result in a HAI [7,8]. At the same time, the emergence and transmission of antimicrobial resistance pathogens represents a major hazard. After decades of exposure to antibiotics in medicine and agriculture, pathogens (i.e. *New Delhi Metallo-Beta-Lactamase* (NDM-1) and *Klebsiella pneumoniae Carbapenemase* (KPC-2)) have evolved and transmitted resistance mechanisms to common and, in some cases, "last resource drugs" (i.e. colistin) [9-12]. The evolution of pathogens had led to the dawn of a post-antibiotic era with heavy economic and human consequences. As such, the World Health Organization is assessing and coordinating global action to tackle this threat to public health [13].

The options available in challenging antibiotic-resistance bacteria are limited. The development of new antibiotics and an increase in control and correct prescription of these substances are common approaches [14,15]. While antibiotic research and correct management can be short-term options, mutations of bacteria will result in antibiotic resistance. A long-term solution, in part, will rely on the development of new bactericidal materials, such as natural biocides. Phoenicians, Romans and Greeks were aware of the bactericidal properties of silver, making use of silver bottles and vessels to prevent water spoilage. Tuberculosis, skin problems and other infections were avoided by the use of copper [16]. These materials and their compounds were

relegated to a second place with the discovery of antibiotics. However, antibiotic-resistant bacteria have awakened the interest in new antimicrobial agents.

The importance of these materials is linked to the origin of nosocomial infections. Recent studies have shown that common Hospital Acquired Infections are related with central line-associated bloodstream infections, catheter-associated urinary tract infections, surgical site infections and ventilator-associated pneumonia [17]. These are the most common infections detected in health care units, but, where do they come from? Environmental contamination in hospitals was deemed as an insignificant contributor to nosocomial infections during the 70s and 80s [18-20]. However, modern studies are showing that sufficient pathogens to cause an outbreak can be found on health care surfaces [21-23] (Figure 1a and 1b). A clear example is shown by Weinstein's analysis of intensive care units, which revealed that 20 to 40 % of nosocomial infections can be attributed to cross contamination due to hand touch after direct or indirect contact with the patient or touch surfaces [24]. Hospital furnishing displays broad use of stainless steels, aluminium, plastics and woods, but most of them are not able to remove such pathogens. Wilks et al. [25] long term analysis of 304 stainless steel shown that large populations of E. coli cells (i.e. 10^5-10^7 viable cells) could survive more than a month on this material, while studies conducted on aluminium display large bacteria concentrations after eight days [26]. Similarly, the work of Milling et al. [27] on the survival of bacteria in wood and plastics revealed that similar populations could survive on these materials for more than nine days. More examples can be found in the extensive review of Kramer et al. [28] and specialized texts [29] which conclude that most nosocomial pathogens can survive weeks or months in most inanimate surfaces. Although the role of touch surfaces in nosocomial infections is still controversial, the long survival times of pathogens deposited on common touch surfaces and the threat posed by the emergence of antibiotic resistant bacteria led to recognize touch surfaces as a potential source of infection.

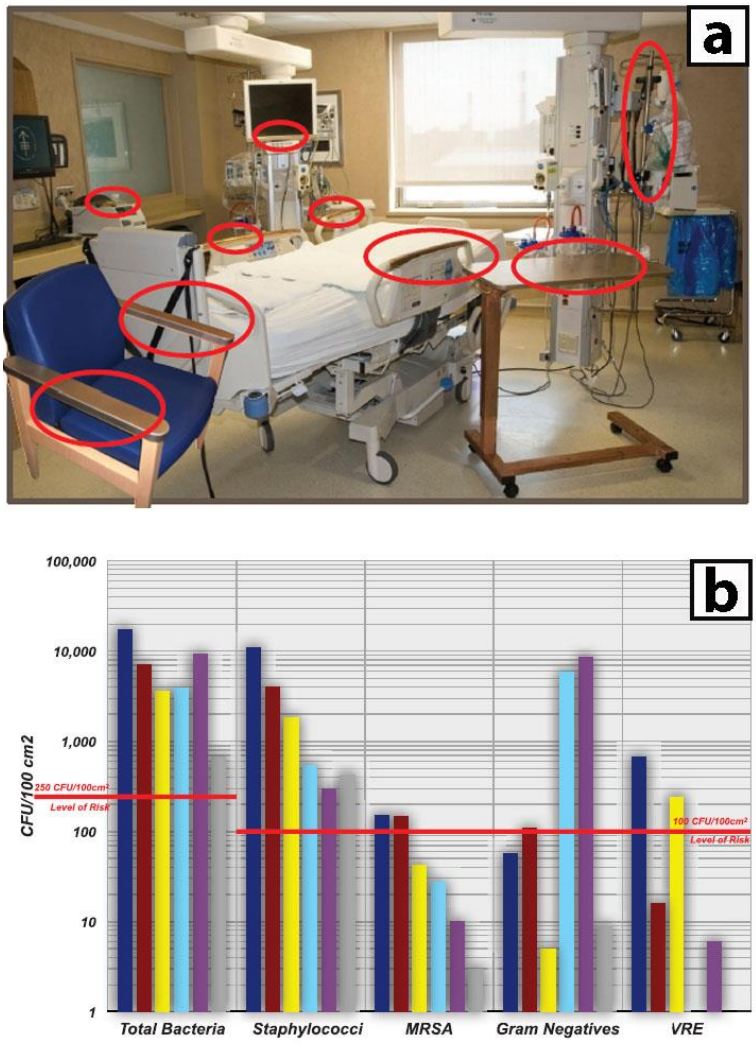

Figure 1 Image showing surfaces susceptible of bacteria colonization (a) in a ward hospital and (b) number of bacteria per cm^2 recovered from bed rails (dark blue bars), call buttons and computer mice (red bars), arms of chairs (yellow bars), tray tables (light blue bars), data input devices and palm rest of laptop computer (purple bars) and IV poles (grey bars) over 23 months [30]. Red lines indicate the number of pathogens susceptible to cause an infection.

Hospital cleaning and disinfection can contribute to control of HAI. Adequate cleaning protocols and proper disinfectants may be of use in infection control. However, cleanliness of hospitals is mostly assessed by simple visual inspection after sterilisation of surfaces with chemicals (i.e. chlorine) [31,32]. The use of visual inspection to evaluate the cleanliness of microorganisms may not be optimal. Microbiological sampling, bioluminescence and ultraviolet marking have been used to increase the awareness in disinfection thoroughness and to assess the validity of

"visual inspection" [32-35]. These analyses revealed that surfaces considered as "clean" did not meet benchmark values in 70% to 90% of the cases, rendering visual inspection as an inadequate method. The implications of these results are especially alarming when some nosocomial infection pathogens (i.e. *Staphylococcus aureus*, *Clostridioides/Clostridium difficile* or *Acinetobacter baumannii*) can survive for weeks in hospital facilities [36,37]. This weakness in preventing nosocomial infections, is not the only one inherent to disinfection. The number of touch surfaces susceptible for bacteria colonization is enormous (towel distributor, light switches, toilets, buttons, door handles, sinks, push plates, bed rails, monkey pulls, bedside tables etc), and disinfection of these surfaces is transient. After the chemical has dried up, surfaces are susceptible to bacteria colonization. The difficulty of maintaining cleanliness in hospital is further increased by the characteristic of most nosocomial pathogens (Table 1). Taking into account the lack of a standard to assess hospital cleaning, the short-term effect of disinfection in hospital furniture and the characteristics of HAI pathogens, it is of great importance to develop touch surfaces with antimicrobial properties.

Table 1 Factors that can facilitate transmission of HAI [38].

Pathogen able to survive for prolonged periods of time on environmental surfaces
Ability to remain virulent after environmental exposure
Contamination of the hospital environment frequent
Ability to colonize patients
Ability to transiently colonize the hands of health care workers
Transmission via the contaminated hands of healthcare workers
Small inoculating dose
Relative resistance to disinfectants used on environmental surfaces

To develop effective antimicrobial materials, it is important to understand the pathogens involved in HAI. The number of pathogens reported as nosocomial

infection sources is impressive, however, four have a major role in Health-care Acquired Infections: the enterococci, *Pseudomonas aeruginosa*, *S. aureus* and *Escherichia coli* [8,39,40]. These four bacteria can be classified by their ability or inability to be stained with Gram's Method, in honour to its developer Hans Christian Gram (1853-1938). This differential staining method divides bacteria in two large groups, Gram-positive (GP) violet stained cells and Gram-negative (GN) pink stained cells (Figure 2).

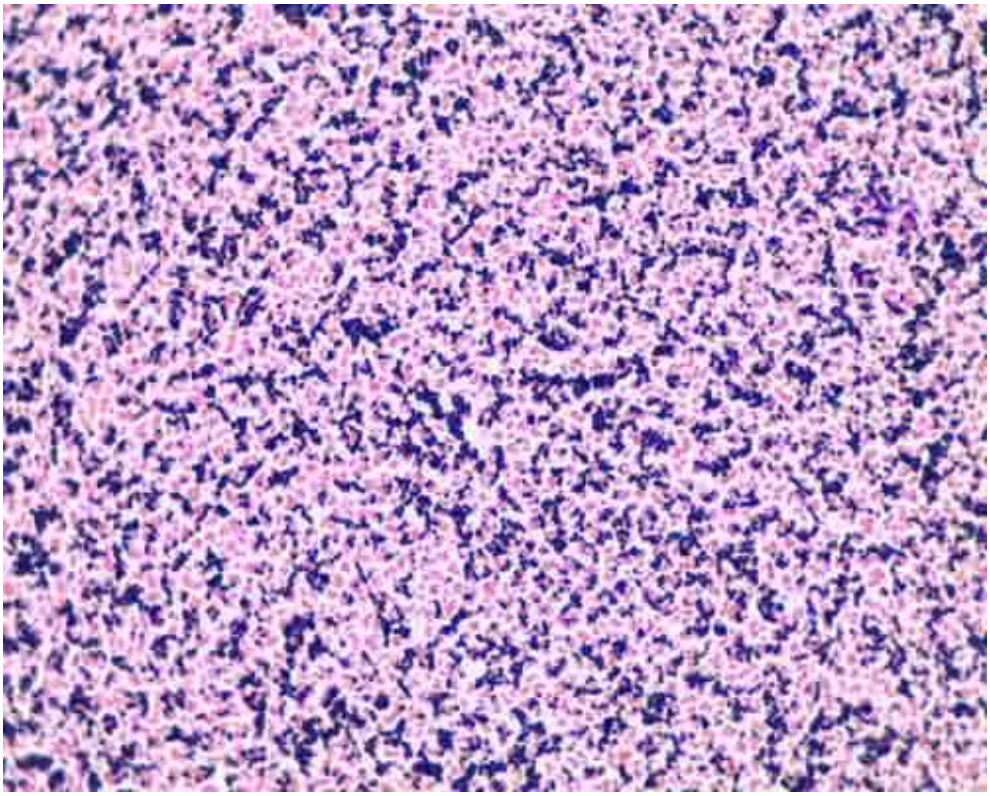

Figure 2 Example of a Gram staining result of a mixture between Staphylococci (GP) and *E. coli* (GN). Gram positive bacteria are stained violet, while Gram negative cells are pink stained [41].

The distinction between pathogens in Gram's staining method is caused by differences in the cell walls between GP and GN bacterium (Figure 3) [42,43]. Gram-positive bacteria cell walls have a thick outer layer of peptidoglycan (a polysaccharide cross-linked by short peptides) that overlays their cytoplasmic membrane. The cell wall of GN bacteria also includes a peptidoglycan layer, but this structure is smaller and enclosed by an outer membrane. The outer membrane is composed of

Lipopolysaccharides (a lipid connected to multiple repeats of a variable polysaccharide) which protects the cell. During staining, the first step is to apply crystal violet as the primary stain and to smear the inoculum with an iodine solution to bind the dye. After this step, all bacteria are dyed violet, as the violet crystals are embedded into the cell walls. The crucial step is to use a decolorizing agent (i.e. ethanol, acetone), which is able to dissolve the outermost cell layer of GN bacteria. The peptidoglycan layer becomes dehydrated and collapses, the extensive matrix formed by the collapsed GP peptidoglycan impedes efflux of the crystal violet-iodine complex. This efflux cannot be prevented by the less extensive collapsed peptidoglycan of GN bacteria, which are decolourised. In the final step, a pink counterstain safranin is applied, conferring GN bacteria their familiar pink staining (Figure 2). In the case of common nosocomial pathogens, the use of Gram's Method results in enterococci and *S. aureus* being Gram-positive (GP) bacteria, while *P. aeruginosa* and *E. coli* are Gram-negative (GN) bacteria.

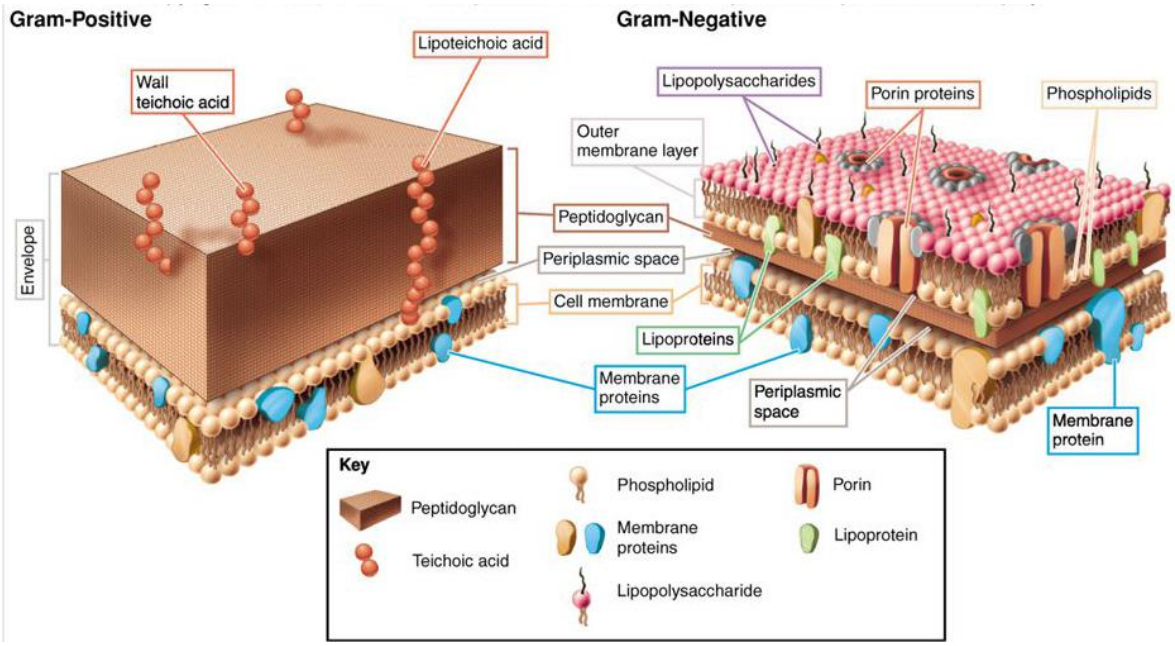

Figure 3 Cell membrane differences between Gram-positive and Gram-negative bacteria [44].

The importance of Gram's classification for reducing nosocomial infections resides in the implications that such differences in cell wall morphology have in the elimination of pathogens. The peptidoglycan structure present in GP bacteria offers high

resistance to physical disruption, desiccation and endurance to some cleaning chemicals [43]. On the other hand, the three-layered structure of GN bacteria provides partial resistance against some antibiotics (i.e. penicillin) while, at the same time, can complicate the administered treatment. When the cell dies, the lipid present in the outer membrane (Lipid A) is released. This organic chemical can cause fever, vasodilation, inflammation, shock and blood clothing, endangering the life of the patient [43]. For these reasons, special care has to be given to eliminate these pathogens.

Due to these differences Gram-negative bacteria, such as *E. coli* and others, are of special concern in HAI [45-47]. Gram negative bacteria display high efficiency in acquiring drug resistance [48]. These pathogens can develop multiple mechanisms against a single drug or multiple mechanisms for different medications, resulting in a high hazard for public safety. Gram negative bacteria have been accounted for approximately 30 % of all nosocomial infection, being of relevance in ventilation-related pneumonia and urinary tract infections [48]. The difficulty in developing new antibiotics, linked to the efficiency of these pathogens to render new medications ineffective, highlights the necessity of new bactericidal materials. Antimicrobial touch surfaces may be of great help in this regard by passively and continuously disinfecting large areas.

It is also important to note here that even if powerful antimicrobial touch surfaces are developed, the role of disinfection and cleanliness standards in healthcare facilities cannot be disregarded. During the second European cost action for AntiMicrobial Coating Innovations (AMiCI, 2017) conference in Pori (Finland) [49], the complications inherent to develop and commercialize new antibacterial products, as well as, the role of antimicrobial materials in HAI and the importance of hospital cleanliness in nosocomial infections were highlighted. In this cost meeting, it was shown that bactericidal materials are not the panacea for HAI, and that they must be used with new standards and protocols of hospital cleanliness.

1.1.2 Antimicrobial mechanisms of touch surfaces

In the following pages the most common antimicrobial metallic agents are presented and analysed from the point of view of bactericidal touch surface development. It should be noted that numerous materials with bactericidal properties can be found in the literature. As an example, there is great interest in bactericidal polymers due to their versatility and the large range of strategies available to modify their behaviour [50-52]. However, some of these materials can be highly toxic for the environment, and long-term antibacterial activity is still a concern for their applications in healthcare facilities [53]. At the same time, this thesis is focused on the development of antimicrobial metallic touch surfaces, letting antibacterial polymers out of the scope of this document.

Before continuing with the description of antimicrobial metals, the distinction between cytotoxic and antimicrobial materials must be explained. Cytotoxicity is defined as the ability of a substance to eliminate living human cells via necrosis or apoptosis. This term is normally referred to as the crucial property for implant development, as it describes the potential for the material to harm the patient. On the other hand, a biocidal or antimicrobial agent is a substance that controls harmful or unwanted microorganisms. While cytotoxicity is of interest for other fields of work, only materials labelled as antimicrobial will be treated in this section.

Four metallic elements have been extensively researched for their high bactericidal properties: copper, silver, zinc and titanium. While other bactericidal metals exist in nature, in fact, most metallic elements are toxic in high enough concentrations (e.g. iron or aluminium) [54], several disadvantages restrict their applications. Metallic elements which require relatively high concentrations to be effective biocidals may pose a hazard in the long term. Other elements like nickel must be disregarded due to their allergenic nature [55]. Those metallic elements which require lower concentrations, such as Gold [56] or Cadmium [57], may be of interest for specific applications. However, their high cost and limited antimicrobial activity when compared with the four mentioned materials, render these other elements as inadequate for high-touch surfaces.

The bactericidal properties of copper have been known since ancient times. The first written record of Cu used to sterilize water and prevent infection of chest wounds is documented in the Smith papyrus, dated between 2600 and 2200 BC [16,58]. Since then, Persians, Phoenicians, Greeks and Romans made use of copper and silver containers to preserve food and water [54]. In the modern era, the discovery that copper workers seemed immune to cholera lead to its use to treat chronic adenitis, eczema, impetigo, scrofulosis, tubercular infections, lupus, syphilis, anemia, chorea, and facial neuralgia [16]. The same interest led to the discovery of the Bordeaux mixture, a blend of $CuSO_4$ and $Ca(OH)_2$, which was used in agriculture to protect crop fields [54]. The interest in copper as an antimicrobial material dwindled with the discovery of antibiotics. Nevertheless, the hazard to healthcare posed by antibiotic-resistant pathogens and the increase in nosocomial infections has reawakened interest in copper.

Copper is one of the best natural antimicrobial agents. In vitro dry studies of this element have showed $\log_{10}$ reductions as high as 8 in just a few minutes [58]. While the antimicrobial activity of copper surfaces is reported to be reduced in wet conditions, this material is able to eliminate “superbugs” like MRSA in one to two hours [58]. This high contact killing efficiency is commonly attributed to the incorporation of Cu ions in the pathogens [59-64], while the work of Hans et al. attributes some of these characteristics to the oxidation of copper ions [65]. However, the main mechanism behind the biocidal properties of copper is not completely understood. Elimination of bacteria by copper has been suggested to occur in three different ways, thereby limiting the risk of emerging bacterial resistance (Figure 4):

- Cell membrane destruction: Copper ions have been found to directly damage the cell membrane of bacteria [58,62,66]. The lack of structural integrity can lead to the destruction of the cell due to inner and outer pressure differences, effectively killing the pathogen.

- DNA degradation: Copper ions have been reported to damage deoxyribonucleic acid (DNA) chains [58,66]. The damage suffered by these structures will destroy the ability of bacteria to synthesize essential chemicals, killing the cell.

- Reactive oxygen species (ROS): Besides the direct damage that copper ions can cause, they promote the generation of highly reactive radicals; in the presence of liquid water, highly damaging species such as hydroxyl radicals (OH^-) from hydrogen peroxide (H_2O_2) [58]. The reaction of copper with water in the environment or within the liquid inside the cell (cytosol or cytoplasmic matrix) causes a Fenton-like reaction, promoting the release of these species. The contact of these species with lipids, proteins, enzymes and DNA can cause their destruction. As such, these substances have a role in DNA degradation and cell membrane destruction.

These three mechanisms, cell membrane destruction, DNA degradation and highly reactive radical formation are the most commonly accepted mechanisms to explain the antimicrobial activity of copper, however, other mechanism had been correlated with the bactericidal effect of metals [54]. Leaving behind the discussion about the most important mechanism which causes the antimicrobial properties of copper, this element is an exceptional biocide. The high antibacterial effect coupled with its relatively low cost has awakened a strong interest in copper, evidenced by the creation of associations like the Copper Development Association, a not-for-profit trade association that supports and promotes copper usage in the UK and the US [67].

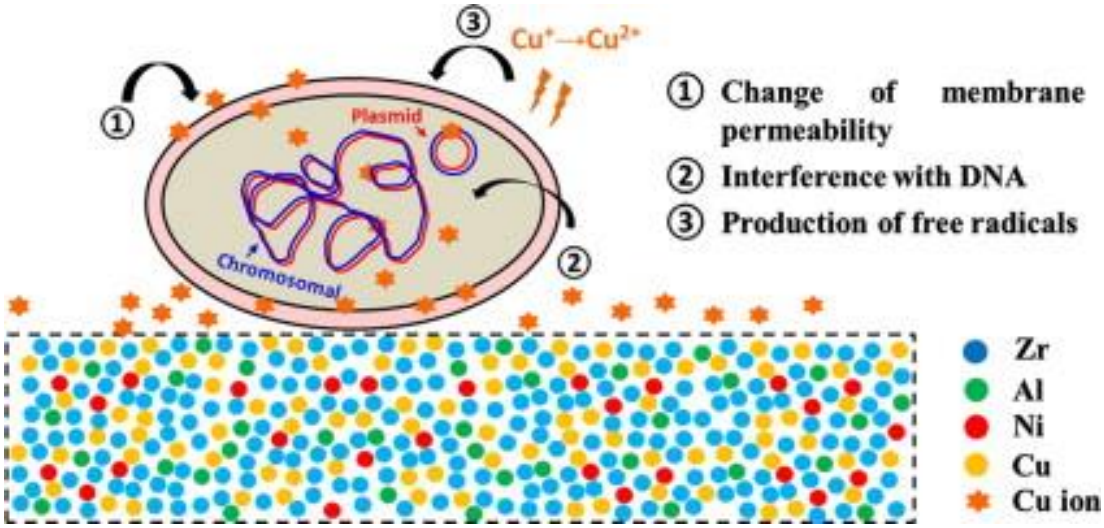

Figure 4 Picture depicting the antimicrobial mechanisms of Cu ions diffused from a Cu-Zr-based bulk metallic glass (BMG) [66].

Similarly to pure copper, the antimicrobial mechanisms of copper oxides are not completely understood [65,68]. These copper species seem to exhibit several mechanisms, however, the primary source of bactericidal properties is the contact between copper and pathogens. Hans et al. [68] work on Cu, CuO and Cu_2O revealed that the formation of copper oxides and the release of Cu ions from these species were fundamental to their antimicrobial properties. Their most interesting result arose from the comparison between antibacterial activity of pure copper and its oxides, as they revealed that the optimal biocidal activity was exhibited by pure copper followed by Cu_2O, with CuO possessing the lowest bactericidal activity of the series (Figure 5). Consequently, copper oxidation may be detrimental to the antimicrobial activity of copper.

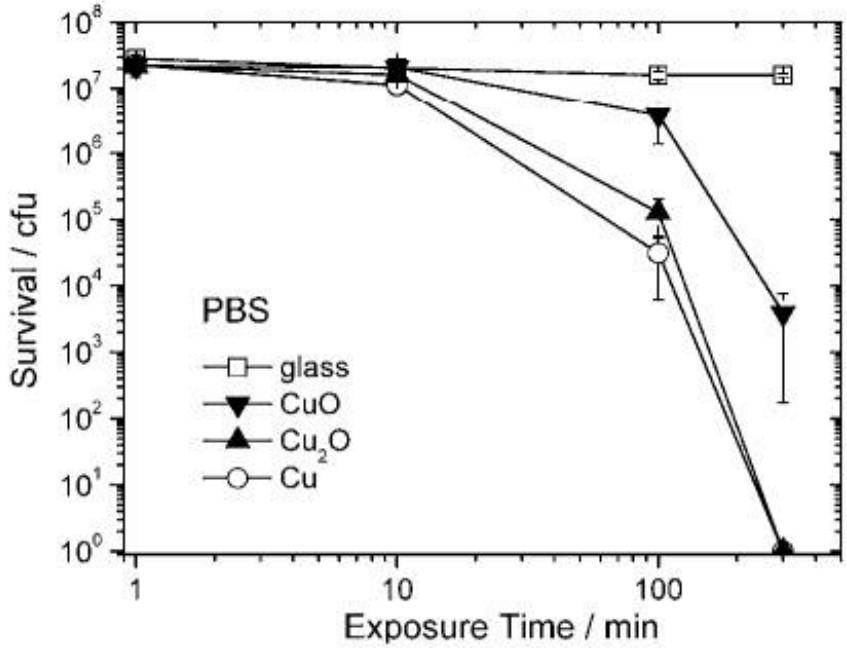

Figure 5 *E. hirae* survivors against time for cultures treated with pure Cu. And copper oxides (CuO and Cu_2O) nanoparticles [68].

The history of silver as a biocide can be traced from ancient times. Similarly to copper, silver containers from Persians, Phoenicians, Greeks and Romans were found to be used to preserve food and water [54]. More recently in the Second World War, it was common to drop silver coins in water containers to prevent the proliferation of bacteria [54]. Although, historically silver has been considered as an antibacterial metal, modern research has shown that pure silver does not exhibit potent antimicrobial properties [69]. The antibacterial properties associated with the metal are now attributed to the release of high toxic ions from silver oxides. Rebelo et al. [70] showed this fact when comparing the antimicrobial activity of Ag_xO thin films with pure silver. In their study, small coupons of silver and silver oxide were placed in contact with *Staphylococcus epidermidis* and *S. aureus* spread onto an agar plate (agar diffusion tests). After 24 h of incubation, the silver oxide coupons revealed a small “halo” of bacterial growth inhibition, while the pure silver samples did not impede normal bacterial growth [70]. While other variables can affect the antimicrobial activity of the samples (i.e. heterogeneous growth of the oxide coatings), it is clear that silver oxides are the compounds accountable for the biocidal properties of silver. This fact has led to a growing interest in developing silver oxide nanoparticles [71-73] or the

enhancement of silver ionization with the oxidising compound sodium hypochlorite [74]. Albeit their antimicrobial activity, the high cost of silver limits the application of silver and silver oxides in healthcare facilities.

Similar to silver, the antimicrobial properties of pure zinc have limitations. Zinc ions (Zn^{2+}) have antimicrobial activity, however, this is restricted to specific strains of microbial and fungal cells [75]. Although the antimicrobial activity of zinc ions is real, their role in the antimicrobial properties of Zinc oxide is still under scrutiny. According to the work of Sawai et al. [76] and Zhang et al. [77], hydrogen peroxide can be generated when zinc oxide and zinc ions react with water. As it will be seen in *section 1.1.3 Antimicrobial surfaces vs common disinfection methodologies*, hydrogen peroxide is a powerful disinfectant, thus indicating that the role of zinc ions in the biocidal properties of this element may be limited. At the same time, zinc oxide has a synergistic effect with certain Ultraviolet Light (UV-A) radiation. This photocatalytic effect is commonly attributed to the release of reactive oxygen species (ROS) through redox reactions [78]. Ercan et al. [79] have shown that irradiation of ZnO nanoparticles can enhance their antimicrobial activity from 0.7 $\log_{10}$ reductions to a 6 $\log_{10}$ reduction after 60 min of contact killing. This enhancement of the antibacterial effect of ZnO coupled with its broader antimicrobial spectrum than pure zinc, has increased the interest of using ZnO as a biocide [75,80]. However, most of the available work has been conducted in nanoparticles, with special focus on the changes in antimicrobial activity caused by variations in particle size. In this regard, it is interesting to consider the comparison between Ag, Zn and Au oxide particles led by Hernández-Sierra [81]. In this paper, it was discovered that smaller particle size displayed better antimicrobial properties, however, composition played a major role in the biocidal properties, silver oxide being the best material. As a result, the implementation of Zinc oxide as a high touch surface may be of interest if UV treatments were included, but more research is necessary.

Photocatalytic disinfection using UV light is of special relevance for the last antibacterial metallic element considered in this section, titanium dioxide (TiO_2) [78,82]. Titanium dioxide is inert to bacterial cells in its natural state but when irradiated with UV light in the 300-500 nm spectrum it exhibits antibacterial activity [83]. Like ZnO, the mechanism responsible of the antibacterial properties of TiO_2 is

the release of ROS and Hydrogen Peroxide on irradiation with UV light (Figure 6). Nevertheless, the literature on the antimicrobial activity and the photocatalytic effect of this material is richer than that available for zinc oxide [78,84-88]. In regards to its antimicrobial properties, some titanium oxide films exposed to UV radiation have achieved reductions of 6 $\log_{10}$ after 3 h of irradiation [84]. This slow contact killing time has been an issue for titanium dioxide materials, but modern research on TiO_2 composites may be the key to succeed in increasing their antimicrobial activity. The biocidal properties of titanium dioxide have been found to be increased by the addition of silver and copper [89-92]. The increase of antimicrobial activity in multi-layered films with silver is especially outstanding. Reddy et al. [93] were able to reduce the contact killing time of *E. coli* in titanium dioxide coatings from 1 h to 16 min. It is possible that this increase in antimicrobial activity is caused by the release of silver ions. In contrast, Page et al. [91] and Akhavan [89] suggest that the combination of these elements enhances only the photocatalytic effect on titanium dioxide. Their comparison between non-irradiated and irradiated composites showed that the non-irradiated films lacked any biocidal effect, while the irradiated composites exhibited higher antimicrobial activity than the TiO_2 films. Consequently, the properties of these composites are subjected to thin film composition and illumination spectrum similarly to titanium dioxide [89]. The extensive research, high stability of the film and self-cleaning properties have increased interest in this material for use in the prevention of nosocomial infections. Nevertheless, only a limited antimicrobial activity has been displayed in real conditions [94].

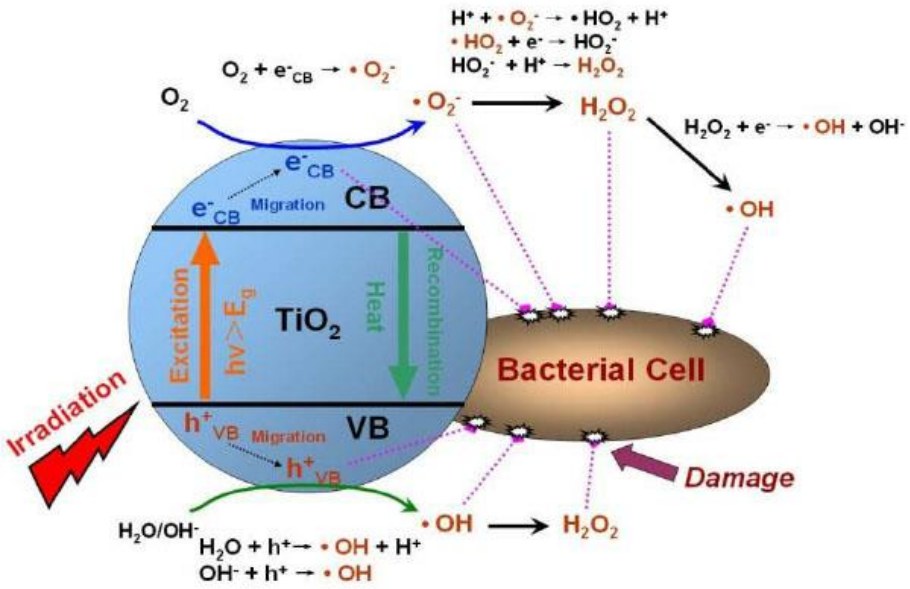

Figure 6 Diagram showing the mechanism behind the photocatalytic disinfection of TiO_2 through the development of ROS (i.e. O_2^-) and Hydrogen Peroxide (H_2O_2) [95].

Until this point, the discussion regarding antimicrobial materials has been centred on the compositional influence that several metals and their oxides have in the bactericidal properties of biocides. The antimicrobial effectiveness of copper, silver, zinc, titanium and their oxides has been already discussed. Thus, the purpose of the next paragraphs is to describe the influence of other physical and chemical factors on the antibacterial properties of these materials; these include the adhesion of bacteria to touch surfaces and the roughness of the substrate. It must be noticed that as far as the author knowns there is no analysis of the influence of structural changes as such as volume fraction in the antimicrobial properties of BMGs. This lack in knowledge is one of the main motivations of the present work and will be carefully covered in *chapter 3*.

The metallic biocides described (i.e. copper, silver or zinc) base their antimicrobial behaviour in the ability to diffuse ions into the pathogen in contact. These ions and the reactive species derived from them are able to inhibit and kill the microbe. Consequently, the nature of the physical contact between the pathogen and the surface is of great interest in touch surface development. This binding process is multifactorial, complex and is not completely understood. The role of bacterial motility,

the ability to move in response to the presence of specific chemicals (chemotaxis), as well as physical features of the bacterial surface (e.g. flagella, glycocalyces, pili or fimbriae) have an active influence in this process [96-99]. The importance of each of these individual parameters in the adhesion of bacteria may be debatable, however, it is commonly accepted that this process is subdivided in two steps [100]. The first step takes place as the bacteria is in an aqueous suspension. During this phase, the ability to approach a surface is based on a combination of Brownian motion, gravimetric forces and the motility of the pathogen, whether this be guided by chemotaxis or not. When the distance between bacteria and surface is low enough (< 5 nm), the electrostatic charge of the surface, van der Waals forces and hydrophobic interactions grow in influence [100]. Once the initial contact has been made, the morphology of the cell influences the avidity of binding and colonisation via biofilm formation. The purpose of these aggregation of cells is to protect the pathogens from harsh environments, enabling further grow and making difficult their removal [101-103]. As such, the prevention of adhesion and biofilm formation, through development of hydrophobic materials (i.e. with contact angles > 65°) or the “lotus effect” (i.e. contact angles superior to 140° exhibited in some plants confer these species self-cleaning properties), have been one of the strategies adopted to develop antibacterial materials [104-106]. However, the lack of contact between an antimicrobial metallic touch surface and bacteria may hinder the interaction between the ions and reactive species responsible of their bactericidal properties. Thus, the promotion of adhesion between the biocide and the pathogen has been considered as a second strategy to increase the antimicrobial properties of touch surfaces [107,108].

Surface topography (roughness) has been revealed as another factor affecting bacterial adhesion [109,110]. Scheueman et al. [109] showed that rough surfaces tend to bacterial adhesion and biofilm formation, while polished surfaces resist this process. Thus, roughness and the presence of superficial defects may influence the antimicrobial properties of materials. The increase of superficial area provided by scratches or grooves of similar size to the pathogens may led to an increase in ion diffusion into the cell, improving the antimicrobial properties of the material. Additionally these grooves and scratches may create anchoring points for the bacteria, which might help establish initial contacts between the substrate and the

cell. Nevertheless, the size of these features cannot be much larger or smaller than the cells to be eliminated, as the bactericidal effect may be compromised [110] and roughness higher than 1.0 μm (120 grit abrasive grinding paper) can led to a decrease in corrosion resistance due to pitting and crevice corrosion [111]. The reduction of antimicrobial activity can be seen when comparing the results obtained by Chu et al. [112] and Sharifahmadian et al. [113]. Magnetron-sputtered copper-based films exhibiting a few nm in roughness were obtained by Chu, while the roughness of wire arc spray copper coatings obtained by Sharifahmadian was in the micrometre range. The antimicrobial activity of the rougher samples was 92 %, compared with the 99.999 % obtained with magnetron-sputtering [112]. However, arc spray wire methods use a rich oxygen atmosphere and as a result, copper oxides may have been formed in Sharifahmadian's less active coatings, leading to the slight reduction in antimicrobial activity, which may have been attributed to differences in the superficial roughness. It should be noted that magnetron sputtering is of interest in the development of antimicrobial materials as it offers a facile route to tune surface roughness using the sputtering power [114] inner chamber pressure [115,116], or the high copper ion diffusion evident in some of the sputtering techniques (e.g. DC and Dual-MS) [117].

1.1.3 Antimicrobial surfaces vs common disinfection methodologies

The importance of hospital cleanliness in controlling nosocomial infections has been emphasised in previous sections. At this point, it is of interest to consider the active substances used in healthcare facilities and their influence on touch surfaces. The effect that such chemicals have on surfaces has been mostly overlooked and few manuscripts address this matter [108]. The same can be said regarding the influence of disinfectants and detergents on antimicrobial performance of copper alloy surfaces [36]. Disinfectants and detergents are frequently used to eliminate pathogens deposited on inert high touch surface materials such as stainless steel. In contrast, a secondary role of such chemicals is expected in antimicrobial surfaces. Cleaning products need to eliminate any residue which may interfere with the bactericidal properties of the substrate. Grease, oils or dust must be removed to maximise

interaction between the surface and pathogen. However, the effectiveness of the material can be compromised, as most chemical compounds can change the surface chemistry. Airel et al. [118] evaluated the influence of 1 % sodium hypochlorite and 70% industrial methylated spirit in continual cleaning on pure copper. After five days of daily cleaning, the accumulation of soil and cells was reported, exemplifying that proper cleaning methods should be developed for each pair of antimicrobial agent and disinfectant.

The selection of an optimal disinfectant involves a complete understanding of the effectiveness of the chemicals and the detrimental effects they may cause on the surface of interest. The key problem in this consideration lays in the complexity of most disinfectants (Table 2). Water is the most abundant element in these products (15 % to 95 %), and may be a cause of concern if it induces oxidation at the treated surface. However, the most important component is the active substance responsible for the antimicrobial properties of the disinfectant (0.1 to 10 wt %). The rapid antimicrobial activity and low cost of sodium hypochlorite (known as bleach when mixed with water), has promoted its use, making this chemical the most frequently-used disinfectant [119]. Besides water and active substances, disinfectants can also include acids and bases (0.1 % to 35 %), but high concentrations may damage the antimicrobial surface. Although, both hydrochloric and sulphuric acids react with copper, low concentrations can be used to eliminate the oxide layer formed on copper plates or to maintain their lustre. At high concentrations, these acids can lead to the destruction of the copper substrate [120]. If such substances need to be applied, corrosion inhibitors will be necessary in the formulation. Another significant aspect of disinfectant use is appropriate waste management and disposal to prevent any potential negative impact on the environment. As an example, Benzalkonium chloride is broadly used as both an industrial and a household disinfectant, however, its residues exhibit high toxicity for aquatic and terrestrial fauna [121]. Other materials are often included at low concentrations making the product more attractive or user-friendly. As an example, pigments can be used to dye a family of disinfectants to the same tonality. If several disinfectants need to be carried at the same time, distinctive colours will reduce the possibility of selecting an inadequate chemical, while perfumes can be added to eliminate the persistent and undesirable scents common in industrial chemicals.

Table 2 Usual composition of cleaning products [122].

Component	Concentration (*w*/*w* %)	Examples of Compounds
Disinfectant (active substance)	0.1–10	Benzalkonium chloride, Sodium hypochlorite
Surfactant	0.1–10	Benzenesulphonic acid, dodecyl-, sodium salt
Base	0.1–25	Sodium hydroxide, Potassium triphosphate
Complexing agent	5.0–30	Pentasodium triphosphate, EDTA
Corrosion inhibitor	1.0–10	Disodium metasilicate
Solvent	0.1–10	2-Propanol
Perfume	0.002–1	Citrus oils, eucalyptus oil
Pigment	0.01–2	
Acid	0.1–35	Phosphoric acid, Citric acid
Diluent	15.0–95	Water

The active substances available to eliminate bacteria and other microorganisms are numerous, but these chemicals may be classified in four categories: hydrogen peroxide solutions, chlorine-releasing compounds, alcohols and aldehydes, and quaternary ammonium compounds [122,123]. These chemicals display high antimicrobial activity, however, their effectiveness may be compromised when used with bactericidal surfaces. When applied, a complete contact between the resident bacteria and the liquid must be ensured, and, at the same time, the chemical must not compromise the antimicrobial surface. Once the liquid has dried, the structure of the substrate must not be damaged, as surface modification (i.e. oxidation) can have a negative impact. In the next paragraphs, these compounds will be analysed and its effects on some of the most important antimicrobial surfaces (*see section 1.1.2*) will be discussed, with special attention to their influence on copper.

The antimicrobial properties of most disinfectants are related to their ability to produce highly reactive or oxidative species (i.e. hydroxide radicals). Hydrogen peroxide (H_2O_2) produces these species by reacting with O_2^- superoxides through a reaction first described by Haber and Weiss [124,125]. The generation of such radicals confer H_2O_2 a high bactericidal effect against many microorganisms including *E. coli* [126,127], *S. aureus* [126-129], *Bacillus atrophaeus* [130], *A. baumannii* [131], *C. difficile* [131] and *Streptococci* [132]. This broad range of activity and lack of significant toxicity [123,133] over the environment has led to the frequent use of hydrogen peroxide as a micro biocidal agent. Dry mist-generated hydrogen peroxide disinfection systems (Figure 7) have been developed for hospital disinfection to disinfect for touch surfaces [130,131]. These release a controlled mist of H_2O_2, effectively disinfecting entire rooms.

Figure 7 Halo disinfection system making use of dry mist-generated hydrogen peroxide technology [134].

Hydrogen peroxide weaknesses arise from its interaction with some antimicrobial surfaces, although reports in the literature are scarce. DeNardis et al. [135] reported high oxidation of copper when exposed to this chemical. After 5 min of contact, an Cu_2O/Cu layer was formed at a copper surface, which developed new species ($Cu(OH)_2$, CuO and Cu_2O) as contact time increased. Pure copper is a potent

bactericidal material and, in contrast to oxides of other antimicrobial metals, oxidized copper species do not exhibit higher antimicrobial properties than the elemental form. In fact, Hans et al. [68] demonstrated that Cu_2O and especially CuO increase the contact killing time when compared with pure copper. On the other extreme of the spectrum, hydrogen peroxide may have a synergistic effect with silver [136]. Although the work of Armon was focused on the use of silver ions to cleanse drinking and wastewater pipes, the synergistic effect can be explained due to the mechanism triggering the bactericidal properties of silver. The reactive radicals produced by silver oxides are the agents behind the elimination of pathogens [69]. The interaction between hydrogen peroxide and silver promote the oxidation of the metallic element, leading to a synergistic effect.

The second category of disinfectants are the chlorine-releasing compounds. Similarly to hydrogen peroxide, chlorine compounds present a broad antimicrobial spectrum and generate low environmental toxicity, while, at the same time, these low cost substances are generally persistent in potable water, do not stain and are non-flammable [119]. A familiar example is sodium hypochlorite (NaClO), the main agent in commercial bleach. The drawback of chlorine-releasing compounds is that they are highly corrosive and oxidising [137]. As showed by Montes et al. [138] copper is easily corroded by these substances with impact upon its antimicrobial properties. Sodium hypochlorite does not form an oxide with silver ($2Ag + 2NaOCl = 2AgCl + 2Na + O_2$), however, zinc oxide can be obtained through the following reaction: $NaClO + Zn = ZnO + NaCl$. As zinc oxide's antibacterial properties are caused by the release of ions during oxidation [75], it may be of interest to investigate the influence of chlorine compounds in the contact killing properties of Zn-rich surfaces. The second weakness of chlorine-releasing compounds is related to the overuse of these chemicals over the years which leads to microbial resistance to chlorine. Biofilms formed by some strains of *Legionella pneumophila* have been reported to have acquired resistance to high concentrations of chlorine [139], leading to the interest in incorporating copper and silver ions in such chemicals [140,141].

An alcohol (e.g. ethanol) can be described as a chemical compound in which a saturated carbon atom is bound to a hydroxyl group (-OH). Their oxidation generates a formyl group (-COH) characteristic of aldehydes. In contrast to the disinfectant

previously discussed, alcohols and aldehydes are mostly used in hand disinfection [142]. Touch surfaces purpose is to eliminate pathogens deposited on them through the air or due to human contact. Alcohols and aldehydes role in disinfection is not focused on enhancing the properties of these surfaces. Their role is to eliminate or decrease the transmission of pathogens through human contact. For this purpose, hand disinfectants such as Sterillium Gel® [143] or ethanol-based rubs with silver [144] or zinc [145,146] are commercially available, and show sufficient activity to comply with the **EU EPA** protocol mentioned later in *section 1.1.4 Antimicrobial standards for hard surfaces*. The use of alcohol-based hand rubs is appealing due to their simplicity of application, but they present a major flaw. To effectively prevent the transmission of pathogens, hand rubs and disinfectants have to be used after each human interaction. Alcohol-based substances cause skin irritation if used frequently, and discomfort may compromise hand disinfection in health care workers, rendering their use as ineffective. Antimicrobial metals may represent a useful alternative in this respect; the alcohol-free hand rub Xgel [147] has a copper-based formulation developed as a viable option to common alcohol based rubs.

The last of the mentioned disinfection classes are the quaternary ammonium compounds. These are positively-charged polyatomic ions of the structure NR^{+4}, R being an alkyl or aryl group. These chemicals can eliminate bacteria by perturbing their cytoplasmic and outer membrane, where present [148]. Their wide antimicrobial range includes bacteria such as *E. coli* [149,150], *S. aureus* [151-153], *Streptococcus mutans*, *Bacillus subtilis*, *P. aeruginosa* [153] and the fungal pathogen *Candida albicans* [151,153] have increased their use in disinfectants, surfactants and softeners [154]. Harrison et al. [155] analysed the influence of commercial disinfectants (Polycide, Stabron 909, isopropanol and Virox) formulated with different metal ions (Ag^{+},Cu^{2+}, Al^{3+}, SeO_3^{2-}, Zn^{2+}), demonstrating that copper ions suspended in these substances exhibited a synergistic effect, enhancing the antibacterial activity against *P. aeruginosa* over 100-fold. For pure copper surfaces, Hegazy et al. [156] discovered an increase in the corrosion resistance of the material after the application of quaternary ammonium compounds. As a result, these compounds can be used in low concentrations as corrosion inhibitors to protect copper-based materials. Caution must be taken, as high concentrations of ammonium-based chemicals heavily corrode copper [137].

Thus far, the impact of disinfectants on some antimicrobial materials has been considered, disregarding the effect of human contact. Touch surfaces are frequently exposed to fingerprint residues and sweat. Thus, it is important to consider the impact of human interaction with antibacterial materials. The literature shows some early interest in the matter with the studies of Collins [157], and more recently by Bond [158]. Bond analysed the visual corrosion of several metallic surfaces (Aluminium, Brass, Copper, Gold, Magnesium, Silver, Steel, Zinc, etc.) by human contact. The study of copper, silver and zinc is of interest for the development of antimicrobial materials. Zinc and silver were not able to show defined fingerprints, while etched fingerprints on copper were perfectly discernible [158]. Although this study is interested in knowing the possibility of obtaining fingerprints for forensic analysis, these results indicate that antimicrobial copper is susceptible to oxidation as a result of human contact.

The analysis of Collins [157] and Bond [158] involve short timeframes or single interactions between human hands and the analysed substrate. Long term analysis of antimicrobial surfaces is of great interest, but the literature is scarce [159-161]. A remarkable study was conducted by Fredj et al. [162] in which pure copper (C110), brass (C260), bronze (C510), a cupronickel alloy (C706) and a copper alloy of nickel-silver (C752) prepared as batons were subjected to real human contact for two years. When analysed, only the cupronickel alloys and the nickel-silver alloys maintained their lustre, while the other alloys developed a dark tonality. This can be explained by the thickness of Cu_2O developed after the experiment in all metals (50 nm for the nickel silver alloy and 230 nm for pure copper) [162]. The appearance of surfaces is important for the furnishing of hospital health-care facilities. Immaculate and unblemished metallic finishes give the appearance of a “clean” facility. Consequently, alloys which remain flawless for long periods of time are desirable. Although cupronickel alloys and nickel-silver alloys would be preferred over pure copper, however, nickel is the most common metallic allergen [55], which heavily restricts its use.

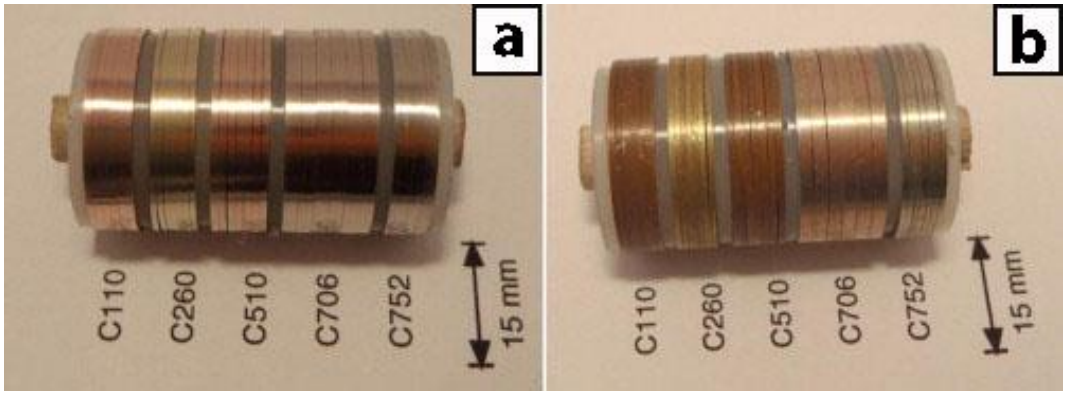

Figure 8 Hand baton (a) before and (b) after two years of discontinuous hand contact used in Fredj's work [162].

The final consideration to undertake in this section is the effect of potential Hydrogen (pH) in antimicrobial surfaces. The complex chemistry of disinfectants include limited amounts of acids, bases and other compounds which influence the number of Hydrogen (H^+) and Hydroxyl (OH^-) radicals. The acidity or alkalinity of a solution plays a role in the corrosion of materials [163-165]. The impact of pH on copper surfaces is relatively low due to a protective layer of Cu_2O created during the firsts stages of contact [165]. This protective layer increases the surface roughness of the material as shown by Daniels et al. [166]. Daniels subjected copper to solutions of various pH (6.5, 7, 8 and 9) for 24 h. Atomic Force Microscope (AFM) measurements showed the maximum increase in roughness of 0.5 µm at pH of 7, in contrast to the 0.26 µm at pH 6.5 and the 0.12 µm at pH 8. Taking into account that a layer of Cu_2O can reduce the antibacterial properties of copper alloys, it may be of interest to use disinfectants with relatively high acidity or alkalinity.

Silver is highly resistant to corrosion induced by acids and bases, being stable in contact with acids such as hydrochloric acid, acetic acid or phosphoric acid [164]. In contrast, silver is oxidised by organic or inorganic sulphuric and with some chloride species, influencing the surface finish of the material [164]. The reaction of silver with highly corrosive oxidising agents such as nitric acid may even lead to potential hazards. Nitric acid reacts with silver to release nitric oxide (NO), silver nitrate ($AgNO_3$) and water. Nitric oxides are brown and flammable in the presence of other substances; its highly toxic fumes can cause nausea, dizziness, shortness of breath, convulsions and unconsciousness.

Zinc can be used as container to store mild detergent and organic chemicals, however, this element is soluble in strong acids (pH < 5) and bases (pH > 12.5) [163]. As zinc reacts with the alkaline or basic chemical, a sponge-like array of zinc oxide forms as it precipitates. Although with copper or silver, the oxides act as protective layer, preventing further corrosion, this is not the case for zinc, as the formation of this "sponge" further increases the oxidation rate of the material [163]. Additionally, this rate can be influenced due to the presence of impurities in the alloy.

1.1.4 Antimicrobial standards for hard surfaces

The number of standards available for the assessment of the antimicrobial properties of hard surfaces is limited. While the interest in developing antimicrobial protocols for bactericidal textiles has led to new standards [167-170], only three standards can be found for the evaluation of the antibacterial properties of hard surfaces (Table 3): Japanese **JIS Z2801:2010** *"Antibacterial products—Test for antibacterial activity and efficacy"* [171], European **ISO 22196:2011** *"Measurement of antibacterial activity on plastics and other non-porous surfaces"* [172] and American **US EPA** "*Protocol for the Evaluation of Bactericidal Activity of Hard, Non-Porous Copper Containing Surface Products"* [173]. From these standards, only Japanese **JIS Z2801:2010** and the American protocol are original, as the European standard is completely based on **JIS Z2801:2010**. Consequently, only two methods are available.

Before analysing these protocols, it is useful to consider the pathogens tested, as well as the existence of a benchmark to consider a product as bactericidal. As it can be seen in Table 3, *S. aureus*, *E. coli* and *P. aeruginosa* are the bacteria recommended in the standards. In *section 1.1.1. Why it is important to develop bactericidal surfaces?* The importance of these bacteria in nosocomial infections was described. *S. aureus* can often colonise the upper part of the throat (nasopharynx) and skin. It is particularly relevant in infections arising from entry via in-dwelling medical devices and wounds, and methicillin-resistant *S. aureus* (MRSA) strains are of great concern [174]. *E. coli* is a very diverse species and many strains are harmless inhabitants of our intestines. However, several strains can cause infection. These pathotypes can cause intestinal diseases (both haemolytic and non-haemolytic diarrhoeas), and infections of the urinary tract, bloodstream and central nervous system [175]. Finally, *P. aeruginosa*

colonises the lungs of patients with congestive lung disorders like cystic fibrosis. This bacterium can also cause infections of wounds and burns and has intrinsic resistance to a range of antibiotics [176].

Table 3 Summary of antimicrobial testing standards.

Standard	Name	Country of Application	Pathogens Analysed	Antibacterial Benchmark
JIS Z2801:2010	Antibacterial products—Test for antibacterial activity and efficacy.	Japan	*S. aureus*, *E. coli*	No
ISO 22196:2011	Measurement of antibacterial activity on plastics and other non-porous surfaces.	Europe	*S. aureus*, *E. coli*	No
US EPA [1]	Protocol for the Evaluation of Bactericidal Activity of Hard, Non-Porous Copper Containing Surface Products	USA	*S. aureus*, *P. aeruginosa*	Yes [2]

1 This document is released as part of a consultation process in the development of the standard. 2 Considered as a sanitizer when more than 99.9% of the pathogens are eliminated.

In **JIS Z2801:2010** and **ISO 22196:2011** a standardised inoculum of bacteria ($6x10^5$ cells per millilitre) is applied on the antimicrobial test surface (40 mm x 40 mm) and on control surfaces without the bactericidal agent. After incubation for 24 h at 35 °C at high humidity (> 90 %), the inoculum is recovered, serially diluted in broth and cultured on agar. The number of survivors is obtained by counting the number of colonies that develop on the agar plates. Quality standards and reproducibility criteria are available. The assessment of the bactericidal properties is done through the antimicrobial activity defined by:

$$R = (U_i - U_0) - (A_i - U_0) = U_i - A_i \quad \textbf{(1)}$$

R; antimicrobial activity.

U_i; average of logarithm numbers of viable bacteria immediately after inoculation on untreated test pieces.

U_0; average of logarithm numbers of viable bacteria immediately after inoculation on untreated test pieces after 24 h.

A_i; average of logarithm numbers of viable bacteria immediately after inoculation on antibacterial test pieces after 24 h.

The protocol developed by the United States Environmental Protection Agency (**US EPA**) is relatively new, and it is being considered for adoption in a consultation process. The preparation of the inoculum and most of the methodology for the inoculation and recovery are similar to the Japanese standard. Nevertheless, three main differences can be found. Firstly, this protocol provides tests to assess the impact of biocidal cleaning liquids (i.e. Sodium hypochlorite, Hydrogen peroxide and Phosphoric acid) on the mechanical and chemical properties of the antibacterial surface. Secondly, it is stated that a material can be considered as a biocide if more than 99.9% of the pathogens are eliminated within 1 h. While **JIS Z2801:2010** gives the framework for studying the antibacterial properties of a large number of materials, it does not provide a benchmark to consider those materials as bactericidal. Finally, the quantification of the antibacterial properties are not done using the concept of antimicrobial activity, but through the use of the reduction percentage:

$$\%\, reduction = \frac{a-b}{a}\, x\, 100 \qquad \textbf{(2)}$$

a= geometric mean of the number of organisms surviving on the inoculated control carriers.

b=geometric mean of the number of organisms surviving on the test carriers.

The Japanese standard is of great use in the industry and it is used over a large variety of products, however, its practical application in research is limited. The large surfaces required in this standard (40 mm x 40 mm) may not be possible for research of samples with small dimensions such as BMGs. At the same time, the concept of antimicrobial activity is not preferred in antimicrobial research. For example, Chu et al. [177] used **JIS Z2801:2010** to analyse the antimicrobial behaviour of Zr-Cu thin

films, but instead of applying the antimicrobial activity, preferred to calculate the antimicrobial rate as $\frac{N_0-N}{N_0} \times 100\%$ where N_0 and N are the number of viable microbes on a control sample and on the antimicrobial surface, similarly to the percentage reduction previously defined (Equation 5). This simple equation is preferred in the antimicrobial field instead of the antimicrobial activity defined in the Japanese standard, and it is normally used to compare the bactericidal properties of several materials [113]. In this regard, the **US EPA** protocol is less limiting in size of the samples, density of the inoculum and mathematical apparatus, but the acceptance of **JIS Z2801:2010** in the field has led to a reticence to using other methodologies.

A limiting factor in both standards is the time of exposure to the antimicrobial surface. The Japanese standard requires 24 h of contact killing between sample and pathogen, which may not be able to prevent the transfer of bacteria in healthcare facilities. High-touch surfaces (i.e. bedrails or door plates) are touched continuously and transfer of cells can take place much earlier than 24 h. Some researchers have proposed 5 min as an optimum time to limit transmission [178]. This time was estimated to be the average for two people to touch the same surface, much lower than the 24 h used by the standards. This is of special relevance for metallic glass composites (MGCs) which exhibit a delay of 3 to 4 hours in their antimicrobial properties [13,179]. The result in these papers show that high bactericidal properties can be displayed much later than the optimum time. Consequently, an antibacterial surface validated by **JIS Z2801:2010** or the American protocol may not be of relevance to prevent nosocomial infections.

As a final remark, both standards encourage the inoculation of bacteria in a container with high humidity to prevent the drying of the inoculum. Touch surfaces present in health-care facilities are normally found in low humidity environments. It has been shown that dry and wet application has an influence in the antimicrobial properties of materials. There is interest in emulating dry, more authentic conditions, especially for copper-based materials [159-161]. In terms of new “dry” lab methodologies the literature is scarce. Most reviews know of this disparity and encourage the use of new in vitro tests [58,63,180]. In this regard, there are two methods described in the literature which can be considered as “dry” antimicrobial tests: aerosol inoculation of bacteria [180-183] and the use of cotton swabs to apply a set amount of pathogens

[184]. Aerosol inoculation tries to simulate the deposition of bacteria due to coughing, sneezing and splashing. Ojeil et al. [183] investigated the influence of relative humidity (RH) and temperature when using several aerosol-inoculated (S. aureus) Cu-based substrates (37 °C, 100 % RH; 20 °C, 40-50 % RH and 20 °C, 100 % RH). Their results showed higher antimicrobial activities under the wet conditions (37 °C, 100 % RH) favoured in the antimicrobial testing standards, and indicated that environmental conditions can influence the contact killing of bactericidal materials. Similar results were obtained by Robine et al. [180] for *Enterococcus faecalis* aerosol inoculations on copper for several RH. Consequently, the possibility of overestimating the antimicrobial properties of materials using wet conditions may be a concern. In regards to the cotton swab methodology, a set amount of bacteria is inoculated onto a sterile cotton swab and applied to the surface. After a few seconds (typically 5 s), the surface is dry, enabling the characterization of real dry conditions [184]. These analyses have revealed a higher density of copper ions in the exposed cell than in those exposed in wet conditions [58,184], which are not into agreement with the results showed in the aerosol inoculated samples. This disparity may be caused by the time required for the liquid to be evaporated. As stated previously, the drying time for a swab inoculated sample is around 5 s, however, aerosol inoculation can require 30-60 min to dry (depending on the RH) [183]. The long exposure of the surface to the aerosol may induce some degree of oxidation at the surface, hindering the diffusion of ions and reactive species. In summary, these two tests are interesting to use as comparison with the known standards, however, both present difficulties and drawbacks. Aerosol methods are difficult to standardize and replicate. The bacterium density, the nozzle size or the inoculation rate are a few of the parameters which complicate this technique, and require extensive expertise in the field to operate reliably. On the other hand, the dry technique described by Santos et al. [184] may induce damage in the cell membrane, destroying the cell's structure [25,58,107,185], indicating a more intense scenario for the bacterium.

It is certain that **JIS Z2801:2010** and the **US EPA** protocol define methods to measure the antimicrobial performance of antimicrobial materials. Difficulties arise, however, when in vitro and in vivo conditions are compared. The size of the samples, time of contact killing and dry plating conditions are weaknesses which should be addressed by the research community. This is of special relevance as materials with high

antimicrobial properties shown in the laboratory fail once applied in Healthcare units [94], which has encouraged the authentic analysis of antimicrobial materials in real healthcare facilities [159-161]. Although the wet conditions imposed by the standards may be inadequate to analyse high-touch surfaces authentically, it has to be noticed that these standards may be of interest in screening bactericidal materials for pipeline systems for further testing in real conditions with tests like that developed by Cervantes et al. [186].

1.1.5 Metallic glasses with bactericidal properties

Metallic glasses (MGs) are a relatively novel class of materials that display high wear resistance, corrosion resistance and mechanical properties of MGs (*section 1.2*). Some of these alloys con contain or be based on the previously discussed antimicrobial elements (i.e. copper or silver), promoting them as interesting candidates for the development of high-touch surfaces. However, the number of manuscripts exploring the antimicrobial properties of MGs is scarce. The available literature can be subdivided in two groups, those researching BMGs and those researching MG coatings. From the point of view of application to touch surfaces in healthcare facilities, coatings are preferred over BMGs. Bulk metallic glasses are heavily restricted by their maximum critical diameter, but rapid solidification is a quick method to obtain BMGs and BMGCs. This method can be used to select the best compositions and conditions that affect the antimicrobial properties of MGs, and as such, facilitate the development of effective biocidal coatings. In this section, the latest research in antibacterial MGs will be presented and discussed.

As far as the author is concerned, the earliest paper assessing the antimicrobial properties of MGs was published in 2012 by Lin et al. [187]. In this manuscript, the antimicrobial properties of Fe-based, Ni-based and Cu-based (non-annealed and annealed) MGs were compared. The methods used by Lin et al. to assess the biocidal properties of the materials were the measurement of the turbidity of *E. coli* cultures grown in contact with the MG (Figure 9a) and the agar diffusion (inhibition zone) method (Figure 9b). For this last test, they dropped a sample in a crystal tube filled with inoculum. After a set amount of time, they measured the turbidity of the inoculum, obtaining the number of suspended bacteria. Their results concluded that differences

in the biocidal properties of these materials were less dependent on their composition, but rather on their non-crystalline structure and the lack of adhesion to the substrate [187]. Consequently, the rather low antimicrobial properties observed indicated that these MGs acted as growth inhibitors rather than biocides. These results are surprising as the previous commented literature suggested that alloy composition is the most important property that affects contact killing. A more detailed analysis of this paper reveals that the density of inoculum used in the experiments was much greater than that suggested in any of the available standards used today (OD_{600} ~ 1.2 when compared to $OD_{600} \leq 0.3$) [187]. The changes to the culture density necessary to indicate activity would require its significant clarification through cell lysis rather than a critical loss of viability that falls short of cellular destruction. Simply, many dead cells could still contribute to the turbidity of the suspension; hence this method is not adequately discriminatory and likely underestimates killing. At the same time, the dynamic immersion tests do not encourage direct contact between the bacteria and surface. As the bacteria move in the relatively large amount of medium present in the test tube, some bacteria can attach to the sample, while the majority will be moving in the liquid, far from the sample. The high incubation times of 8 h and the high inoculum density may lead to the formation of biofilms on the surface of the MGs, protecting the other pathogens. In all the tests, an iron nail was used as a control, revealing lower than expected antimicrobial properties of all the materials tested (Figure 9a and 9b). However, the iron in the nail must have undergone significant oxidation, releasing ROS which would account for the reported antibacterial properties. Consequently, the methodology used by Lin et al may not be the most appropriate to quantify the antimicrobial effect of MGs. On the other hand, this analysis shows the importance of using appropriate inoculum densities and controls.

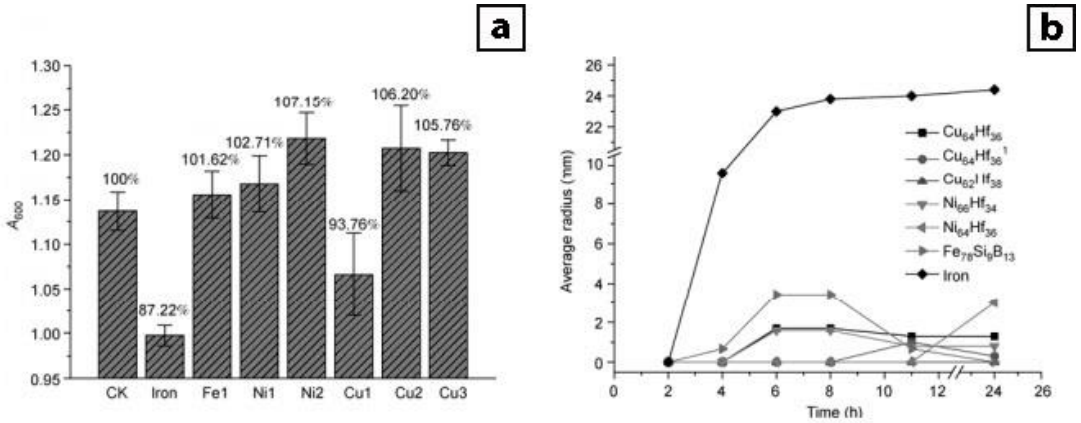

Figure 9 Images showing the (a) changes in turbidity between six MGs and an iron nail and (b) inhibition zone measurements for the same materials [187].

Huang et al. [66] analysed the biocidal properties of Cu-containing Zr-based BMGs, comparing their contact killing with pure copper and Ti-6Al-4V.Their methodology involved a similar immersion in growing bacteria to that used by Lin et al. [187] as well as recovery of surface-inoculated bacteria directly from the material. The dynamic immersion essays showed that there was no difference between the MG and Ti-6Al-4V alloy, while copper was able to reduce the bacteria present in the inoculum by 1 order of magnitude [187]. As mentioned earlier, dynamic immersion tests to assess the biocidal properties of materials is not adequate for touch surfaces. The importance of this study is in the second method used. In this essay, Huang inoculated the metallic alloys with 1 µL of OD_{600} ~ 0.3 inoculum using a sterile loop. After 4 h, they recovered bacteria and cultured the recovered *S. aureus* cells on agar plates. This method is of great importance as it better simulates direct contact between bacteria and surfaces, and adequately discriminates between dead and living cells. This analysis showed that copper was able to eliminate all the deposited bacteria, while the $Zr_{55}Al_{10}Ni_5Cu_{30}$ and $(Zr_{55}Al_{10}Ni_5Cu_{30})_{99}Y_1$ (at. %) BMGs eliminated one order of magnitude of bacteria more than the Ti alloy [187]. The relatively poor antimicrobial activity was explained by the limited number of Cu ions present in the BMG when compared to pure copper. As a result, the contact killing ability of the materials was dependent on the composition of the material, contrary to the results of Lin et al. [187].

The possibility of coating cheap substrates with antimicrobial materials is appealing from a cost-effective point of view. As such, it is not surprising that, to date, most research on the antimicrobial activity of MGs has been performed on thin films. In this regard, magnetron sputtering has been the preferred technique to make amorphous alloys [188,189]. During magnetron sputtering, high purity targets are subjected to a controlled voltage and current, creating a plasma flow between the targets and the substrate. The target's ions travel to the substrate's surface, creating a thin layer of material whose composition can be adjusted.

The number of biocidal metallic systems analysed to date is rather restricted. Most of these systems are Zr- or Ti-based alloys with a small addition of copper, silver or both (e.g. $Zr_{53}Cu_{30}Ni_9Al_8$ [177], $Zr_{53}Cu_{33}Al_9Ta_5$ [190] or $Ti_{40}Cu_{30}Pd_{14}Zr_{10}$ [191]). From all of the Cu-Zr-based alloys, CuZrAlAg [114,192] and similar alloys [193-195] seem to be the most extensively researched. However, the antimicrobial activity of other systems has been assessed [112,196]. The high bactericidal effect of pure copper has been discussed already, and it has been mentioned its ability to eliminate most bacteria after one hour [63,197,198]. For this reason, it is surprising that most of the previously described systems show copper contents of around 30 to 40 at. %. The research into Cu-based MGs is limited, and mostly focused on the $Cu_{90}Ti_{10}$ alloy [106,117,199]. Regardless of the exact composition, all the MGs coatings developed include one or several antimicrobial agents such as copper or silver.

The evaluation of the antibacterial activity of materials can be achieved through several methodologies [200]. However, the available literature in MG thin films focuses on methodologies such as agar diffusion method, solution suspension, and plate count method. The diffusion method involves the placement of samples on an agar plate spread with bacteria. As the metallic ions diffuse in the agar plate, the bacteria surrounding the sample will be inhibited or killed. After incubation, the antimicrobial properties can be assessed by the radius of inhibition surrounding each sample [187]. The solution suspension method or dynamic immersion tests involve dropping a small coupon into a test tube with a bacteria culture. The antibacterial properties are, then, calculated by measuring the turbidity of the liquid after cultivation [187]. For the plate contact method, a small aliquot of inoculum is deposited on the sample. After a set amount of time, the bacteria is recovered, diluted serially and

cultured on agar plates. After cultivation, the plates will reveal the presence of small colonies of bacteria that can be counted, each considered as arising from a single viable cell. The antimicrobial activity can be quantified by the number of colonies generated, indicting the size of the surviving population at the time of sampling [177]. Other variations can be found in the literature (i.e. the cultivation of bacteria while in contact with the substrate [114]), but these three methodologies are the most employed. Besides these differences in core methodologies, the contact times differ between manuscripts. These time ranges can be extended from hours [106,191] to days [114]. Other differences can be found between manuscripts, authors tend to use different bacteria or even when using the same species, different strains may be used (e.g. *K12* or *W110 E. coli*), while the optical density of the inoculum applied may vary between papers. These differences in methodologies complicate an exhaustive comparison of the available literature. However, some Ag- thin films exhibit antimicrobial activity comparable to that of pure silver [112], while copper-based MGs reveal lower bactericidal properties than pure copper [66].

As the antimicrobial properties of the aforementioned materials have been related in terms of the release of copper ions, the compact structure proper of MGs may limit the diffusion of metallic ions, thereby reducing their contact killing properties. In this regard, the presence of crystalline phases and grain boundaries in MGCs may provide a better basis to develop novel biocides as these inclusions may promote the diffusion of metal ions, effectively improving the contact killing. However, there is a gap in knowledge in the antimicrobial properties of MGCs. The influence of volume fraction and composition of crystalline phases in the antimicrobial properties of these materials is mostly unknown. Consequently, the development of new antimicrobial MGs must encompass the formation and analysis of MGCs.

1.2 Metallic glasses and their composites

1.2.1 Description of metallic glasses

Metallic glasses (MG) are a new kind of metallic alloys where the atoms exhibit short range order (Figure 10a), in contrast to the long range ordered structure present in crystalline materials (Figure 10b). This atomic structure can be achieved by rapid solidification, when the melted alloy is cooled down rapidly enough (cooling rates in the order of 10^6K/s) to prevent atomic diffusion and crystallization.

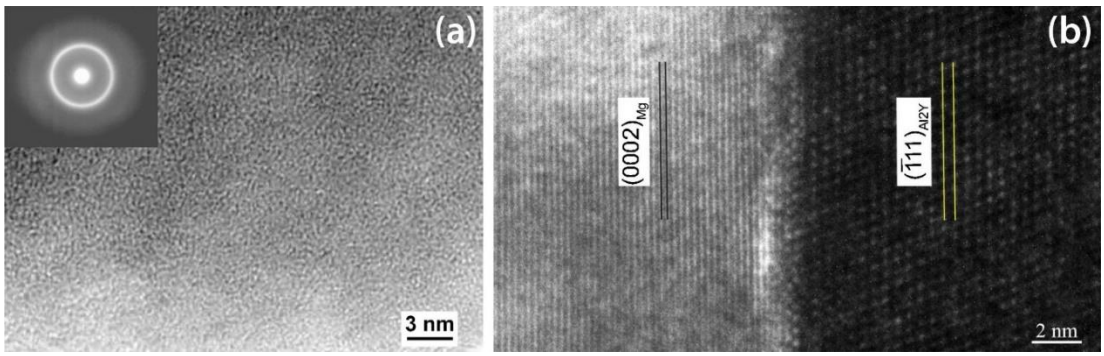

Figure 10 Bright field TEM image of (a) a MGs [201] and (b) a crystalline material exhibiting typical interface between two crystalline phases [202].

The ability of a metallic alloy to form an amorphous structure, Glass Forming Ability (GFA), is dependent on many parameters such as the composition and thermal properties of the alloy. Consequently, slight variations of composition or the presence of impurities hinder the formation of amorphous structures. Nevertheless, the interest in these novel materials stems from their superior properties such as soft magnetism, high mechanical properties (Hardness, yield strength, fracture toughness, specific strength, resilience and low dampening), corrosion resistance, wear resistance, biocompatibility (i.e. CaMgZn and ZrTiCuFeAl systems) and aesthetics (i.e. for high-end “life-style” products) [203-206]

Before delving into the differences between MG and crystalline materials, it is necessary to consider the terms “noncrystalline”, “amorphous” and “glassy”. The first

term, “noncrystalline”, is generically used to describe a lack of crystallinity in a material. On the other hand, the distinction between “amorphous” and “glassy” materials is dependent on the processing of the material. A “glassy” alloy is a noncrystalline metal obtained by continuous cooling from the liquid state (i.e. rapid solidification). In contrast, an “amorphous” alloy is a noncrystalline metal obtained from any other method (i.e. solid-state processes). As both terms refer to noncrystalline material, this distinction is mostly non-existent and both terms are often used interchangeably.

Contrary to MGs, common metallic alloys are either polycrystalline or monocrystalline (Figure 11). During the relatively slow cooling of a casted metal or alloy, the atoms diffuse and tend to rearrange into a lower energy state (crystal lattice) initially establishing small nuclei that grow to form crystalline grains. Metallic alloys generally exhibit a polycrystalline structure composed of multiple grains of different sizes, morphologies and even compositions. The interfaces between grains are called grain boundaries and are constituted by low atomic packed structures that are prone to crack formation (see red lines in Figure 11). Additionally, grain boundaries are preferential sites for precipitation and, therefore, for the formation of galvanic pairs and corrosion, thereby limiting the mechanical performance of metallic alloys [207,208].

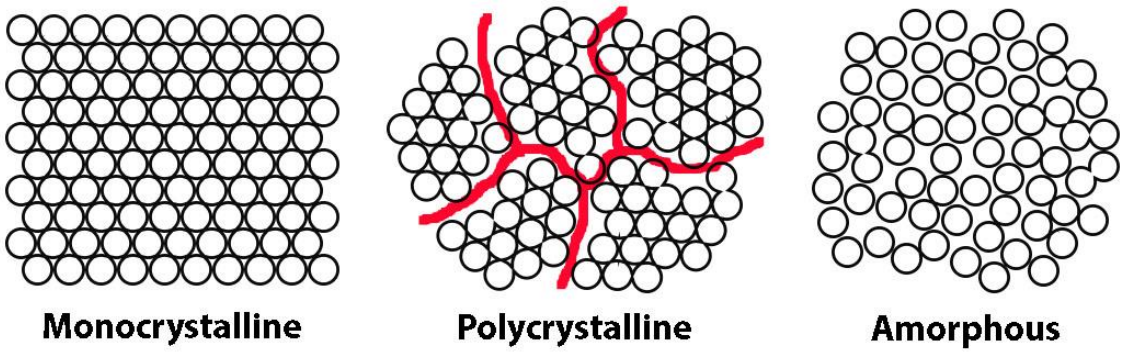

Figure 11 Sketch showing the differences between atomic rearrangement between monocrystalline, polycrystalline and amorphous materials.

Plastic deformation of a crystal is caused by the slipping of well-defined parallel crystalline planes when the critical resolved stress is reached (Schmid’s law) [209].

This slip between crystalline planes is responsible for the formation of a defect in the long range structure known as a dislocation; these strongly influence the mechanical properties of crystalline materials. In polycrystalline materials, the random crystallographic orientations of neighbouring grains arrest the movement of dislocations, thus increasing their resistance to plastic flow. Consequently, a higher volume fraction of grains can enhance the mechanical properties of the alloy over those of a metallic alloy of the same overall chemical composition, as stated by the Hall-Petch equation [209,210]. These defects coupled with the presence of imperfections in the three-dimensional arrangement and spacing of crystals (i.e. vacancies, interstitials, dislocations plane misalignment), result in poorer mechanical performance than the theoretical limits. These drawbacks can be overcome by producing monocrystal structures rather than polycrystal materials. Monocrystalline materials consist of a single crystal, retaining the long range order proper of crystalline materials (lattice) while lacking grain boundaries (Figure 11). This structure is of special interest in preventing plastic flow of metals under stresses lower than the yield stress (creep or cold flow), or in decreasing resistance to electric flow. Consequently, monocrystalline components have been of special interest in jet turbines (monocrystalline turbine blades) [211] and solar panels (monocrystalline cells) [212].

In contrast to monocrystalline and polycrystalline materials, MGs have a frozen-in liquid structure characterized for being a dense and random aggregation of atoms (Figure 11). As the material cools down, the high density of the molten metal prevents atoms from diffusing [213]. As the temperature of the melt reaches a value lower than the glass transition temperature (T_g), the viscosity of the melt suddenly increases (from 10^{-3} Pa s to 10^{12} Pa s) and the atomic structure is frozen, thus inhibiting nucleation and crystallization [214,215]. Lower cooling rates are required to attain a fully glassy structure at room temperature if the atoms in the molten state are highly packed, since this hampers the atomic diffusion. This results in a dense, random, aggregation of atoms proper of MGs. Therefore, these materials do not present grain boundaries or structural imperfections, which can explain their interesting properties (Table 4).

Table 4 Advantages and drawbacks of MGs [203,216,217].

Advantages	Drawbacks
Elevated toughness	Brittleness (catastrophic failure)
High strength	High cooling rates necessary for their formation
Wear resistance	Geometrical and size constrictions
Corrosion resistance	Costly elements necessary
Damping	
Soft-magnetic properties	Small fluctuations in composition cause drastic changes in properties
Biocompatibility and Bactericidal effect (dependant on composition)	Sensitive to oxygen impurities (Vacuum casting required)

Due to the interesting mechanical properties displayed by MGs, intensive research has been conducted since their discovery. As an example, higher elastic limit can be observed in most amorphous materials when compared to crystalline alloys with the same main element (i.e. Fe-based MGs vs stainless steels), nearing the theoretical strength (Figure 12). However, these materials present some drawbacks that limit their implementation in industry (Table 4); namely: their brittleness, the necessity of high cooling rates, which limits the size and geometry of the samples, the costly elements used in the alloy systems, their sensitivity to compositional fluctuations and the requirement of vacuum casting to prevent the presence of oxygen and other impurities that decrease the GFA.

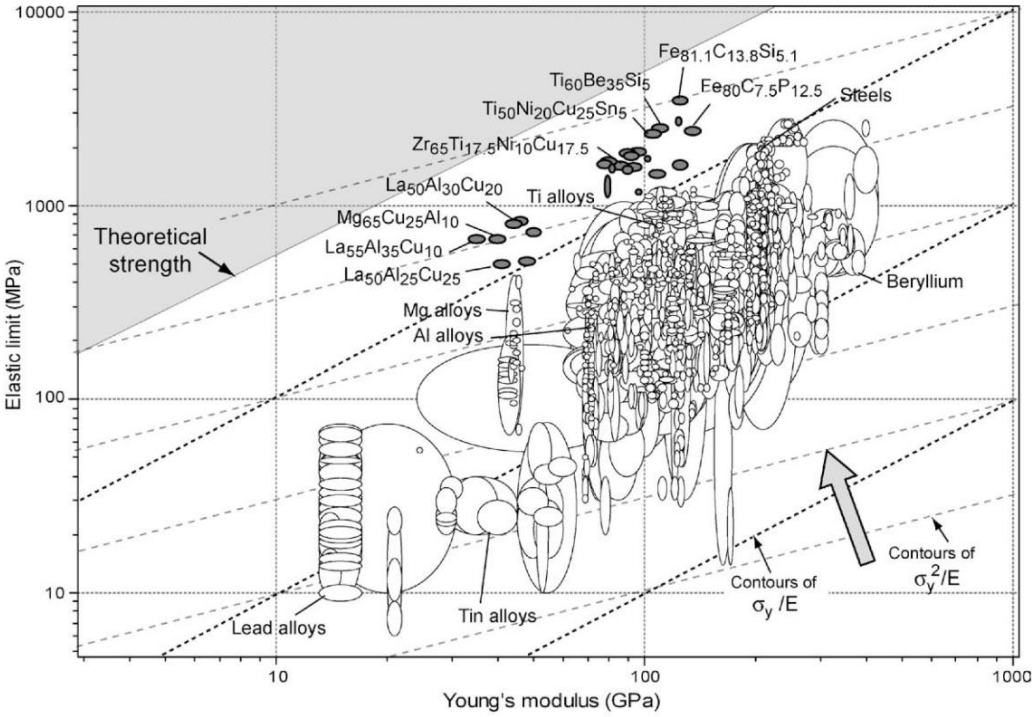

Figure 12 Elastic limit (σ_y) versus Young's modulus (E) for several crystalline metallic alloys, composites and MGs [203].

During the last two decades, the study of amorphous glassy alloys has made possible the minimization of most of the listed disadvantages. One of the most important constraints limiting the use of MGs as structural materials, has been their brittleness. The deformation mechanism of MGs is the nucleation and propagation of shear bands (Figure 13). In the most brittle MGs, deformation occurs within a single shear band that propagates across the material, thus resulting in catastrophic failure (*section 1.2.4*). The strategy to increase the ductility of these alloys is to increase the density of shear bands and to arrest or deflect their propagation [218]. This can be achieved by developing metallic glass composites (MGCs); i.e. by promoting the presence of crystalline phases embedded in the amorphous matrix. As the load applied to the material increases, the stress distribution around the particle increases in multiple directions, leading to the formation of multiple shear bands. At the same time, the propagation of shear bands is arrested or deflected when a particle is in their path, limiting the size of the shear band. Consequently, MGCs exhibit higher overall ductility than MGs, making possible their use as structural materials [203].

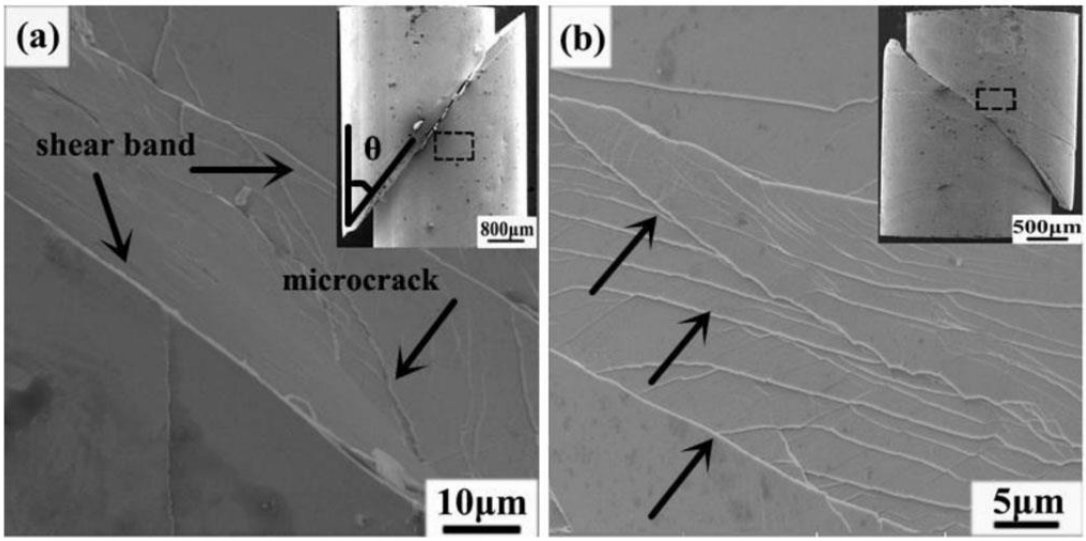

Figure 13 SEM images showing the lateral surfaces of compression BMGs samples. Note the serrated-flow behaviour and fracture mechanism is caused by multi-step shearing due to energy dissipation through shear banding [219].

MGCs can be subdivided into two different categories, “in situ” and “ex situ”, depending on the processing. The “ex situ” MGCs are obtained by adding the particles externally in a post processing of an existing amorphous material. In this case, the MG is obtained by either mechanical alloying of powders or atomization of the MG and reinforcing particles, or by particle or fibre reinforcement of the MG by melt infiltration [220]. On the other hand, “in situ” MGC are obtained during the solidification of the melt or by a second treatment of the MG precursor [220]. “In situ” composites contain particles or dendrites that can be used to reinforce the amorphous matrix.

As previously mentioned, a limiting factor of MGs use is the high cooling rates necessary to obtain the amorphous structure. The high instability of metastable liquid causes the rapid nucleation and crystallization of most metallic alloys. Vitrification of the melt, necessary to obtain amorphous metals, requires high cooling rates which can only be achieved in materials with small dimensions, such as ribbons or coatings, leading to the third disadvantage of MGs (geometrical and size constrictions) [217]. This limited the industrial use of MGs, further stimulating interest in finding new alloys with adequate Glass Forming Ability (GFA), reducing the cooling rate requirements, and enabling their fabrication in bulk shape ($\phi \geq 1$mm). In this regard, the discovery

of new Mg-, La- or Zr-based alloys with high GFA have facilitated the use of rapid solidification to obtain BMGs with critical diameters of a few centimetres [218]. First generation MGs were Au, Pt or Pd -based systems, resulting in serious limitations for their use (Table 4), however, the discovery of metallic alloys of the Fe-, Cu-, Zr-, Mg- or Ti- systems with high GFA makes their implementation more likely [218,221].

Despite the great effort and discoveries of the last three decades, the main drawbacks in MG commercialization and its industrial implementation remain. Amorphous structures are highly dependent on compositional changes, oxygen, impurities and partial crystallization [218]. Oxygen impurities are a special concern as only 3000 atomic parts per million can led to the complete crystallization of BMGs [222], causing changes in the crystallization kinetics and severe embrittlement of the alloy [223,224]. Nonetheless, companies specialised in the commercialization of MGs do, in fact, exist. The most prominent is Liquidmetal® Technologies, which specialises in injection moulding of the Vitreloy series of commercial MGs. Successful applications have been developed in the electrical (low-loss power distributor transformers) [225], military (Kinetic Energy Penetrators) [226], sport (golf clubs) [216] electronics (sensors) [227] or biomedical (implants and devices) [228] industries.

1.2.2 Short history of metallic glasses

The history of MGs is intrinsically related to the interest of developing advanced materials through non-equilibrium processes [215,229]. Today, numerous methods such as solid-state quench, mechanical alloying or Irradiation/ion implantation provide means to process materials in a non-equilibrium state. Nevertheless, the origin of amorphous materials is commonly attributed to the work of Duwez et al. [204,230,231]. During the mid-60s, Duwez and his colleagues were interested in obtaining a solid solution of Cu-Ag by rapid solidification of the melt. To achieve the high cooling rates necessary, they fired small drops of melt into a cooled copper surface using the rapid solidification process known as “gun technique” (Figure 14), where a shock wave propels a drop of molten alloy at sonic velocity onto a chill substrate to form thin (~ 1 μm) samples. This technique produced what it is widely accepted as the first amorphous metallic alloy, a 75 at. % Au and 25 at. % Si foil [232]. However, Duwez doubted the amorphicity of the material. The reticence of Duwez to

publish its early discoveries was evident in the carefully selected title “Non-crystalline structure in solidified gold–silicon alloys” and that Duwez’ students were cited as the main authors of the paper [233,234]. While Abrosimova and Aronin [235] attribute the first amorphous alloys to the work of Miroshnichenko and Sally [236] and Ecker et al. [220] reference the work of Kramer [237], Drenner et al. [238] and Buckel et al. [239,240], Duwez et al. are considered as the pioneers in glassy alloys.

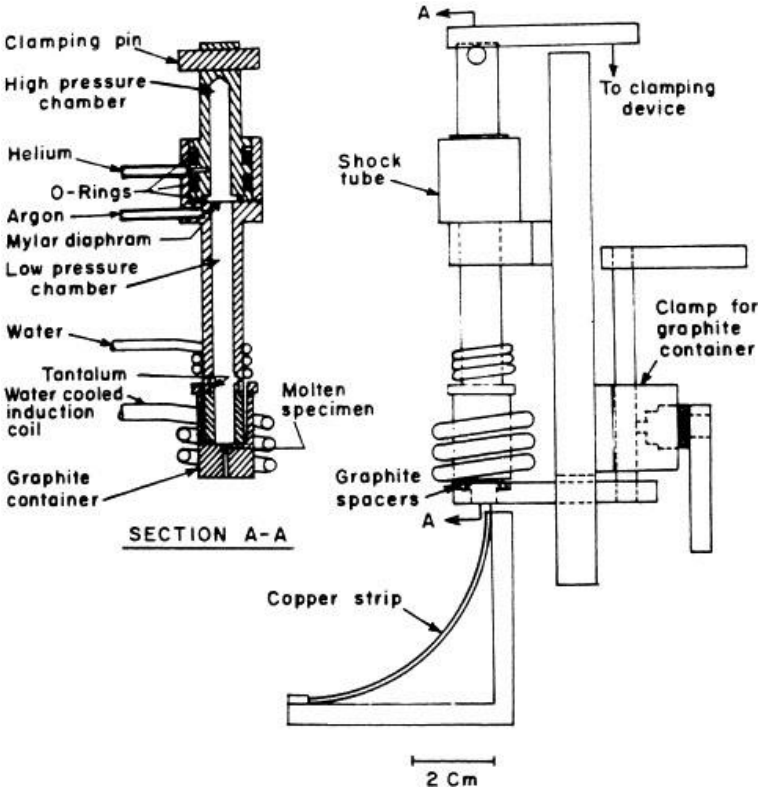

Figure 14 Design of Duwez’s gun technique of splat quenching [241].

During the following decades, hundreds of papers delving in the mysteries of MGs have been developed. On one hand, some researchers devoted themselves to understanding the theory behind the non-equilibrium amorphous transformation [242]. On the other hand, the difficulty of finding a complete theory encompassing this transformation led to more experimentally-focused research, resulting in the development of new rapid solidification techniques and the discovery of new amorphous systems [204]. Even twenty years after Duwez’s discovery, the high cooling rates necessary to obtain amorphous samples, in the order of 10^6 K/s,

restricted the dimensions of the samples to small foils or ribbons of 20-50 μm in thickness [215]. This circumstance started to change with the discovery of new metallic systems such as the Pd-P-Ni system [243] and the multicomponent La-, Mg-, Zr-, Pd-, Fe-, Cu-, and Ti-based alloys developed by Inoue et al. with critical cooling rate between 1-100 K/s [226]. The relatively low cooling rate required for these alloys opened the possibility of obtaining bulk samples, BMGs, by simple quenching, increasing the critical diameter to values higher than 3 mm. From 1990 onwards, a second surge in MG research, which still continues today, took place. Due to this interest in MG development, the first commercial MG alloy, Vitreloy 1 ($Zr_{41}Ti_{14}Cu_{12}Ni_{10}Be_{22}$), was developed, opening the use of amorphous materials into a broader industry [225]. In the early 2000s, it was recognized that inclusions of crystalline phases in an amorphous matrix (MGCs) enabled the control of shear band formation and propagation, effectively reducing the brittle nature of glassy alloys [244].

The purpose of this section was to introduce some of the most important milestones in the history of MG research. A comprehensive description of the history of MGs is out of the scope of this thesis; much more information can be found in complete texts dedicated to the subject [233] and review articles [218,245].

1.2.3 Glass forming ability

Since the pioneering work of Turnbull [242], great interest has been placed in unravelling the mysteries surrounding good MG formers. The ability of an alloy to reach a complete amorphous structure (GFA), can be experimentally measured with relative ease by changing the dimensions of the sample. The GFA of BMGs is characterized by the critical cooling rate R_c or the maximum diameter for which the casted alloy is completely amorphous [246]. Variations in the sample diameter can impede the vitrification of the melt in the center of the rod, leading to the partial crystallization of the alloy. This effect can be seen in Figure 15, where a Cu-based alloys was casted using a wedge-shaped mould [247].Consequently, most of the GFA research is purely guided by experimental “phase diagrams and empirical rules” [248]. Great effort is being put into developing a complete theoretical and mathematical framework to generate new MGs, However, the complexity of the thermodynamics

and kinetics surrounding the amorphous state of glassy alloys has complicated the theoretical analysis of these materials. Even today, there is not a complete understanding of the variables which determine their GFA.

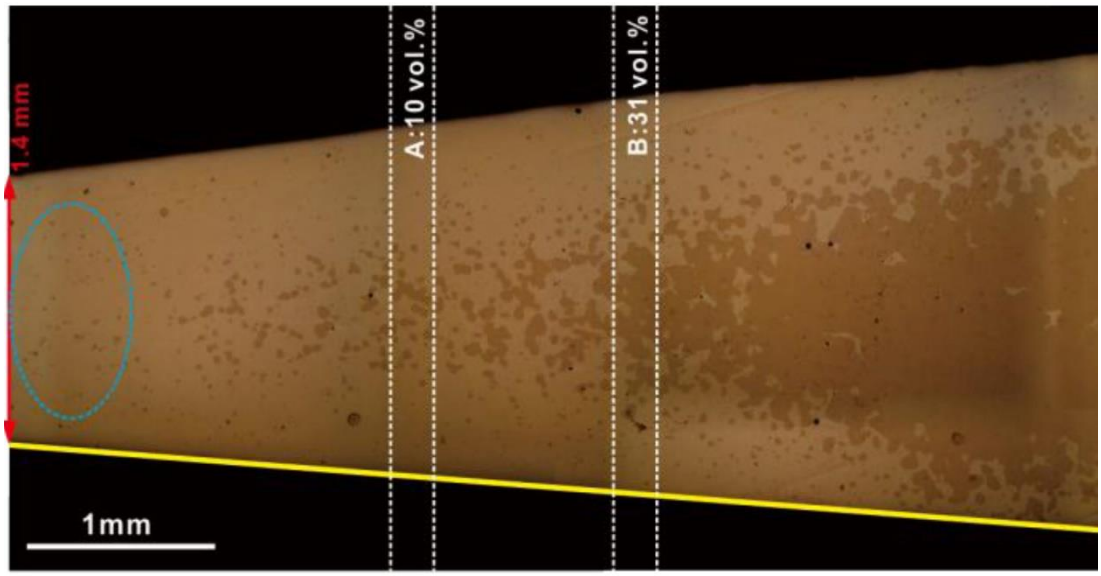

Figure 15 Section of a Cu-based alloy casted in a wedge-shaped mould [247]. The increase in cross section lowered the cooling rate in the centre of the sample, causing the crystallization of the melt from completely crystalline (blue oval) to higher volume fractions (i.e. section A 10 % and section B 31 %).

As dictated by the homogeneous crystal nucleation theory, nucleation is highly dependent on the diffusivity, and thus, the viscosity of the supercooled melt [213]. Crystallization is thermodynamically possible when the melted alloy reaches a temperature below the liquidus temperature (T_L). In contrast, vitrification of the melt, primordial for MGs, takes place for lower temperatures than the glass transition temperature (T_g where $T_L > T_g$). Once the cooling of the melt reaches the T_g, the atomic movement of the elements halts, hindering the nucleation and growth of crystals. Therefore, glass formation is a struggle between the liquid stability and the formation of crystalline solid phases. Consequently, the formation of a MG alloy would be enhanced in alloys displaying high undercooled density and higher reduced glass temperature ($T_{rg}=T_g/T_L$), common in eutectic compositions [231]. To understand the importance of eutectics in MG formation, let us consider the role of the liquidus temperature in the stabilization of crystalline phases. The possibility of nucleation in a melted alloy is increased as the difference between the liquidus temperature and

the glass transition temperature increases. For this reason, a fast transition between liquidus to solidus would be of interest to obtain an amorphous structure. This can be achieved by eliminating the liquidus+solid phase commonly seen in phase diagrams. These points are known as eutectics and are determined by the composition of the alloy. The cooling of a melted alloy through an eutectic ensures a quick transition of phases (liquidus to solidus), which is highly desirable for MGs. Consequently, the development of MGs using eutectics has been a thriving point in MG research.

It is commonly accepted that high values of T_g indicate great resistance to crystallization, while high values of the liquidus temperature points to an increased instability of the liquid [249]. Taking this into account, it is of no surprise that one of the first indicators of glass formation is the reduced glass transition temperature (T_{rg}). In his famous paper, Turnbull showed that crystal nucleation is lowered by higher values of the reduced glass transition temperature (T_{rg}), being immeasurably small for T_{rg} ~ 2/3 (Turnbull's criterion) [242]. The reduced glass transition temperature and Turnbull's criterion have been invaluable tools during the development of MGs, however, this criterion is not applicable to all glass forming alloys [246,250], and other criteria had been developed by including the offset crystallization temperature (T_x) and the temperature of the first crystallization peak (T_p).

The utmost importance of the liquidus, glass transition and crystallization temperatures has been shown by the different number of Glass Stability criteria developed since Turnbull's first steps. Some of them like the reduced glass transition temperature, the thermal stability range or Hruby's [251] criterion had been known and used since forty years ago, while others like Lu and Liu's γ parameter [252] are relatively new (Table 5). These parameters are of great importance in the field as indicators of possible directions in which better glass forming alloys can be obtained. GFA of MGs is affected by numerous parameters (*section 1.2.1*), and oversimplification by simple, although reasonable, thermodynamic parameters may be insufficient. The literature contains several works in which numerous parameters are compared, revealing that not all metallic systems can be correlated with a single parameter [253-255], showing that empirical parameters based on the liquidus, glass transition and crystallization temperatures are not enough to describe the GFA of amorphous materials. This has been recognized and attempts to include other

parameters (i.e. entropy of fusion, and kinetic fragility) had led to more reliable empirical criterions [256,257].

Table 5 Some of the most common and accepted GFA criteria.

Criterion	Formula	Reference
Reduced Glass Transition Temperature	$T_{rg} = \frac{T_g}{T_L}$	[242]
Thermal Stability Range	$\Delta T = T_x - T_g$	[258]
Hruby's criterion	$H_R = \frac{T_c - T_g}{T_L - T_c}$	[251]
Weighted Thermal Stability Range	$H' = \frac{T_x - T_g}{T_g}$	[259]
Saad and Poulain parameter	$S = (T_c - T_x)\frac{T_x - T_g}{T_g}$	[259]
Donald and Davie's parameter	$\Delta T^* = \frac{T_L^{mix} - T_L}{T_L^{mix}}, where\ T_L^{mix} = \sum_i^n n_i T_L^i$	[260]
Lu and Liu γ parameter	$\gamma = \frac{T_x}{T_g - T_L}$	[252]

Historically, it is well known that MG formation is highly dependent on the alloy-chemical factors: heat of formation, valence electron concentration and atomic size ratio [261]. It is commonly accepted that low values of Gibb's free energy (ΔG=ΔH-TΔS) promote MG formation [257]. The heat of formation has been an effective pointer of possible glass-forming alloys, as negative heat of formation or slightly positive heat of formation ensures that the constituent elements will mix completely in the liquid state [261]. Thus, negative heats of mixing raises the energy barrier between the liquid-solid interface reducing the diffusion of atoms upon cooling [225]. Nevertheless, it is the importance of the atomic ratio between the constituents and the electronic interaction in the alloy, which has led to the development of better glass-forming indicators.

The presence of atoms with different sizes is well known to lead to higher random atomic packing densities. Mismatched atoms can decrease the size of interatomic voids (i.e., free volume) present in the amorphous state [262]. Experimental data regarding the minimum solute concentration to form a glass was correlated with the volume mismatch of binary alloys ($\frac{\Delta v}{v_A}$) proposed by Egami and Waseda [261]. This led to the appearance of what will be called the λ parameter and the condition for crystal instability, from which the minimum solute concentration to form a glass can be calculated [261]:

$$|\lambda_0| = C_B^{min} \left|\frac{\Delta v}{v_A}\right| = C_B^{min} \left|\left(\frac{r_B}{r_A}\right)^3 - 1\right| \simeq 0.1 \qquad \textbf{(3)}$$

where C_i^{min}, v_i and r_i are the minimum solute concentration to form a glass, the atomic volume and the atomic radii of element i, respectively, where A is the matrix or host element and B the solute. This expression is nothing more than a criterion for structural instability for Dense Random Packed (DRP) structures as showed by the mathematical analysis of Egami [263]. In this paper, the same expression was reached using geometrical constrictions in the coordination number (N_C) and considering the solid-state amorphization as a melting phenomenon. Using expression and available data on glass forming alloys, Senkov and Miracle developed a topographic criterion for MG formation [262,264]. These authors noticed an interesting correlation between the shape of the concentration vs radii plot of the constituent elements. High glass-forming alloys were found to have single-peak distributions with concave downward shape (Figure 16), which could be used as a complementary indicator of GFA.

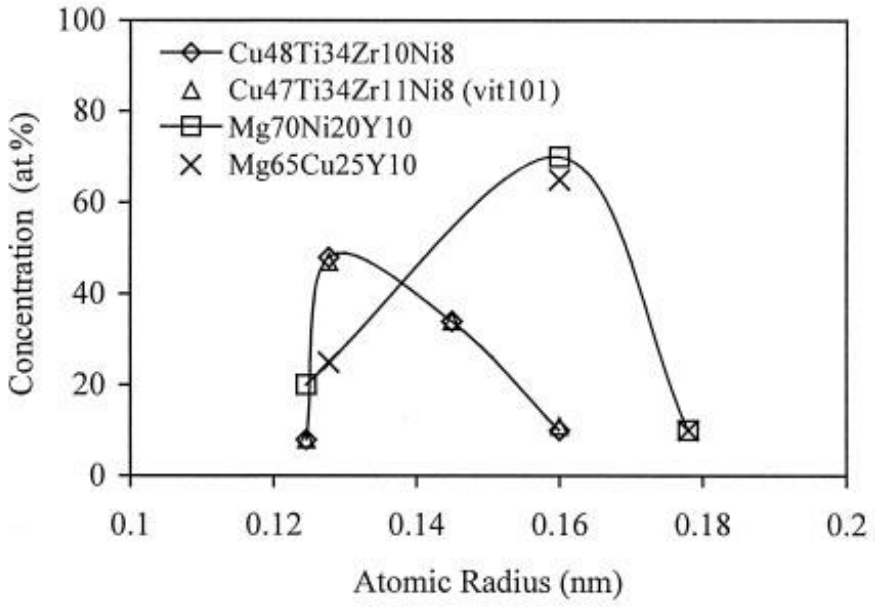

Figure 16 Concentration vs radii plot of the constituent elements with concave downward shape [262].

Turning now to the electronic parameters of the MG constituents and the ability of the alloy to form MGs, solid solutions and stoichiometric compounds are prone to formation if the constituent elements have low differences in electronegativity [265]. Consequently, the electronic state of the elements may be an indicator of the GFA [266]. This premise coupled with the work of Egami and Waseda was explored by Olive et al in several works, which showed promising results [267-269]. However, the use of electronegativity to search for good glass formers is relatively new, and more research is required.

As can be seen from the GFA criteria discussed, the quantity of parameters affecting the glassy state of metallic alloys is too numerous to use a simple equation to predict the formation of amorphous structures upon cooling. In order to simplify the finding of new glass-forming alloys, different principles such as the “confusion principle” (i.e. the existence of multiple possible phases with similar energy competing during crystallization that hamper each other), defined by Greer [270], were proposed. Some years later, Inoue expanded this idea and proposed three empirical rules to predict high glass-forming alloys [254]:

- Elements composing the metallic alloy must have an atomic difference greater than 12%.
- The mixing enthalpy of the atoms involved in the amorphous phase should have a negative mixing enthalpy.
- The amorphous state is favoured by the presence of multiple elements, leading to the "confusion state" of the alloy.

Multiple authors realised the importance of the atomic size, mixing enthalpy and number of constituents in the melt. However, Inoue quantified the importance of these parameters in the existing MG formers through “three rules of thumb” [254], clarifying routes by which high GFA alloys could be obtained. These rules, similar to the indicators selected by other authors [248], serve as general indicators to predict higher glass formers. However, exceptions have been found over the years by different authors [252,271,272].

1.2.4 Mechanical behaviour of MGs and MGCs

The mechanical properties of MGs are greatly influenced by changes in the atomic bonding of neighbouring atoms. It should be noted that the atomic bonding in MGs is weaker than in their crystalline counterparts (seen in the smaller Young modulus of MGs). The rearrangement of atoms in MGs under stress leads to the nucleation and formation of shear bands, releasing the stress energy. Although the correlation between atomic motion and shear band formation is not completely understood, the free volume theory initiated by Cohen and Turnbull [273] is commonly used to explain MG deformation. The main argument in this theory is evident; only when enough space is created can an atomic jump occur (Figure 17a), i.e., shear formation requires the presence of “free volume”. This idea was further developed by Spaepen [274], who analysed the competition between structural relaxation and free volume formation. However, simulations have shown that the formation of free volume is a more collective process (Figure 17b) [275]. As a result, the formation of free volume is more similar to the theory proposed by Argon where a local cluster of ~ 100 atoms undergoes an inelastic shear distortion referred as a “flow defect” or Shear Transformation Zone (STZ) [276,277].

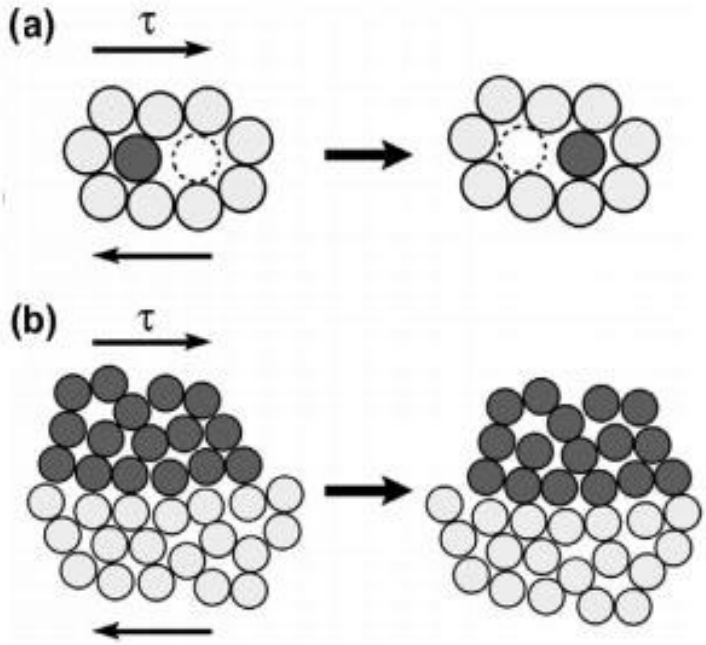

Figure 17 Deformation models for MGs (a) Spaepen and (b) Argon [278].

The plastic deformation in MGs is caused by the accumulation of shear band and free volume redistribution. At room temperatures, this process takes place as an inhomogeneous flow due to localization in a small number of shear bands, thus resulting in their brittle behaviour. For stresses lower than the yield strength, the deformation energy can be stored elastically. As the stress increases, the flow of localized regions occurs, causing strain softening and an increase in the plastic flow [279]. Finally, the stress is relaxed when the deformation energy has been lowered under a threshold value. If the first shear banding arrests, further deformation is accommodated by new shear bands, causing a common “serrated” appearance of the profile in the load vs deformation plots [279,280]. However, MGs fail catastrophically due to the initiation and propagation of a single shear band [244]. Consequently, multiplication of shear bands and shear band arrest are of utmost importance for any MG’s development. Nevertheless, shear band localization is not completely understood. The adiabatic nature of shear banding has led to the possibility of shear localization due to an increase in temperature during shear formation. Experimental measurements have shown that shear formation causes a localized increase in temperature [281], although, the role of this phenomenon in shear localization is still debatable [279].

MGs loaded in uniaxial conditions fail catastrophically due to the formation of a few dominant shear bands [244,282]. The formation of few shear bands causes a limited plastic deformation until failure (Figure 18c). Consequently, a strategy to enhance the plastic deformation in MGs, and thus, its ductility, implies the increase of shear band density. While some MG systems have shown higher ductility due to shear band branching [283,284], higher ductility has been obtained by shear band confinement in MG composites [244]. In MGCs, the crystalline phases embedded into the amorphous matrix can arrest and deflect the propagation of formed shear bands (Figure 18a and 18b). The presence of hard particles in the path of propagating shear bands causes an increases in the energy necessary to develop the existed shear bands. Due to the limited growth imposed, further softening, free volume redistribution and shear band nucleation is increased. As a result, the MG deforms through highly organised and distributed shear bands which can be controlled by the volume fraction of crystalline phases [244]. However, special care should be taken, as volume fractions higher than the percolation threshold will led to the embrittlement of the BMGCs [254,285,286], and work hardening of the embedded particles may not be enough to compensate for the lower mechanical properties of some intermetallics [287].

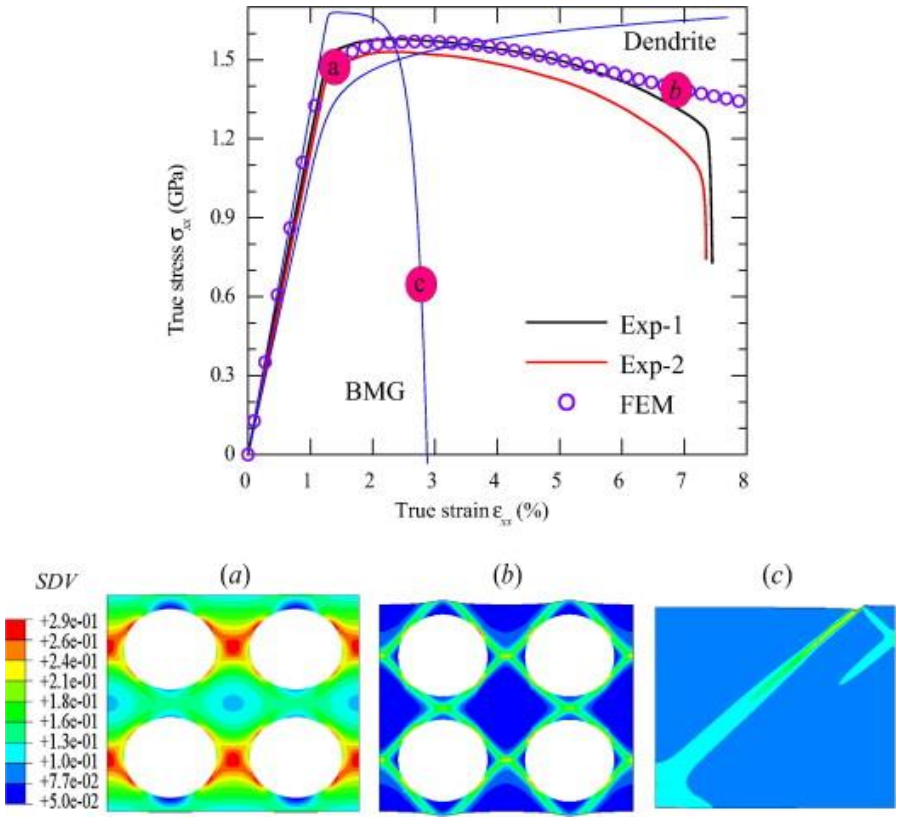

Figure 18 Tensile test numerical simulation showing the increase in ductility caused by crystalline inclusions in BMGs (a and b) in contrast to the (c) brittle behaviour inherent to BMG. Lower panels display the shear band formation for a BMGC (a) v_f = 43 % ε_{xx} = 1.5 %, (b) v_f = 43 % ε_{xx} = 6.5 % and BMG (c) ε_{xx} = 1.5 % [288].

1.2.5 Wear performance of metallic glasses

Touch surfaces are subjected to continuous friction. Healthcare professionals, patients and visitors touch, scratch and stain these materials. Thus, it is important to know the behaviour of metallic surfaces under these conditions. Wear, or the removal of material due to the contact between two surfaces is a complex phenomenon. The different mechanisms responsible for such phenomena do not have to be caused only by mechanical interaction. The realization of this fact can be seen in the change of texts dedicated to tribology through the years. As an example, older manuscripts focused on the origin of friction, the equations governing the contact between solids and mechanical wear [289], while the role of oxidation and corrosion was analysed later [290]. Modern texts account for all these mechanisms and a few more, in six categories: abrasive, adhesive, fatigue, erosion, chemical and electric-arc induced

wear [291,292]. Of these, only the abrasive, adhesive and fatigue wear are directly associated with wear in MGs, while oxidation (chemical wear in an oxygen rich atmosphere) is related to the increase of temperature caused by continuous friction. The smeared oxides can reduce the wear of MGs, acting as a protective layer [293]. Erosion and arc-induced wear are not applicable to metallic surfaces designed as touch surfaces, and, as such, are not considered in this thesis. Although other mechanisms like fretting can be found in the literature, they are mostly a combination of the six aforementioned mechanisms [292]. The high number of mechanisms and the interaction between them complicates the analysis of metallic surfaces. Maps depicting the most prominent mechanism of wear and its dependence on the normal load and sliding velocity have been developed for several steels and other metals [294]. However, it is normal to find all these mechanisms acting at the same time (Figure 19).

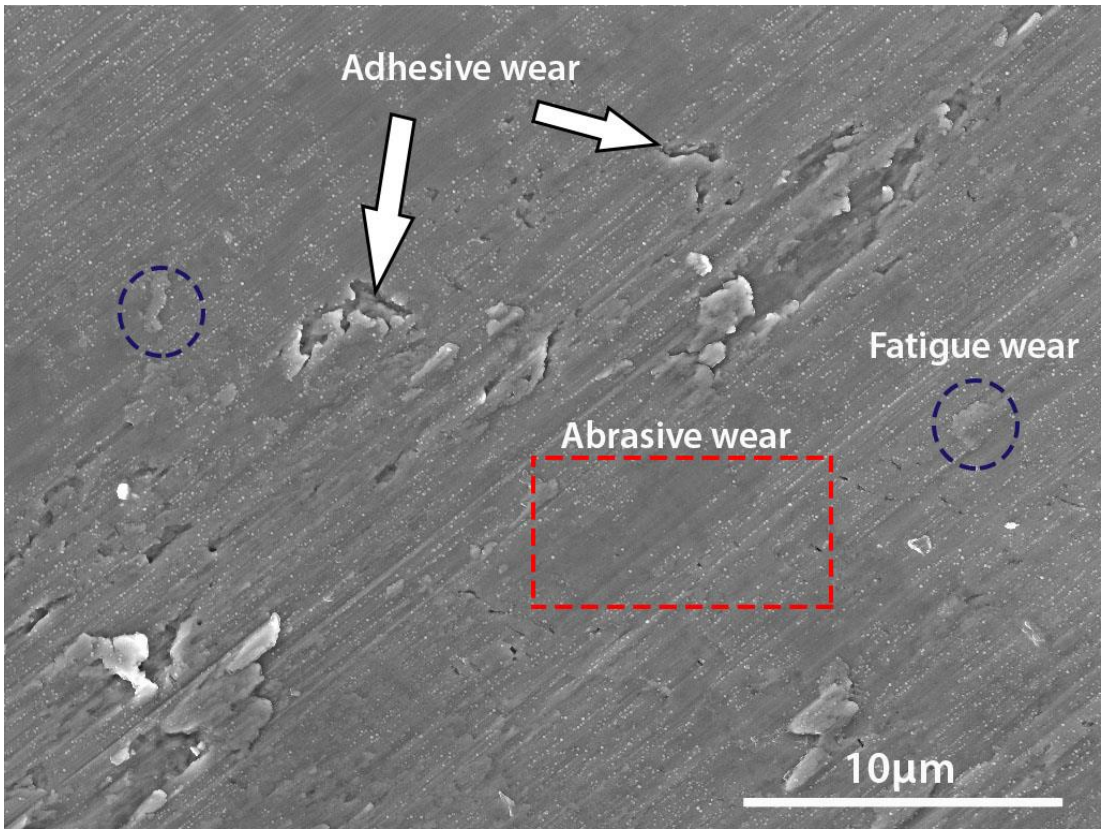

Figure 19 CuZrAl bulk sample subjected to a scratch test showing the three common mechanisms of abrasive, adhesive and fatigue wear.

Abrasive wear takes place when hard asperities or particles slide on a softer material, damaging the interface by fracture or plastic deformation. As these asperities or particles remove material, cutting, fracturing, ploughing or grain pull out can take place. If the wear between surfaces is caused by the interaction between asperities, the abrasive wear is called two-body mode, while, if the wear is caused by the detachment of abrasive particles it would be referred as three-body mode. This mechanism is complex and depends on the properties of the two materials (i.e. hardness), the contact parameters (i.e. load, sliding speed) and the morphology of the asperities and particles (i.e. asperity angle or size) [291]. Despite it's complexity, abrasive wear can be easily discerned by the characteristic long and thin grooves left in the worn surface (Figure 19).

Adhesive wear is caused by the detachment of material due to the contact between asperities. The real area of contact between two bodies is much lower than the apparent macroscopic surface. When two bodies come together, the asperities intrinsic to any untreated material will touch. As the distance between the two bodies diminishes, the asperities deform, first elastically, and finally plastically. The deformation of these materials ends once the number of asperities in contact equals a real area capable of sustaining the normal load. Consequently, there is a high stress applied to the microscopic asperities. These stresses can cause a strong adhesion between asperities, leading to the detachment and fragmentation of particles due to plastic shearing of successive layers [292]. This interaction results in the presence of transferred material smeared onto the surfaces and the existence of holes into the weaker material (Figure 19).

The sliding of two bodies causes the shifting and deformation of the material beneath the surface. The Hertzian theory of non-adhesive elastic contact shows that the maximum shear stress and, as such, the Von Mises stress take place beneath the two surfaces in contact [295] (Figure 20). The accumulation of high stresses and deformations over time, can lead to crack formation under the surface of the material. Continuous sliding causes the growth of these cracks and, once the crack reaches the surface, the sliding forces remove the affected material. As such, the surface reveals delamination and chipping, easily discernible in the wear track (Figure 19).

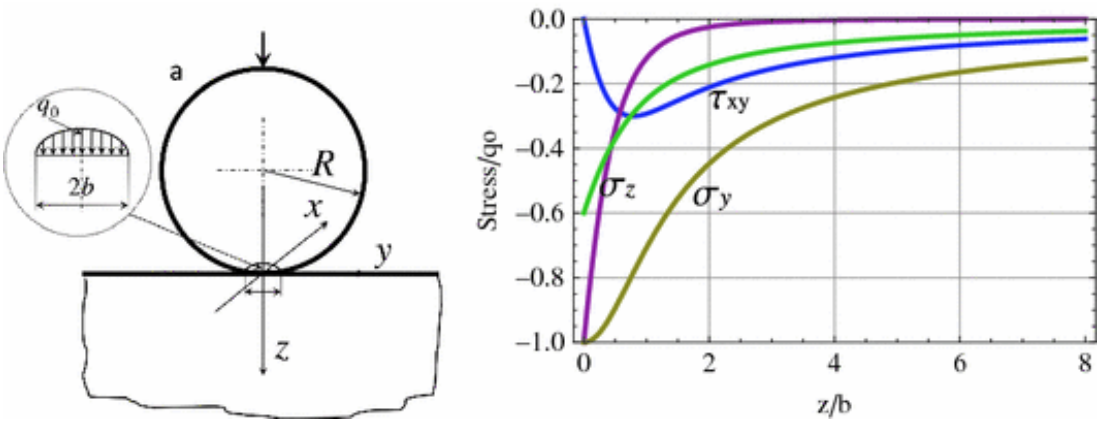

Figure 20 Stress components as a function of the maximum stress (q_0) and the ratio between the contact depth (z) and the radius of the circle of contact (b) [296].

These wear mechanisms are commonly observed during the tribological analysis of MGs and MGCs. As mentioned in *section 1.2.1* the hardness, fracture toughness and high strength proper of MGs indicate that good tribological properties can be expected. Authors such as Greer et al. [297], Fleury et al. [298] and Yokoyama et al. [299] revealed that MGs can show lower wear rates than crystalline materials. Nevertheless, experimental investigation of Vitreloy by Fu et al. [300] (dry conditions) and by Blau [301] and Bakkal [302] (lubricated conditions) has demonstrated that some amorphous alloys can show coefficients of friction (COF) and wear rate values similar or worse than those of common 52100 steel. These results have led to a more detailed investigation of the parameters that affect the tribological behaviour of MGs. The role of load [303], sliding speed [303-305], counterpart material [306], sliding distance [303] and roughness [307] in several MGs compositions has been studied. Most of the cited analysis reveal that wear in MGs start as abrasive wear, while higher loads and sliding speeds increase the influence of adhesive and fatigue wear. However, differences in composition and testing methods have been reported to cause differences in the wear rates of MGs [298], while the continuous friction between the MGs and counterpart materials have shown to cause oxidation and nanocrystallization [300,303,308], making an accurate description and comparison difficult. Consequently, it can be said that MGs can exhibit higher wear resistance than their crystalline counterparts, but it is hard to account for the influence of all the parameters affecting the tribological properties of these materials. As such, more in depth analysis is necessary.

From all the parameters mentioned, the contact temperature is one of the most important during the assessment of MG wear resistance. Part of the energy created in the interaction of two bodies during sliding is transformed into heat. The heat flux created is redirected into the two materials and, depending on the resulting temperatures, nanocrystallization, crystal growth or even viscous flow can be caused. In pin-on-disc configurations, this value may be high enough to affect the structure of the samples. While the average contact temperature would not be high enough to change the wear rate, localized increases of temperature of small duration can take place due to the high stresses and deformations in a few asperities. As a result, this flash temperature may influence the tribological properties of sliding bodies. This is suggested by the work of Rahaman et al. [309,310], Kong et al. [311] and Wu et al. [312] who have tried to correlate the tribological properties of MGs with the contact temperature of two sliding bodies. These analyses revealed the presence of nanocrystals or viscous flow possible only if the temperature has risen over the T_g of the MG.

Similarly, analysis of a Cu-Zr-Al-Ni system indicates that pin-on-disc configurations can lead to structural changes in the contact surfaces [293]. Figure 21 shows how the microstructure of a Cu-Zr-Al-Ni BMGCs has been affected due to increases in load and microalloying. In the low load modes (Figures 21a and 21c), the volume fraction is relatively low, but increases with the applied load by the recrystallization of the material (Figure 21b) and the appearance of large oxides in the samples (Figure 21d). These structural changes are related to the contact temperature rise, which can be estimated assuming a stationary pin (material 2) and a moving flat steel disk (material 1) using the following equation [312]:

$$\Delta T_{max} = \frac{1.32 b \mu p V}{\sqrt{\pi\left(K_1\sqrt{1.2344 + Pe_1} + K_2\sqrt{1.2344 + Pe_2}\right)}} \quad \textbf{(4)}$$

where b, μ, p, V, K and Pe are the contact radius, friction coefficient, normal pressure, sliding velocity, thermal conductivity and the Peclet number ($Pe = \frac{Vb\rho C}{2K}$) respectively, while some of these parameters depend on the elastic constants (E and ν), the density (ρ), the thermal conductivity (K) and the specific heat (C). This localized

increase in temperature can be near or greater than the glass transition temperature of the alloy [293], leading to the oxidation and structural changes shown in (Figure 21b). These changes harden the analysis of touch surfaces, suggesting that pin-on-disc configurations may not be the best method to analyse the wear performance of high-touch surfaces.

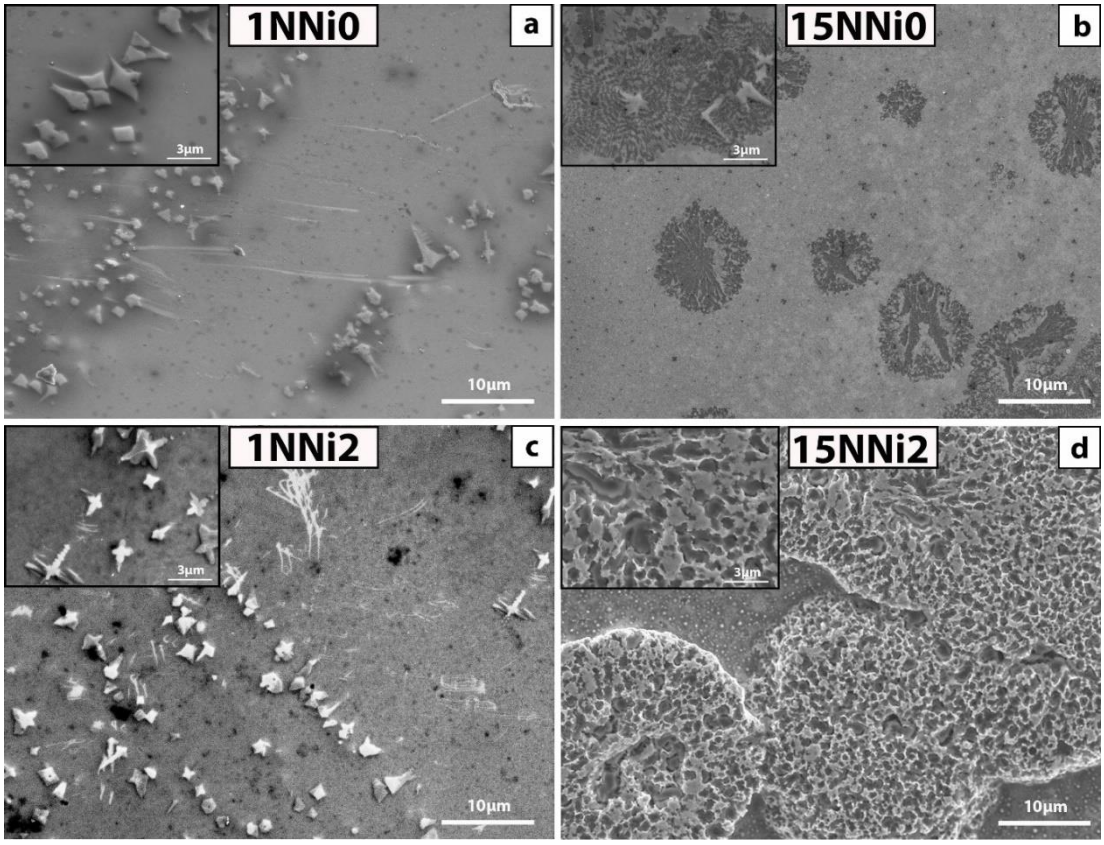

Figure 21 Image depicting the structural changes in a Cu-Zr-Al-Ni alloy due to the sliding contact of a pin-on-disc configuration as composition and load increased [293].

In contrast to pin on disc, the assessment of tribological properties can be made using other configurations such as the scratch test. During the scratching process, a stylus sinks in to the material and then, as it slides, the material is pushed aside and collects at the edge of the track to form the pile up, rather like the bow wave in a moving boat. The material is plastically deformed and moved to the edge of the track by plastic flow. This does not necessarily lead to wear as material is displaced from the centre to the edge of the track but the pile-up is irregular and depends on the local flow conditions and material microstructure. It is this that creates the apparent particles of

material displaced from the groove. If wear occurs it will be in the regions at the edge of the groove where the material flow has resulted in material that exceeds the plastic strain limit for the material. Consequently, it is of great interest to analyse the ratio between the cross-section area of the groove and the pile-up [13,179,313] (Figure 22).

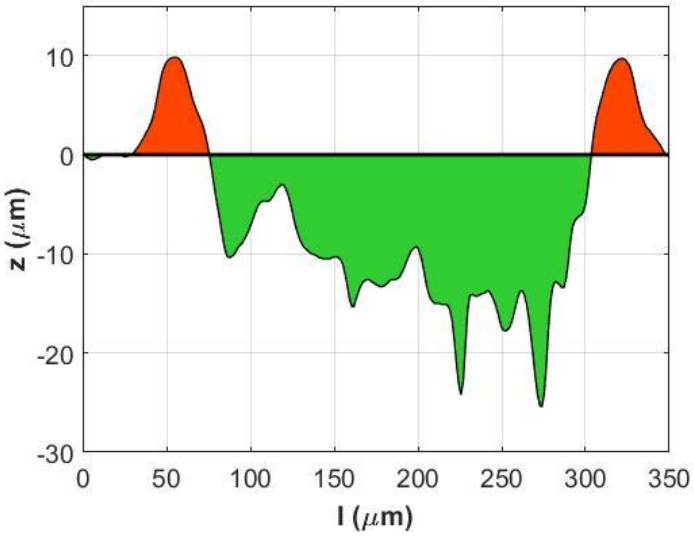

Figure 22 Scratch test profile showing the total pile-up area (red) and the groove cross section area (green).

Besides the groove to pile-up area ratio, the standard test method **ASTM G171-03** [314] can be used to quantify the hardness of the tested material regardless of its nature; it has been used with metals [315], polymers [316], ceramics [317], composites [318] and coatings [319]. The scratch hardness number can be calculated from the scratch width using the following equation:

$$H_s = q\frac{4 * P}{\pi * w^2} \quad \textbf{(5)}$$

where H_S [Pa], P [N] and w [m] refer to scratch hardness, normal load and scratch width respectively and q is a constant dependent on the materials mechanical response and how it supports the indenter (q ~ 2 for rigid plastic behaviour and 1 < q < 2 for viscoelastic plastic materials) [320]. Due to the nature of MGs, the material

behaviour in that equation has been approximated as a rigid plastic, which is consistent with the available literature in MGCs [318].

Before finishing this section, it should be noted that pin-on-disc and scratch tests are direct measurements of wear resistance. In contrast to these methods, the correlation between hardness (H) and reduced Young's modulus (H/E_r), where $E_r=E/(1-v^2)$, of a material can be used as an indirect measurement of wear resistance [321]. At the same time, the yield pressure between a rigid ball and a plate is equal to $P=0.78r^2(H^3/E_r^2)$, where r is the contacting sphere radius [321]. This correlation indicates that the contact pressure is highly dependent on the mechanical properties of the tested material. Thus, (H^3/E_r^2) can be an indirect indicator of the wear resistance [322]. The hardness and reduced Young's modulus of a material can be easily obtained during nanoindentation. As a result, these two correlations H/E_r and H^3/E_r^2 are of special interest to estimate the tribological properties of nanomaterials (i.e. thin film coatings).

1.2.6 Cu-Zr-Al system and Cu-based BMG

In the previous sections, the importance of different MG formers has been overviewed. Late transition metal-based BMGs, and more specifically, the Cu-Zr glassy alloy are of great interest due to their high GFA. This system has been known as a potential amorphous alloy since the early 1980s due to it's relative high glass-forming ability near the deep eutectic [323,324] (Figure 23). Further investigation of alloying in the Cu-Zr system led to what is considered as the first Cu-based BMG ($Cu_{60}Zr_{30}Ti_{10}$) [325]. The impressive mechanical behaviour (σ_{max} ~ 2000 MPa) and the possibility of obtaining bulk samples (ϕ_{crit}=4mm) increased the interest in the Cu-Zr-Ti system [325]. Nonetheless, the brittle mode of failure common to glassy alloys is showed in this system, limiting its potential uses.

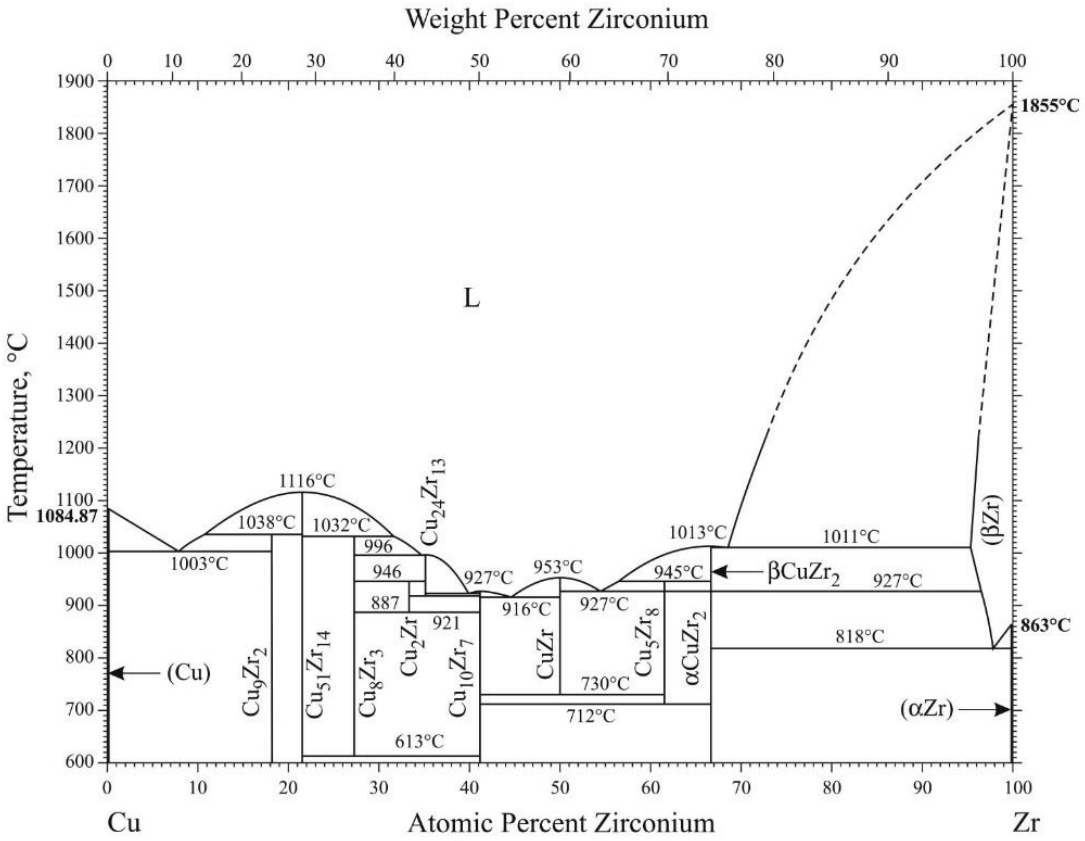

Figure 23 Cu-Zr phase diagram [326].

The Cu-Zr-Al ternary system was reported to be a better glass former than the previously studied Cu-Zr-Ti, Cu-Hf-Ti, Cu-Zr-Hf-Ti, Cu-Zr-Ti-Y and Cu-Zr-Ti-Be systems [325,327]. The high GFA was explained by considering the presence of deep eutectics and the compliance with the three previously mentioned empirical component rules: multicomponent alloy, negative heat of mixing and large atomic size differences among constituent elements (Table 6). Years later, Eckert et al. [328] developed alloys corresponding to the Cu-Zr-Al system with increased ductility (up to 18% strain to failure) that was attributed to the increase of shear banding nucleation and propagation upon deformation. Their relatively low cost, high fracture strength, high GFA and their proposed “ductility” makes these alloys great candidates for use as structural materials [329,330].

Table 6 Atomic radii (nm) and enthalpy of mixing (ΔH_{AB}^{mix}) for the elements discussed [331].

Atomic number	Element	Atomic radii (nm)	Enthalpy of mixing (KJ/mol)											
			Be	Al	Ti	Ni	Cu	Y	Zr	Nb	Mo	Ag	Hf	Ta
4	Be	0.113		0	-30	-4	0	-32	-43	-25	-7	6	-37	-24
13	Al	0.143	0		-30	-22	-1	-38	-44	-18	-5	-4	-39	-19
22	Ti	0.147	-30	-30		-35	-9	15	0	2	-4	-2	0	1
28	Ni	0.125	-4	-22	-35		4	-31	-49	-30	-7	15	-42	-29
29	Cu	0.128	0	-1	-9	4		-22	-23	3	19	15	-42	-29
39	Y	0.182	-32	-38	15	-31	-22		9	30	24	-29	11	27
40	Zr	0.162	-43	-44	0	-49	-23	9		4	-6	-20	0	3
41	Nb	0.143	-25	-18	2	-30	3	30	4		-6	16	4	0
42	Mo	0.136	-7	-5	-4	-7	19	24	-6	-6		37	-4	-5
47	Ag	0.144	6	-4	-2	15	15	-29	-20	16	37		-13	15
72	Hf	0.16	-37	-39	0	-42	-42	11	0	4	-4	-13		3
73	Ta	0.143	-24	-19	1	-29	-29	27	3	0	-5	15	3	

Since its discovery, additional investigation in the Cu-Zr-Al system has led to more phenomena which increase the appeal of this family of alloys. Firstly, the high GFA can be further increased with minor Y, Nb, Sn, Mo and Ag additions [332-334], while proper alloying can enhance specific properties like corrosion resistance [335]. The possibility of tuning the mechanical properties of this system suggests great versatility, vastly increasing the possible applications in the industry.

In order to further increase the ductility of BMGs and BMGs composites, numerous authors have tried to use the traditional existing theories in crystalline materials. Along with the dislocation/shear band arrest, the stress-induced martensitic effect observed in shape memory alloys can be used. Shape memory alloys exhibit the ability to recover some degree of plastic deformation [336]. This phenomenon is based on the microstructural change triggered by the increase of stress during loading. In SMAs, austenite transforms into martensite upon stress. Considering that martensite is harder than austenite, the SMA work-hardens, thus increasing the ductility of the alloy. This deformation can be recovered when the martensite transforms into

austenite upon heating [336]. The practical applications of SMAs are focused in high wear resistance material, however, the main focus of the MG community in this regard is linked to the possibility of producing a Transformation-Induced Plasticity in a BMG. From all the available species in the Cu-Zr and Cu-Zr-Al phase diagrams, the CuZr can exhibit a reversible martensitic transformation from a cubic primitive CuZr B2 to a monoclinic B19' [337]. CuZr is a metastable species which decomposes into $Cu_{10}Zr_7$ and Cu_5Zr_8 at 730 °C and into $Cu_{10}Zr_7$ and βZr_2Cu at 712 °C, making it unavailable in equilibrium conditions. Nevertheless, the non-equilibrium conditions caused by high cooling rates in MGs can maintain the CuZr phase in a MGC [338,339]. The stress field at the particle/amorphous phase interphase and the increase in shear band formation caused by small particles embedded into an amorphous matrix, in addition to the martensitic effect of the metastable CuZr, can lead to superior mechanical properties, increasing the interest in Cu-Zr-Al composites [339].

Finally, it should be noted that Phase Diagrams can be used to find best glass-forming alloys and to understand the possible crystal phases formed in MGCs. Two component phase diagrams may be useful while the content of the third element is low, but even small quantities of a third element can cause important changes in the crystallization kinetics of the melt. As such, it is important to use three phase diagrams when those are available, however, our understanding of both Cu-Zr and Cu-Zr-Al phase diagrams is limited. Several authors have used computational and experimental methods to investigate the Cu-Zr system, however, discrepancies, such as the stability of Cu_5Zr_8 and $Cu_{10}Zr_7$ for high temperatures, remain unsolved [340-344]. This lack of information is more pronounced in the Cu-Zr-Al system. Some information can be found in the literature [345,346], while, experimental and computational research are being carried out [347-350] (Figure 24a and 24b). To completely understand the crystallization kinetics of BMGs, TTT diagrams (i.e. Time Temperature Transformation diagram) should be used, but the literature is scarce [351-353], making necessary the use of phase diagrams. Nevertheless, a complete Cu-Zr-Al Phase diagram is not available which coupled with the shifting of the phase diagrams lines caused by the high cooling rates inherent to MGs formation shows that phase diagrams can only indicate the most probable crystalline phases formed and more research is required.

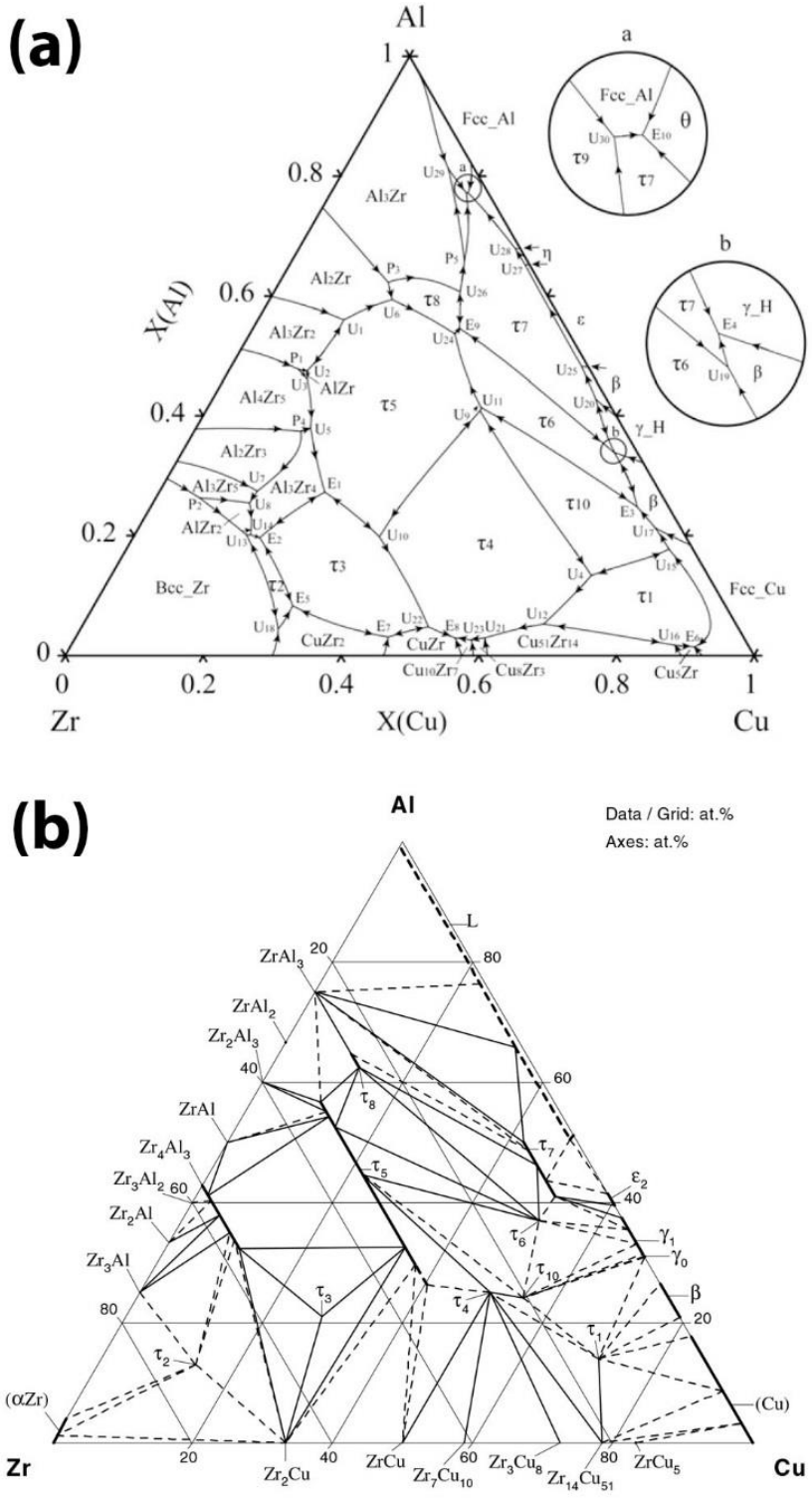

Figure 24 Evaluated isothermal sections of the Al-Cu-Zr system for (a) liquidus [349] and (b) 800°C [354].

1.3 Scope and objectives of the thesis

MGs and MGCs exhibit interesting mechanical and chemical properties, which make them an interesting candidate for developing antimicrobial touch surfaces. Although silver, zinc and other metallic elements have the ability to eliminate pathogens adhering to their surface, the outstanding biocidal properties of copper reveal that Cu-rich alloys are more desirable for their application in healthcare facilities. Thus, combining the high wear and corrosion resistance inherent to MGs and MGCs, with the superior antimicrobial properties of copper is of great interest in the prevention of hospital-acquired infections.

The main aim of this work is to enhance the antimicrobial performance and wear resistance of Cu-based MGs to replace common stainless steel surfaces susceptible of bacterial colonization. This will be done by the preparation of Cu-based bulk MGs which display hard, rich copper intermetallics. For this purpose, it is necessary to characterise the parameters that affect both wear and antimicrobial properties of Cu-based MGs and MGCs to develop tuneable alloys with an optimal combination of both properties. To accomplish this aim, a thorough analysis has been carried out to accomplish several objectives:

- Shed light in the role of both overall chemical composition, microstructure and volume fraction of crystalline phases in the wear and biocidal properties of the Cu-Zr-Al system (*chapter 3*). For this purpose, the selected alloys display relatively high GFA coupled with the possibility of changing the nature and volume fraction of crystalline phases through modifications in the casting process and master alloy composition.

- Investigate the role of mechanical, roughness, and chemical, oxidation, superficial modifications on the antimicrobial performance of the aforementioned alloys (*chapter 4*).

- Evaluate the antimicrobial properties of Cu-based thin film metallic glasses (TFMGs). As thin films are more appealing for use on large surfaces due to their relative ease of application will evaluate the antimicrobial activity of Cu-

Zr thin films with high Cu content and the possibility of enhancing their properties by changes in the deposition parameters, pressure and temperature, (*chapter 5*).

- Compare wet and dry antimicrobial tests and their influence in the contact killing mechanics. The development of “dry” antimicrobial tests will be performed, while both copper diffusion and drying impact in *E. coli* and *S. aureus* cells will be studied (*chapter 5*).

- Analyse the influence of copper ions on the outward and inner morphology of bacteria. Three different mechanisms were mentioned to explain the high antimicrobial performance of copper, but little do we know about the relative importance of structural damage in the contact killing of MGs. As such, it is necessary to correlate the effects seen in pathogens deposited on MGs with those observed on copper-rich surfaces (*chapters 4* and *5*).

All chapters will include a small section with the main findings revealed using the experimental methodologies described in chapter 2. Finally, chapter 6 will show the main contribution to knowledge as well as the future directions which naturally emerged after the current work was completed.

2 Materials and methods

In this chapter all materials, methods and equipment required to carry out the present work will be described. Special attention to the development of antimicrobial tests will be taken, while commonly accepted methodologies will be only mentioned.

2.1 Sample preparation

Bulk metallic samples were prepared from elements with purity higher than 99.9 at. % (Table 7). Before melting, all elements were cleaned in an ultrasound bath using pure ethanol for 5 min and left to dry at room temperature. The weight of the master alloy was 0.8 g for the 2 mm copper mould, while 3 mm samples required 1.5 g of alloy to ensure a complete filling. The master alloys were re-melted three times to attain good chemical homogeneity in a Zr-gettered high purity argon atmosphere. Composition of all samples was checked using Electron Dispersive X-ray Spectrophotometry (EDX) and weight loss due to alloying was monitored using an analytical balance (Acculab Sartorius group, ±0.1 mg). For the Cu-Zr thin films, a rectangular Cu target and a circular Zr target, both with ≥ 99.9 % purity, were selected (Table 7).

Table 7 Elements used in the preparation of BMGCs and TFMGs.

	Element	Purity	Shape	Supplier
BMGCs	Aluminium	99.998	Foil 2 mm	Alfa Aesar®
	Copper	>99.9	Shot (1-10 mm)	Alfa Aesar®
	Zirconium	>99.9	Foil 0.025 mm	Alfa Aesar®
TFMGs	Copper	99.99	Rectangular target 248 mm x 133 mm x 10 mm	Testbourne Ltd.
	Zirconium	99.9	Circular target 100 mm x 3 mm	Testbourne Ltd.

2.2 Suction casting

All bulk metallic samples were prepared through suction casting in a Compact Arc Melter MAM-1 (Edmund Bühler GmbH, Figure 25a and 25b). The machine was equipped with water-cooled copper crucibles regulated through a chiller (temperature range between 10-20 °C) and copper moulds with 2 mm or 3 mm inner diameters. Contaminant oxygen was removed through subsequent fluxing cycles of the chamber with pure Argon, while, prior to casting, the chamber was evacuated to a pressure of 3-5x10^{-5} mbar. Once evacuated, the chamber was filled with Argon until a pressure of 0.4 bar was achieved, while the pressure in the vacuum cylinder was set up to 1x10^{-2} mbar or lower and the mould temperature to 10 °C. All samples were re-melted three times during 10 s each by setting the MAM-1 dial to an intensity of “3-4” to ensure the homogeneity of the melt with no excessive loss of material. For casting, the intensity was raised to “5” and applied to the sample for 5-10 s, obtaining 35 mm long rods with diameters between 2 or 3 mm (Figure 25c). Under these conditions the overall cooling rate will be up to 150K/s enabling to obtain BMGCs [355-357].

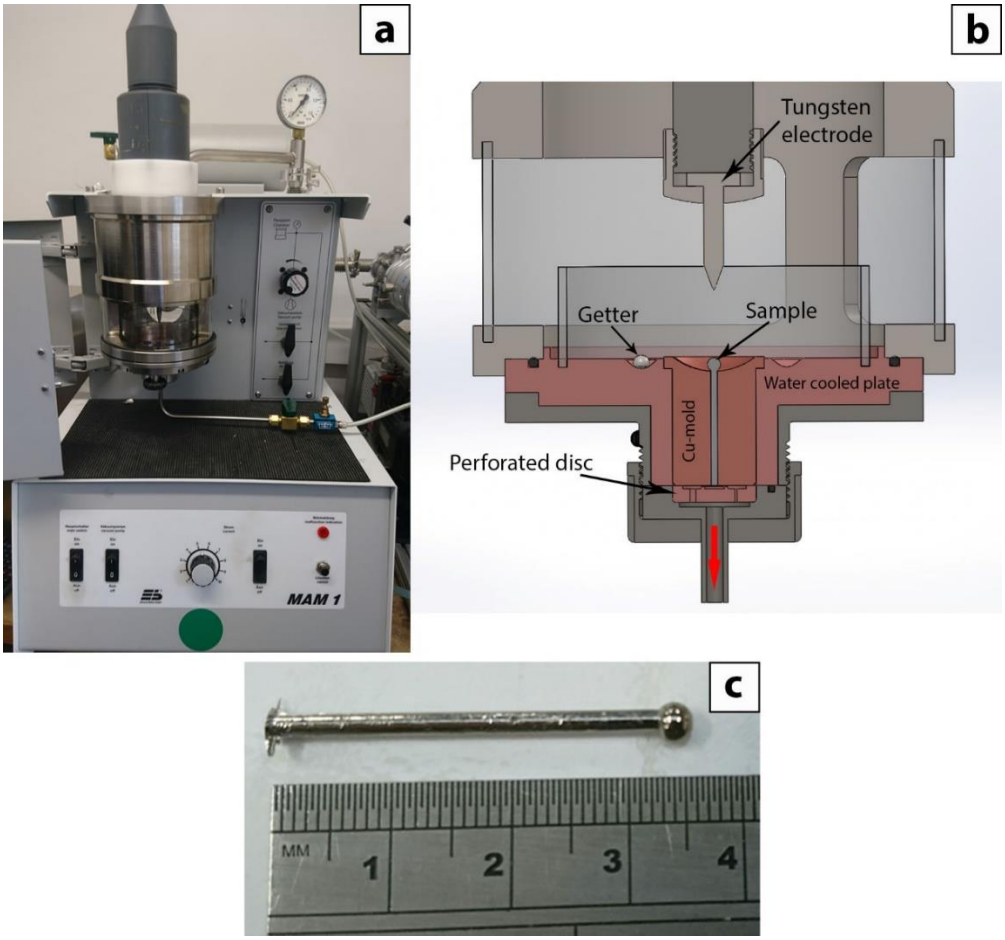

Figure 25 Compact Arc Melter MAM-1 (a) equipment, (b) schematic 3D model of the chamber and (c) Cu-Zr-Al 2 mm rod.

2.3 Magnetron sputtering

Cu-Zr thin films were prepared by magnetron sputtering using a Teer Coatings UDP multi-cathode deposition plant. 314 Stainless Steel coupons (5 x 5 x 1 mm thick) with a superficial roughness lower than 0.5 µm and soda lime glass slides (25.4 x 76.2 x 1 mm thick) were prepared as substrates. Before deposition, all samples were degreased and cleaned for 60 seconds with a 1:5 ratio of DECON90 solution in deionised water (DW). Once thoroughly cleaned, substrates were rinsed in DW and dried with nitrogen. Samples were mounted in the carrousel, and the chamber was evacuated to a base pressure of 1.5×10^{-5} Pa. Argon bleeding gas was introduced at the required flow rate to control the working pressure, 5×10^{-4} Pa. To eliminate any oxide in the metallic targets, the copper and zirconium targets were sputtered cleaned

at dc powers of 200 W and 160 W respectively for 10 minutes. Finally, the cathode shutters were opened and both targets were co-sputtered for 90 minutes onto the substrates mounted at a distance of 130 mm on the central carousel, rotating at a fixed speed of 5 rpm

2.4 X-ray diffraction (XRD)

The microstructure of the samples was analysed by X-ray diffraction patterns, using a XRDs: Siemens D5000 diffractometer with Cu Kα radiation (λ = 1.54184 Å) at 40 kV and 40 mA, with a scanning speed of 0.01°/s in the 2θ range 10°-90° All samples were cut into slices of 1.5 mm in length using a slow cutting machine equipped with a diamond disc. Both sides of these pieces were manually ground using SiC paper with decreasing grit (600 → 1200 → 2400 → 4000) to a sample height of 1 mm. Before XRD analysis, all samples were cleaned in an ultrasound bath with pure ethanol for 5 min and left to dry. XRD peaks were analysed using the library available in the equipment. All crystallographic phases detected in the present thesis can be found in Table 8. XRD scans were analysed to estimate the volume fraction of crystalline phases in the samples by calculating the ratio between the area of the Braggs peaks (i.e. after removal of the amorphous halo) to the area of the unprocessed XRD scan using DIFFRAC.EVA.

Table 8 Crystalline phases detected in the analysis of all samples**.**

Formula	Crystal system	Space group	a (Å)	b (Å)	c (Å)	α (°)	β (°)	γ (°)	Reference code
$AlCu_2Zr$	Cubic	Fm-3m	6.1900	6.1900	6.1900	90.00	90.00	90.00	03-065-6362
Cu	FCC	Fm3m	3.6070	3.6070	3.6070	90.00	90.00	90.00	00-002-1225
CuO	Monoclinic	C2/c	4.6530	3.4100	5.1080	90.00	99.48	90.00	01-074-1021
Cu2O	Cubic	Pn3m	4.2520	4.2520	4.2520	90.00	90.00	90.00	01-074-1230
CuZr (aust.)	Cubic	Pm-3m	3.2562	3.2562	3.2562	90.00	90.00	90.00	00-049-1483
CuZr (mart.)	Monoclinic	P21/m	3.2370	4.1380	5.4490	90.00	105.19	90.00	01-079-5510
$CuZr_2$	Tetragonal	I4/mmm	3.2204	3.2204	11.1832	90.00	90.00	90.00	03-065-7783
Cu_8Zr_3	Orthorhombic	Pnma	7.8686	8.1467	9.9770	90.00	90.00	90.00	00-042-1186
$Cu_{10}Zr_7$	Orthorhombic	Aba2	9.3470	9.3130	12.6750	90.00	90.00	90.00	01-078-3211
ZrO_2	Tetragonal	-	5.0700	5.0700	5.1600	90.00	90.00	90.00	00-002-0733

2.5 Scanning Electron Microscopy (SEM)

The surface and chemical composition of the samples was analysed using a Tescan Mira 3, Scanning Electron Microscope (SEM) with 3-15 kV of acceleration voltage, equipped with an Oxford Instruments X-Max 150 Energy Dispersive X-ray (EDX) detector. Before analysis, a sample used after XRD was mounted in 15 mL of conductive Phenolic Mounting Resing (CONDUCTO-MOUNT, MetPrep Ltd.). Mounted samples were manually ground using SiC paper with decreasing grit (600 → 1200 → 2400 → 4000) and further polished with 3 µm and 1 µm Polycrystalline Diamond Suspension (MetaDi™ Supreme, Buehler) to a mirror finish. Samples were attached to a 25 mm aluminium stud with a 25 mm Leit Adhesive Carbon Tab.

To analyse the morphological changes of bacteria deposited on the surfaces, inoculated samples were subjected to a variation of the method described by Fisher et al. [358]. Inoculum and deposition was prepared as described in *section 2.8 Antimicrobial tests.* After the desired contact time, each sample was moved into a well of a 24 well plate and 1 mL of 2.5 % glutaraldehyde was dispersed against the wall of the well to regulate the flow across the samples. After 1 h submerged in 2.5 % glutaraldehyde, each sample was rinsed with Phosphate-Buffered Saline (PBS) three times for 2 min each. Samples were then subjected to a graded ethanol series dehydration (25 %, 50 %, 75 % and 95 %) using 1 mL of each dilution for 5 min, and introduced in pure ethanol for 10 min. Finally, samples were left to dry and coated with 2-3 nm of platinum using a Q150R Rotary-Pumped Sputter Coater (Quorum Technologies). This method allowed the capture of high resolution images of bacteria where pili can be observed (see arrow and inset in Figure 26a). This process enabled the observation of morphological differences in the cells' envelope due to external parameters (i.e. incubation time: 1 day Figure 26a and 7 days Figure 26b) which will be of interest in *chapters 4* and *5*.

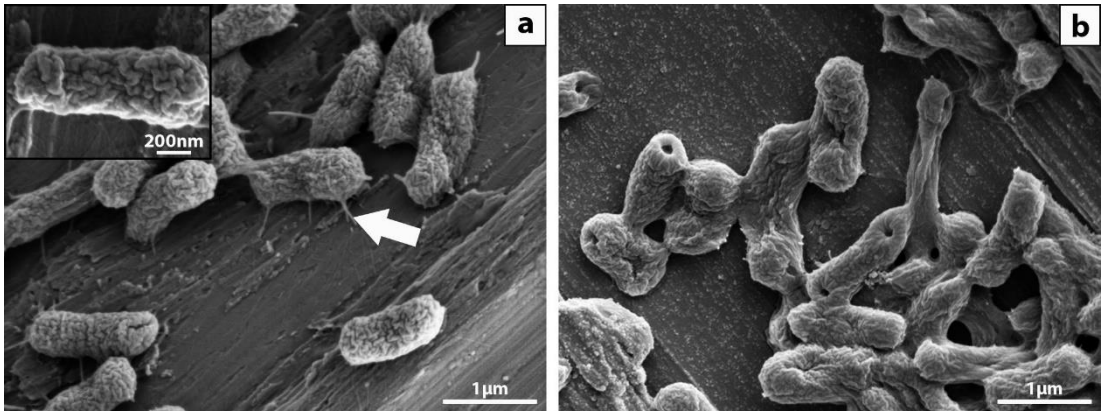

Figure 26 Example of SEM images obtained for *E. coli* cells deposited on stainless steel after (a) 1 and (b) 7 days of incubation.

2.6 Profilometry and Atomic Force Microscopy (AFM)

Superficial roughness and scratched morphology of the bulk samples was measured using a 3D optical profilometer (InfiniteFocus, Alicona). The instrument was equipped with x20 and x50 objective magnification lenses, achieving a minimum measureable roughness of 0.15 and 0.03 µm respectively.

The surface topography and roughness of Cu-Zr thin films was measured with a Digital instrument Dimensions™ 3100 Atomic Force Microscope (AFM) in contact mode across a 3 x 3 μm^2 sample area. Gwyddion software was used for data visualisation, while further processing was conducted using MATLAB software suite. Film thickness was measured using a Dekatak XTL stylus type profilemeter equipped with a 12.5 µm tip in a square edge step created in the films using a strip of 3mm wide Kapton tape, that was removed after deposition.

2.7 Scratch tests

All scratch test were carried out using a Teer Coating Limited scratch tester model ST220 equipped with a Rockwell C diamond stylus (cone angle 120°, radius of spherical tip 200 µm). Tests were performed in mounted and polished samples at a load of 30 N and a ramp rate of 10 mm/min. After the scratch tests, samples were attached to a 25 mm aluminium stud with a 25 mm Leit Adhesive Carbon Tab. To

improve the SEM imaging, a strip of adhesive carbon tape was placed touching a side of both the metallic sample and aluminium stud, and coated with carbon using a Q150R Rotary-Pumped Sputter Coater (Quorum Technologies).

2.8 Nanoindentation

Polished samples were used to perform Nanoindentation experiments. All tests were carried out at room temperature at approximately half the radius distance from the centre in a UMIS equipment from Fischer-Cripps Laboratories configured in the load control mode (max load of 300 mN) with a Berkovich-type diamond tip.

2.9 Sessile drop technique

Wettability of the samples was analysed using contact angle measurements performed with the sessile drop technique (Krüss drop size DSA30 analyser). 1 µL of deionised water was deposited at a rate of 30 µL/min on the surface and the angle was immediately captured and measured to prevent distortions due to evaporation.

2.10 Antimicrobial tests

The antimicrobial properties of the prepared samples was estimated through the reduction in recovered colony forming units (CFU/mL) over time, Figure 27, using *E. coli K12* (Gram-negative) and *S. aureus NCTC 6571* (Gram-positive). All bacteria were grown in an orbital incubator (37 °C, 200 rpm), in 25 mL of LB (Luria Bertani) broth for 16 h. To reduce bacteria aggregation, the inoculum was diluted in sterile LB broth to an optical density (OD_{600}) of 0.01 and incubated until the culture yield reached OD_{600} ~ 0.3. Samples and stainless steel controls were degreased and disinfected by immersion and sonication in pure ethanol for 5 min. After drying, samples were placed inside a sterile petri dish containing a cloth wetted with 1 mL of LB broth to prevent the inoculum's evaporation (Figure 28). For the "dry" tests, no wetted cloth was added, while inoculated samples were placed 100 mm away from a Bunsen burner with the lid partially open until all liquid evaporated (around 8-9 min). In both "wet" and "dry" tests, all petri dishes were kept on a bench at room temperature.

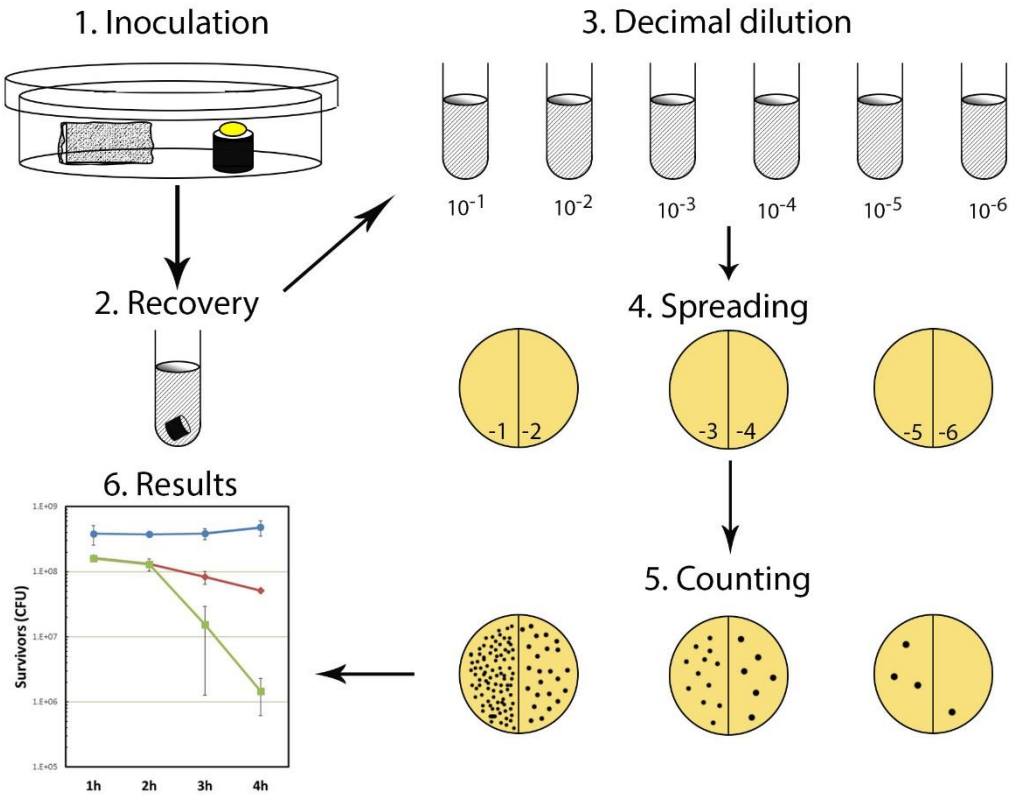

Figure 27 Schematic diagram showing the antimicrobial tests.

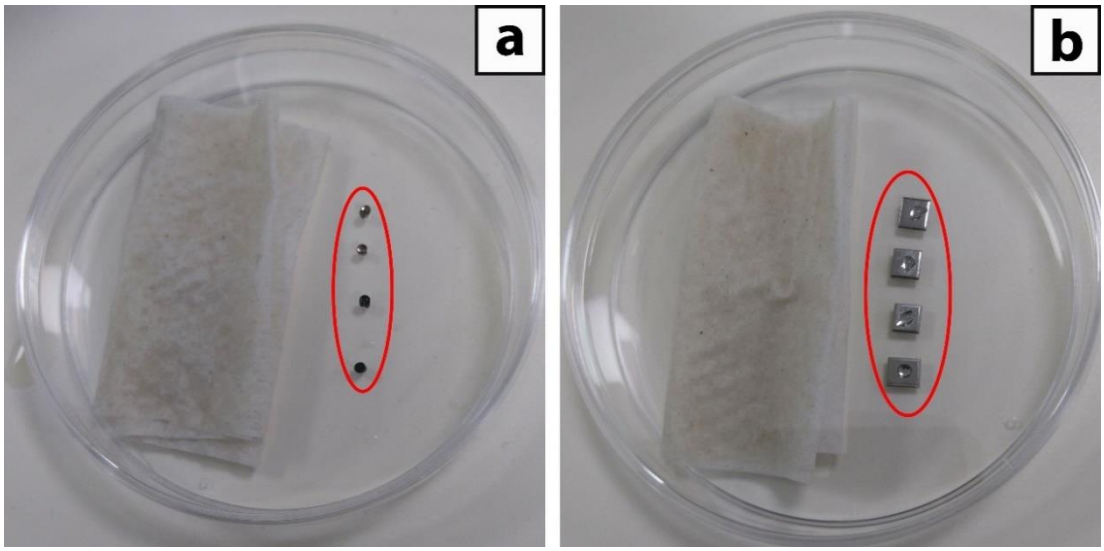

Figure 28 Example of inoculated and sealed samples: (a) BMGs and (b) stainless steel.

Once the desired contact time was achieved, bacteria was recovered by introducing each sample into an sterile Eppendorf tube with 198 µL of an aqueous solution of Tween 20 0.148 g/L (2 × CMC) and sonicated for 5 min. The suspension was subjected to serial decimal dilution, spread onto LB agar plates and resulting colonies were counted after 16 h of incubation at 37 °C. All tests were performed five times, with mean counts and standard deviation reported (Figure 29).

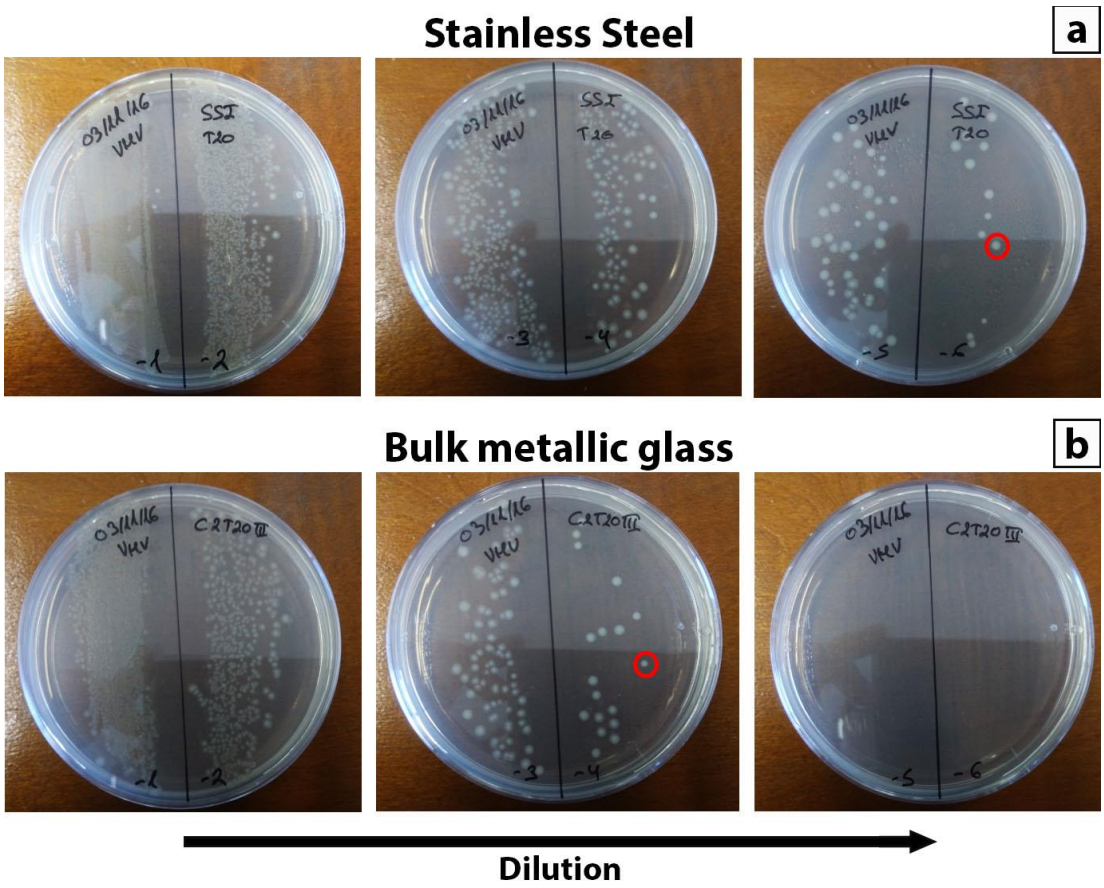

Figure 29 Example of LB agar plates of *E. coli* serial dilutions after 1 h of contact in (a) stainless steel and (b) Cu-based BMGC. Note that each colony (see red circles) corresponds to a single *E. coli* cell, which survived the antimicrobial tests.

2.11 X-ray photoelectron spectroscopy (XPS)

X-ray Photoelectron Spectroscopy (XPS) tests were done using a K-Alpha (Thermo Scientific) instrument with Al Ka radiation (1486.6 eV). Samples were analysed

measuring directly from the surface and after sputtering with Ar ions at 4 keV for 180 s. All spectral positions were charge-corrected taking C 1 s peak at 285 eV.

2.12 Inductively coupled plasma optical emission spectrometry (ICP-OES)

The measurement of Cu ions released by the developed metallic alloys was carried out by Inductively Coupled Plasma spectrometry (PerkinElmer Optima 8000 ICP-OES). After disinfection, samples were inoculated with 2 µL of pure LB broth and left inside a sterile petri dish using the same methods described in *section 2.8 Antimicrobial tests*. The analysed MGs were introduced in disinfected universal bottles containing 10mL of sterile deionized water (autoclaved dH_2O from a Mil-li-DI purification system). Samples were sonicated for 5 minutes, recovered and dilutions were processed through ICP-OES using dH_2O and two dilutions of Cu (i.e. 0.2 ppb and 0.02 ppb) prepared with a Copper atomic absorption standard solution (10,050 µg/mL of Cu in ≤ 3 wt. % HNO3 d 1.023).

2.13 Transmission Electron Microscopy (TEM)

To analyse the influence of copper ions on *E. coli* and *S. aureus* bacteria, samples inoculated with bacteria were analysed with a Philips Cm 100 Compustage (FEI) Transmission Electron Microscope (TEM) at 100kV while digital images were collected using an AMT CCD camera (Deben). Inoculum and deposition was prepared as described in *section 2.8 Antimicrobial tests*. Cells were recovered by placing the samples in an sterile Eppendorf tube with 198 µL of an aqueous solution of Tween 20 (2 x CMC) and sonicated for 5 min. A pellet was formed by centrifuging in cycles of 5 min at 5000 x g rcf until a pellet was visible, and the supernatant was removed using a micropipette without disturbing the pellet. Bacteria were re-suspended in 2 % glutaraldehyde in sodium cacodylate buffer (4 °C) for 1 h. From now onwards, between each step all samples were centrifuged at 3000 rpm in 5 min cycles until a pellet was visible in the bottom of the Eppendorf. Pellets were rinsed in cacodylate buffer twice for 10 min each, followed by a secondary fixation in 1 % osmium tetroxide for 30 min. After fixing, samples were washed in deionised water twice for 10 min and exposed to serial dehydration through acetone diluted in dH_2O

(25 %, 50 %, 75 % for 15 min each) and twice in pure acetone for 20 min each. Then, TAAB epoxy resin in acetone (25 %, 50 %, 75 % resin) and 100 % resin for a minimum of 3 changes over 24 h were used to impregnate the samples. To fix the processed pellet, 100 % fresh resin was introduced in the Eppendorfs re-suspended and polymerised at 60 °C for 24 h. 0.5 µm sections were cut and stained with 1 % toluidine blue in 1 % borax and ultrathin sections (~ 70 nm) were obtained through a diamond knife on a RMC MT-XL ultramicrotome. Finally, ultrathin sections were stretched with chloroform and mounted on Pioloform-filmed copper grids.

3 Influence of composition, cooling rate and annealing on the wear performance and antimicrobial behaviour of a Cu-Zr-Al metallic glass composite

The purpose of this chapter is to analyse the influence of composition and cooling rate on the wear and antimicrobial properties of BMGCs corresponding to the Cu-Zr-Al system. As discussed in *sections 1.2.6 Cu-Zr-Al system and Cu-based BMG and 1.2.4 Antimicrobial mechanisms of Touch surfaces*, the microstructure for the Cu-Zr-Al system is very sensitive to changes in composition. In addition, their high Cu-content makes this alloy system suitable for antimicrobial applications. At the same time, Inoue et al. [357] analysis of the $Cu_{95-x}Zr_xAl_5$ alloys (x ≡ 35-50 at. %) had reported a maximum critical diameter of 3 mm and observed that it is highly dependent on the composition. Working with compositions close to the critical diameter (D_c) (i.e., fully amorphous for smaller diameters and partly crystalline for larger diameters) results in large differences in mechanical behaviour with small changes in composition. This enables to easily optimize the performance of this alloy system. For this reason, the effect of composition (*section 3.1*) and cooling rate (*section 3.2*) on the performance of various Cu-Zr-Al alloys will be studied in this chapter. This analysis will reveal which parameters are fundamental in the wear and antimicrobial behaviour of MGCs, enabling the optimization of such alloys for their use as antimicrobial surfaces.

3.1 Effect of composition in the wear and antimicrobial performance of a Cu-based BMG composite

3.1.1 Effect of the composition on the microstructure

To understand the effect of the composition on the microstructure of the Cu-Zr-Al system, three alloy compositions, $Cu_{50}Zr_{44}Al_6$, $Cu_{53}Zr_{41.4}Al_{5.6}$ and $Cu_{56}Zr_{38.7}Al_{5.3}$, close to one of the eutectic reactions of the Cu-Zr system, were prepared and studied. The XRD scans of rods 2 mm in diameter for the $Cu_{50+x}(Zr_{44}Al_6)_{50-x}$ system (x = 0, x = 3 and x = 6 at. %) can be seen in Figure 30. For the $Cu_{50}Zr_{44}Al_6$ sample (Figure 30a), the XRD scan reveals a broad halo, indicating the presence of an amorphous phase.

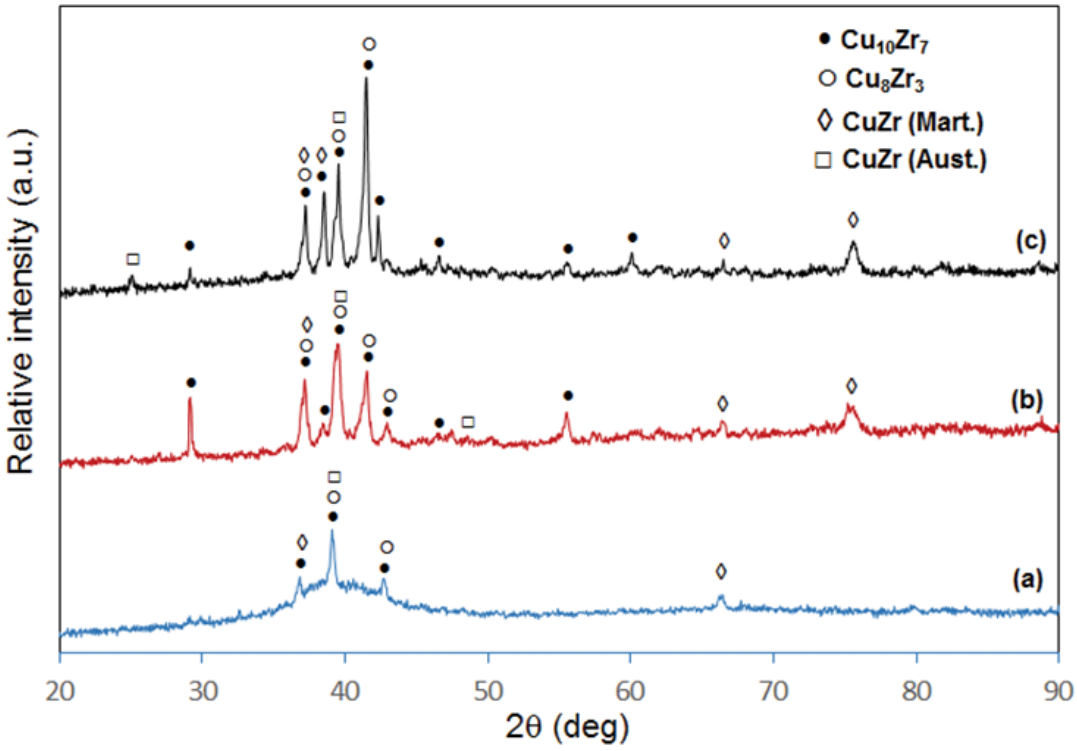

Figure 30 XRD scans for samples (a) $Cu_{50}Zr_{44}Al_6$ (b) $Cu_{53}Zr_{41.4}Al_{5.6}$ and (c) $Cu_{56}Zr_{38.7}Al_{5.3}$ alloys [179].

At the same time, several peaks indicating the presence of a crystalline phase can be discerned at 35-45° and 68°. These peaks can be associated to orthorhombic $Cu_{10}Zr_7$ (a = 0.9347 nm, b = 0.9347 nm, c = 1.2675 nm), orthorhombic Cu_8Zr_3 (a=0.78686nm, b=0.81467nm, c=0.9977nm), cubic austenite B2 CuZr (a = 0.3256 nm, b = 0.3256 nm, c = 0.3256 nm) and monoclinic martensite B19´ CuZr (a = 0.3237 nm, b = 0.4138 nm, c = 0.5449 nm). It can be deduced that an increase of 3 % at. copper, $Cu_{53}Zr_{41.4}Al_{5.6}$ (Figure 30b) led to the increase in number and size of the crystalline phases, while the broad halo diminished. No new phases could be discerned for this sample, but peaks attributed to $Cu_{10}Zr_7$ and Cu_8Zr_3 increase in intensity while some new peaks associated with austenite B2 and martensite B19′ are detected. Further increase in copper, for $Cu_{56}Zr_{38.7}Al_{5.3}$ (Figure 30c), shows a similar trend. The broad halo typical of amorphous materials is practically undetectable, while the peaks corresponding to $Cu_{10}Zr_7$ and Cu_8Zr_3 increase in intensity, with minor changes in the austenite B2 and martensite B19′ peaks. Their narrower peaks coupled with their higher intensity suggest a growth in crystalline size. These results show that for this

system, the increase in copper content leads to a reduction in GFA. The crystalline phases obtained here are consistent with the available literature [201,285,359].

The formation of the intermetallic phases can be deduced from the heat of mixing (also called enthalpy of formation) and their concentration in the alloy. For the Cu-Zr-Al alloy system, Cu and Zr atoms tend to easily form stable intermetallic phases [360] as can be deduced from the high heat of mixing (ΔH_{mix}) of the Cu-Zr pair, −23 kJ/mol, [361]. Although the heat of mixing of Zr-Al is even larger, −44 kJ/mol [360], than that of Cu-Zr, no XRD peaks could be associated with any of the Zr-Al crystalline phases, which can be explained by the low concentration in Al of the alloy. Also, it must be taken into account that no Al-Zr phase can be observed in the Cu-Zr-Al phase diagram for alloys with relatively low aluminium content [349,354] (*section 1.2.6*), suggesting a preference in forming Cu-Zr phases, while Al may end as solid solution into the formed crystalline phases.

To better understand the microstructures of the three alloys, they were observed under a scanning electron microscope (SEM) in SEI mode at different magnifications (Figures 31). Images were taken at half the radius distance (0.5 mm) of the 2 mm diameter rods. The SEM images confirm the same trend previously described. As the copper content increases, the size and number of crystalline phases grows appreciably. The lower copper content alloy (Figure 31a), reveals the presence of small geometrical particles, up to 5 μm, embedded in a featureless amorphous matrix. A slight increase in copper for the $Cu_{53}Zr_{41.4}Al_{5.6}$ alloy (Figure 31b) causes the development of more complex dendritic structures with long arms up to 10 μm in length, while small round particles up to 1 μm are homogeneously distributed in the matrix. The large dendrites seem to be surrounded by a clearer phase different from the amorphous matrix, which suggests a growth pattern similar to previous reports [362]. The last alloy (Figure 31c) reveals an analogous, but more crystalline microstructure to the previously discussed one, since the presence of an amorphous matrix seems almost non-existent.

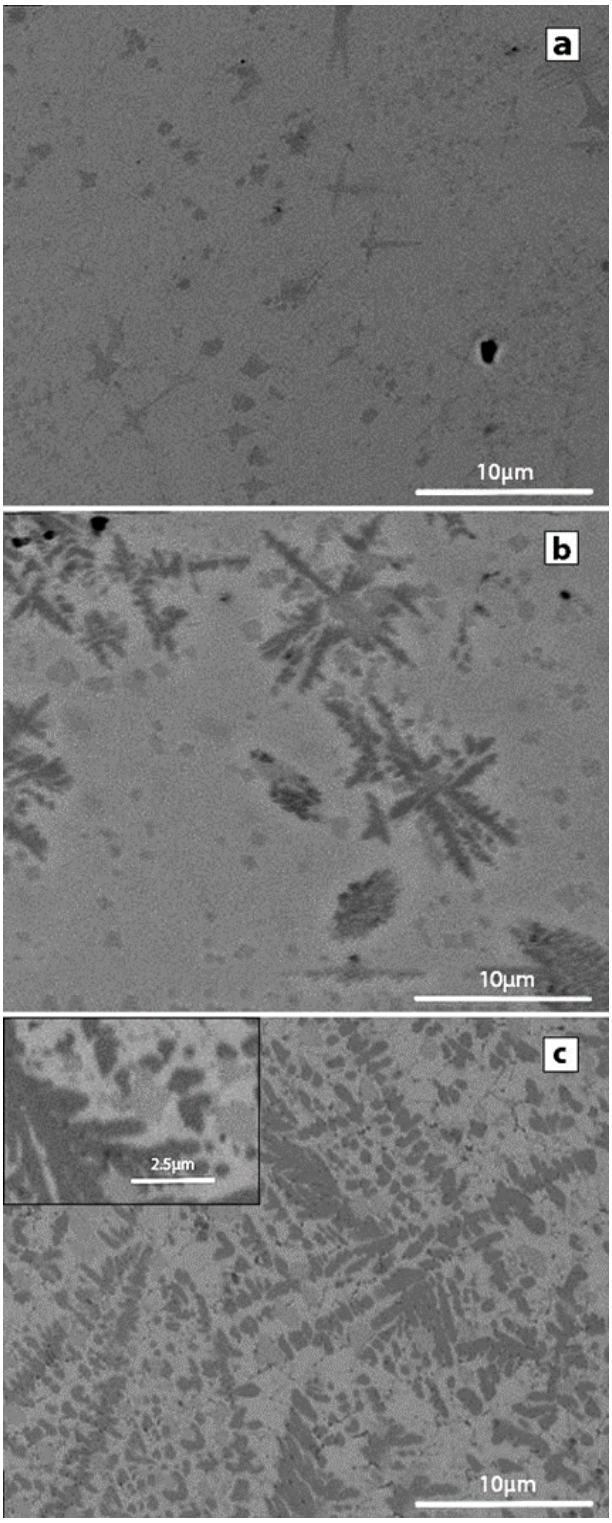

Figure 31 Backscattered SEM images taken from the middle radius for (a) $Cu_{50}Zr_{44}Al_6$, (b) $Cu_{53}Zr_{41.4}Al_{5.6}$ and (c) $Cu_{56}Zr_{38.7}Al_{5.3}$ alloys [179].

To gain a deeper understanding of the differences in composition, backscattered SEM images (Figure 32) from the middle radius have also been taken. In addition, compositional measurements of the labelled phases in Figure 32 were obtained by EDX (Table 9). It should be mentioned that the tonality of backscattered images is correlated with differences in atomic weight, i.e., brighter regions indicate the presence of higher atomic weight elements. As the atomic weight of the elements present in these alloys are: Cu: 63.546 g/mol, Zr: 91.224 g/mol and Al: 26.9815 g/mol [363], the order from brightest to darkest phases would be: CuZr, $Cu_{10}Zr_7$ and Cu_8Zr_3.

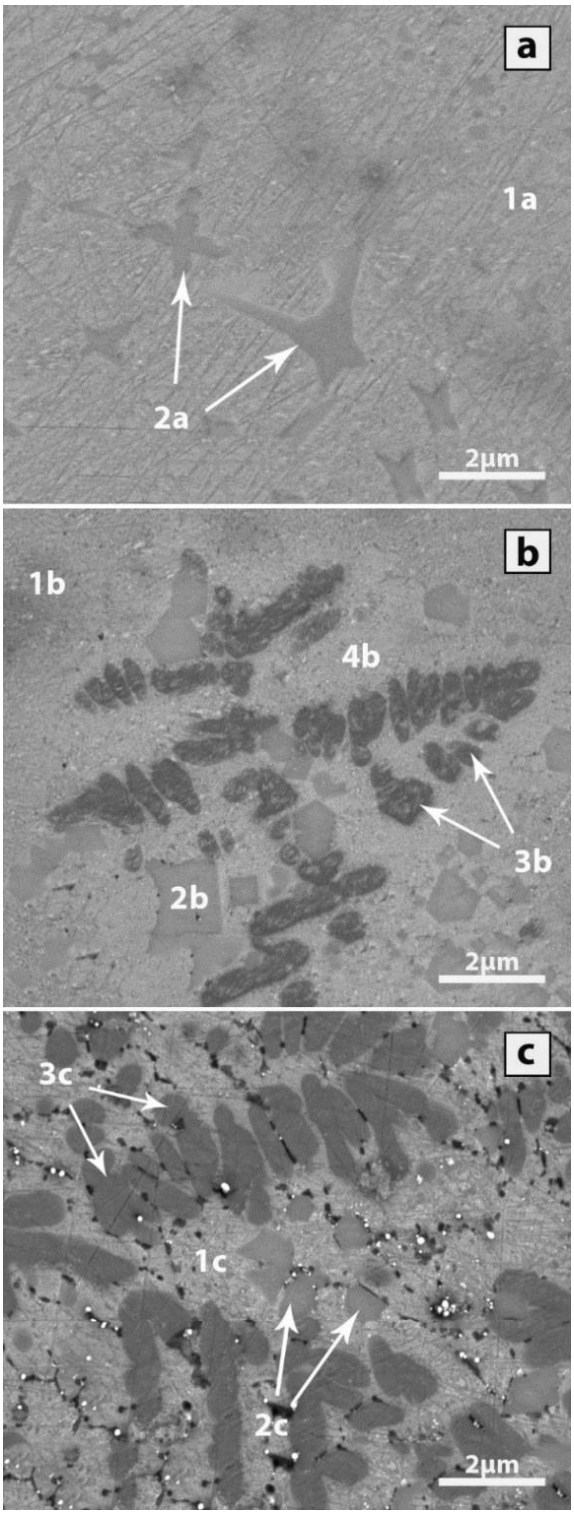

Figure 32 Magnified backscattered SEM images taken from the middle radius for (a) $Cu_{50}Zr_{44}Al_6$, (b) $Cu_{53}Zr_{41.4}Al_{5.6}$ and (c) $Cu_{56}Zr_{38.7}Al_{5.3}$ alloys [179].

Table 9 Composition in at. % of the areas labelled on Figure 32 and phases to which they can be attributed.

	1a matrix	1b matrix	1c halo	2a large dendrites	2b geometric particles	2c geometric particles	3b dendrites	3c dendrites	4b halo
Cu	54.3 ± 0.3	55.0 ± 0.6	55.3 ± 0.7	50.2 ± 0.8	42.5 ± 3.0	39.6 ± 1.8	58.7 ± 3.0	61.2 ± 1.2	53.5 ± 1.0
Zr	40.0 ± 0.3	39.3 ± 1.2	42.3 ± 0.7	35.4 ± 1.3	46.2 ± 2.8	48.1 ± 1.3	32.5 ± 3.3	28.3 ± 1.1	42.7 ± 0.8
Al	5.6 ± 0.3	5.7 ± 0.7	2.4 ± 0.4	14.5 ± 0.5	11.3 ± 1.3	12.3 ± 0.6	8.8 ± 0.5	10.5 ± 0.2	3.9 ± 0.7
Phase	Nominal composition	Nominal composition	$Cu_{10}Zr_7$	$Cu_{10}Zr_7$	CuZr	CuZr	Cu_8Zr_3 + $Cu_{10}Zr_7$	Cu_8Zr_3	$Cu_{10}Zr_7$

The composition of the small dendrites and particles present in the $Cu_{50}Zr_{44}Al_6$ alloy (Figure 32a), noted as phase 2a in Table 9, is $Cu_{50.2}Zr_{35.4}Al_{14.5}$ at. %, richer in Cu and Al, while poorer in Zr when compared to the nominal composition. The copper to zirconium ratio of this phase is around 1.4, suggesting that it can be attributed to $Cu_{10}Zr_7$, which is consistent with the XRD analysis, as most of the peaks could be correlated with this crystalline phase. On the other hand, the CuZr peaks seen in Figure 30a may be attributed to the presence of smaller phases between the larger dendrites, however, EDX measurements were not reliable due to the small phase size. Measurements of the amorphous matrix, phase 1a, revealed a composition of $Cu_{54.3}Zr_{40}Al_{5.6}$ at. %, which is closer to the nominal composition.

The number of crystalline phases and their size increases drastically for the $Cu_{53}Zr_{41.4}Al_{5.6}$ sample (Figure 32b). The darkest particles, phase 3b, exhibit a complex structure composed of two different phases. EDX measurements revealed a composition of $Cu_{58.7}Zr_{32.5}Al_{8.8}$ (Cu/Zr=1.79) that cannot be associated with any crystalline phase of the Cu-Zr-Al system [349,354]. The Cu/Zr ratio of this phase is between that of Cu_8Zr_3 (2.66) and $Cu_{10}Zr_7$ (1.43), while at the same time, the backscattered images show two different tonalities. Thus, this crystalline phase would correspond to the mixture of Cu_8Zr_3 and $Cu_{10}Zr_7$ detected in the XRD scans. Next to these dendrites, smaller geometric particles, phase 2b, can be seen ($Cu_{42.5}Zr_{46.2}Al_{11.3}$). The Cu/Zr ratio of these phases suggests that they correspond to CuZr, also detected in the XRD scan. Surrounding the dendrites and particles, a decolouration of the matrix is clearly noticeable. EDX analysis of this material, phase 4b, showed a composition of $Cu_{53.5}Zr_{42.7}Al_{3.9}$, which is poorer in Al than the nominal composition. This indicates that the growth of the intermetallics Cu_8Zr_3 and $Cu_{10}Zr_7$ likely took place by the absorption of Al from the amorphous matrix, phase 1b ($Cu_{55}Zr_{39.4}Al_{5.7}$).

The last alloy, $Cu_{56}Zr_{38.7}Al_{5.3}$, (Figure 32c) shows the presence of similar dark dendrites, phase 3c, as discussed in the previous paragraph. The composition of these dendrites is $Cu_{61.2}Zr_{28.3}Al_{10.5}$, richer in copper than the last sample. As the Cu/Zr ratio of these phases is about 2.16, the volume fraction of Cu_8Zr_3 seems much higher. For the geometrical particles, phase 2c, their similar content in copper and zirconium suggests that they correspond to the CuZr phase, which is similar to the previous

alloy. All these phases are embedded in a matrix, phase 1c, with composition $Cu_{55.3}Zr_{42.3}Al_{2.4}$ similar to the halo revealed in the $Cu_{53}Zr_{41.4}Al_{5.6}$ alloy and attributed to $Cu_{10}Zr_7$. All these phases have been previously reported by Yokoyama et al. [364] in alloys of the CuZrAl system. Finally, small white and dark spots can be observed near the grain boundaries of the described crystalline phases. Microanalysis of these phases did not reveal a composition different to that of the matrix, probably because of the lack of reliability of the measurement due to the small size of the particles.

3.1.2 Scratch tests

As mentioned in *section 1.2.5*, pin-on-disc wear tests can induce changes in the microstructure due to the local increase in temperature, especially in rapidly solidified alloys. For this reason, the wear performance of the casted Cu-based BMGCs was analysed using scratch tests at the middle radius. The contact temperature between the diamond tip and the samples was not measured, however, considering the low load (30 N) and low sliding speed (10 mm/min), no crystallization should be expected [303,365]. This is especially applicable for Cu-Zr-Al alloys as their glass transition temperature is relatively high (above 400 °C) [357].

The wear behaviour of these BMGCs was estimated from the analysis of the scratch morphology for low and high magnifications (Figure 33). The pile-up, groove deepness, at the centre and the maximum depth, the scratch width, the average roughness (R_a) and total roughness (R_z) were measured, as well as, the scratch hardness calculated as indicated in *section 1.2.5* (Table 10). When comparing the three scratches, a clear evolution in crack formation and propagation can be noticed. For the $Cu_{50}Zr_{44}Al_6$ alloy (Figure 33a), these cracks are located near the pile-up region and separated about 25 to 50 µm from each other. The cracks formed in this sample are confined to the pile up region and seem to be unable to propagate further on, thus leading to relatively short cracks (about 50 µm). The increase in copper for the $Cu_{53}Zr_{41.4}Al_{5.6}$ alloy (Figure 33b) seems to have resulted in an increase in crack density as well as a significant increase in length (up to 150 µm). As a result, the confinement of cracks to the pile up region displayed by the previous alloy is absent in the higher copper content alloys. This trend is especially noticeable in the richest copper content alloy ($Cu_{56}Zr_{38.7}Al_{5.3}$), where cracks extend well beyond 200 µm,

propagating not only outwards from the track, but also into the scratch track (red square in Figure 33c). The increase in crack formation suggests an embrittlement of the MGCs as the copper content increases, which is consistent with the larger volume content of brittle intermetallic phases [366]. This embrittlement also agrees with the nanoindentation results (Table 11) since the hardness and Young modulus of the alloy rises as the copper content increases.

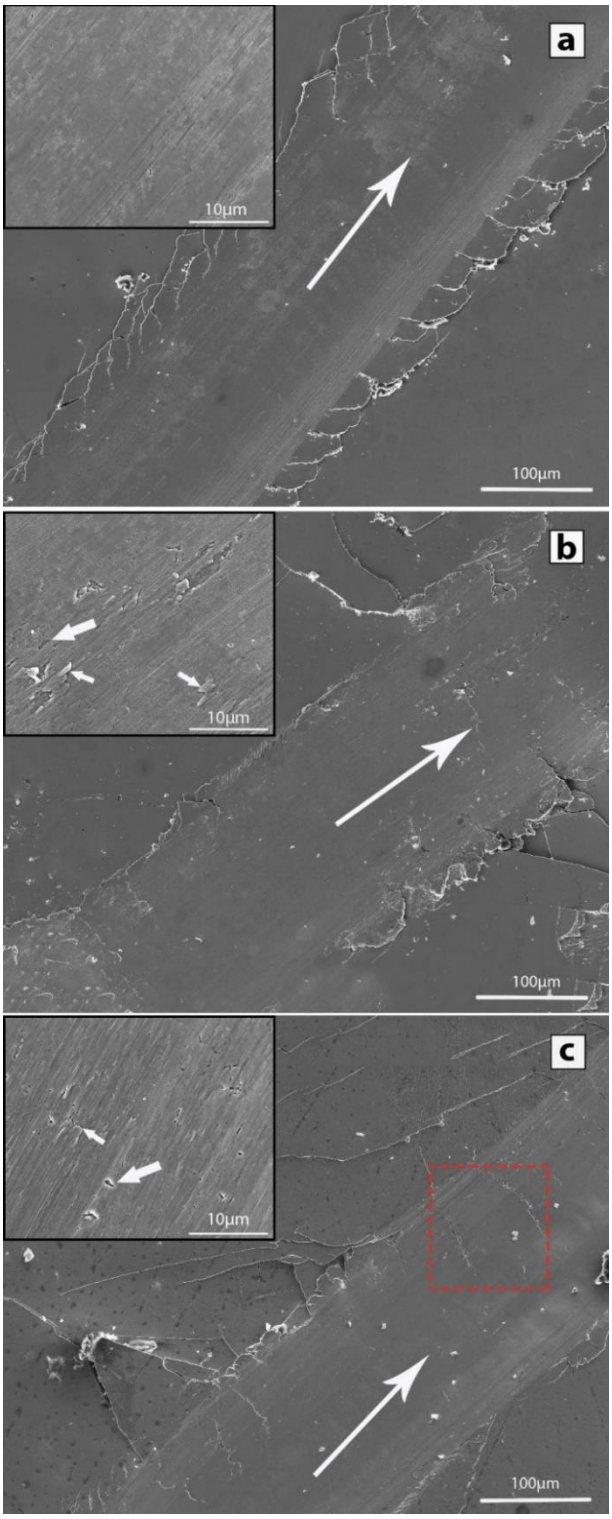

Figure 33 Images showing the scratches at the middle radius of the samples (a) $Cu_{50}Zr_{44}Al_6$ (b) $Cu_{53}Zr_{41.4}Al_{5.6}$ and (c) $Cu_{56}Zr_{38.7}Al_{5.3}$ alloys [179].

Table 10 Summary of the pile-up height, groove deep at the centre and maximum, groove area over the pile-up area, track width, scratch hardness number, arithmetic average of the roughness profile and average distance between the highest peak and lowest valley for $Cu_{50+x}(Zr_{44}Al_6)_{50-x}$ (x = 0, x = 3 and x = 6).

Sample	Pile-up (μm)	Centre (μm)	Maximum (μm)	Groove Area/ Pile-up Area	Scratch Width (μm)	Scratch Hardness Number (GPa)	Ra (nm)	Rz (nm)
$Cu_{50}Zr_{44}Al_6$	4.13 ± 1.98	14.08 ± 1.20	22.20 ± 3.95	6.35 ± 0.84	143.14 ± 2.46	3.73 ± 0.13	1198.84 ± 524.77	2425.24 ± 1069.08
$Cu_{53}Zr_{41.4}Al_{5.6}$	2.65 ± 1.71	20.10 ± 7.08	31.13 ± 4.60	15.27 ± 3.76	160.3 ± 2.26	2.97 ± 0.08	1278.00 ± 258.21	3522.92 ± 627.84
$Cu_{56}Zr_{38.7}Al_{5.3}$	2.10 ± 0.84	20.00 ± 2.02	31.42 ± 5.56	51.36 ± 7.34	178.48 ± 8.57	2.41 ± 0.23	1400.94 ± 239.15	3449.36 ± 1187.06

Table 11 Summary of the mechanical properties of the $Cu_{50}Zr_{44}Al_6$, $Cu_{53}Zr_{41.4}Al_{5.6}$ and $Cu_{56}Zr_{38.7}Al_{5.3}$ alloys after nanoindentation using a maximum load of 300 mN. The values of hardness (H), reduced Young´s modulus (E_r, H/E_r, H^3/E_r^2) ratios and maximum indentation depth (h_{max}) are given in the table.

Property	$Cu_{50}Zr_{44}Al_6$	$Cu_{53}Zr_{41.4}Al_{5.6}$	$Cu_{56}Zr_{38.7}Al_{5.3}$
H (GPa)	8.46 ± 0.45	9.37 ± 0.28	10.15 ± 1.87
E_r (GPa)	107.96 ± 3.57	121.19 ± 1.87	123.36 ± 6.89
H/E_r	0.078 ± 0.007	0.077 ± 0.003	0.082 ± 0.020
H^3/E_r^2 (GPa)	0.052 ± 0.006	0.056 ± 0.007	0.069 ± 0.046
h_{max} (μm)	1.485 ± 0.035	1.403 ± 0.017	1.372 ± 0.081

Another interesting morphological change takes place in the pile-up height and groove depth. Figure 33a shows a homogeneous and cracked pile-up in the form of individual isles up to 40 μm in length with a height of 4.13 ± 1.98 μm. The track width is relatively small (143.14 ± 2.46 μm) and a centre depth of 14.08 ± 1.20 μm (maximum of 22.20 ± 3.95 μm). The increase in copper content led to the disappearance of the pile up for the $Cu_{53}Zr_{41.4}Al_{5.6}$ (Figure 33b) and $Cu_{56}Zr_{38.7}Al_{5.3}$ (Figure 33c) alloys. Pile-up measurements reveal a steady reduction of this feature as the copper percentages changes from 53 % (2.65 ± 1.71 μm) to 56 % (2.10 ± 0.84 μm), while the centre and maximum depth is practically the same for these two samples (20.10 ± 7.08 μm and 31.13 ± 4.60 3 μm for the $Cu_{53}Zr_{41.4}Al_{5.6}$ alloy, and 20.00 ± 2.02 μm and 31.42 ± 5.56 μm for the $Cu_{56}Zr_{38.7}Al_{5.3}$ sample respectively). This reduction in pile-up is a clear indicator that these high copper content alloys are much more brittle than the base alloy, which is consistent with the crack formation discussed in the previous paragraph. Also, it is interesting to notice that the scratch width of the $Cu_{53}Zr_{41.4}Al_{5.6}$ (160.3 ± 2.26 μm) alloy is greater than that measured for the $Cu_{50}Zr_{44}Al_{6}$. This trend continues as the copper content increases, leading to the highest track width 178.48 ± 8.57 μm for the $Cu_{56}Zr_{38.7}Al_{5.3}$ sample. The increase in track width suggests an apparent reduction of the scratch hardness as the alloys increases in crystallinity 3.73 ± 0.13 GPa, 2.97 ± 0.08 GPa and 2.41 ± 0.23 GPa, indicating that copper alloying leads to a reduction on wear performance. However, this seems contradicting as nanoindentation results (Table 11) show a slight increase in the H/E_r and H^3/E_r^2 parameters, suggesting a slight rise in wear resistance.

The differences caused by copper addition can also be analysed in terms of the ratio between the groove and the pile-up section areas. As it was mentioned in *section 1.2.5*, the movement of a diamond tip induces the ploughing of material, moving it to the sides of the scratch. The mechanical properties of the alloy dictate if all of the material from the groove will be pushed to form the pile-up (ductile material) or if the material will break into smaller particles, which will be removed by the movement of the tip (brittle material). In the case of a ductile material, the groove to pile-up ratio should be around 1, as the cohesion of the deformed material will ensure that most of the scratched material will end as pile up. On the contrary, brittle materials should display much higher values, as the material breaks into smaller particles which cannot remain attached to the main surface. The values of such ratio are 6.35 ± 0.84 for

$Cu_{50}Zr_{44}Al_6$, 15.27 ± 3.76 for $Cu_{53}Zr_{41.4}Al_{5.6}$ and 51.36 ± 7.34 for $Cu_{56}Zr_{38.7}Al_{5.3}$. These values support the same trend that has already been discussed, i.e., an increase in copper content lowers the ductility of the material.

To assess the wear mechanisms involved in the scratch test of each sample, the scratches have been observed under the microscope. The SEM images for the scratch surface of the $Cu_{50}Zr_{44}Al_6$ alloy (inset of Figure 33a) shows a smooth surface with clear signs of abrasion and smearing, suggesting ductile ploughing and plasticity [367]. The increase of copper to 53% (inset of Figure 33b) reveals the same general smooth surface, but signs of detachment (chipping indicated by small arrows) and smearing are clearly noticeable. These features and the small pits (wider arrow) can be associated to adhesive transfer between the tip and the sample. The presence of pits may be explained by a weak cohesion force between the crystalline phases and the amorphous matrix, where the crystalline particles are pulled out from the matrix by the movement of the tip. These particles end up sliding over the surface, and, as the smaller intermetallic particles are harder, cause surface roughening of the sample. The presence of detachment and pits can also be found in the $Cu_{56}Zr_{38.7}Al_{5.3}$ alloy (inset of Figure 33c); however, they are larger and more prominent, which is consistent with the increase in volume fraction of crystalline phases. The chipping and smearing development driven by compositional differences generates rougher surfaces, consistent with the increase in the measured R_a and R_z (Table 10). These features indicate the presence of both abrasive and adhesive wear similar to that observed in other BMGs [368]. The complexity of the microstructure has led to the co-existence of multiple wear mechanisms: $Cu_{50}Zr_{44}Al_6$ (ductile ploughing and plasticity detected as a smeared surface), $Cu_{53}Zr_{41.4}Al_{5.6}$ (adhesive wear with some abrasive wear and stripping) and $Cu_{56}Zr_{38.7}Al_{5.3}$ (highest adhesive wear and highest stripping along with similar abrasive wear to $Cu_{53}Zr_{41.4}Al_{5.6}$ alloy).

As the crystallinity of the material increases, the hardness of the alloy rises, as seen by the brittle mode of failure and the nanoindentation results (Table 11). However, the size of the grooves, track depth, scratch width and scratch hardness seem to decrease thus suggesting a decrease in wear resistance. A priori, it should be expected that the mechanically harder alloys would display higher wear resistance, which is not consistent with these observations. The mode of deformation

corresponding to scratch testing is more complex than the stress field imposed upon the material when tested using indentation. As such, scratch tests are more sensitive to the size of precipitates and hardness of the matrix, as a softer matrix will allow the dragging of precipitates, which cannot take place in indentation tests. The volume fraction of precipitates for $Cu_{56}Zr_{38.7}Al_{5.3}$ is very large with abundant dendritic and round particles, which tend to detach more easily than heavily branched dendrites, resulting in the formation of large grooves. At the same time, the detachment and dragging of hard particles can accumulate on the sides and under the tip, creating a two body or three body mode of wear [313], leading to an increase in groove depth and scratch width. These pulled-out particles will be responsible for the apparent decrease of wear resistance ,which seems to contradict the increase in hardness expected from the nanoindentation results (Tables 10 and 11).

The change in mechanical properties can also be analysed from the point of view of volume fraction of crystalline phases through the analysis of the XRD scans (Figure 30). The ratio between the area underneath the crystalline peaks and the as obtained scan can be used to estimate the volume fraction for the different alloys: $Cu_{50}Zr_{44}Al_6$ (~ 21.0 %), $Cu_{53}Zr_{41.4}Al_{5.6}$ (~ 45.1 %) and $Cu_{56}Zr_{38.7}Al_{5.3}$ (~ 59.1 %). Fu et al. [286] and Pauly et al. [285] reported that the percolation threshold (i.e. the crystalline to amorphous ratio for which connectivity of the crystalline phases occurs) for similar MGCs is in the range of 30 % to 50 %, which is close to that of the $Cu_{53}Zr_{41.4}Al_{5.6}$ alloy, explaining the large difference in mechanical properties between the low and high Cu content alloys (Figure 33). It is known that once the percolation threshold is reached, the alloy loses its ductility, abruptly changing its mechanical properties [369]. When the critical crystallinity is reached, the viscosity and elastic modulus of the alloys increases suddenly, while the fracture stress, yield strength and ultimate strength are reduced [369,370]. This effect can be seen in the nanoindentation tests (Table 11) where the Young modulus increases from 108 GPa in the Cu 50 % alloy to 121 GPa for the Cu 53 % sample, while the Cu 56 % only reveals a slight increase (123 GPa). As the volume fraction reaches the percolation threshold, the alloy undergoes embrittlement as deduced from the formation of cracks and lower pile-up, thus suggesting that these intermetallic phases are inherently brittle [286].

3.1.3 Antimicrobial and wettability tests

Before analysing the antimicrobial properties of the selected alloys, it is interesting to estimate the adhesion of bacteria to these surfaces. For antimicrobial materials, it is more beneficial to increase the adhesion of pathogens, effectively increasing their exposure to copper ions diffusing from the surface (*section 1.1.2*). Ista et al. [371] have shown that there is a correlation between wettability and bacterial adhesion. For this reason, the wettability of the three compositions was estimated through the contact angle of sessile water droplets. Figure 34 shows the contact angle of deionised water on the three alloys $Cu_{50+x}(Zr_{44}Al_6)_{50-x}$: 101.8 ± 0.7° for x=0, (Figure 34a), 99.8 ± 1.9° for x=3, (Figure 34b) and 90.2 ± 1.6° for x=6 (Figure 34c). The most amorphous alloy ($Cu_{50}Zr_{44}Al_6$) displays a contact angle similar to those detected by Chu et al. [190] in fully amorphous $Cu_{48}Zr_{42}Ti_4Al_6$ thin films (106.6°), which agree with the results available in the literature. From the contact angle measurements, it can be inferred that an increase in copper causes a decrease in contact angle. As the contact angle decreases, the alloy becomes more hydrophilic, thus, favouring the adhesion of bacteria. This change may not be completely attributed to changes in composition, as previous studies of MG thin films show similar values of CA for larger differences in composition [190]. As such, the increase in bacterial adhesion are most likely driven by the differences in microstructure. However, the increase in copper content has an effect on the size and nature of the crystalline phases appearing in the sample, making it difficult to discern if size of the crystals or composition of the phases, or both, account for these changes.

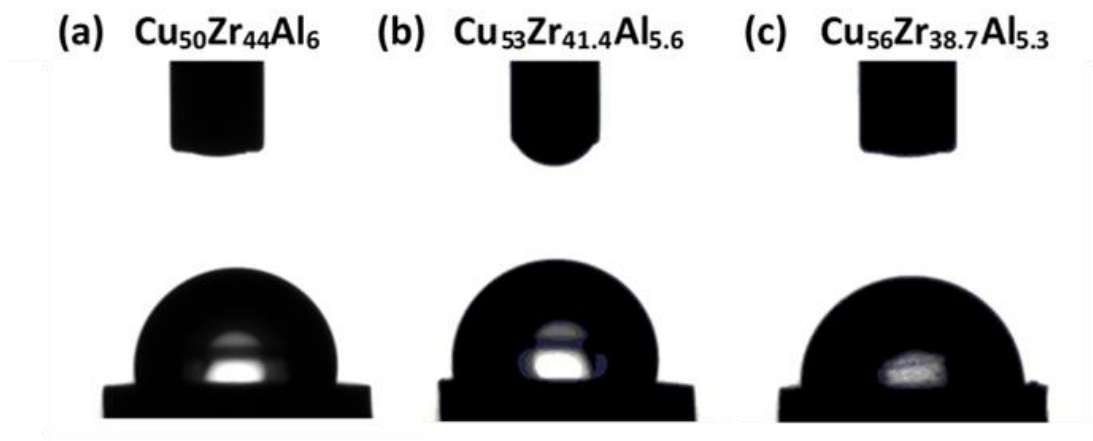

Figure 34 Average water contact angle on Cu-Zr-Al alloys (a, b and c) [179].

To assess the antimicrobial activity of the samples, the reduction of viable cells or Colony Forming Units (CFUs) over time was used for two different bacteria, *E. coli* (gram negative, GN) and *B. subtilis* (gram positive, GP). The first experiment involved a rather large density of bacteria (OD_{600} = 0.3 ~ 3×10^8 CFU/mL) acting on the antimicrobial surfaces for 4 h (Table 12). This experiment revealed an almost null decrease in bacteria for the "low" content alloy, while the highest copper content alloy reduced the number of bacteria by one order of magnitude (from 10^8 CFU/mL to 10^7 CFU/mL).

Table 12 Antimicrobial activity of samples.

Sample	Colony forming units/ml (log_{10})	
	B. subtilis 168	*E. coli* K12
Plastic	8.4	8.5
Copper	ND*	ND*
$Cu_{50}Zr_{44}Al_6$	8.8	8.5
$Cu_{53}Zr_{41.4}Al_{5.6}$	7.9	8.2
$Cu_{56}Zr_{38.7}Al_{5.3}$	7.4	7.3

*ND = None detected.

The antimicrobial properties of the $Cu_{53}Zr_{41.4}Al_{5.6}$ and $Cu_{56}Zr_{38.7}Al_{5.3}$ samples were further analysed by reducing the initial density of the inoculum to about 1×10^6 CFU/mL (Figure 35). The time-kill graph revealed a progressive elimination of bacteria during the first three hours of contact, which increased after 4 hours, with $\log_{10}$ reductions consistent with other studies performed in other copper-based materials [372,373]. Although the two alloys were able to eliminate all cells after 4 h, these antimicrobial properties were not observed during the first experiment, suggesting that the analysed alloys display low antimicrobial activity for very high inoculum densities. In contrast, pure copper was not affected by the high density of the inoculum. At the same time, the killing-time curve (Figure 35) suggests that *E. coli* is slightly less resistant to copper surfaces than *B. subtilis*, which is consistent with the inner structure of GP and GN bacteria (*section 1.1.1*) and the ability of *B. subtilis* to produce endospores that are resistant to copper surface killing [374]. It is important to state that the decrease in inoculum density helped to reveal the antimicrobial properties of the samples. However, this reduction is not desirable, as it indicates that the materials do not display high antimicrobial properties, while, at the same time, this reduction decreases the resolution of the method and may compromise the correct estimation of the contact killing kinetics.

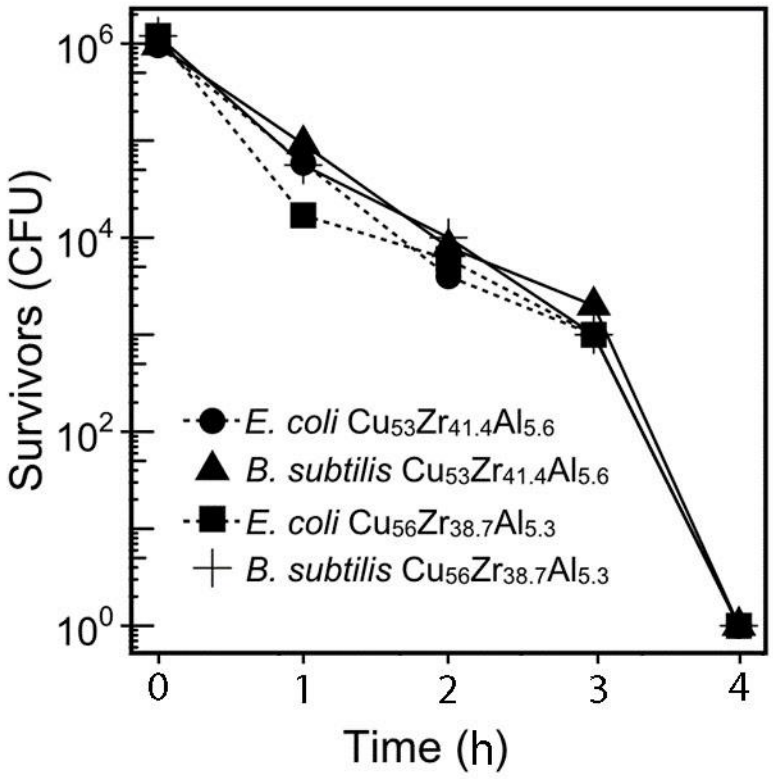

Figure 35 Time-kill curve of *E. coli K12* and *B. subtilis 168* exposed to Cu-Zr-Al alloys for up to 250 min [179].

The wettability and antimicrobial tests indicate that the increase in crystallinity and copper content led to more hydrophilic alloys. Consequently, the cell-surface contact area should increase, which can be one of the causes of the higher antimicrobial properties of $Cu_{53}Zr_{41.4}Al_{5.6}$ and $Cu_{56}Zr_{38.7}Al_{5.3}$ than that of the alloy with lowest copper content. In addition, the change in composition effectively increased the volume fraction of crystalline phases as well as the number of Cu-rich intermetallic phases. Larger crystals lead to the formation of larger volume fraction of grain boundaries between the amorphous matrix and the crystalline phases, increasing the number of paths for Cu ions to diffuse into the bacteria. This is especially noticeable for the $Cu_{56}Zr_{38.7}Al_{5.3}$ alloy, where more than 50 % of the surface area consisted of Cu-rich crystals. Nevertheless, there is no significant difference between the antimicrobial properties of $Cu_{53}Zr_{41.4}Al_{5.6}$ and $Cu_{56}Zr_{38.7}Al_{5.3}$, suggesting that the volume fraction rather than the composition of the phases may be the factor accountable for the change in antimicrobial properties.

3.2 Influence of cooling rate and annealing in a Cu-rich metallic glass composite

3.2.1 Effect of changes in diameter and cooling temperature in the microstructure

In the previous section the influence of composition in the wear and antimicrobial properties of a Cu-rich alloy was analysed, however, it was not possible to ascertain the role that volume fraction and crystalline phases per-se had on these results. Thus, a similar composition, $Cu_{52}Zr_{41}Al_7$, was subjected to changes in the cooling rate through changes in rod diameter and in the cooling system (chiller on or off) of the Mini Arc Melter system. The idea is to promote an increase in volume fraction of the crystalline phase, without changing the composition or the nature of the crystalline phases formed. The increase in rod diameter will result in a lower cooling rate, which can be further lowered by changing the water temperature in the cooling unit. This will allow to analyse the role of volume fraction of crystalline phase and compare these results with those obtained in *section 3.1* to understand the role of crystalline phases and composition in the wear and antimicrobial properties of BMGC. Before starting with the analysis of the results, it should be noted that, for convenience, samples will be referred to via a simple convention; those obtained with the chilling system on will be referred to as CH followed by the diameter of the rod (i.e. CH2 for the sample 2 mm in diameter casted with the chiller on), while samples quenched with the chiller off will be named as NCH followed by the diameter of the rod (Table 13).

Table 13 Codenames for the samples analysed in this section

Code	Diameter (mm)	Chiller
CH2	2	On
NCH2	2	Off
CH3	3	On
NCH3	3	Off

The crystallinity and phases of the $Cu_{52}Zr_{41}Al_7$ samples were analysed using XRD scans (Figure 36). The two rods cast with a 2 mm copper mould (Figures 36a and 36b) display high intensity peaks arising from orthorhombic $Cu_{10}Zr_7$ (a = 0.9347 nm, b = 0.9313 nm, c = 1.2675 nm), orthorhombic Cu_8Zr_3 (a = 0.7868 nm, b = 0.8146 nm, c = 0.9977 nm), cubic austenite B2 CuZr (a = 0.3256 nm, b = 0.3256 nm, c = 0.3256 nm) and monoclinic martensite B19´ CuZr (a = 0.3237 nm, b = 0.4138 nm, c = 0.5449 nm). As expected from a MGC, a broad halo can be seen superimposed on the high intensity peaks, revealing the presence of an amorphous matrix. A slight decrease in the amorphous halo and a new peak at around 47° can be noticed in the NCH2 rod, but both samples remain much similar in microstructure.

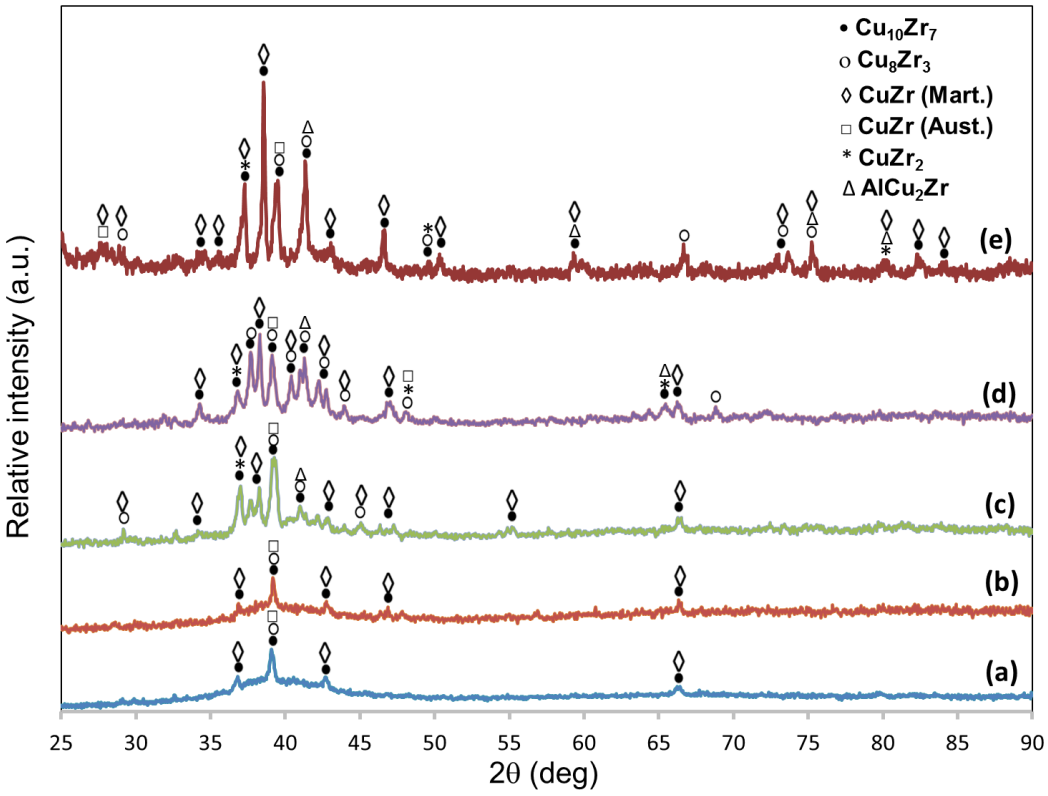

Figure 36 XRD scans for $Cu_{52}Zr_{41}Al_7$ at. % alloy (a) CH 2 mm diameter, (b) NCH 2 mm diameter, (c) CH 3 mm diameter, (d) NCH 3 mm diameter and (e) 3 mm annealed at 850 °C for 48 h [13].

The crystalline phases of the 3 mm rods (Figures 36c and 36d) are mostly similar to the ones previously discussed, but small peaks associated with tetragonal $CuZr_2$ (a = 0.3220 nm, b = 0.3220 nm, c = 1.1183 nm) were found. As expected, the decrease in cooling rate reveals a clear influence in the volume fraction. The CH3 sample reveals the presence of numerous high intensity peaks, while the amorphous halo is almost undiscernible. In contrast to the NCH2 sample, the peak at 39.3° ($Cu_{10}Zr_7$, Cu_8Zr_3 and austenite B2 CuZr) increases in magnitude followed by the peaks detected at about 38.3° and 41.2°. This trend is followed by the NCH3 alloy, where the number of peaks increased drastically, and the broad halo seen in all other samples is not exhibited. To complement these measurements, a NCH3 sample was annealed at 850 °C for 48 h (Figure 36e). The XRD scan reveals a complete crystalline structure without any amorphous halo. The heat treatment has developed a more complex microstructure, as suggested by the great number of high XRD peaks. While most of the crystalline phases are those previously discussed, although with higher intensities (especially for the peaks corresponding to $Cu_{10}Zr_7$, B19´ CuZr and $CuZr_2$), the annealing has led to the formation of an unexpected peak at 41.3°. This peak and others found in Figure 36e can be associated with cubic $AlCu_2Zr$ (a = 0.6190 nm, b = 0.6190 nm, c = 0.6190 nm).

Similarly to *section 3.1*, the microstructure of the metallic alloys was analysed through backscattered SEM images (Figure 37) obtained from the middle radius of the samples. The nature of the crystalline phases was evaluated from EDX measurements (Table 14), always given in at. %, of magnified backscattered images (insets of Figure 37). The CH2 sample (Figure 37a) reveals the presence of small crystalline phases embedded in an amorphous matrix. These particles are round and irregular up to 2 µm in size with no clear differences in tonality observed, suggesting that their composition is homogeneous. EDX measurements indicated that the composition of such particles was $Cu_{43.3}Zr_{44.9}Al_{11.9}$ (phase 2a), while the composition of the amorphous matrix was $Cu_{51.2}Zr_{43.1}Al_{6.8}$ (phase 1a), near the nominal composition of the alloy. The darker tonality of these crystalline phases suggests a lower atomic weight than the matrix, which coupled with a Cu/Zr ratio near 1 suggests that these particles may be correlated with CuZr, commonly found in similar Cu-based alloys [375,376].

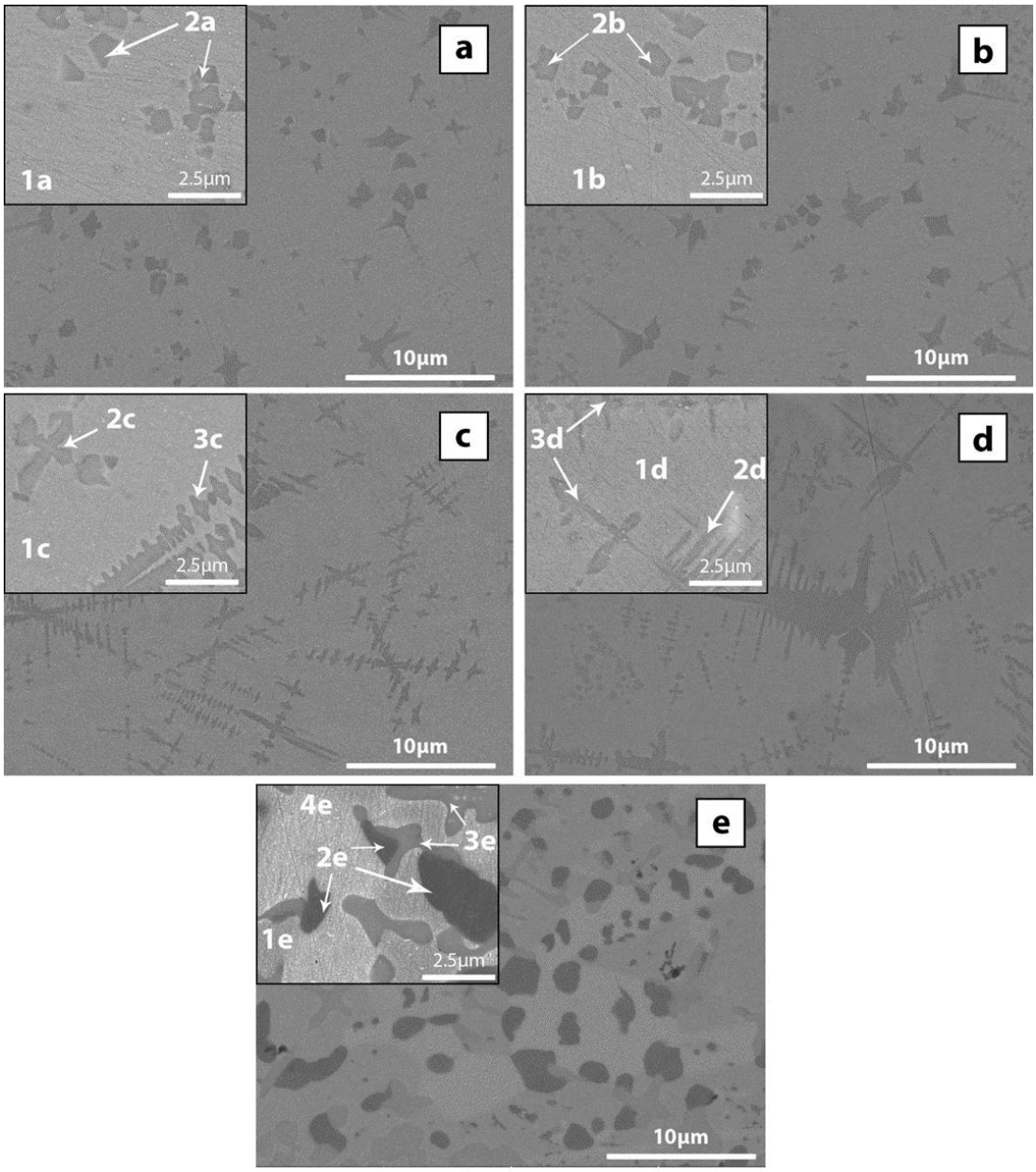

Figure 37 Backscattered SEM images taken from the middle radius for $Cu_{52}Zr_{41}Al_7$ at. % alloy (a) CH 2 mm diameter, (b) NCH 2 mm diameter, (c) CH chilled 3 mm diameter, (d) NCH 3 mm diameter and (e) 3mm crystallized sample [13].

Table 14 Composition in at. % of the areas labelled on Figure 37 and phases to which they can be attributed.

	1a matrix	1b matrix	1c matrix	1d matrix	2a Dendrites I	2b Dendrites I	2c Dendrites I	2d Dendrites I	3c Dendrites II	3d Dendrites II	1e matrix	2e Geometric particles	3e Dendrites	4e Clear matrix
Cu	51.2 ± 0.2	51.1 ± 0.4	52.1 ± 0.4	52.5 ± 0.6	43.3 ± 3.0	45.6 ± 0.8	45.6 ± 1.0	45.9 ± 1.5	37.7 ± 0.1	37.3 ± 1.3	54.9 ± 1.0	54.8 ± 1.3	36.7 ± 1.5	46.8 ± 0.7
Zr	43.2 ± 3.3	42.6 ± 0.2	42.1 ± 1.9	40.4 ± 0.5	44.9 ± 1.8	43.6 ± 1.8	43.0 ± 0.7	43.0 ± 1.2	48.3 ± 0.2	49.4 ± 1.0	43.3 ± 0.9	28.5 ± 1.7	49.6 ± 0.9	51.1 ± 0.5
Al	6.8 ± 0.2	6.3 ± 0.4	5.85 ± 1.7	7.15 ± 0.7	11.9 ± 1.4	10.7 ± 1.2	11.4 ± 0.7	11.1 ± 0.7	13.9 ± 0.2	13.46 ± 0.5	1.9 ± 0.3	16.7 ± 1.2	13.8 ± 1.6	2.2 ± 0.6
Phase	Nominal comp.	Nominal comp.	Nominal comp.	Nominal comp.	CuZr	CuZr	CuZr	CuZr	$CuZr_2$	$CuZr_2$	$Cu_{10}Zr_7$	Cu_2ZrAl	$CuZr_2$	CuZr

The NCH2 backscattered SEM image (Figure 37b) is similar to that described for the CH2 rod, however, the embedded particles are slightly larger (up to 4 μm), and while the volume fraction of CH2 is around 20.2 %, the reduction in cooling rate led to a volume fraction of around 24.2 %. The volume fraction of these samples is far from the percolation threshold [285], indicating that no great differences in mechanical behaviour can be expected between the CH2 and NCH2 samples. EDX analysis of the crystalline particles revealed a composition of $Cu_{45.6}Zr_{43.6}Al_{10.7}$ (phase 2b), suggesting the presence of CuZr, while the composition of the matrix, $Cu_{51.4}Zr_{42.5}Al_{6.3}$ (phase 1b) is close to the nominal composition ($Cu_{52}Zr_{41}Al_7$). Consequently, there is no great change in the structure of these two rods, which agrees with the XRD scans.

The change in sample rod diameter has caused a dramatic change in microstructure as deduced from the XRD scans. The CH3 sample (Figure 37c) exhibits large dendrites with long arms up to 10 μm in length and smaller particles (around 4 μm) embedded in an amorphous matrix. The volume fraction is about 41.8 % approaching the percolation threshold, emphasized by the connection between some of the dendrites. The composition of the geometric particles was $Cu_{45.6}Zr_{43.0}Al_{11.4}$ (phase 2c), revealing that these phases correspond to the CuZr intermetallics observed in the 2 mm samples. On the other hand, EDX analysis of the dendritic feature was $Cu_{37.7}Zr_{48.3}Al_{13.9}$ (phase 3c), and its Cu/Zr ratio of about 0.78 indicates that these dendrites may correspond to $CuZr_2$ [223,375,377,378]. Finally, the matrix has a similar composition, $Cu_{52.0}Zr_{42.1}Al_{5.9}$ (phase 1c), as that of the nominal composition of the master alloy.

For the NCH3 rod (Figure 37d), similar particles and dendrites can be observed, but these features have developed, with dendritic arms reaching up to 18 μm in length and particle sizes of around 6 μm. This size increase has led to a rise in volume fraction of crystalline phases to 55.2 %, indicating that connectivity between the crystalline phases is taking place. The compositional analysis of these features showed similar values to those measured in the CH3 sample, being $Cu_{45.9}Zr_{43.0}Al_{11.1}$ (phase 2d) for the dendritic phases, $Cu_{37.3}Zr_{49.4}Al_{13.5}$ (phase 3d) for the particles and $Cu_{52.5}Zr_{42.1}Al_{7.2}$ (phase 1d) for the matrix. Thus, the structure of the NCH3 rod is similar to that of the CH3, CuZr particles and $CuZr_2$ dendrites embedded in an amorphous matrix, but much more developed. This agrees with Gonzalez et al. [362] who

observed the growth of one crystalline phase from the previously formed phase during the crystallization process. Both CH3 and NCH3 samples display a slight decolouration around the large dendrites. The small size of this feature does not make it possible to obtain a reliable measurement, but in *section 3.1* a similar feature was found to be $Cu_{10}Zr_7$.

The microstructure suffers a second dramatic change when the alloy was annealed at 850 °C for 48 h (Figure 37e). Several phases can be observed: dark geometric particles up to 5 μm surrounded by grey dendrites of smaller size (up to 4 μm) and a lighter-coloured phase. From EDX analysis, the composition of the dark particles (phase 2e) is $Cu_{54.8}Zr_{28.5}Al_{16.7}$ and therefore can be attributed to the Cu_2ZrAl ternary phase. The dendrites near these dark particles had a composition of $Cu_{54.8}Zr_{28.5}Al_{16.7}$, suggesting the presence of $CuZr_2$ found in the 3 mm alloys. In regards to the clear and dark structures surrounding the dendrites and particles, it was found that the clearer feature may be correlated with CuZr ($Cu_{46.8}Zr_{51.0}Al_{2.2}$, phase 4e), while the darker structure can be considered as $Cu_{10}Zr_7$ ($Cu_{54.9}Zr_{43.3}Al_{1.9}$, phase 1e).

3.2.2 Scratch test

The wear performance of the previously described alloys was assessed performing scratch tests at approximately half the radius distance (Figure 38) of the 2 and 3 mm diameter rods. The magnified images of the centre of the scratch track are shown in insets of Figure 38. Similarly to the analysis developed in *section 3.1,* the pile-up height, groove deep at the centre and maximum, groove area over the pile-up area, track width, scratch hardness number, arithmetic average of the roughness profile and average distance between the highest peak and lowest valley of the MGCs, for the annealed sample and a pure copper rod were measured (Table 15). All results were obtained from at least ten measurements, while, similarly to *section 3.2.1*, the low sliding speed (10 mm/min) and load (30 N) should not raise the temperature high enough to induce crystallization [303].

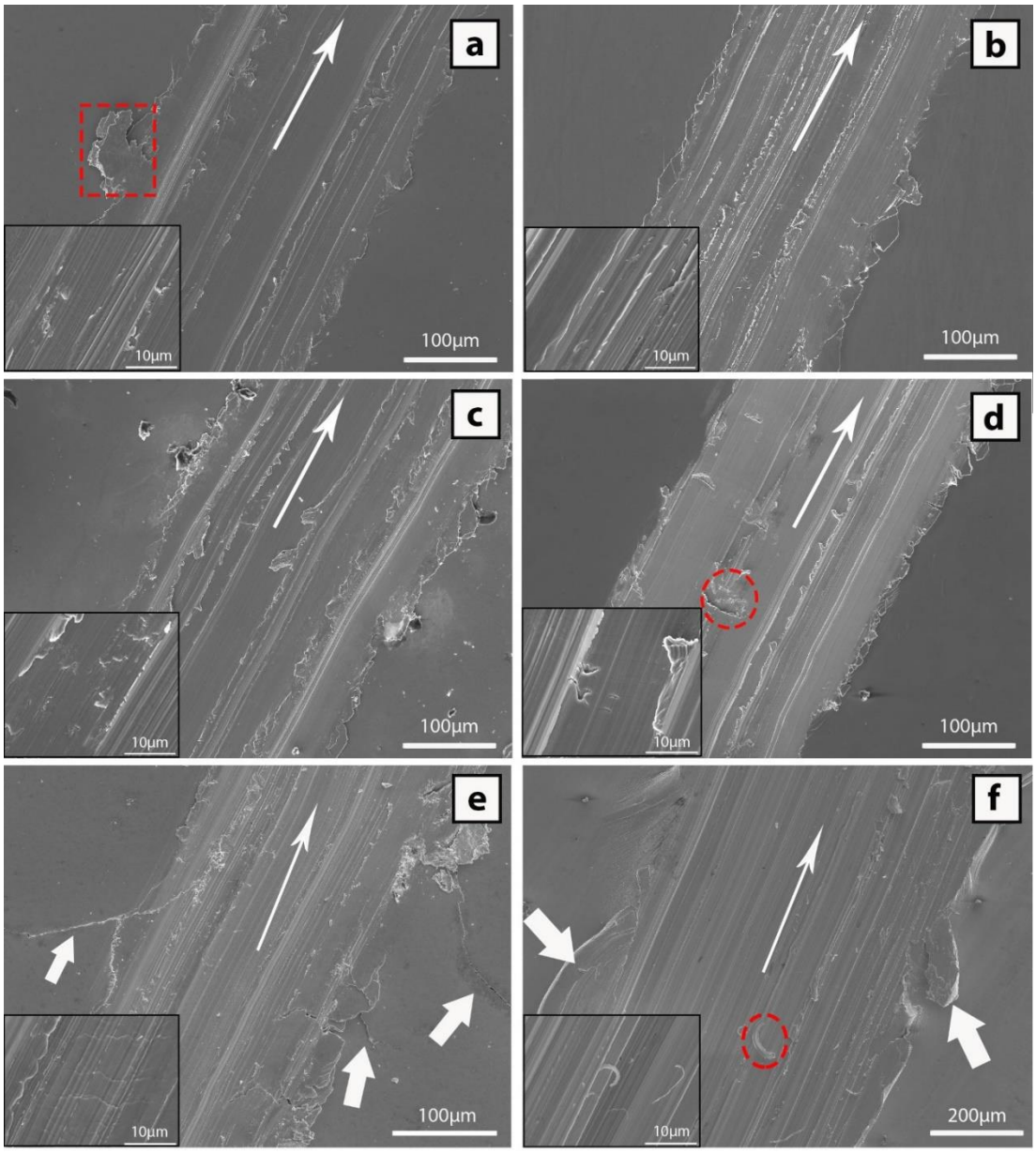

Figure 38 Images showing the scratches at the middle radius of the samples (a) CH 2 mm diameter; (b) NCH 2 mm diameter; (c) CH3 mm diameter; (d) NCH 3 mm diameter; (e) 3 mm annealed at 850 °C for 48 h and (f) pure copper [13].

Table 15 Summary of the pile-up height, groove deep at the centre and maximum, groove area over the pille-up area, track width, scratch hardness number, arithmetic average of the roughness profile and average distance between the highest peak and lowest valley for the samples: CH 2 mm diameter, NCH 2 mm diameter, CH3mm diameter NCH 3 mm diameter, 3 mm annealed at 850 °C for 48 h and pure copper.

Sample	Pile-up (µm)	Centre (µm)	Maximum (µm)	Groove Area / Pile-Up Area	Scratch width (µm)	Scratch hardness number (GPa)	Ra (nm)	Rz (nm)
CH 2mm	5.05 ± 1.92	15.70 ± 1.22	20.79 ± 1.41	10.05 ± 3.87	243.16 ± 2.36	1.29 ± 0.02	1438.44 ± 258.30	4528.70 ± 1532.68
NCH 2mm	3.71 ± 1.58	17.46 ± 0.85	21.82 ± 1.45	14.51 ± 5.87	241.25 ± 2.23	1.31 ± 0.02	1566.47 ± 179.20	4123.45 ± 681.11
CH 3mm	2.78 ± 1.09	17.48 ± 1.79	19.82 ± 2.22	17.20 ± 3.72	240.30 ± 2.98	1.32 ± 0.03	1596.15 ± 221.62	5216.74 ± 822.11
NCH 3mm	2.63 ± 1.51	21.92 ± 1.83	26.51 ± 2.42	31.83 ± 5.90	229.44 ± 5.99	1.45 ± 0.08	1974.25 ± 364.28	6540.84 ± 1355.79
850C 48h	3.86 ± 2.79	17.47 ± 1.13	20.74 ± 1.22	13.97 ± 6.75	196.08 ± 1.57	1.99 ± 0.03	1106.54 ± 101.22	3407.08 ± 624.26
Copper	40.91 ± 12.08	61.93 ± 3.97	66.34 ± 2.92	2.97 ± 0.88	426.54 ± 3.61	0.42 ± 0.01	1631.62 ± 58.67	8273.16 ± 511.49

The morphology of the scratch for the CH2 sample (Figure 38a) shows a relatively high pile-up dispersed into large volumes of material (dashed square). This material is the result of the natural movement of the material during the scratch process. As the stylus tip sinks into the material and slides, the removed and plastically deformed material is pushed to the sides of the track by plastic flow. The presence of such large volumes of material suggests that the alloy is relatively ductile, however, the pile-up suffers a great variation in height along the side of the track (5.05 ± 1.92 μm). The groove centre depth and maximum depth are relatively small, 15.70 ± 1.22 μm and 20.79 ± 1.41 μm, respectively, but the track width is the highest from all samples analysed (243.16 ± 2.36 μm) and therefore results in the lowest scratch hardness (1.29 ± 0.02 GPa) according to Equation 3. The general surface of the groove reveals long continuous lines of smeared material, typical of adhesive wear. The high shear stresses promote plastic deformation and adhesion of material to the tip, and, as the diamond tip continues its movement, this material will be reattached onto the surface, leaving continuous lines of smeared material. The magnified image of the track centre (inset of Figure 38a) is relatively smooth (1438.44 ± 258.30 nm) and shows signs of abrasion and chipping. These features suggest ductile ploughing and plasticity [367] with some signs of abrasive wear, suggesting that the $Cu_{52}Zr_{41}Al_7$ alloy is more ductile and the wear performance of the Cu-Zr-Al system is highly dependent on composition.

For the NCH2 alloy (Figure 38b), the wear track presents longer (up to 300 μm) and narrower (10 μm) lines of smeared material, however, the pile up is smaller 3.71 ± 1.58 μm, while the depth in the centre (17.46 ± 0.85 μm) and at the maximum depth (21.82 ± 1.45 μm) are larger. This is consistent with the slight increase in volume fraction of brittle crystalline phases (Figure 38b). The low cohesion between matrix and crystalline phases causes the particles to be dragged forward by the movement of the diamond tip through a mechanism of shearing and cracking [313]. Consequently, these particles act as a secondary source of wear, leading to a slight increase in roughness of the groove surface (1566.47 ± 179.20 nm) with signs of chipping. The wear track decreases slightly, leading to a small increase in scratch hardness (241.25 ± 2.23 μm and 1.31 ± 0.02 GPa, respectively). Together, these features indicate adhesive and abrasive wear, however, the adhesive wear is the main wear mechanism involved, as shown by the large number of smeared lines.

The drastic microstructural changes seen in the CH3 sample (Figure 38c) has not greatly changed the track morphology (Figure 38c). Long and continuous lines of smeared material are present, and slightly more prominent, probably due to the large size of the dendritic phases. The long arms of these crystalline phases constrain the movement of the relatively ductile matrix, holding large parts of the matrix attached to the dendrites. As the tip moves over the crystalline phases, the large contact area between these features and the tip, and the attachment of matrix and dendrites leads to an increase in plastic deformation of the matrix, explaining the increase of smeared material. Nevertheless, the changes in pile up are not drastic. While the pile up displays a slight decrease, 2.78 ± 1.09 μm, the depth of the groove at the centre and its maximum depth remain similar to those displayed by the NCH2 rod (17.48 ± 1.79 μm and 19.82 ± 2.22 μm respectively). The magnification of the groove centre (inset of Figure 38c) reveals detachment and pitting with minor chipping and cracking, similar to the features observed by observed by Zhong et. al. [368] in Zr-based BMGs. The track width and scratch hardness do not change drastically when compared to the NCH2 sample (240.30 ± 2.98 μm and 1.32 ± 0.03 GPa, respectively), probably because the alloy has yet to reach the percolation threshold. All these features reveal that adhesive wear is the most important wear mechanism, while the presence of some minor abrasive wear can be observed.

For the NCH3 BMGC (Figure 38d), long lines of smeared material can be observed, however, the most interesting feature are the large pits (~ 50 μm) present in the middle of the wear track. Although some pits were found in the previous samples, the NCH3 rod reveals larger and more abundant pits than those observed in any of the other alloys. This is consistent with the change in microstructure driven by the increase in rod size and the lack of chiller. The shear and compressive stresses applied by the diamond tip coupled with the formation of Zr-rich intermetallic phases, may have led to the attachment of those particles to the tip in the form of Zirconium carbide. The movement of the tip and the chemically-bound phases will cause the pull out of the crystalline phases from the amorphous matrix. To confirm this, the position of the pits has been analysed. Most of the pits can be noticed near the centre of the track, where direct contact between the tip and the substrate takes place. Closer inspection of the worn surface (inset of Figure 38d) shows the presence of smaller pits between 2 and 5 μm and a more grooved profile (Table 15). The presence

of pits and smearing/grooving indicates that adhesive and abrasive wear had taken place, similarly to that observed in the previous samples. At the same time, the lower pile up (2.63 ± 1.51 μm) reveals an embrittlement of the sample which is consistent with the XRD scans (Figure 36d) and the increase in scratch hardness (1.45 ± 0.08 GPa). This embrittlement can be partially explained by the increase in volume fraction, as this sample reached the critical volume fraction, thus leading to a marked change in mechanical properties [369]. Finally, it should be noted that the depth of the track in the centre and the maximum depth of the groove (21.92 ± 1.83 μm and 26.51 ± 2.42 μm respectively) increases dramatically. This increase suggests that the hard intermetallic particles pulled out have a key role in the second wear mechanism, similar to the one observed in *section 3.1*.

For comparison purposes, all the described analysis was performed on a NCH3 $Cu_{52}Zr_{41}Al_7$ rod annealed at 850 °C for 48 h (Figure 38e) and on a 3 mm pure copper rod (Figure 38f). The pile up of the annealed sample is significantly smaller, however, some sites display a high pile up, thus generating the large standard deviation, 3.86 ± 2.79 μm. The depth of the groove at the centre and the maximum depth (17.47 ± 1.13 μm and 20.74 ± 1.22 μm respectively) are more similar to the CH3 sample than to the NCH3 rod. These results indicate a harder surface with consequent embrittlement of the material, showed by long cracks situated at both sides of the track. Contrary to the previous samples, the annealed rod does not have a relatively ductile matrix from which hard intermetallics can be pulled out. Consequently, the large stresses can only be released through the formation and propagation of cracks, resulting in a smooth surface (1106.54 ± 101.22 nm) with cracks up to 15 μm in length propagating transversely to the scratch direction (inset of Figure 38e). This can be further confirmed by the decrease in scratch width (196.08 ± 1.57 μm) and rise of scratch hardness (1.99 ± 0.03 GPa), which are consistent with the change in microstructure seen in Figure 37e. Thus, the annealing of the alloy led to the further increase in hardness and wear resistance observed in the $Cu_{52}Zr_{41}Al_7$ BMGCs.

Finally, the scratch track on the pure copper sample (Figure 38f) is much wider (426.54 ± 3.61 μm), deep (61.93 ± 3.97 μm, centre, and 66.34 ± 2.92 μm, maximum) and displays the highest pile up (40.91 ± 12.08 μm) among any of the BMGCs. Further magnification of the centre of the groove (inset of Figure 38f) shows a heavily

smeared and grooved surface (1631.62 ± 58.67 nm) with hook-like structures, commonly observed in plastically deformed materials. These features are consistent with the high ductility and low wear resistance of copper, indicated by the low scratch hardness value calculated, 0.42 ± 0.01 GPa.

In a similar way to *section 3.1*, the change in wear performance can be analysed with the ratio between the pile-up area and the groove area (Table 15). The increase in crystallinity and embrittlement of the BMGCs caused by the rise in volume fraction is revealed by the increase of the groove to pile-up ratio from 10.1 for the CH 2 mm sample to 31.8 for the NCH 3 mm sample. Interestingly, the annealed sample has a relatively low ratio (i.e. 14.0), but as previously discussed, the pile-up of the sample is heavily affected by the presence of local isles of material. For the copper sample, this ratio is the lowest of all the analysed samples (i.e. 3.0), expected from a ductile material.

3.2.3 Antimicrobial and wettability tests

Before assessing the antimicrobial properties of the BMGCs, the attachment of bacteria to the samples mirror-polished (4000 grit size) was estimated by analysing the wettability through contact angle tests [371]. Figure 39 shows the contact angle of deionised water sessile droplets deposited on the analysed surface, revealing an average value of: 88.6 ± 1.1° for CH2 (Figure 39a), 91.9 ± 1.5° for NCH2 (Figure 39b), 96.7 ± 1.4° for CH3 (Figure 39c), 96.2 ± 2.7° for NCH3 (Figure 39d), 94.6 ± 5.1° for the annealed sample (Figure 39e), 93.9 ± 4.5° for pure copper (Figure 39f) and 41.5 ± 4.6° for stainless steel (Figure 39g). These BMGCs reveal greater disparities on CA values due to changes in rod diameter rather than with the change in cooling system, which is consistent with the microstructural changes found in the XRD analysis. It is important to notice that the increase in volume fraction increases the hydrophobic nature of the $Cu_{52}Zr_{41}Al_7$ alloy, thus, predicting a reduction in the adhesion of bacteria. On the other hand, the annealed alloy reveals a wettability similar to that of pure copper, probably caused by the increase in Cu-rich crystalline phases. These results indicate that bacteria will be able to attach better on samples with lower volume fraction, however, these samples will have a limited number of grain boundaries, likely compromising their antimicrobial properties.

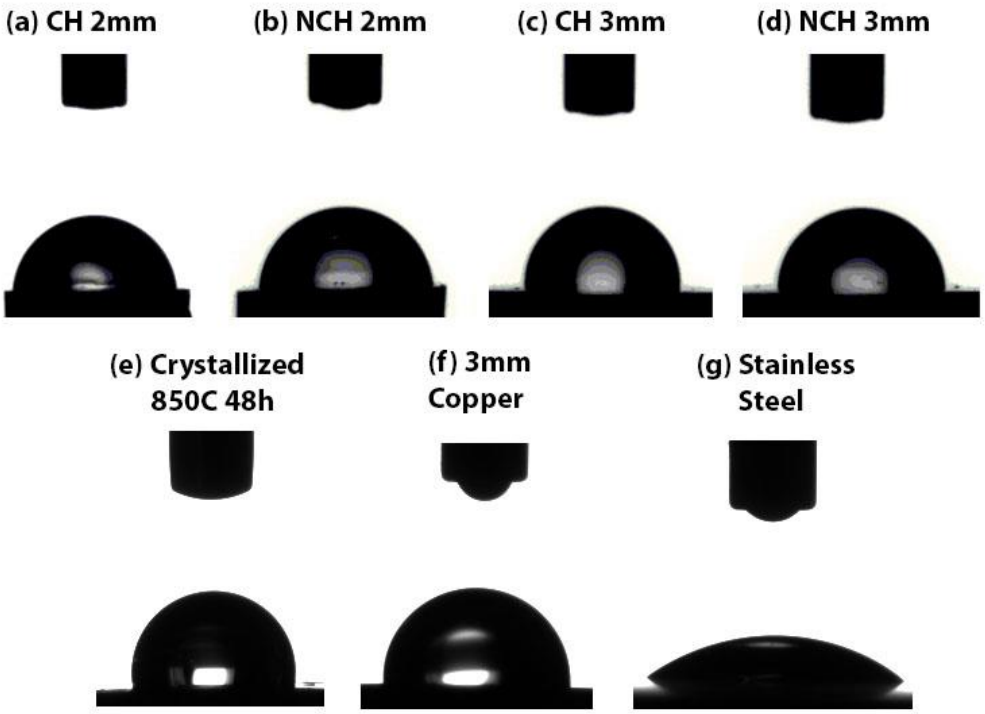

Figure 39 Average water contact angle $Cu_{52}Zr_{41}Al_7$ at. % alloy (a) CH 2 mm diameter, (b) NCH 2 mm diameter, (c) CH 3 mm diameter, (d) NCH 3 mm diameter, (e) Crystallized at 850 °C for 48 h, (f) 3 mm pure copper and (g) Stainless Steel [13].

The antibacterial properties of the casted alloys were estimated through the reduction of *E. coli* colony forming units (CFU/mL) after 1, 2, 3 and 4 hours of contact time. This test was carried out for two BMGCs (CH2 and NCH3) and a material without antimicrobial properties (stainless steel) to be used as a control (Figure 40). The recovery of bacteria from the stainless steel reveals a practically constant amount of bacteria (~ $3.8x10^8$ CFU/mL) with a slight increase after 4 h, consistent with the expected lack of antimicrobial activity. On the other hand, recovery of *E. coli* cells from both Cu-rich BMGCs display a reduction cells as the contact time increases. Both samples do not reveal great differences in antimicrobial activity for the first two hours, but the number of recovered cells diminishes appreciably after 3 h and 4 h. This change is especially dramatic for the NCH3 sample, able to eliminate two orders of magnitude more of *E. coli* cells than the CH2 sample. The change in antimicrobial kinetics can be quantified through a similar equation to the reduction percentage defined in *Equation 5*. This equation has been reported by Chu et al. [177] and differs by using the geometric mean of the number of survivors as inputs instead of the

arithmetic mean. The results can be seen in Figure 41 where the percentage of survivors on the CH2 and NCH3 samples is displayed for different contact times. After 2 h of contact killing the percentage of survivors is practically the same in both samples (~ 35 %), however, only 0.3 % of *E. coli* cells remain alive on the NCH3 rod after 4 h, while for the same time, 10.7 % survived on the CH2 sample.

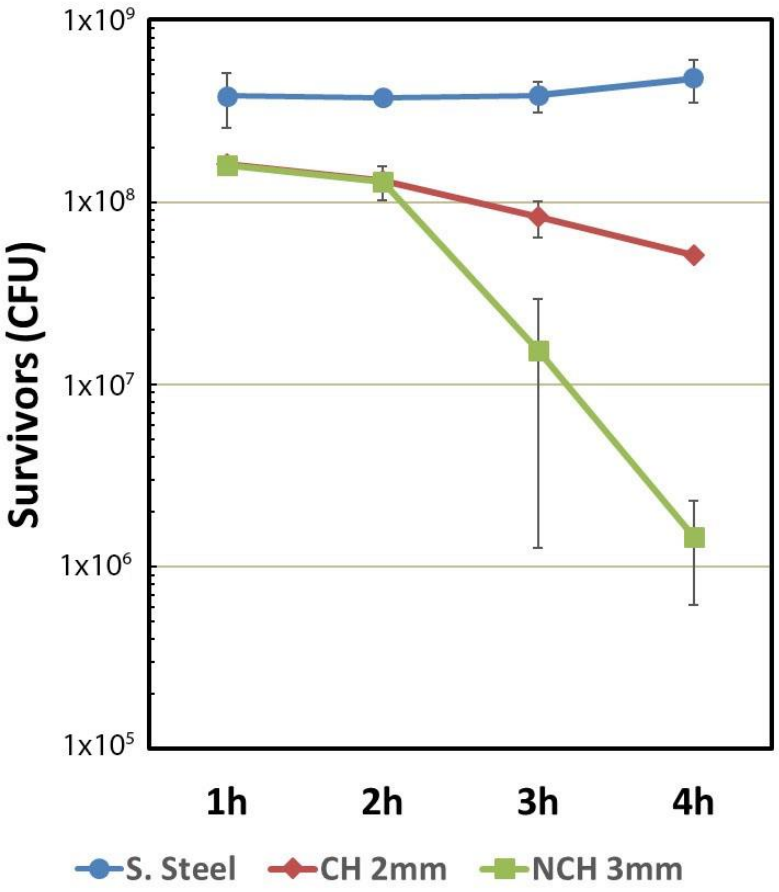

Figure 40 Recovery of *E. coli* exposed to indicated substrates. Each surface was inoculated with 1 µL of bacterial culture grown until OD_{600} = 0.3 [13].

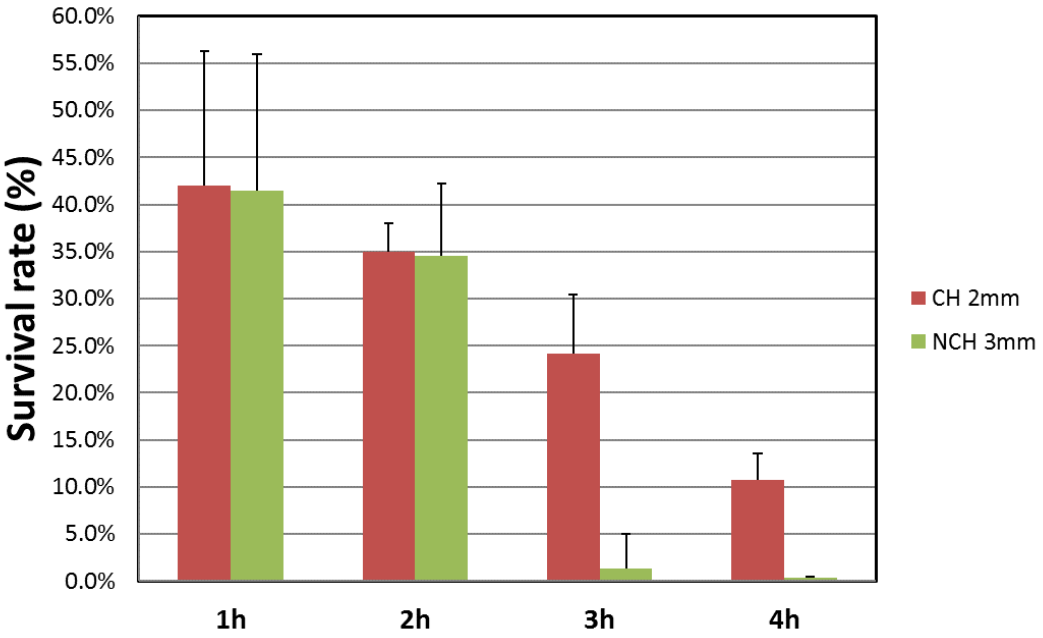

Figure 41 Survival rate values for samples with highest difference in cooling rate (2 mm chiller and 3 mm no chiller) after 1, 2, 3 and 4 hours using the stainless steel CFU as 100% survival ratio [13].

The similarity in the number of *E. coli* cells recovered during the first two hours in the two samples might be explained by the formation of dead cellular material, creating a protective "barrier" capable of protecting the remaining cells, i.e. those bacteria most intimately attached to the surface would absorb most damage after the point of their own death. As the time of contact increases, the exposure of the rest of the population to copper ions rises rendering this protective "layer" less effective, increasing the killing rate of *E. coli* cells. Settling of bacteria toward the surface may also increase their exposure to Cu ions and increase the apparent killing rate. On the other hand, the difference in slope observed in Figure 40 can be explained due to the dissimilarities in microstructure seen in the XRD scans. The nature of crystalline particles in the CH2 and NCH3 samples does not differ greatly. Both samples revealed the presence of CuZr crystals, being the greatest difference the appearance of low Cu content dendrites ($CuZr_2$) in the NCH3 samples. Thus, the differences in crystalline phases do not seem able to explain the sudden increase in antimicrobial properties. On the other hand, the volume fraction differs greatly in both rods, and, grain boundaries are known to be easy paths of diffusion [379]. As such, the larger

grain boundaries displayed between the particles and dendrites of the NCH3 may be the main contributors to the rise in killing rate.

To further analyse the role of crystalline phases' nature and volume fraction in the antimicrobial properties of Cu-rich alloys, the annealed $Cu_{52}Zr_{41}Al_7$ alloy was subjected to the same antimicrobial tests. The microstructure of the annealed sample full of Cu-rich crystalline phases (i.e. $Cu_{10}Zr_7$ and Cu_2ZrAl) coupled with the great density of grain boundaries would be expected to dramatically rise the antimicrobial properties of this alloy. The recovery of bacteria showed that after one hour of contact only 17.3 % of *E. coli* cells remained alive on the surface, while after two hours no viable bacteria were recovered. These results and the previous analysis of the BMGCs reveal that the microstructure is of utmost importance in developing highly efficient antimicrobial materials, but the main driving parameter responsible for the biocidal properties of these materials seems to be the volume fraction of crystalline phases rather than their composition. Interestingly, these results suggest that crystalline Cu-rich materials should be preferred over BMGCs. Nevertheless, after the antimicrobial experiments the samples displayed a black appearance and embrittlement, breaking solely by being handled using metallic tweezers. This suggests intergranular corrosion and oxidation which can affect the antimicrobial properties and the long term use of the alloy [68,108]. This change in colouration and brittleness was not found in the BMGCs and therefore these alloys are the most suitable candidates for antimicrobial applications.

In *section 1.1.4*, three standards capable of quantifying the antimicrobial properties of hard materials were introduced, namely: the **"Antibacterial products-Test for antibacterial activity and efficacy"** (Japanese Industrial Standard Z 2801:2010, First English edition published in 2011-12, Tokyo, Japan), the **European "Plastics-Measurement of antibacterial activity on plastic surfaces"** (International Organization for Standardization 22196:2007, First edition 2007, Switzerland) and the **American (Environment Protection Agency: EPA) "Protocol for the evaluation of bactericidal activity of hard, non-porous Copper containing surface products"** (Environmental Protection Agency, latest version 2016, United States of America). The quantification of this property was calculated using the method proposed by Chu et al. [177], but it is of interest to contrast the previous

results with the available standardized method described in these documents. It must be mentioned that the recommended density of inoculum in these documents is $6x10^5$ CFU/mL in the Japanese standards and 4-5 logs/carrier in the EPA standard, but, as mentioned in *section 3.1.3*, larger densities are desirable, which is further emphasized by the available literature [66,112,177].

Antimicrobial activity and percentage reduction were calculated according to these standards (Equations 4 and 5) for each of the BMGCs (Tables 16 and 17). The nature of both equations (one linear and other logarithmic) does not make it possible to compare both methods, however, they show a similar trend to the one observed in the previous analysis. The maximum antimicrobial activity and percentage reduction is accomplished by the NCH3 sample (2.51 and 99.91%), while the CH2 sample achieves a maximum of (0.97 and 94.18 % respectively). The values revealed by the NCH3 rod are near the threshold provided by the **American protocol** to consider an antimicrobial surface as effective (3 $\log_{10}$ reduction). Finally, it should be noted that the equations provided in the standards use logarithms and geometric mean which are more robust than mere arithmetic mean, which may result in more reliable results than the ones used by Chu et al. [177].

Table 16 Antimicrobial activity calculated using **JIS Z 2801:2010** Antibacterial products -- Test for antibacterial activity and efficacy [171].

	1h	2h	3h	4h
CH 2mm	0.38	0.46	0.67	0.97
NCH 3mm	0.38	0.46	1.4	2.51

Table 17 Reduction of bacteria percentage calculated using **US EPA** Protocol for the Evaluation of Bactericidal Activity of Hard, Non-porous Copper Containing Surface Products [173].

	1h	2h	3h	4h
CH 2mm	38.73%	44.57%	93.09%	94.18%
NCH 3mm	39.52%	43.22%	99.71%	99.91%

3.3 Discussion

In *sections 3.1* and *3.2*, the wear and antimicrobial properties of Cu-rich bulk metallic composites has been analysed and correlated with the literature. The purpose of this section is to compare the obtained results and analyse the main factors that influence the properties through changes in composition and cooling rate.

The four alloys analysed ($Cu_{50}Zr_{44}Al_6$, $Cu_{53}Zr_{41.4}Al_{5.6}$, $Cu_{56}Zr_{38.7}Al_{5.3}$ and $Cu_{52}Zr_{41}Al_7$) do not differ greatly in their composition, however, drastic changes in microstructure were observed. It was found that the 2 mm rods of $Cu_{50}Zr_{44}Al_6$ and $Cu_{52}Zr_{41}Al_7$ alloys display the highest GFA, while minute changes in composition and cooling rate increase the volume fraction of crystalline phases. The nature of these crystalline phases is similar in all of the analysed alloys and most of the phases are detected by SEM, with exception of $Cu_{10}Zr_7$ and Cu_8Zr_3 phases in the low copper alloys. The lack of these phases could be attributed to the sensitivity of the XRD technique to small volume fraction of crystalline phases, which may only be detected by TEM [293]. An analysis of the equilibrium binary Cu-Zr (Figure 42) and ternary Cu-Zr-Al (Figure 43) diagrams shows that the main crystalline phases ($Cu_{10}Zr_7$, Cu_8Zr_3, CuZr, $CuZr_2$ and Cu_2ZrAl) are stable and metastable intermetallics expected in compositions similar to the ones studied. Nevertheless, compositional analysis reveals that the detected phases do not exactly correspond to the ones estimated in the equilibrium diagrams (i.e. $CuZr_2$ should not be expected in $Cu_{52}Zr_{41}Al_7$). The reason for this discrepancy comes from the high cooling rates common in the preparation of MGs and their composites [380], and can explain the presence of $CuZr_2$ in Cu-Zr-Al alloys with relatively low Zr content [378,381]. Nevertheless, the microstructure of the Cu-based

alloys shows mostly the presence of $Cu_{10}Zr_7$, Cu_8Zr_3 and CuZr, which can be expected as these alloys are close to two deep eutectics located between the $Cu_{10}Zr_7$ and CuZr phases [382]. On the other hand, the Cu-Zr diagram indicates the presence of Cu_5Zr_8 should take place first before the apparition of $CuZr_2$ (Figure 42), however, the equilibrium diagram of the ternary Cu-Zr-Al system shows the following two deep eutectic reactions: liquid → CuZr + τ_3 + $CuZr_2$ and liquid → $Cu_{10}Zr_7$ + τ_4 + CuZr [349]. These reactions, coupled with the fact that higher Al contents tend to stabilize the ternary system [348] would explain the favoured $CuZr_2$ phase in the $Cu_{52}Zr_{41}Al_7$ alloy.

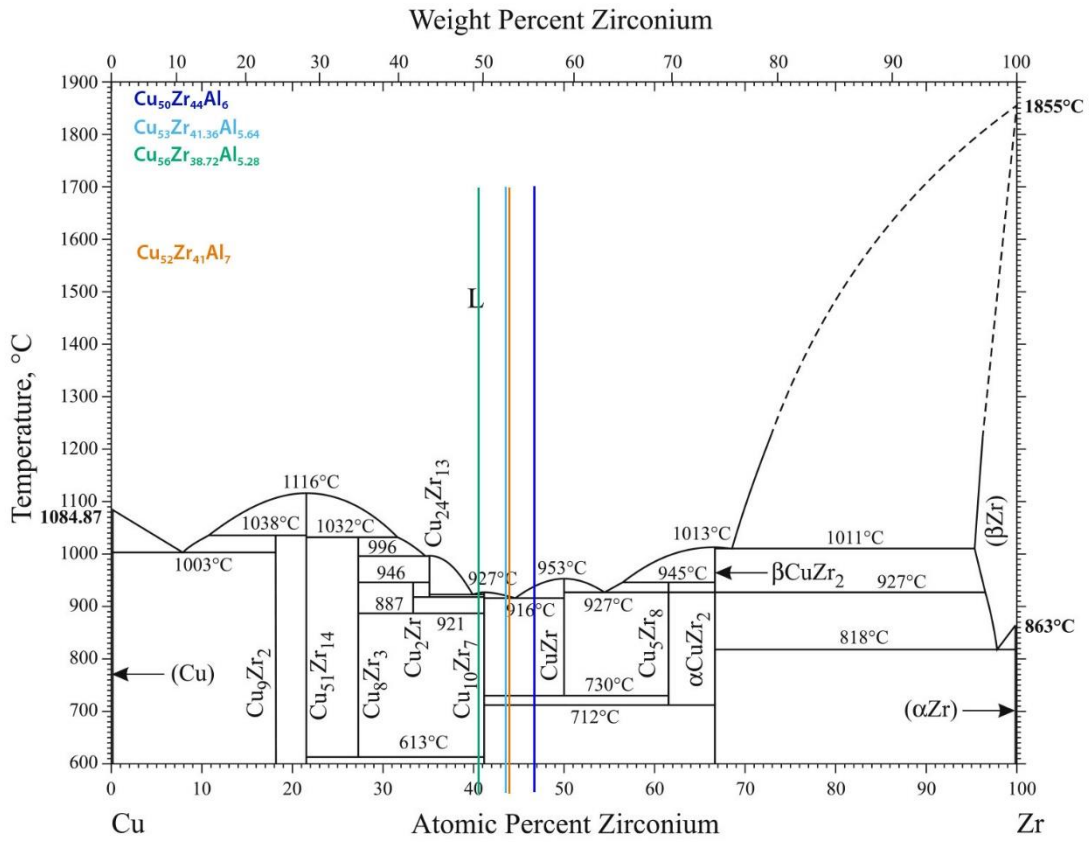

Figure 42 Cu-Zr phase diagram [326] with the compositions analysed in this chapter.

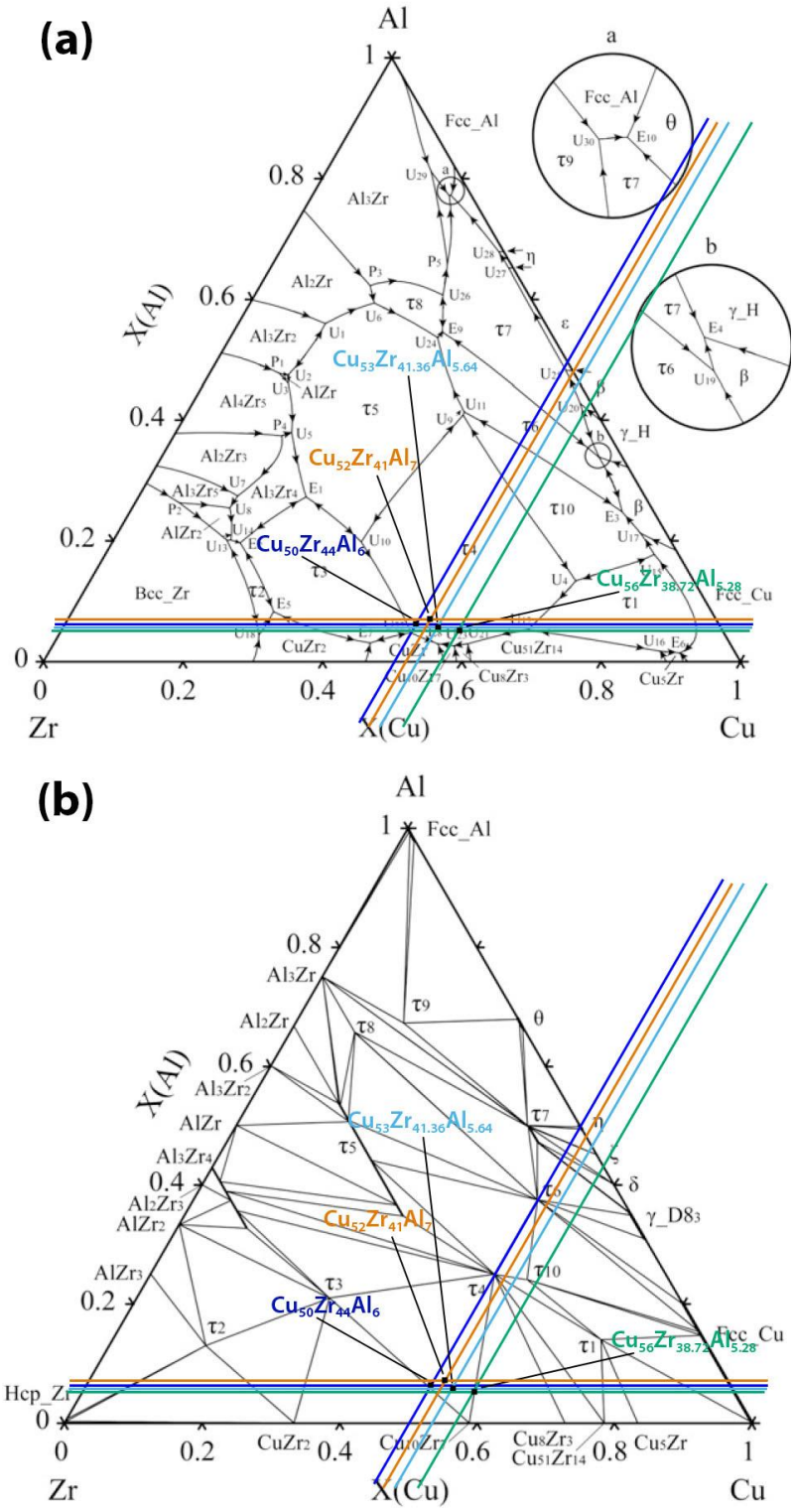

Figure 43 Evaluated isothermal sections of the Al-Cu-Zr system for (a) liquidus [349] and (b) 800 °C [354] with the compositions analysed in this chapter.

For the scratch test, the increase in copper content, as well as, the reduction of cooling rate leads to an increase in the volume fraction of brittle crystalline phase, and therefore results in an embrittlement of the alloy. However, one should notice the difference in wear mechanisms and wear behaviour between the alloys. In one hand, the alloys analysed in *section 3.1* display higher abrasive wear, while the alloys studied in *section 3.2* show both abrasive and adhesive wear. The main difference between the two alloys is the relatively high content in aluminium of the latter, 7 %. It is broadly known that MGs are heavily dependent on their composition, and that small compositional changes can lead to drastic changes in their mechanical performance [201,359]. This change in composition may be the cause behind the lower scratch hardness of the $Cu_{52}Zr_{41}Al_7$ alloy (maximum of 1.45 GPa) when compared to the $Cu_{50}Zr_{44}Al_6$ alloy (3.73 GPa), and the higher ductility of the of alloys seen in *section 3.2*. On the other hand, it must be said that the trends observed in both sets of alloys are completely different. The increase in wear resistance was effectively lowered as the copper content increased, from 3.73 GPa to 2.41 GPa, while the reduction in cooling rate raises the wear resistance of the alloy, from 1.29 GPa to 1.45 GPa. The small increase in wear resistance due to cooling control indicates that volume fraction is of importance in the wear resistance of the alloy, but the higher differences driven by compositional changes show that composition may be of greater influence. The increase in volume fraction did not greatly change the wear behaviour for values below the percolation threshold, and, once reached, the mechanical properties of the alloys underwent an embrittlement, as suggested by the formation of numerous cracks in the $Cu_{56}Zr_{38.7}Al_{5.3}$ and $Cu_{52}Zr_{41}Al_7$ NCH3 rods. In common crystalline materials it has been shown that the increase in hardness causes a rise in wear performance [291,292], nevertheless, the interaction between a relatively ductile matrix with the harder intermetallic particles may cause an increase in wear through secondary wear mechanisms (as seen in the $Cu_{56}Zr_{38.7}Al_{5.3}$ alloy). Finally, the use of nanoindentation to indirectly estimate the wear performance showed that the increase in copper content caused a slight rise in the H/E_r, H^3/E_r^2 parameters, suggesting better wear behaviour of the alloys with high copper content. On the contrary, these samples revealed a decrease in scratch hardness (i.e., wider scratch values), which suggests lower wear resistance. Nanoindentations performed at high enough load to embrace all the crystalline phases of materials with fine homogeneous microstructures at the nanoscale enables to get an average value and therefore it can be of great use. However, the studied alloys have large heterogeneous crystalline phases at the

microscale and therefore the indents (even at the highest applied loads) are not large enough to embrace all the phases and get an average value. Thus, scratch hardness tests would be a better indicator of wear performance.

The differences in bacterial adhesion predicted form the sessile drop tests are subtle, and the trend observed in *section 3.1* is completely opposite to the one seen in *section 3.2*. On one hand, the increase in copper content decreased the contact angle on the first set of alloys, while higher volume fractions in the cooling rate samples effectively increased the contact angle. Considering these results, it may be said that two opposite phenomena are interacting and changing the superficial energy of these samples. The increase in crystallinity tends to increase the CA, while the presence of Cu-rich phases appears to decreases the CA. These two driving forces are of great interest as they would be expected to have a direct impact on the adhesion of bacteria. As a result, small crystals of high Cu-rich phases would be expected to create a hydrophilic surface. This surface would be able to increase the adhesion of bacteria, which linked to the diffusion of copper ions, may enhance the antibacterial activity.

A comparison of the antimicrobial properties obtained reveal that changes in volume fraction as well as the nature of the crystalline phases have had a direct impact in the killing of bacteria. All samples analysed showed low antimicrobial activity for times lower than 2 h, which drastically changed after 3 and 4 hours. In both sets of samples, the alloys with higher volume fraction of crystalline phase showed killing rates higher than 1 $\log_{10}$ reduction after 4 hours of contact killing (for a density of 10^8 CFU/mL). However, only the sample with the highest volume fraction reached an antimicrobial activity of 2.51, suggesting that volume fraction is more likely to be the main property affecting the antimicrobial properties of MGCs. It is true that the $Cu_{56}Zr_{38.7}Al_{5.3}$ alloy eliminated 1 $\log_{10}$ of bacteria more than the more amorphous $Cu_{50}Zr_{44}Al_6$ sample, and backscattered images showed large round particles occupying more than 50 % of the sample, but the grain boundaries of round particles are much lower than the dendritic structures seen in the NCH3 alloy. For this reason, it can be said that variations in the morphology of the crystalline phases and, as such, increases in grain boundary density will be more likely the cause for the increase in percentage reduction for both samples, rather than an overall change in nominal composition. Thus, the hypothesis

that a highly bactericidal alloy would be that containing large branched dendrites mixed in an amorphous matrix, instead of highly crystalline densities of round particles. The increase in diffusion paths will enhance the movement of copper into bacteria, effectively rising the antimicrobial properties of the material [65].

In summary, changes in wear and antimicrobial properties have been correlated with variations in cooling rate and composition for several Cu-rich alloys. The conducted analysis had indicated that volume fraction of crystalline phases and their morphology are the key parameters ruling both properties. Thus, it has been demonstrated that the wear and antimicrobial performance of BMGCs can be effectively tuned through cooling rate and composition. These results have shown that high volume fractions in the range of the percolation threshold will improve the antimicrobial properties of the alloy. On the other hand, the nominal composition can be controlled to obtain a relatively hard ($Cu_{56}Zr_{38.7}Al_{5.3}$) or ductile material ($Cu_{50}Zr_{44}Al_{6}$), but special consideration has to be taken to reduce the wear introduced by secondary wear mechanisms.

4 Impact of surface roughness and oxidation on the antimicrobial activity of a Cu-based BMGC

In the previous chapter, the influence of composition and cooling rate on the wear resistance and antimicrobial behaviour of a Cu-based BMGCs was investigated. Increasing the crystallinity was observed to improve the antimicrobial behaviour not only because of the formation of Cu-rich crystalline phases but probably also due to the large volume fraction of grain boundaries that act as diffusion paths.

Besides controlling the composition and casting parameters, another strategy to enhance the wear resistance of Cu-rich alloys is promoting the formation of copper oxides [383]. However, Hans et al. [68] analysis of pure copper, Cu_2O and CuO have shown that copper oxides can display lower antimicrobial properties than pure copper. Thus, the superior wear resistance of oxidised alloys may have a detrimental effect on the contact killing behaviour. Surface engineering can be a second method to increase the antimicrobial performance, as changes in roughness will influence the wettability and, as such, the bacteria-surface attachment [384,385]. Surfaces analysed in the literature have mostly focused on controlling the parameters (height, width and spacing) of several geometries (e.g. pillars, hexagons) in the nanometre to micron size [384]. The magnitude of such geometries are in the same scale as that of bacteria and, consequently, they are expected to have the largest impact on bacteria-surface attachment. Albeit patterning may be an interesting option to impact cell attachment to small surfaces, this process may not be feasible to produce commercial large surfaces for use in hospital touch surfaces. As far as the author is concerned, the impact of roughness from simple grinding on the antimicrobial performance of Cu-rich alloys has not been studied before, and might reveal an interesting cost-effective method to improve the performance of such materials.

Taking into account the previous paragraphs, the purpose of this chapter is to shed light on the impact of oxidation and roughness on the contact killing efficiency of a Cu-Zr-Al BMGCs. For this purpose, 2 mm rods with composition of $Cu_{55}Zr_{40}Al_5$ at. % were cast and ground using different SiC grinding paper, while half of those samples were oxidised in air at 703 K for 5 h. Besides its antimicrobial behaviour, the effect of contact time on the morphology of *E. coli* will be studied and compared with cells exposed to controlled dosages of copper

ions in liquid culture. Finally, the results will be used to propose the development of antimicrobial maps to ease the research of high antimicrobial performance materials.

4.1 Oxidation and roughness analysis

4.1.1 Examination of the microstructure

XRD scans of the as-cast and oxidized samples can be observed in (Figure 44a), alongside their corresponding SEM backscattered images (Figures 44b and 44c, respectively). The as-cast sample reveals high intensity peaks overlapped to an amorphous hump, indicating the presence of crystalline and amorphous phases. These peaks can be associated to orthorhombic $Cu_{10}Zr_7$ (a = 0.9347 nm, b = 0.9347 nm, c = 1.2675 nm), orthorhombic Cu_8Zr_3 (a = 0.78686 nm, b = 0.81467 nm, c = 0.9977 nm), austenite B2 CuZr (a = 3.2562 nm, b = 3.2562 nm, c = 3.2562 nm), monoclinic martensite B19´ CuZr (a = 0.3237 nm, b = 0.4138 nm, c = 0.5449 nm) and tetragonal $CuZr_2$ (a = 0.3220 nm, b = 0.3220 nm, c = 1.1183 nm).

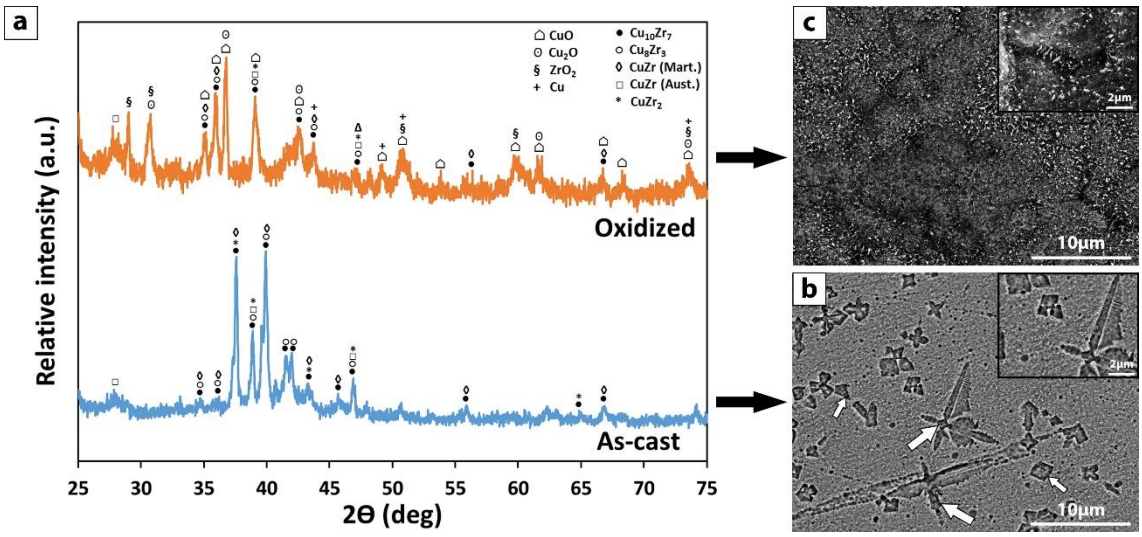

Figure 44 (a) XRD scans for the as-cast and oxidised $Cu_{55}Zr_{40}Al_5$ (at. %) BMGCs with the corresponding SEM backscattered images for the (b) as-cast and (c) oxidized samples.

On the other hand, the oxidised sample does not show such a noticeable amorphous hump, suggesting that the oxide layer thickness is enough to mask the signal from the amorphous phase present in the sample. The oxidised sample shows the presence of similar peaks to

those previously mentioned, however, the oxidation process has caused the appearance of additional peaks matching monoclinic CuO (a = 0.4653 nm, b = 0.3410 nm, c = 0.5108 nm), cubic Cu_2O (a = 0.4252 nm, b = 0.4252 nm, c = 0.4252 nm), tetragonal ZrO_2 (a = 0.5070 nm, b = 0.5070 nm, c = 0.5160 nm) and face-centred cubic Cu (a = 0.3608 nm, b = 0.3608 nm, c = 0.3608 nm).

The as-cast surface (Figure 44b) reveals particles of cubic (small arrows) and dendritic (large arrows) shape up to 5 µm in size fixed in a featureless matrix. EDX measurements of the cubic particles and dendrites showed a composition of $Cu_{36.2}Zr_{51.0}Al_{12.8}$ and $Cu_{46.3}Zr_{41.1}Al_{4.7}$ respectively, indicating that the latter can be matched with $CuZr_2$ while the former can be attributed to CuZr. The featureless matrix surrounding the crystalline phases showed a composition equal to that of the nominal composition ($Cu_{55}Zr_{40}Al_5$). The oxidation process at 703 K for 5 h (Figure 44c) has led to a dramatic change in the microstructure. The surface is composed of granules similar to those observed in the $Cu_{60}Zr_{30}Ti_{10}$ alloy by Tam et al. [386], but the ones seen in these samples are coarser (~ 5 µm), probably caused by the higher oxidising temperature used (the cited work used 573 K not 703 K). Beside the black granules, small white needles can be discerned homogeneously distributed on the surface (inset of Figure 44c).

The nature of the oxides obtained was analysed through a cross-section of a sample prepared with 240 grit paper (Figure 45). The secondary electron image (Figure 45a) exposes a layered structure divided by what seems to be a porous intermediate layer. Further analysis of this structure with backscatter SEM imaging (Figure 45b) reveals a complex multi-layered structure with different compositions. This compositional difference is especially noticeably in the elemental EDX mapping of the cross-section (Figure 45c) where Al-rich (green), Cu-rich (blue), Zr-rich (red) and O-rich (orange) regions can be clearly discerned. This analysis indicates that the maximum oxygen content can be found near the surface, while the O content diminishes with increasing depth from the surface. The outermost dark layer up to 0.7 µm thick has a composition of $Cu_{51.1}O_{49.9}$ and is attributed to CuO. The second layer of brighter tonality reveals a composition poorer in oxygen, $Cu_{68.2}O_{31.8}$, which can be matched with Cu_2O. The following porous layer is composed of a mixture of pure copper and some copper oxides. The final layer before the as-cast BMGCs revealed a composition of $O_{54.0}Zr_{26.9}Cu_{15.8}Al_{3.4}$, indicating the presence of Zr_2O with some traces of copper and aluminium.

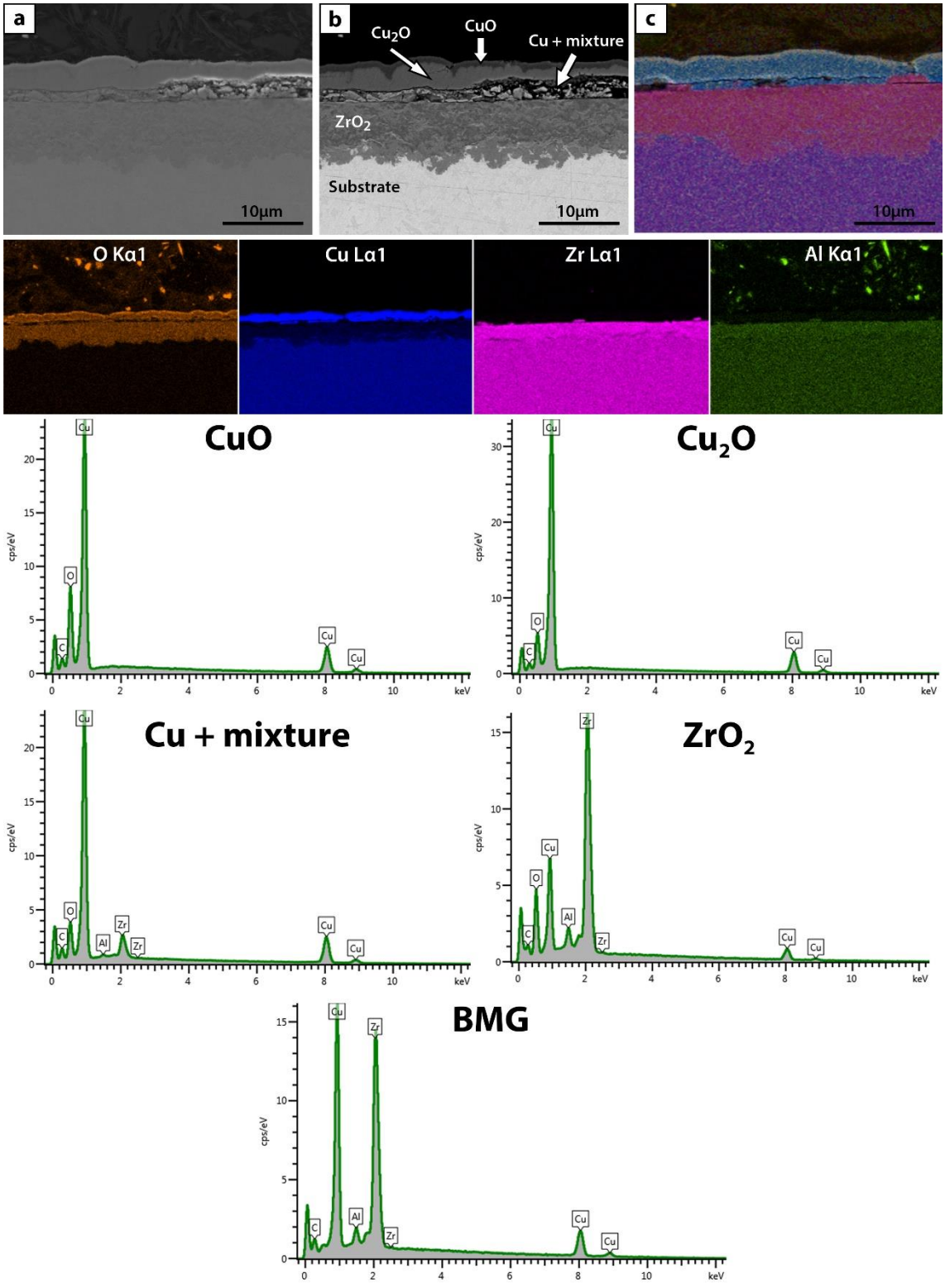

Figure 45 (a) Secondary electron and (b) backscattered SEM images for the cross section of the 240 grit oxidized sample. (c) Compositional EDX mappings corresponding to Cu, Zr, O and Al. EDX spectra for all phases shown in the cross section backscattered image.

The formation of a complex oxide layer in Cu-based BMGs has already been reported in the literature [383,386,387]. The electrode potential of Zirconium (-1.553 V, Zr/Zr^{4+}) is much lower than that of copper (+0.337 V, Cu/Cu^{2+}), indicating a preferential oxidation of Zr to ZrO_2 [388,389]. During the first stages of oxidation, a porous layer of ZrO_2 will be formed on top of the substrate, allowing the diffusion of oxygen and further oxidising the alloy. The decreasing content of elemental Zr will cause the segregation of metallic copper and will move outward as a new layer of ZrO_2 is formed beneath the diffused copper, resulting in a ZrO_2-Cu-ZrO_2-BMG layer. Asami et al. [388] had shown that further contact of the tetragonal ZrO_2 layer with oxygen and moisture will cause a tetragonal to monoclinic transformation followed by degradation and cracking of the layer. The ZrO_2 layer will leave the segregated copper in contact with air, resulting in the formation of Cu_2O and CuO [388].

Although EDX can give information about the composition of the material, it can be difficult to quantify the exact amount of lighter elements, such as oxygen [390], present on the samples. For this reason, X-ray Photoelectron Spectroscopy (XPS) was carried out on the surface of the oxidized samples both as prepared (Figure 46a) and after argon ion sputtering (Figure 46b). The spectra of both scans reveal the presence of O, Cu, Zr and Al with minor quantities of C, N and Si from surface contamination. The intensity of the peaks indicates that the stoichiometry of the material between the unsputtered and sputtered conditions is different, with higher concentrations of copper in the untreated surface and higher Zr content in the treated surface. This suggests a layered structure rich in copper near the surface, consistent with the EDX measurements.

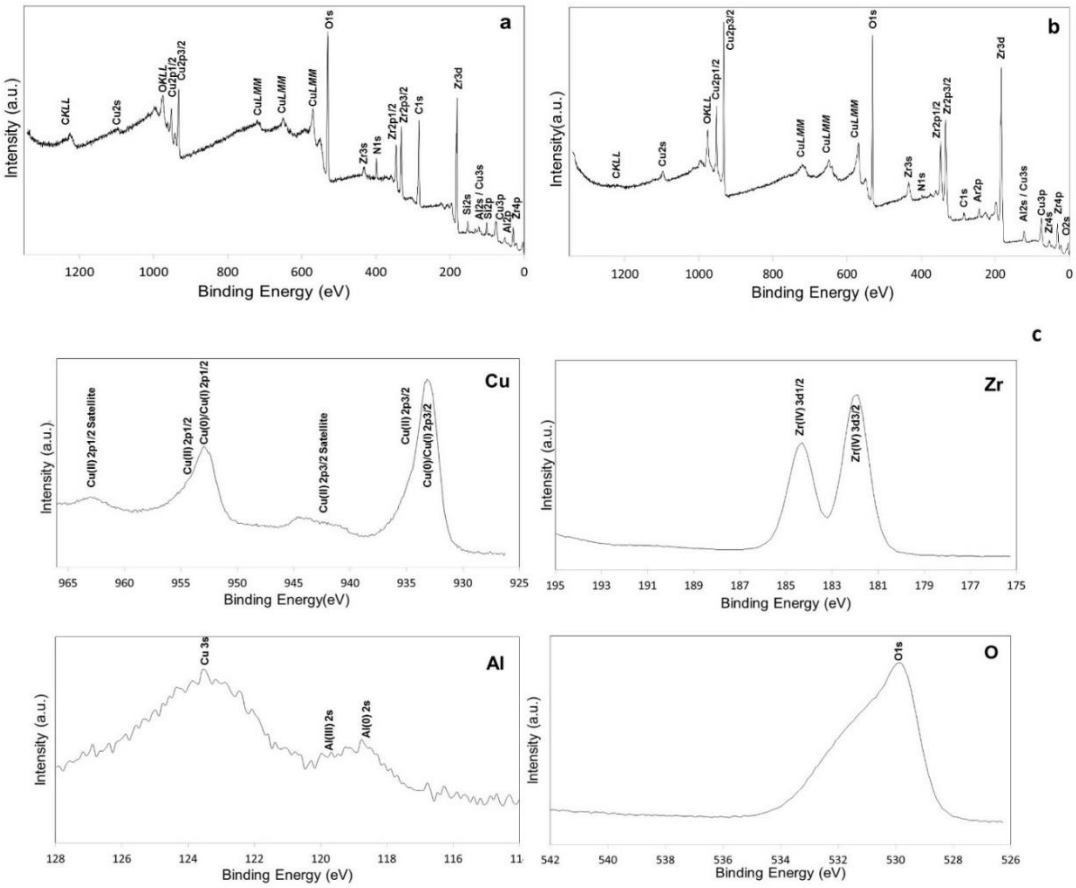

Figure 46 XPS spectra of the oxidized $Cu_{55}Zr_{40}Al_5$ sample at 703 K for 5 h in the (a) untreated and (b) sputtered surface. In addition, Cu 2p, Zr 3d, Al 2s and O 1s core-level XPS spectra (c) from the oxidized sample without sputtering are shown.

The oxidation states of the metal at the surface of the sample (i.e. Cu 2p, Zr 3d, Al 2s and O 1s) before sputtering can be seen in Figure 46c. The copper 2p peak splits into $2p_{3/2}$ and $2p_{½}$ components (931.8 eV and 951.6 eV, respectively), and is compatible with Cu^{1+} and elemental Cu, while the small satellite below 945 eV and the asymmetry of the peaks indicates a small amount of Cu (II) present on the sample. On the other hand, the Zr doublet located at 182.0 and 184.3 eV (Zr $3d_{5/2}$ and Zr $3d_{3/2}$, respectively) can be attributed to Zr^{4+}. The aluminium peak (Al_{2s}) consists of two chemically shifted species Al(0) (118.8 eV) and Al(III) (119.9 eV), while the O_{1s} peak is caused by metal oxides and contaminants. These results indicate the presence of oxidized species, especially Zr, in the sputtered sample, which are into agreement with the SEM and EDX data.

4.1.2 Influence of oxidation in the roughness of the metallic glass composites

To assess the effect of oxidation on the roughness, as-cast samples were ground with several SiC abrasive grinding papers of different grit size (240, 1200 and 4000), and half of the ground samples were oxidized. All sample surfaces were studied using an optical profilometer Figure 47, obtaining the arithmetic average of the roughness profile, R_a, and average distance between the highest peak and lowest valley, R_z, (Table 18). The roughness measurements show a clear increase in roughness after oxidation, which intensifies with reduced SiC grit size (from ~ 4 times rougher in the smoother surface to ~ 1.4 rougher in the highest grit size). This trend can also be noticed in the average distance between the highest peak and lowest valley, indicating that the oxidation granules observed in Figure 44c had replicated and intensified the roughness of the as-cast samples.

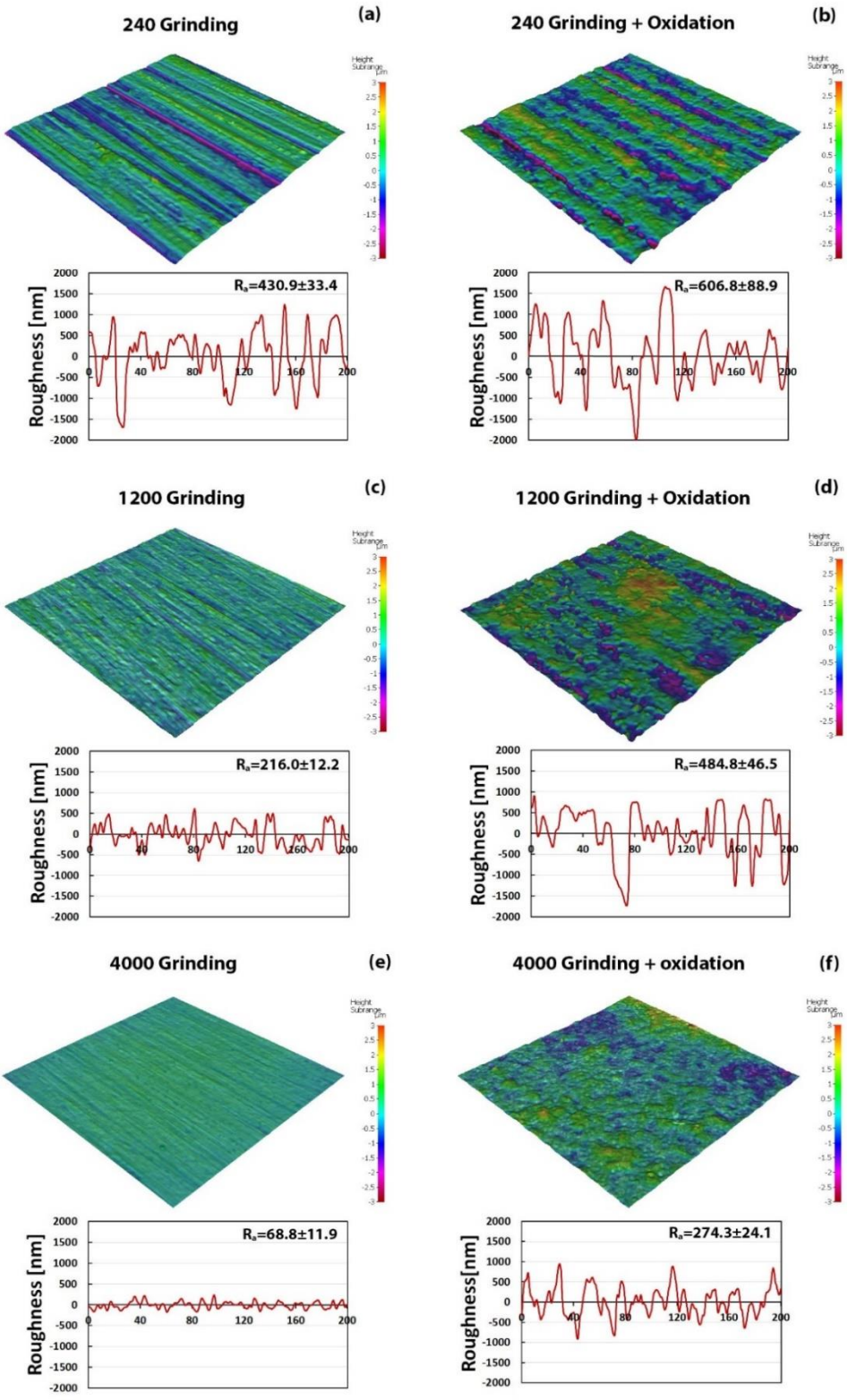

Figure 47 Surface topography for all ground samples (240, 1200 and 4000) before and after oxidation.

Table 18 Summary of the arithmetic average of the roughness profile and average distance between the highest peak and lowest valley for several grit papers.

	Grit size					
	4000		1200		240	
	R_a (nm)	R_z (nm)	R_a (nm)	R_z (nm)	R_a (nm)	R_z (nm)
As-cast	68.8 ± 11.9	422.6 ± 75.9	215.9 ± 12.2	1257.1 ± 94.3	430.9 ± 33.4	2392.7 ± 189.7
Oxidized	274.3 ± 24.1	1237.1 ± 201.7	484.8 ± 46.5	2500.2 ± 307.9	606.8 ± 88.9	2720.7 ± 421.5

4.2 Analysis of the Cu ion impact in the recovery and morphology of *E. coli* cells

4.2.1 Antimicrobial tests

Similarly to *chapter 3*, the antimicrobial behaviour of the as-cast and oxidized samples (240, 1200 and 4000 grit sizes) were analysed through the reduction in *E. coli* colony forming units per millilitre of broth (CFU/mL) deposited on the surface after 1, 2.5 and 4 h of contact time (Figure 48). The number of colonies counted on the 314 stainless steel coupons is practically constant through all the contact times used in the study (~ $5x10^8$ CFU/mL), suggesting that there are no external factors influencing the experiments. In addition, secondary electron SEM images of the bacteria on contact with stainless steel (Figure 48a) and the 4000 ground as-cast (Figure 48b) and oxidized (Figure 48c) samples are shown.

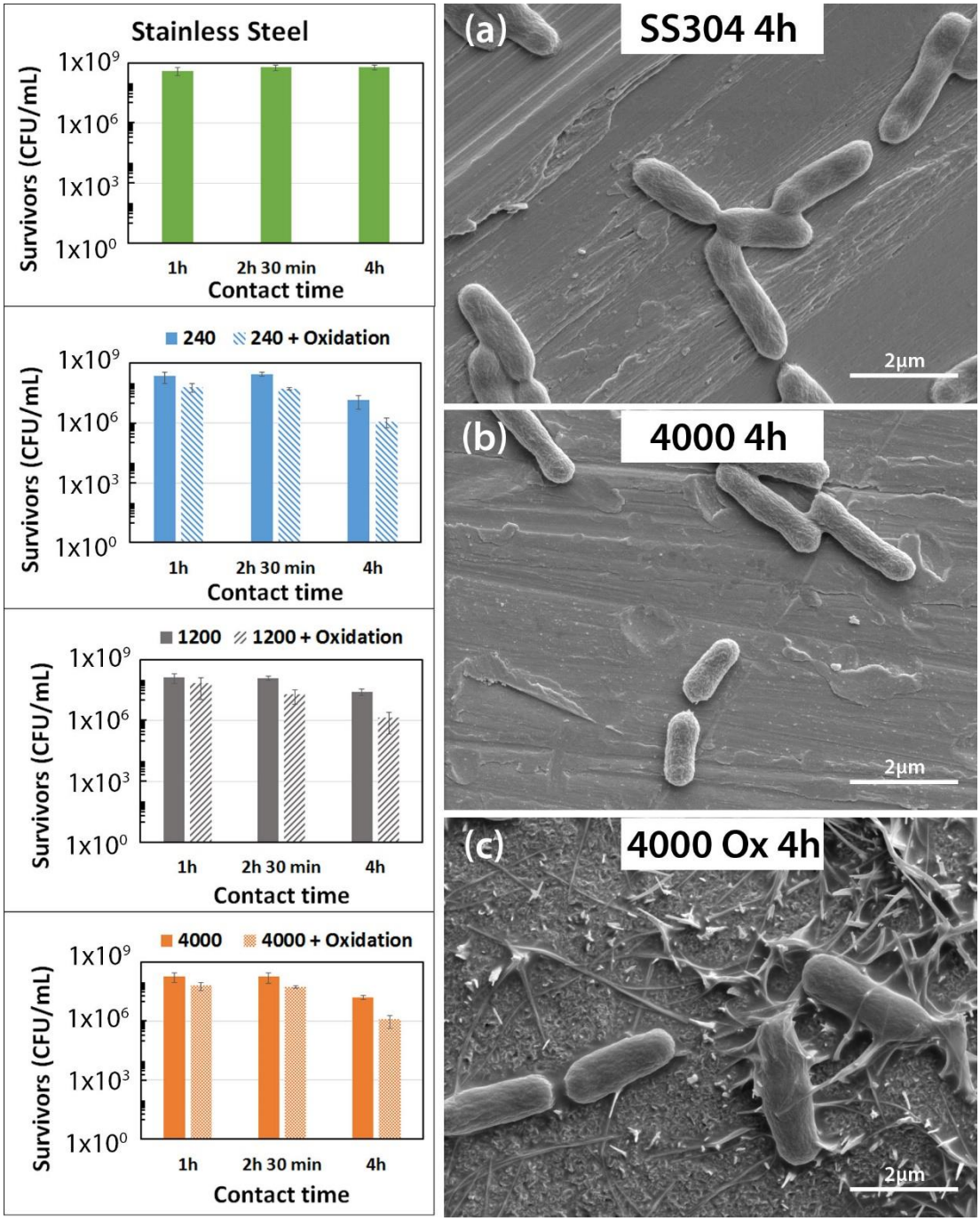

Figure 48 Number of surviving *E. coli* cells deposited on steel and both as-cast and oxidized samples with different toughness for 1, 2.5 and 4 h of contact time. Morphology of the deposited *E. coli* bacteria on (a) 314SS, (b) 4000 as-cast and (c) 4000 oxidized samples after 4 h.

The antimicrobial performance of all the as-cast BMGCs is similar regardless of the difference in roughness (68.8 ± 11.9 µm to 430.9 ± 33.4 µm), phenomenon that can

also be observed in the oxidized samples (274.3 ± 24.1 µm to 606.8 ± 88.9 µm). In contrast, oxidation of the as-cast samples has revealed a significant increase in the antimicrobial activity for all contact times studied (1, 2.5 and 4 h) when compared to the as-cast alloy. At the same time, a slight delay in antimicrobial reduction can be seen during the first 2.5 hour of contact time. Comparable number of *E. coli* bacteria were recovered in the as-cast samples after 1 and 2.5 hours (~ $2x10^8$ CFU/mL), but a sudden decrease can be observed after 4 hours of surface-bacteria contact (~ $1.5x10^7$ CFU/mL). This also occurs in all oxidized samples, $6x10^7$ CFU/mL in 1 h, $3x10^7$ CFU/mL in 2.5 h and $8x10^5$ CFU/mL in 4 h of contact killing time, and is consistent with the results seen in *sections 3.1.3 and 3.2.3*.

The analysis of *E. coli* deposited on steel (Figure 48a) show apparently undamaged cells with an intact envelope adhering to the substrate surface [391]. The outer envelope of the cells deposited on the 4000 as-cast sample (Figure 48b) are similar, but they are noticeably smaller and more slender. In contrast, the bacteria adhered on the 4000 oxidized sample (Figure 48c) look larger and rounder than the ones deposited on the stainless steel 314 control, and covered by a layer of material on top of the *E. coli* cells near the substrate needles. Changes in morphology similar to those observed in the oxidized samples can be seen in the literature regarding bacteria in contact with Cu-rich materials, and have been suggested as indicators of damaged bacteria [192,392,393]. It is of interest to notice that the needles observed in Figure 48c appear more developed that those observed in the oxidized surface before contact with *E. coli* (inset of Figure 44c). EDX measurements of this feature before and after contact with the bacteria ($O_{53.0}Cu_{47.0}$ and $O_{56.5}Cu_{43.5}$) suggest that they can be associated to CuO needles corresponding to the first layer seen in the EDX mapping (Figure 45b). On the other hand, the layer observed near the bacteria in contact with the CuO needles may be escaping cellular contents from partially lysed cells, but the relatively undamaged cells seem to indicate that it is not the case. Instead, this might be the result of secreted polysaccharides developed as a response to osmotic stress [394], triggered by stimulation of mechanosensitive channels by the development of the aforementioned needles [395] and appropriate with the formation of a biofilm.

The independence between superficial roughness and antimicrobial activity is interesting, as Mann et al. [396] micropatterning of acrylic surfaces with patterns inspired by shark skin, suggested that roughness could affect the wettability and, as such, bacterial-surface adhesion [397,398], biofilm formation and antimicrobial performance [114]. In this case, the major superficial change is the growth of CuO needles in the oxidized sample, probably caused by further oxidation of the surface promoted by the contact with the NaCl-rich bacterial culture broth [399]. This apparent small change may have altered the curvature of the *E. coli* cell membrane, causing a response through the mechano-sensitive channels (Figure 49) present in the plasma membrane [395]. The main purpose of these sensors is to regulate the permeability of ions entering and exiting the cell, and, as Sachs and Morris [400], Matinac et al. [401] and Buechner et al. [402] have shown, these channels can be triggered by mechanical stimuli. The most studied mechanosensitive channels in *E. coli* cells are the Mechanosensitive channel of Small conductance (MscS) and Mechanosensitive channel of Large conductance (MscL), and while MscS favours chlorine over potassium, MscL are permeable to any anion and cation [403]. Changes in membrane curvature can activate these channels when the tension applied exceeds values of ~ 6.0 (MscS) mN/m and ~ 12.0 mN/m (MscL) [404-406], opening the channels and, therefore, increasing the permeability of the cell to cations and anions. The growth of the CuO needles near the cells may have triggered the mechanosensors in the deposited *E. coli* cells, intensifying the flow of copper ions into the bacteria. These ions will lead to the killing of the cell by disrupting homeostasis of other metals, DNA damage, and production of Reactive Oxygen Species (ROS), which modify proteins, lipids and nucleic acids [407-409]. The death of *E. coli* bacteria through mechanisms taking place inside the cell would agree with the limited damage observed in the SEM images of deposited cells (Figure 48). This will also explain the high degradation of the external envelope seen in studies of morphological changes in *E. coli* caused by contact with copper nanoparticles [392,393]. In these papers, the cell envelope suffered severe degradation through cell shrinkage, appearance of pits and cavities with loss of its rod shape, explained by the degradation of proteins present in the cell membrane [392,393]. The lack of changes in the cell membrane curvature will not cause the opening of mechanosensitive channels, leading to the elimination of cells by cell envelope degradation.

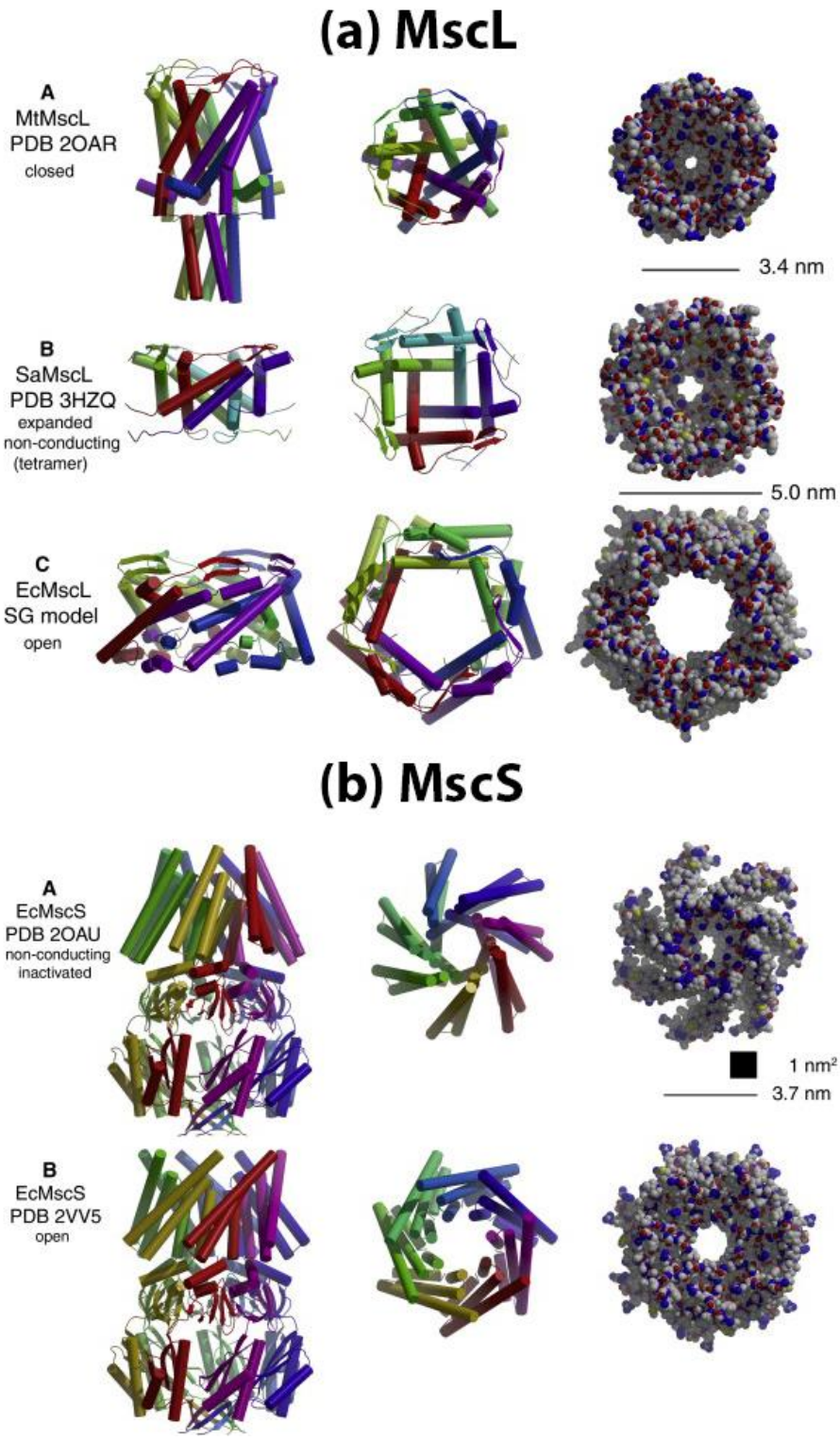

Figure 49 Mechanosensitive channels of (a) large and (b) small conductance [395].

In addition to the growth of CuO needles, the oxidized samples reveal the presence of copper ions in both possible oxidation states Cu^{1+} (Cu_2O) and Cu^{2+} (CuO). The available literature seems to indicate that the oxidation state of copper may have an influence over the antimicrobial performance of the material, but this point is still controversial. Some authors have suggested that Cu^{1+} ions are less toxic to cells than Cu^{2+} ions due to the high affinity of the latter with phosphorus- and sulphur-compounds present inside the cell [410-412]. However, the work of Hans et al. [68] on *Enterococcus hirae* (GP) deposited on pure copper, CuO and Cu_2O indicated that Cu_2O (Cu^{1+}) is more toxic than CuO (Cu^{2+}). For the oxidized samples both species are present and, compared to the as-cast sample ($Cu_{55}Zr_{40}Al_5$ at. %), their nominal composition is slightly richer in copper. The increase of available copper ions as the potential opening of the mechanosensitive channel could explain the increase in antimicrobial performance.

4.2.2 Cu ion diffusion

To better understand the changes in copper ion diffusion caused by oxidation, the number of copper ion released by the 4000 ground as-cast and oxidized samples was measured by Inductively Coupled Plasma Optical Emission Spectrometry, ICP-OES, (Table 19). After 1, 2.5 and 4 hours of contact with sterile LB broth, it can be seen that the number of copper ions released in both conditions rose steadily as the contact time increases. More interestingly, the ions were released at approximately five-fold higher concentrations in the oxidized samples (up to 1232.0 ± 368.9 ppb against the 262.0 ± 103.2 ppb measured in the as-cast alloys). The release of ions from these samples is much higher than those observed in other amorphous alloys. For example, Chu et al. [177] measured the release of copper ions from a Zr–Cu–Ni–Al amorphous thin film, obtaining values ranging from 35 ppb after 1 day of contact to 11990 ppb after 21 days of contact. The as-cast BMGCs was able to release 60.2 ppb after one hour, double than those obtained by Chu et al. [177] after one day of surface-liquid interaction. At the same time, the 1232.0 ppb measured on the oxidized sample after 4 hour of contact with the broth are comparable to the copper ion particles obtained in the Zr–Cu–Ni–Al amorphous thin film after two weeks [177]. This higher Cu ion release appears consistent with the increase in diffusion paths and the higher real area. Both BMGCs and oxidized samples present numerous grain boundaries that

are expected to facilitate the flow of copper ions to the surface of the samples, and, as such, enhance their ability to eliminate bacteria [379].

Table 19 Copper ion release (ppb) for the 4000 as-cast and 4000 oxidized samples.

		Copper ion release (ppb)	
		As cast	Oxidized
Contact time	1h	60.2 ± 60.9	320.1 ± 60.9
	2.5h	167.4 ± 64.0	992.1 ± 450.0
	4h	262.0 ± 103.2	1232.0 ± 368.9

4.2.3 Minimum Inhibitory Concentration tests

In the previous sections, the number of *E. coli* survivors were measured and correlated with the copper ions released from the surface of the as-cast and oxidized samples. In the SEM images of the deposited bacteria (Figure 48), no significant changes in their envelope were observed. As previously mentioned, the literature shows that copper killing can lead to a significant degradation of the cell membrane [392,393], but the concentration for which this phenomenon occurs is not completely understood. To clarify this point Minimum Inhibitory Concentration (MIC) tests following the procedure published in the Clinical and Laboratory Standard Institute (CLSI) approved standard M07-A9 [413] were conducted, and SEM images of *E. coli* cells in contact with several concentrations of copper (II) chloride dihydrate ($CuCl_2 \bullet 2(H_2O)$) were taken (Figure 50). MIC tests revealed that the minimum concentration of $CuCl_2$ necessary to inhibit *E. coli* in LB broth medium was 3.5 mM (222.4 mg/mL of Cu), shown by the clear liquid inside the test tubes, which agrees with the results of Santo et al. [414] and Ruparelia et al. [415]. More interesting than the quantity of copper ions to inhibit the bacteria are the changes in morphology observed as the copper concentration increases. SEM images taken for bacteria treated with 0.1 mM, 3.5 mM and 5 mM of $CuCl_2$ reveal a progressive degradation of the cell envelope. The lower concentration of copper analysed (Figure 50a) shows cells without any apparent damage, with fimbriae adhering to the steel surface and

bacteria division-taking place. When the concentration is raised to 3.5 mM (Figure 50b), the bacteria seem larger and rounder, but the clearest change in morphology is shown from those bacteria that have lost structural integrity of their envelope layers. Further increase of copper (II) chloride dihydrate to 5 mM (Figure 50c) have caused a complete lysis with no undamaged cells detected on the surface of the 314 stainless steel coupon. Punctual agglomerations of an organic substance could be seen, which are similar to an amalgam of cell membrane remains, indicating the complete disintegration of *E. coli* cells.

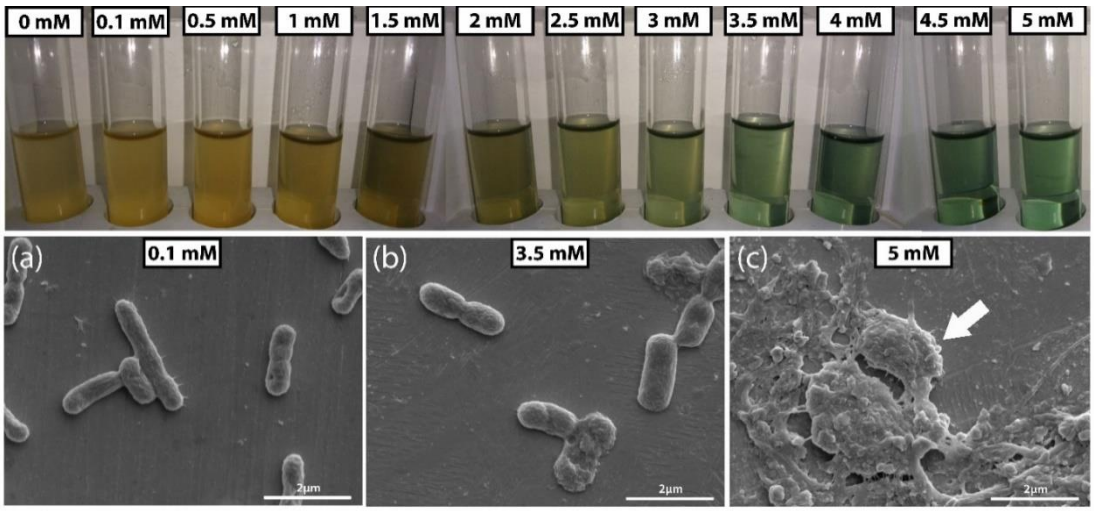

Figure 50 Minimum Inhibitory Concentration tests performed following the CLSI M07-A9 standard [413] and SEM images of *E. coli* treated with (a) 0.1 mM, (b) 3.5 mM and (c) 5.0 mM of $CuCl_2$ deposited on 314 stainless steel.

There is an interesting contrast between the ICP and MIC tests that should be discussed. The highest number of copper ions released in the oxidized samples was 1232.0 ± 368.9 ppb or approximately 0.02 mM of copper, slightly lower than the 0.1 mM used in the lowest concentration of the MIC tests. Those results (Figure 50a) indicate that cells treated with 0.1 mM of $CuCl_2$ or lower should remain alive and keep their ability to reproduce. In contrast, the antimicrobial tests reveal that the oxidized samples are able to kill the deposited bacteria, displaying a relatively high antimicrobial activity (Figure 48). To explain this apparent contradiction, it is necessary to understand the differences between both experiments. Each test tube shown in the MIC tests was inoculated with a set amount of copper compound, while

the copper concentration in the contact killing tests rises as time increases, as demonstrated by the ICP measurements. Cells dying in the MIC tests will be acting as reservoirs of copper ions, lowering the copper which can affect the remaining cells. On the other hand, the concentration of copper absorbed by dead cells in the antimicrobial tests does not reduce the availability of copper to other cells, as it is constantly renewed. Also, the cells in the MIC test are suspended in a nutrient-rich liquid medium, protecting them from stresses relating to dehydration and also allowing them significant nutritional resource that may afford them greater protection from their copper tolerance systems that actively pump copper ions out of the cell's cytoplasm. Besides this difference, it is interesting to notice the similarities in the morphology between *E. coli* cells deposited during the antimicrobial tests (Figure 48), and the results seen in the MIC tests with 0.1 mM of copper (Figure 50a). These similarities strengthen the idea that the initial steps in the contact killing process of Cu-rich surfaces are dominated by interference with homeostasis of other metals, DNA damage, and production of Reactive Oxygen Species (ROS), which modify (and thus damage) proteins, lipids and nucleic acids [407-409], rather than the sudden and catastrophic degradation of the cell envelope.

4.2.4 Antimicrobial maps

Assessing the antimicrobial properties of new materials can be a relatively simple process, however, the experiments can be time-consuming when large batches and conditions need to be analysed. In the previous sections, it was shown that the antimicrobial activity of Cu-rich materials is heavily dependent on the number of copper ions released from the surface. As such, we propose the development of "antimicrobial maps" (sketch shown in Figure 51) to ease the selection of conditions to further analyse. This chart will correlate the number of copper ions released by the material with the contact time and the reduction percentage of recovered colony forming units (CFU/mL). The map will be subdivided in several regions depending on the reduction percentage obtained (i.e. < 60 % red, 50-60 % blue, 60-99 % green and > 99 % white) and compiled into a database. Once the map has been obtained, a quick estimation of the antimicrobial behaviour of the material can be done by simply measuring the number of copper ions released after a set amount of time, simplifying the development of new materials. Other advantages of these maps will be the

possibility of selecting an antimicrobial material depending on the time for which a set elimination of bacteria is needed. Touch surfaces such as those necessary in intensive care units require the elimination of pathogens in timeframes ranging from mere minutes to a few hours. In contrast, other hospital surfaces (e.g. furniture walls) do not need such low killing times. This will ensure that the most suitable material is selected per the necessary antimicrobial activity required.

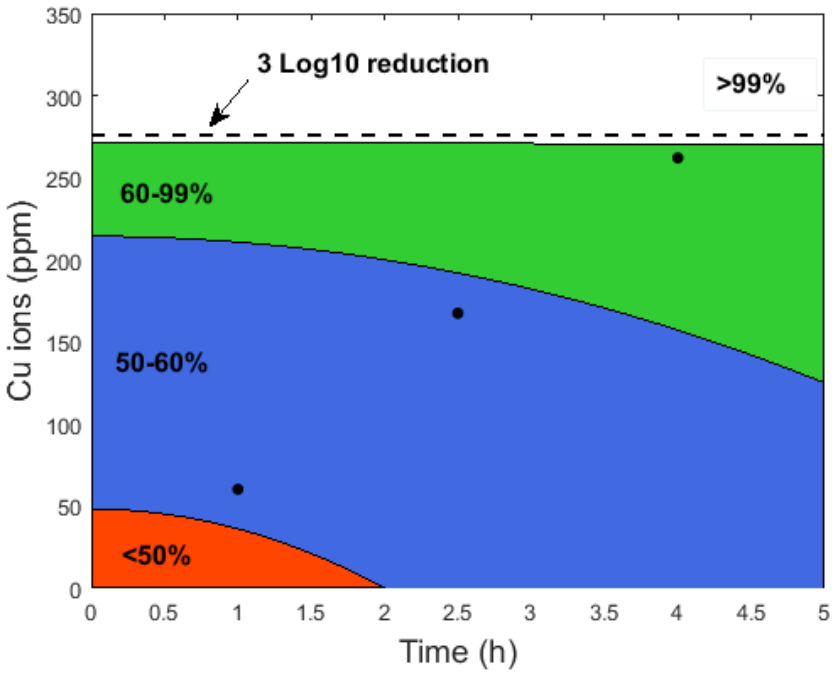

Figure 51 Sketch of an antimicrobial map for the current work: *E. coli* deposited on a BMGCs using LB broth as a growth medium.

The last use of this map will be to analyse if a material complies with the limits imposed by the United States Food and Drug Administration (3 $\log_{10}$ reduction in 1 h) [173]. Figure 51 shows a dashed line indicating the estimated number of released copper ions necessary to consider a material as antimicrobial using the US EPS protocol. For the analysed BMGCs, the diffusion of copper ions will only reach a 3 $\log_{10}$ reduction after more than four hours of contact killing, indicating that it cannot be labelled as an antimicrobial material. This method might make it possible to consider if a material meets a specific standard just by measuring the quantity of copper ions released in one hour.

Although Figure 51 shows an approximate sketch of an antimicrobial map, several points must be addressed when preparing such charts. Each map will be dependent on the pathogen deposited (e.g. *E. coli K12*) and growing broth (e.g. LB broth), as corrosion is dependent on the composition of the broth (i.e. concentration of NaCl) while different species have different Microbiologically Influenced Corrosion rates [399,416-420]. The shape of lines of constant percentage reduction (isolines) can vary as contact time increases. Materials with low release of copper ions will be unable to inhibit the growth of bacteria, revealing concave isolines caused by the division and growth of new cells, while high rates of copper diffusion may be related convex isolines, as cell division will be halted. In regards to boundary conditions, the number of copper ions necessary to immediately eliminate bacteria should tend to infinite, therefore, all isolines would be steep near the origin, and quickly stabilize as convex or concave.

4.3 Conclusions

The analysis of oxidation and roughness in the antimicrobial behaviour of a Cu-Zr-Al BMGCs has led to several interesting findings:

- In contrast to other reports, variations in the roughness of both as-cast and oxidized samples did not have an impact in the antimicrobial performance of these materials.
- Changes in composition, especially the formation of CuO and Cu_2O layers on the surface of the oxidized sample, played a major role in increasing the release of copper ions and, as such, the antimicrobial activity of the alloy. This suggests that increasing the number of copper ion diffusion paths is the main way to enhance the antimicrobial properties of the alloys (consistent with the findings exposed in *chapter 3*).
- SEM images of the bacteria treated with a copper compound revealed that cell membrane degradation can take place, but the release of copper ions for the as-cast and oxidized samples is not enough to damage the cell envelope over the time frame of these assays. As such, elimination of bacteria deposited on Cu-rich surfaces seems to be dominated by processes taking place inside the cell, rather than by cell envelope degradation.

- Finally, the creation of antimicrobial maps that, while not exact, can facilitate the development of new antimicrobial materials was proposed

5 Effect of magnetron sputtering pressure and temperature in the “wet” and “dry” antimicrobial properties of Cu-based thin films

The previous chapters have focused on analysing the influence of composition, volume fraction, roughness and oxidation in the wear and antimicrobial performance of Cu-based BMGCs. The use of BMGCs facilitated the analysis of such variables but, as shown in *section 1.2*, their applicability to high-touch surfaces is heavily restricted by the critical diameter (D_c). In contrast, thin films can be applied with relative ease to touch surfaces, conferring antimicrobial properties to cheap surfaces (i.e stainless steel) through the deposition of a thin layer of a Cu-rich alloy. Although other techniques for depositing amorphous coatings, such as electroless plating [421], can be found in the literature, the most widespread methods are vapour-depositing techniques. Magnetron sputtering is a vapour deposition technique which offers widely controllable microstructure and composition [422,423], making it possible to co-sputter binary Zr_xCu_{100-x} TFMGs in a large range of compositions (up to 80 % at Cu) [424].

The development of antimicrobial thin films containing Cu, Zn and Ag has been scarce, and the possibility of using different methodologies to estimate their antimicrobial activity complicates the comparison. During the first steps on the development of antimicrobial coatings, researchers were mainly focused on the use of silver, attributing the contact killing properties of the alloys to the release of Ag ions, practically disregarding the toxicity of copper [112,425]. As a consequence, the field of antimicrobial thin films was focused in Ag-rich or Ag-containing thin films [426]. It is true that silver has the ability to eliminate Gram-positive and Gram-negative bacteria by interaction of Ag ions with the thiol groups of bacteria proteins, affecting the replication of DNA, uncoupling the respiratory chain from oxidative phosphorylation or collapsing the proton motive force across the cytoplasmic membrane [54]. However, the antimicrobial performance is relatively low, dependent on ambient temperature and humidity [427] and is suggested to be caused by silver oxide rather than pure silver [69,73,428].

Acceptance of the outstanding antimicrobial properties of copper due to the release of toxic Cu^{1+} and Cu^{2+} ions [407-409] changed the development of biocidal coatings to Cu-rich alloys such as the Cu-Zr-Ag [426] and Cu-Ti [106] systems which are able to exhibit antimicrobial properties even with relatively low copper content (~ 30 at. %) [66,187]. In this regard, the Cu-Zr alloy system shows high GFA with interesting antimicrobial properties, but the available literature does not delve into the properties of higher Cu-content alloys (between 80 and 97 at. %) [424] and the influence of deposition temperature and pressure on their performance. Consequently, in this final chapter the possibility of developing tuneable antimicrobial coatings with high contact killing properties for their use in high-touch surfaces in healthcare furnishing will be analysed.

5.1 Structure and physiochemical properties of the deposited thin films

The aforementioned deposition variables were analysed by selecting four different conditions, varying working pressures of 0.1, 0.3 and 0.5 Pa deposited at room temperature and a batch deposited at a working pressure of 0.3 Pa and a substrate temperature of 403K. Such variables were selected as the extremes reachable in the deposition plant. Samples were deposited on both 314 stainless steel (314SS) (5 x 5 x 1 mm thick) with a surface roughness R_a < 0.5 µm and soda lime glass slides (25.4 x 76.2 x 1 mm thick). For convenience, all samples will be referred to with the batch ID shown in Table 20, where all details of the deposition conditions can be found.

Table 20 Summary of the deposition parameters used during the preparation of the Cu-Zr thin films.

Batch ID	Base pressure (Pa)	Ar flowrate (sccm)	Working pressure (Pa)	Substrate temperature (K)	Cathode power (W)	
					Cu	Zr
1RT	$5x10^{-4}$	10	0.1	R_T	200	160
3RT	$5x10^{-4}$	30	0.3	R_T	200	160
5RT	$5x10^{-4}$	45	0.5	R_T	200	160
3HT	$5x10^{-4}$	30	0.3	403	200	160

5.1.1 Roughness and microstructure analysis

Compositional analysis and profilometry measurements of all samples deposited on both stainless steel 314 (314SS) and soda lime glass slides as the average of at least 5 film samples from each batch can be found in Table 21. EDX results show a composition near the target 85/15 at. % with a slight increase in copper as the deposition pressure increases, probably caused by changes in the plasma flow between sample and target [429]. A similar thickness was achieved in all samples deposited at room temperature (between 1.02 to 1.19 µm), while the increase in deposition temperature to 403 K seems to have caused an increase in thickness, especially noticeable on the coating prepared on steel (up to 1.33 µm).

Table 21 Compositional analysis and thickness measurements of the Cu-Zr thin films.

Batch ID	Composition (at.%)		Film thickness (µm)	
	Cu	Zr	Glass	314SS
1RT	84.13 ± 0.16	15.87 ± 0.16	1.02 ± 0.02	1.12 ± 0.04
3RT	84.70 ± 0.12	15.30 ± 0.12	1.10 ± 0.06	1.07 ± 0.05
5RT	85.65 ± 0.23	14.35 ± 0.23	1.06 ± 0.06	1.19 ± 0.13
3HT	84.62 ± 0.08	15.38 ± 0.08	1.17 ± 0.10	1.33 ± 0.05

The X-ray diffraction patterns obtained from the thin films deposited on soda lime glass (Figure 52) reveal a relatively broad halo in the 35-50° range. This feature and the lack of high intensity peaks suggest a low ordered structure similar to the experiments and molecular dynamic simulations of Xie et al. [424].

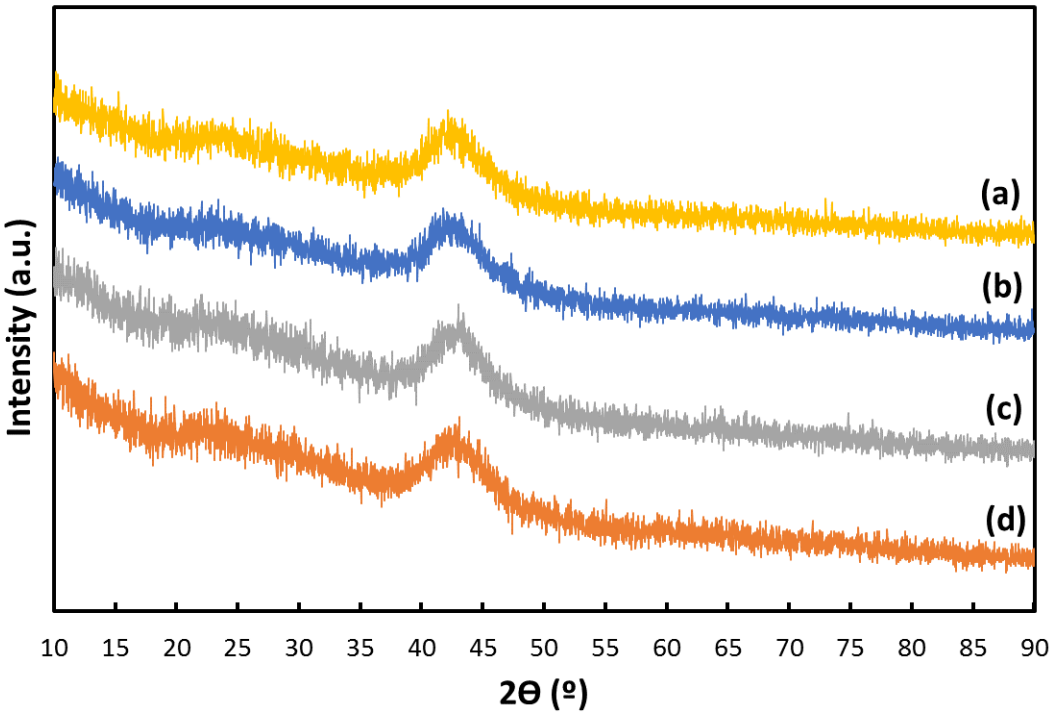

Figure 52 X-ray diffraction scans for the thin films used in the present study (a) 1RT, (b) 3RT, (c) 5RT and (d) 3HT.

To analyse the impact of pressure and temperature in the morphology of the thin films, secondary electron SEM images of the cross-section and surface of the $Cu_{85}Zr_{15}$ alloy deposited were taken (Figure 53). The superficial morphology of the films is fine-grained homogeneous except for punctual nodular growth flaws (see arrows) caused by substrate imperfections. The grains are similar in the films deposited at room temperature and common to multi component thin films due to the reduction in grain boundary scattering [430,431], but the increase in substrate temperature to 403 K caused the refinement of the grains into smaller columnar structures. More appreciable changes can be observed in the cross-section of the thin films deposited on glass. The coating prepared at room temperature and 0.1 Pa of sputtering pressure is very dense, while all other films present a porous texture dominated by voids and columns of alloy. Few differences can be seen in those films, but a slightly more fibrous structure seems to be noticed as the temperature increases [432]. All these changes are consistent with the Structural Zone Model (SZM) developed by Thornton [433]. This model shows that increasingly higher gas pressure raises the number of Ar adatoms adsorbed at the surface, lowering the mobility of

deposited atoms and causing the appearance of a porous structure. On the other hand, the mobility and bulk diffusion of the arriving atoms can be enhanced by increasing the substrate temperature, leading to more columnar grains with denser boundaries similar to that observed for the 3HT film.

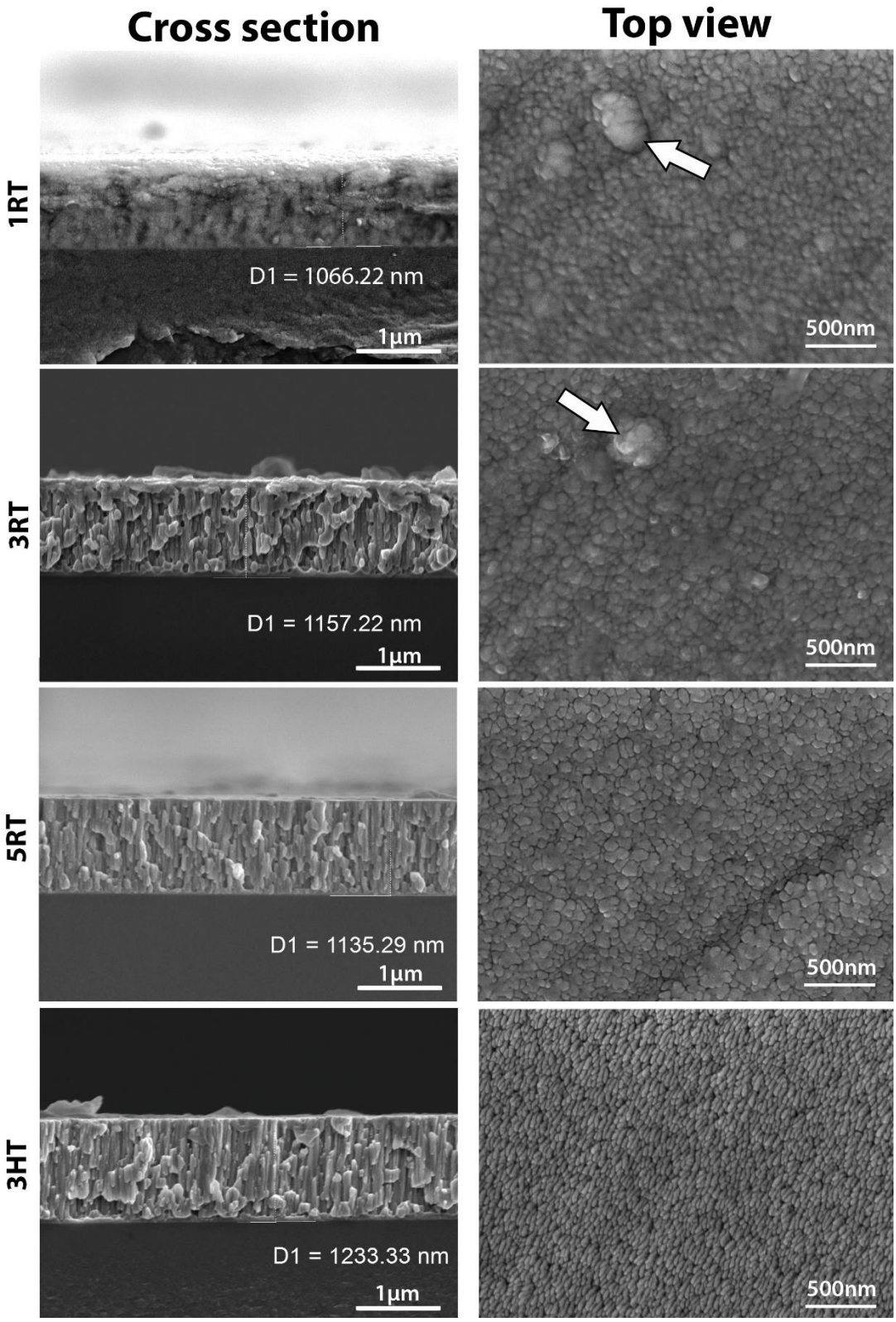

Figure 53 SEM micrographs showing the cross-section and superficial morphology of the $Cu_{85}Zr_{15}$ coating.

Figure 54 shows a depiction of the aforementioned model with four points indicating the position of these samples. This image reveals that the sample deposited at 0.5 Pa lies in Zone 1, which is defined by tapered columnar grains separated by voids [189,434]. Lower pressures and/or increasing temperatures led to Zone T or the Transition Zone, where thin films retain the columnar morphology seen in Zone 1 but with less voids and increasing compactness [189,434]. This change into a denser film is clearly observed in the 1RT sample, while the columns seen in the films deposited at 0.3 Pa (3RT and 3HT) seem wider suggesting a slightly more compact structure.

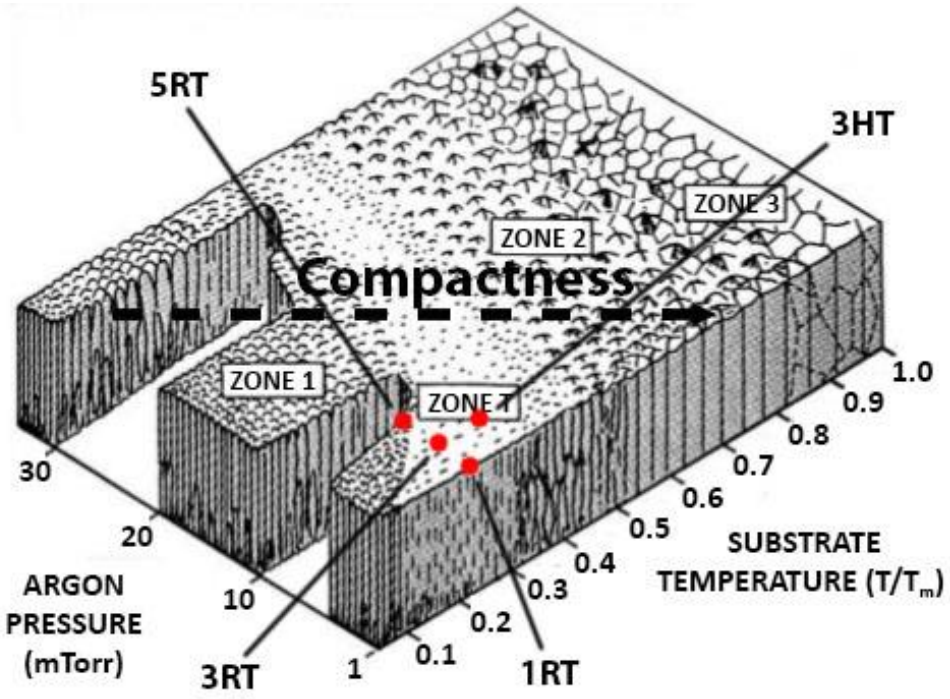

Figure 54 Depiction of Thornton's Structural Zone Model (SZM) of sputtered coatings (T_m~1333 K) [326]. Adapted from [435].

To further analyse the changes driven into the Cu-Zr thin films by differences in pressure and temperature, AFM scans were taken on the films deposited on Stainless Steel (314SS) Figure 55. The 3D images reveal a homogeneous surface dominated by small grains in all samples, while, at the same time, the roughness of the substrate can be noticed. This is consistent with sputtered thin films, as they tend to magnify the morphology of the substrate [433]. Some superficial changes can be seen when

the arithmetic average of the roughness profile (R_a) and average distance between the highest peak and lowest valley (R_z) are calculated (Table 22). Thin films deposited on soda lime glass show an average decrease in roughness (from 4.59 to 3.62 nm) as sputtering pressure and substrate temperature increase, suggesting a more compact columnar structure with less voids. On the other hand, thin films deposited on stainless steel do not display a clear trend, decreasing from 4.97 to 6.02 nm between the 1RT and 3RT samples while the roughness of 5RT and 3HT samples is similar (5.33 and 5.77 nm respectively). In this case, only the average distance between the highest peak and lowest valley (R_z) can be said to be reduced with increases in the aforementioned parameters.

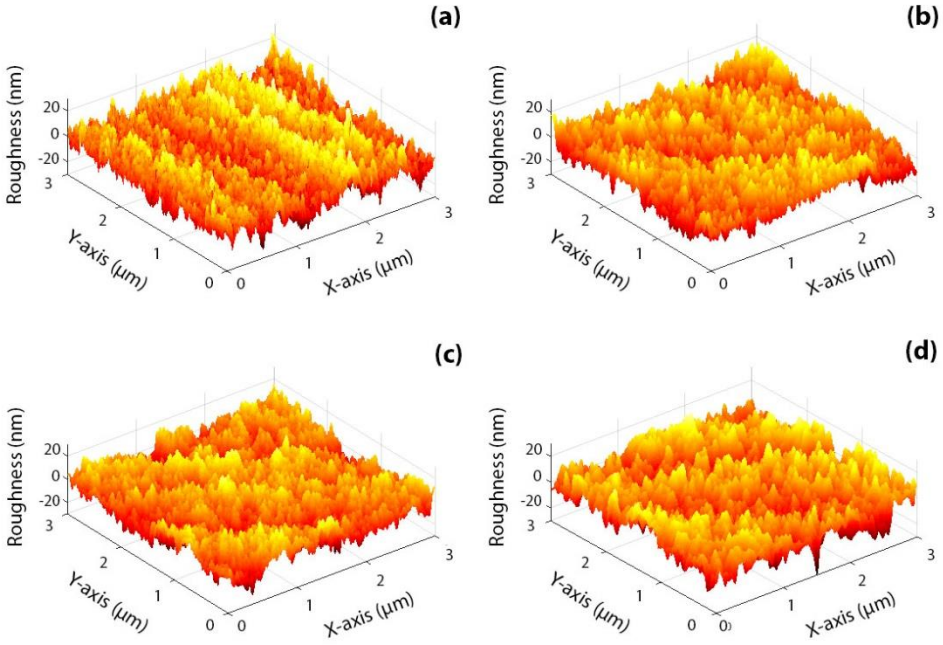

Figure 55 Atomic Force Microscope scans of the thin films deposited on steel (a) 1RT, (b) 3RT, (c) 5RT and (d) 3HT.

Table 22 arithmetic average of the roughness profile (R_a) and average distance between the highest peak and lowest valley (R_z) for the substrate and Cu-Zr thin films.

	Glass		Stainless steel (314SS)	
	R_a (nm)	R_z (nm)	R_a (nm)	R_z (nm)
Substrate	0.08 ± 0.01	0.49 ± 0.05	3.49 ± 0.38	15.83 ± 2.94
1RT	4.59 ± 0.15	25.96 ± 1.45	6.02 ± 0.44	26.39 ± 3.33
3RT	4.14 ± 0.89	19.41 ± 4.23	4.97 ± 0.34	22.46 ± 2.90
5RT	3.98 ± 0.40	17.50 ± 2.25	5.33 ± 0.63	20.79 ± 2.24
3HT	3.62 ± 0.92	18.45 ± 1.61	5.77 ± 0.70	21.74 ± 2.03

5.1.2 Wettability tests

To estimate the adhesion of bacteria to the Cu-Zr thin films [371], water contact angle measurements were performed using the sessile drop technique (Figure 56). Stainless steel coupons displayed a contact angle of 79.12 ± 4.62° which contrasts with the higher values obtained for the Cu-based coatings: 88.95 ± 3.77° (1RT), 88.70 ± 5.17° (3RT), 93.04 ± 3.39° (5RT) and 93.18 ± 5.46° (3HT). The results obtained in the wettability tests are similar to those observed in other Cu-Zr (87° to 108°) [436] or Cu-rich alloys (ZrCuNiAl, 99.5° and 104.0°) [177], but lower than those displayed by Cu-based Cu-Zr coatings (74.1°) [177]. The increase in contact angle suggests that thin film deposition may be an effective technique to change the interaction between substrate and bacteria, of great interest as discussed in *section 1.1.2*. Subtle changes can be noticed between the different thin films with a slight increase in contact angle as pressure and temperature rises. It must be remembered that hydrophobic materials (CA > 90°) have been said to prevent cell attachment [407,437], indicating that high contact angles may be preferred for the prevention of biofilm formation [397,398], while hydrophilic (CA < 90°) surfaces promote the adhesion of bacteria and may be proven beneficial in rising the antimicrobial activity of the thin films [190,425]. Taking these two ideas into account, the 1RT and 3RT should be able to trap more bacteria on their surface than the 3HT and 5RT samples, however, the high standard deviation between samples may indicate that the antimicrobial properties of all films

could be similar. Nevertheless, differences between measurements are obscured by the relatively large error ranges, suggesting that the previously described changes are not substantial.

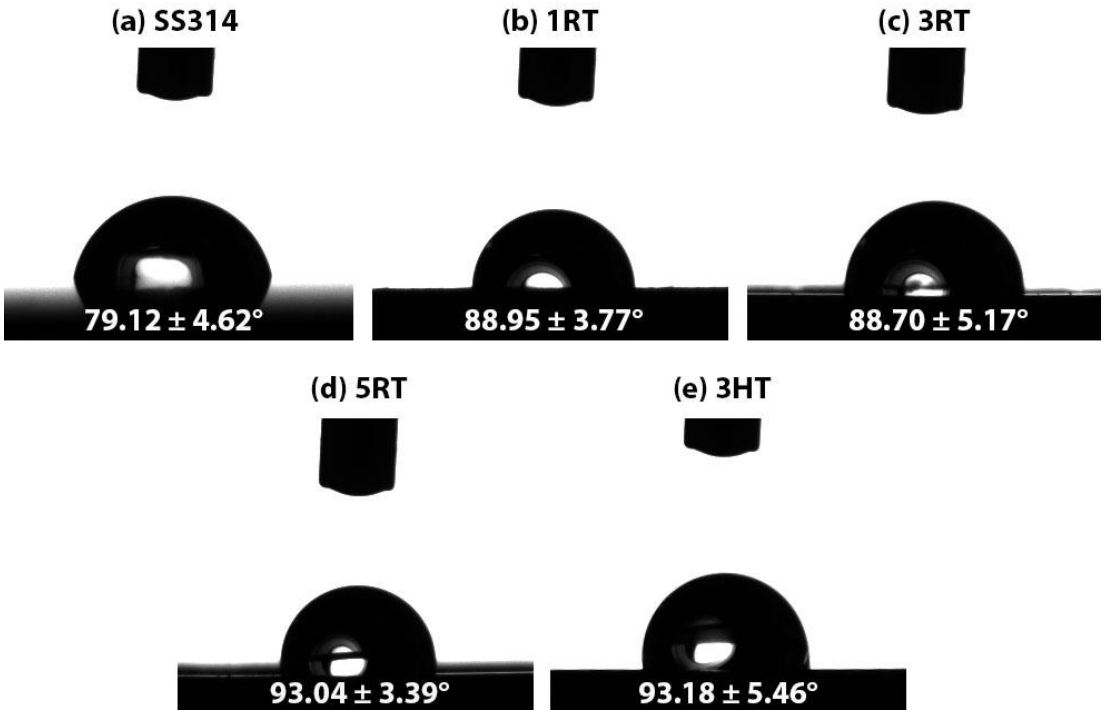

Figure 56 Water contact angle images obtained for (a) 314 Stainless Steel, (b) 1RT, (c) 3RT, (d) 5RT and (e) 3HT.

Changes in wettability during the analysis of BMGs shown in *chapter 3* were attributed to variations in composition and volume fraction. The microstructure and composition in all deposited films is similar, being only different in their superficial morphology (roughness). Kubiak et al. [438] used a combination of Wenzel's and Cassie-Baxter's theory to correlate superficial roughness (up to about 300 µm) with contact angle measurements. Their model and experiments revealed that for low roughness, increases in this parameter will lead to decreasing contact angle values until a minimum is reached. In *section 5.1.1*, it was discovered that increases in sputtering pressure and substrate temperature caused a decrease in the average roughness of thin films deposited on glass, while alloys deposited on steel displayed similar values of R_a. Only the average distance between the highest peak and lowest valley (R_z) was reduced when pressure and temperature were raised. Those samples with lower

roughness displayed higher contact angle and, therefore, it can be said that changes in morphology affected the contact angle measurements following the trend described by Kubiak et al. [438].

5.2 Antimicrobial tests, “wet” vs “dry”, a first approach to real conditions

Antimicrobial evaluation of MGs has been done through numerous methods like by measuring the area of microbe growth [425,439], by immersion of a thin film in the bacteria growth, [106,192] or using the Japanese JIS Z2801:2010 “Antibacterial products—Test for antibacterial activity and efficacy” standard [177,194]. A comparison between these antimicrobial methods reveals that all protocols involve a long-term contact between the material tested and the culture broth more similar to those observed in catheters or drainages. Contact between a liquid medium and a metallic surface will lead to the oxidation and degradation of the surface. The mechanism that confers copper its high antimicrobial performance is still not completely understood (i.e. cell membrane interference, DNA degradation, reactive hydroxyl radicals generated in Fenton-type reactions) [58,408,440], however, it is commonly accepted that the killing of bacteria is correlated with the exposure to copper ions such as Cu^{1+} and Cu^{2+} [410-412]. A change in the physicochemical properties of the material tested driven by the “wet” conditions imposed in the antimicrobial tests will have a direct impact on the results. Surprisingly, the number of papers focusing on this aspect is scarce [61,63,441], especially when the “natural” conditions of bacteria deposited on high-touch surfaces for applications in healthcare facilities involve dry surfaces and some antimicrobial materials fail when exposed to “in situ” analysis [94]. Thus, in the following sections a comparison between antimicrobial tests in “wet” and “dry” conditions will be performed, paying great importance to the influence of drying of the material tested and the bacteria selected.

5.2.1 Influence of drying in the bacteria recovery

The first step to compare the antimicrobial activity of samples tested in both “wet” and “dry” conditions is to assess if the change in methodology could influence the number of bacteria recovered. For this purpose, *E. coli* and *S. aureus* cells were inoculated

on stainless steel (SS 314) coupons, recovered and plate counted after 0, 15, 30 and 45 min of “dry” contact time (Figure 57). Stainless steel is a material which lacks any antimicrobial activity, however, the number of recovered bacteria was reduced in both Gram positive and Gram negative species. This is particularly concerning for the *E. coli* cells which display a 5 $\log_{10}$ reduction, enough to consider it as an antimicrobial material through US EPA standard. Normally, Gram positive bacteria (e.g. *S. aureus*) can endure desiccation better than Gram negative bacteria (e.g. *E. coli*) [442]. Differences in the peptidoglycan situated in the outer layer of both Gram negative bacteria (*E. coli*) and Gram positive bacteria (*S. aureus*) may have enhanced the resistance of *S. aureus* to drying, while the cell membrane of *E. coli* is unable to shield these cells from the effect of drying [43]. Although other variables should be considered, like an increase in adhesion between sample and bacteria due to adaptive responses to changes in the environment, (i.e. synthesis of adhesion molecules).

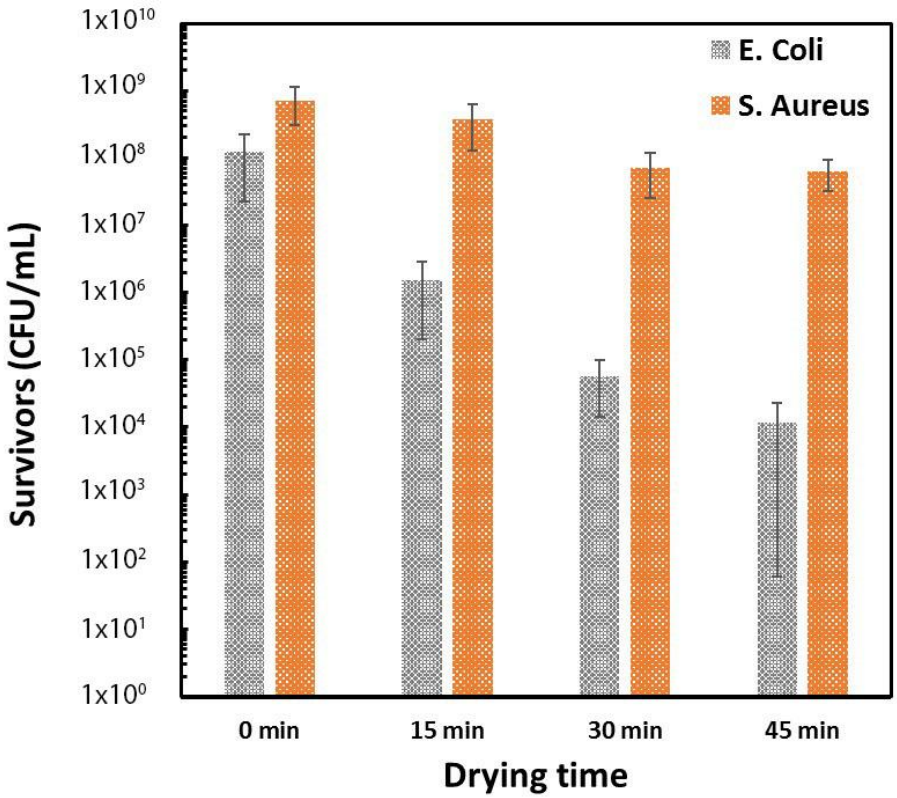

Figure 57 Number of *E. coli* and *S. aureus* Colony Forming Units per millilitre recovered from stainless steel in “dry” after 0, 15, 30 and 45 min of contact time.

The effect of air drying on the morphology of *E. coli* and *S. aureus* is not completely understood [443,444]. For this reason and to complement the results displayed in Figure 57, both *E. coli* and *S. aureus* cells were deposited on stainless steel coupons using “wet” and “dry” methods and observed through SEM (Figure 58). The *E. coli* cells deposited using “wet” conditions display a smooth surface with small bumps and valleys on the outer membrane layer (Figure 58a). In contrast, the air-drying has caused the shrivelling of the cell envelope with slight changes in size (Figure 58c). The length of both sampled cells is similar, about 2.5 µm, but a slight decrease in width can be observed between the former (~0.7µm) and the latter (~0.5 µm) caused by the different conditions of inoculation.

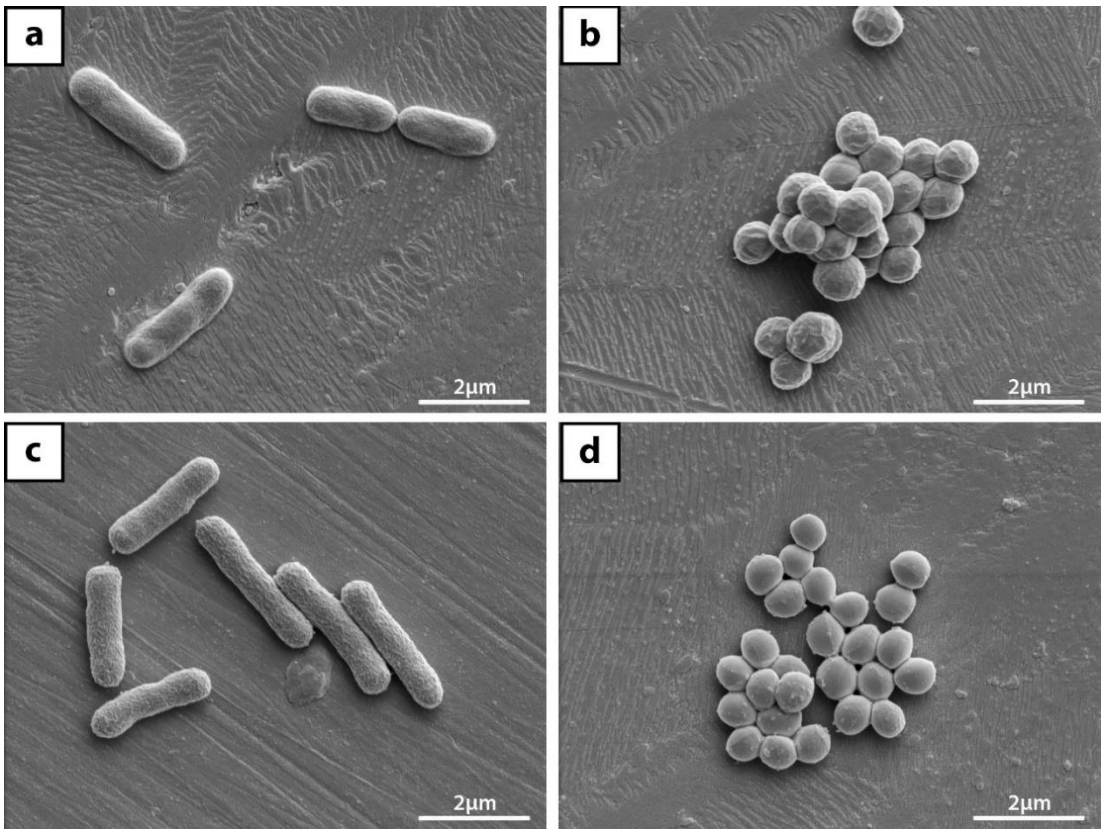

Figure 58 SEM images of “wet” (a,b) and “dry” (c,d) *E. coli* and *S. aureus* cells deposited on stainless steel after 1 h.

On the other hand, the influence of air-drying on *S. aureus* cells is more subtle. Bacteria deposited using the “wet” methodology (Figure 58b) show a relatively rough surface, while dried cells are smoother (Figure 58d). Umeda et al. [445] analysed *S.*

aureus via TEM, their images showed a fuzzy layer on the cell envelope of these bacteria, which was attributed to be an agglomeration of fine fibres of teichoic acids and proteins. Further investigation of this layer revealed that if damaged (i.e. during fixation of the cells) it can be removed during bacteria processing. Consequently, the rough outer layer seen in the undried cells could be this agglomeration of fine fibres, while drying has caused the damaging of such a feature removed during the chemical fixing for SEM imaging.

To assess the influence of culturing liquid drying, stainless steel coupons were inoculated with sterile LB broth, air-dried and analysed using SEM imaging (Figure 59). The surface is rich in dendritic crystals, branching up to 500 µm, and a chemical composition of $C_{60.0}Cl_{14.2}Na_{13.9}O_{8.6}Zn_{0.5}Cu_{0.4}K_{0.2}P_{0.2}Fe_{0.2}S_{0.1}$. Taking into account the EDX measurements and the chemistry of the Luria Bertani broth used in this work (Peptone 10 g/L, Yeast 5 g/L, and NaCl 5 g and Agar 12 g/L), the dendrites will likely be the result of Sodium Chloride and other components crystallizing during the air-drying of the aqueous solution. The appearance of these crystals coupled with changes in osmotic pressure during and after drying may be the reason behind the decrease in viable cells seen in Figure 57, especially as high concentrations of NaCl can act as an antimicrobial and preservative for both *E. coli* and *S. aureus* [446]. As mentioned before, *S. aureus* can endure desiccation better than Gram negative bacteria (e.g. *E. coli*) [442], which explains the higher number of recovered *S. aureus* cells during desiccation, and, consequently, a careful selection of culture broth (i.e low sodium content) has to be done to develop reliable antimicrobial “dry” tests for Gram negative bacteria.

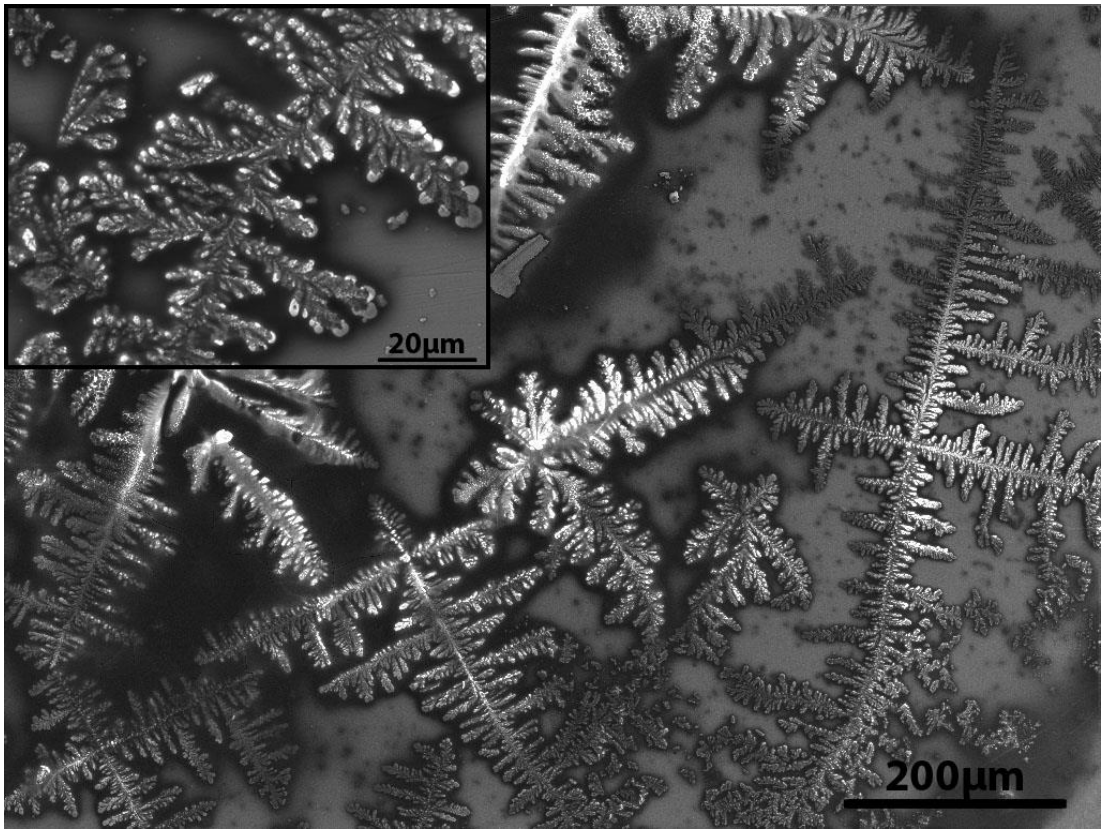

Figure 59 SEM image showing the presence of NaCl crystals after the drying of LB broth.

5.2.2 "Wet" and "dry" tests

The initial purpose of this chapter was to analyse differences in the number of recovered *E. coli* and *S. aureus* bacteria in both "wet" and "dry" conditions. Although it is possible to recover *E. coli* cells reliably in "wet" conditions for the most extreme contact time (Figure 60), the elimination of most *E. coli* bacteria during air-drying (see *section 5.2.1*) made it impossible to develop a reliable comparison. Antimicrobial tests for *E. coli* bacteria deposited in "dry" conditions were performed several times in the 1-4 hour timeframe, but all agar plates were devoid of any colony. Consequently, antimicrobial tests were only performed for the Gram positive bacterium selected (*S. aureus*), but all bacteria (GP and GN) deposited in "wet" and "dry" conditions will be analysed using SEM and TEM imaging.

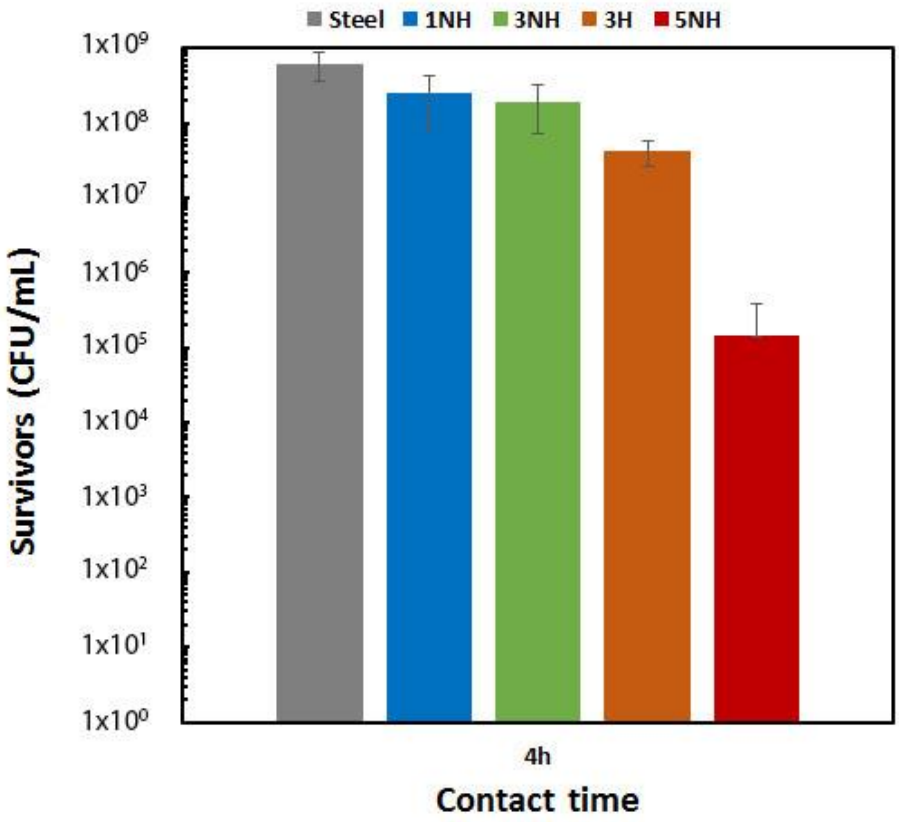

Figure 60 Number of *E. coli* Colony Forming Units per mL (CFU/mL) recovered in "wet" conditions after 4 h of contact time.

Figure 61 shows the number of *S. aureus* CFU/mL recovered in "wet" and "dry" conditions for 1, 2.5 and 4 hours of contact time. The number of bacteria recovered from the stainless steel (314SS) controls is practically constant during all timeframes, but the quantity of *S. aureus* cells diminishes between wet and dry conditions, from ~ $3x10^8$ CFU/mL in "wet" to ~ $5x10^7$ CFU/mL in "dry", after 2.5 h of contact. This reduction can be correlated with that observed in the previous section as a consequence of air-drying, which has to be accounted for in order to obtain antimicrobial activity and percentage reduction values which are only caused by the exposure to copper ions.

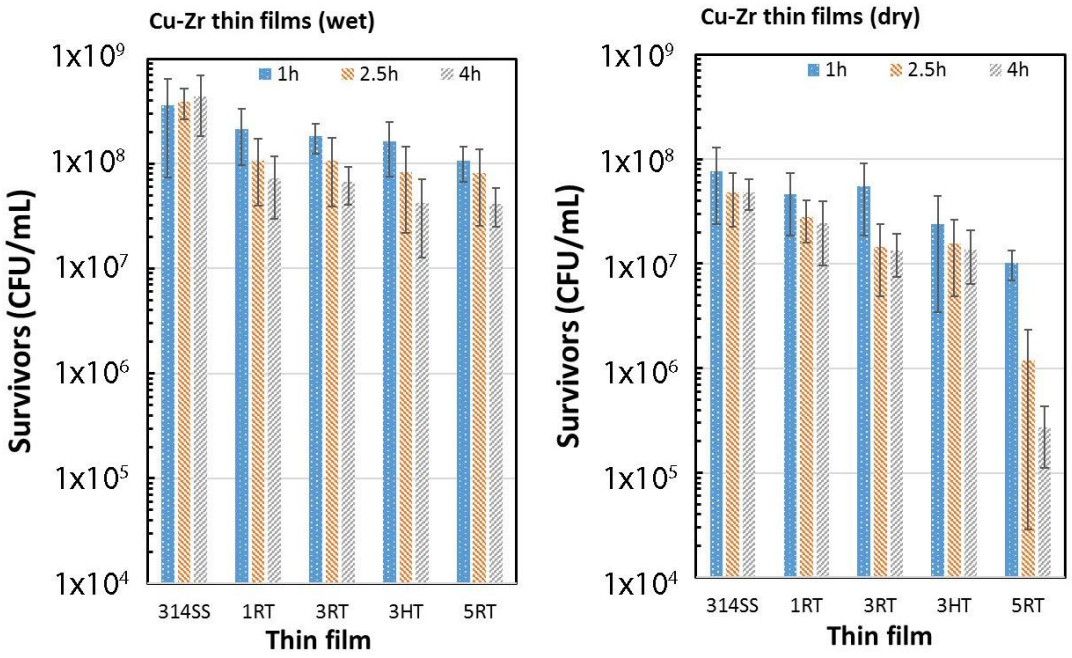

Figure 61 Number of *S. aureus* Colony Forming Units per mL (CFU/mL) recovered in "wet" and "dry" tests after 1, 2.5 and 4 h of contact with stainless steel and the Cu-based thin films.

The antimicrobial performance of thin films tested in "wet" conditions is similar during the first hour of contact (~$2x10^8$ CFU/mL) with further elimination of bacteria as the contact time increases. This reduction is comparable in the 1RT and 3RT films for the next times analysed, but the antimicrobial activity of both 3HT and 5RT coatings is slightly higher, with about ~ $3x10^7$ CFU/mL remaining after 4 h. The overall performance of samples analysed in "dry" conditions is comparable to those observed in the "wet" tests, however, the number of recovered bacteria is much lower in all conditions analysed (a consequence of air-drying). The thin film deposited at 0.1 Pa (1RT) still displays the highest number of recovered cells (~ $2x10^7$ CFU/mL), although, 3RT has a level of recovered bacteria similar to that of 3HT (~ $1x10^7$ CFU/mL after 4 h of contact killing). The most noticeable difference between the films deposited in the "dry" and "wet" tests comes from the outstanding antimicrobial behaviour of the 5RT sample, reaching a minimum of $2x10^5$ CFU/mL.

The number of recovered bacteria estimates the antimicrobial behaviour of the samples, nevertheless, to better assess this property, the antimicrobial activity (Table

23) and the reduction percentage (Table 24) were calculated using the Japanese JIS Z2801:2010 “Antibacterial products—Test for antibacterial activity and efficacy” and the American US EPA “Protocol for the Evaluation of Bactericidal Activity of Hard, Non-Porous Copper Containing Surface Products” standards (see *section 1.1.4*). These two parameters are similar in that they give an estimation of the antimicrobial performance, but the antimicrobial performance uses a more accurate logarithmic scale, log_{10} reduction, while the American standard use a more intuitive % reduction. Therefore, both parameters were calculated and compared.

Table 23 Antimicrobial activity of the thin films obtained as stated in **JIS Z 2801:2010** “*Antibacterial products—test for antibacterial activity and efficacy*” [171].

Sample	Antimicrobial activity					
	Wet			Dry		
	1h	2.5h	4h	1h	2.5h	4h
1RT	0.23	0.56	0.77	0.22	0.23	0.29
3RT	0.30	0.56	0.81	0.15	0.53	0.55
5RT	0.53	0.68	1.02	0.88	1.61	2.25
3HT	0.35	0.67	1.01	0.51	0.49	0.54

Table 24 Percentage reduction of the thin films obtained as stated in **U.S. EPA** "*Protocol for the Evaluation of Bactericidal Activity of Hard, Non-Porous Copper-Containing Surface Products*" [173].

Sample	Percentage reduction					
	Wet			Dry		
	1h	2.5h	4h	1h	2.5h	4h
1RT	28.14	56.87	74.66	12.02	64.09	51.09
3RT	33.78	60.02	80.40	18.41	83.07	73.91
5RT	61.55	67.82	83.90	94.50	99.20	99.47
3HT	45.63	65.90	83.15	70.00	75.98	74.16

For the "wet" tests, the antimicrobial activity and percentage reduction exhibited by the deposited thin films rises as the contact time increases, but these values are relatively low (between 0.77 and 1.02 $\log_{10}$ reductions and percentage reductions between 74.66 % and 83.90 %) and is consistent with the low order structure of these films. Higher antimicrobial behaviour can be seen in the literature but, as mentioned before, the timeframes normally used in those papers are much longer (i.e. 24 h), limiting their applicability as biocidal touch surfaces [194,426]. The rise in both antimicrobial activity and percentage reduction is related to changes in processing pressure and temperature, as an increase in both, led to optimized antimicrobial performance in "wet" conditions for the 3HT and 5RT coatings. These enhanced antimicrobial properties strengthen the idea proposed by Chiang et al. [425] that not only composition can alter the antimicrobial performance of thin films, but that the deposition parameters influence their antimicrobial properties.

A similar trend can be observed in the "dry" tests. The lower antimicrobial activity (between 0.29 to 0.55 $\log_{10}$) and percentage reduction (between 51.09 % and 74.16 %) are displayed by films deposited at low temperatures and pressures (1RT and 3RT), and comparable values for the heated sample (0.54 $\log_{10}$ or 74.16 % reduction). In contrast, the coating deposited at 0.5 Pa shows much higher antimicrobial rates

(2.25 $\log_{10}$ or 99.47 % reduction), analogous to those reported for other Zr-Cu-based thin films after 24 h of contact killing [426]. The optimal performance of the 5RT film can be correlated with the lower compactness indicated by Thornton's structural zone model (Figure 54) [433]. The 1RT is the denser film, which should lead to lower copper ion diffusion, and is consistent with it exhibiting the poorest antimicrobial performance of all thin films prepared. Increases to both processing temperature and pressure (3RT and 3HT) caused a decrease in compactness, facilitating the movement of copper ions into the deposited bacteria; maximum in the 5RT film. Finally, a comparison between the antimicrobial activity or percentage reduction in "wet" and "dry" conditions reveals that although the reduction of colony forming units is higher in the latter, the overall antimicrobial performance of tests developed in "wet" conditions are higher. These results seem to contradict the findings of Warnes et al. [61,63] who suggested that drying tests could enhance the copper ion intake of bacteria.

5.2.3 Copper ion diffusion of Cu-Zr thin films

To better understand the relationship between deposition parameters and antimicrobial properties ICP-OES measurements of thin films produced under the two most extreme conditions (1RT and 5RT) were taken in both "dry" and "wet" conditions (Table 25). The release of copper ions is always higher in the thin films deposited at 0.5 Pa (i.e. maximum of 1088.13 ± 305.19 ppb after 4 h in "wet" conditions), agreeing with the lower compactness of the film suggested by Thorton's model (Figure 54). In all cases, the measured copper ions increase with the contact time, but there are differences between tests carried out on "wet" and "dry" conditions. For the 1RT thin film, the number of copper ions in "wet" conditions is lower than those measured in "dry" conditions (i.e. 132.60 ± 49.89 ppb in the former and 262.21 ± 81.34 ppb in the latter). However, after 4 h of contact this trend reverses, with higher copper ion release in the "wet" conditions (i.e. 349.51 ± 139.37 ppb in the former and 270.45 ± 74.40 ppb in the latter). In contrast, the 5RT sample always displays higher diffusion of copper ions in "wet" conditions, probably caused by superficial damage promoted by the sodium chloride present in the broth. Similarly to *section 4.2.2*, the mobtained measurements are much higher than those reported by Chu et al. [177] (i.e. 45 ppb after 24 h of contact). However, the copper content of our samples is 85 at. %, while

for the Zr-Cu-Ni-Al alloy deposited in the aforementioned paper the maximum copper content is 30 at. %.

Table 25 Copper ion release (ppb) for the 1RT and 5RT thin films

	Contact time			
	1h		4h	
Condition	wet	dry	wet	dry
1RT	132.60 ± 49.89	262.21 ± 81.34	349.51 ± 139.37	270.45 ± 74.40
5RT	841.43 ± 267.77	632.24 ± 192.22	1088.13 ± 305.19	934.97 ± 103.77

5.2.4 Influence of Cu-Zr thin film contact in the internal and external morphology of bacteria

S. aureus cells were deposited on the 1RT and 5RT samples for 4 h (minimum and maximum antimicrobial activity, respectively) in both “wet” and “dry” conditions and analysed using SEM to ascertain the influence of contact killing in the bacterial morphology (Figure 62). The changes in outer envelope are subtle with a round rough surface in the bacteria deposited on the 1RT sample in “wet” conditions (Figure 62a) which becomes slightly smoother after 4 h of contact in “dry” conditions (Figure 62c). A similar change, but more pronounced, can be noticed in cells deposited on the 5RT sample in “wet” (Figure 62b) and “dry” (Figure 62d) conditions. The lack of morphological changes such as flattening, pitting and lysis is of great interest, as those had been reported to be indicators of copper ion damage to bacteria [447,448] and one of the mechanisms proposed to cause the death of bacteria in contact with this element (*section 1.1.2*). The low contact timeframes used in this study (1, 2.5 and 4 hours) are evidently not long enough to cause any substantial change to the cell envelope, but the antimicrobial tests show a reduction in colony forming units. Consequently, the antimicrobial mechanism dominating the killing rates of bacteria deposited in the current conditions seems to be more likely correlated with the diffusion of copper ions into the cell and internal damage.

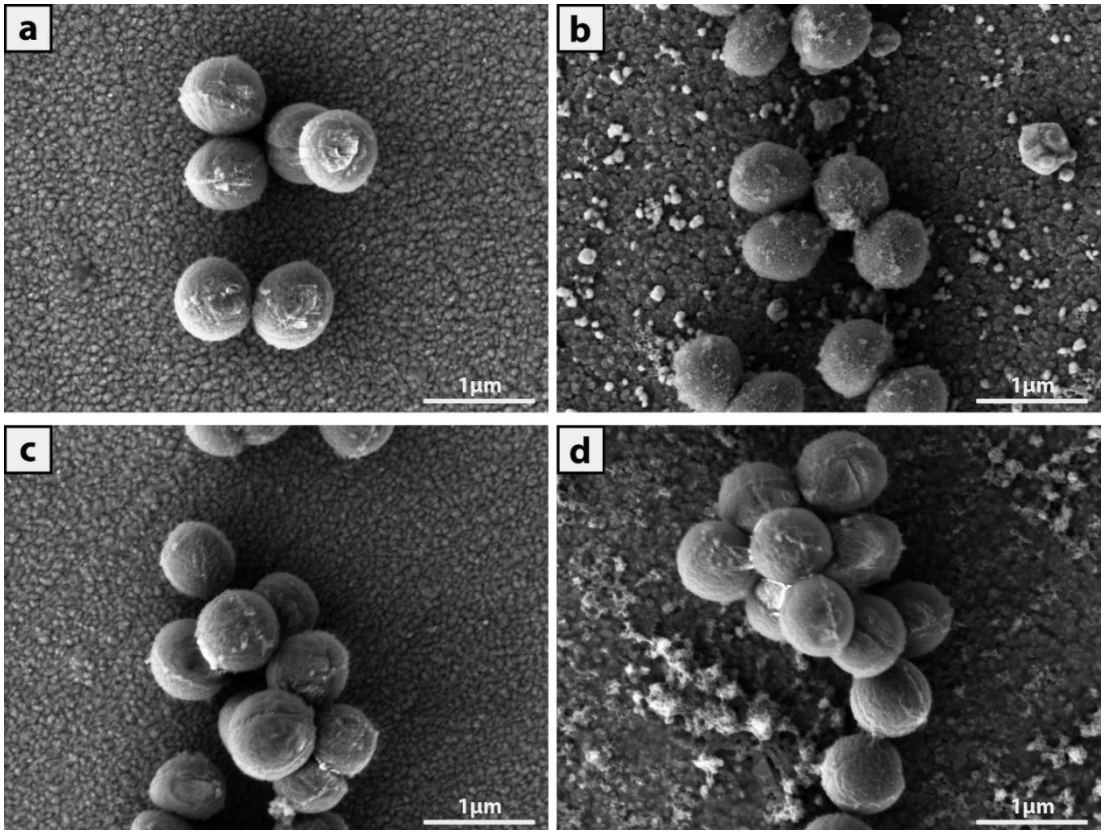

Figure 62 SEM images of *S. aureus* deposited for 4h on 1RT in a) “wet” and c) “dry” conditions and 5RT in b) “wet” and d) “dry” conditions.

To better understand the morphological changes driven by Cu-based thin films to *E. coli* and *S. aureus* cells, TEM images of bacteria recovered from stainless steel coupons and the film deposited at 0.5 Pa (5RT) in “dry” conditions were taken (Figure 63). *E. coli* cells deposited on steel display an undamaged envelope similar to that observed in other TEM analysis [449]. In contrast, deposition of these bacteria on the Cu-based coating has caused partial lysis (i.e. disintegration of a cell by rupture of the cell wall or membrane) while some dark spots can be seen inside the cells, which may be the consequence of copper oxidising [392,450]. The untreated (Figure 63b) and treated *S. aureus* (Figure 63d) do not display any great morphological difference, in agreement with the SEM images previously observed (Figures 58b and 58d), but air-drying and copper diffusion seem to have caused a slight detachment of the cytoplasmic membrane with a clear decolouration surrounding the inner side of this membrane.

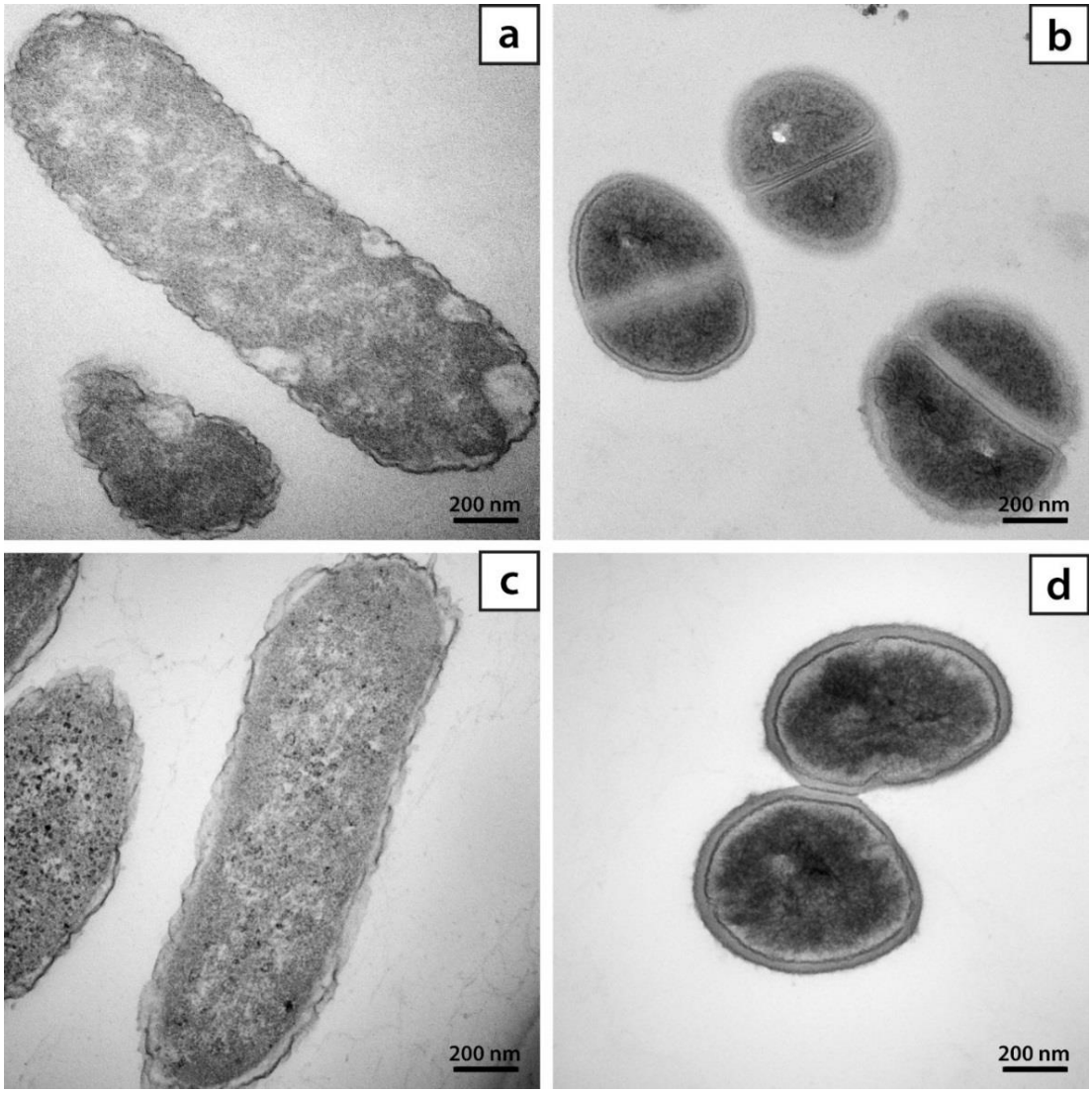

Figure 63 TEM images of *E. coli* and *S. aureus* deposited for 4 h on Stainless Steel (a, b) and the 5RT thin film (c, d).

Reports of contact between copper-rich surfaces and *E. coli* commonly shows damage to the cell's envelope [192,392,393], but most of these reports involve the use of copper nanoparticles, while SEM [192] or Fluorescence microscopy [63] are preferred to analyse Cu or Cu-based surfaces. This damage usually comes in the form of pits, cavities and loss of its natural rod shape, but as previously mentioned, most of the analysis involve high contact times. This progressive damage to the envelope is similar to that reported in Gram positive cocci bacteria (e.g. *Streptococcus mutans*) [451], but in a similar way, *S. aureus* cells are mostly analysed through SEM imaging [447,448] and Fluorescence microscopy [448,452], for much longer

timeframes. Most of the previously cited reports normally link the cell envelope damage to dead cells, but such large timeframes do not clarify if changes in morphology occurred before or after the cell was killed. Thus, copper exposure may have killed the bacteria first, while the external damage occurred after, when the concentration of copper ions was much higher. The literature shows that the antibacterial effect of copper can be caused by several mechanisms, such as, cell membrane interference, DNA degradation or reactive hydroxyl radicals generated in Fenton-type reactions [440]. The TEM images previously discussed seem to suggest that punctual degradation of the cell envelope (partial lysis) would have increased the inflow of copper ions into the cell, oxidizing inside the bacteria. This strengthens the idea that copper ions alter the permeability of cellular membranes and destabilize the outer cell wall by degrading its amino acids and proteases [392,393], but here the killing of bacteria is not primarily caused by this process and its more likely related with DNA degradation, reactive hydroxyl radicals generated in Fenton-type reactions and the high affinity of Cu ions with phosphorus- and sulphur- containing compounds situated in the inner part of the cells [177,440,453]. At the same time, *S. aureus* is more resistant to damage caused by copper due to their morphology, the ability to agglomerate and the numerous mechanisms available to resist environmental copper [454]. Consequently, it is reasonable to think that apparent cell damage will be more noticeable in *E. coli* rather than *S. aureus*, explaining the SEM and TEM results.

5.2.5 Impact of bacteria deposition in the morphology of the films

The influence of contact killing in *S. aureus* morphology has been analysed in the previous section, however, the changes inflicted upon the coatings due to contact with an aqueous solution rich in NaCl and living organisms required study. For this reason, SEM images of all thin films before and after 4 h of contact killing in both “wet” and “dry” conditions were taken (Figure 64). The surface of 1RT, 3RT and 3HT coating seems mostly unchanged, suggesting a limited impact in the chemistry of the films driven by the contact with LB broth. However, the 5RT thin film displays a rougher surface filled with protrusions undetected in the as-prepared film. Similarly to most “wet” samples, the 1RT surface is practically equal to the untested sample, but all other samples had suffered morphological changes. For the 3RT sample, the presence of small “islands” of oxidized material can be observed, increasing the

overall roughness of the sample. On the other hand, both 3HT and 5RT display cracks, but the latter includes large particles which may be oxidized material detached from the surface due to internal stresses.

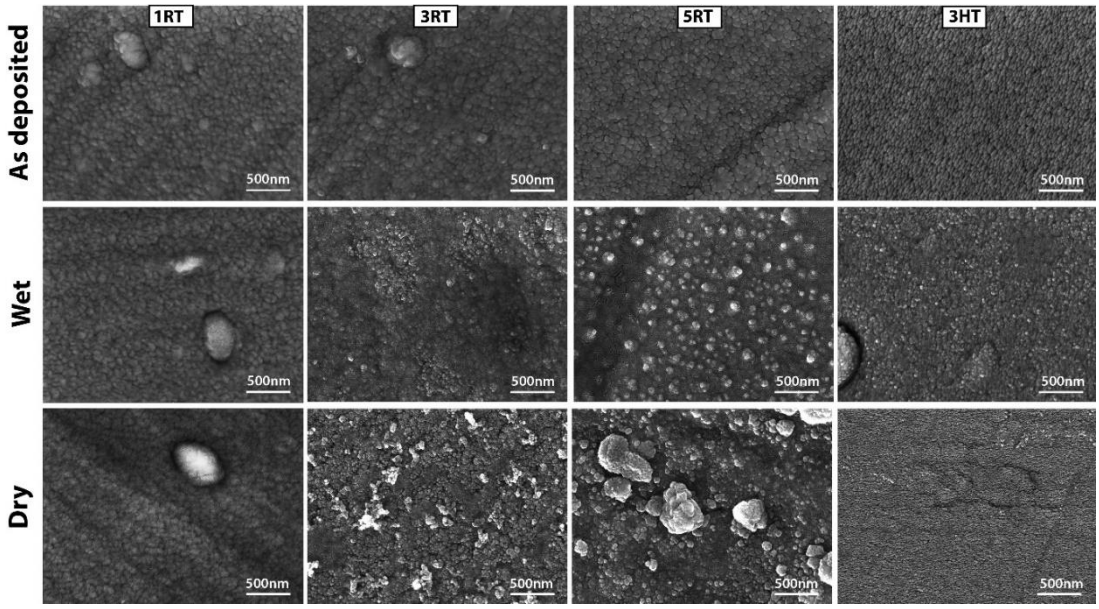

Figure 64 SEM images of the Cu-Zr thin films after 4 h of contact with the LB broth in "wet" and "dry" conditions.

The corrosion of Cu-Zr alloys is a complex process where ZrO_2 will be formed preferentially over CuO [417]. In Cu-Zr thin films where the copper content is much higher than Zr, the rearrangement of copper will lead to the formation of a protective Cu-rich layer [416,455]. Although relatively stable, the passivation of the protective layer has been shown to be highly dependent on the chemical composition of the aqueus solution. Bouala et al. [426] and Etiemble et al. [193] analysis of Cu-based thin films suggests that Cl containing media, such as the broth used in the preparation of antimicrobial tests, can cause the depassivation of the thin film surface, further increasing the flow of ions into the deposited bacteria. Lu et al. [399] have shown that the degradation of this Cu-rich layer can only take place when the anodic potential is higher than the equilibrium potential of Cu/Cu^{2+} (e.g. +0.337 V) [389]. The presence of Cl^-allows the formation of a slightly soluble porous film of CuCl following the corresponding Nenst equation ($E = -0.105 - 0.059 \cdot \log[Cl^-]$) [399]. The concentration of Cl^- ions for the Luria Bertani used in this study is 5 g/L of NaCl or 0.141 mol/L of Cl^-,

which returns an anodic potential of -0.055 V. Consequently, the corrosion of Cu will be heavily enhanced by the presence of Chlorine.

The morphological changes displayed by the films are similar to those reported in the literature as signs of corrosion due to the presence of chlorine salts in Cu-based thin films [193,426]. Taking into account the results of the antimicrobial tests, the superficial changes observed in Figure 64 and Thornton's Structural Zone Model (SZM), the increase of antimicrobial properties with higher substrate temperatures and chamber pressures seems likely to be caused by a slight degradation of the film due to the content of NaCl in the culture media. The compactness of the 1RT film will complicate the interaction between LB broth and surface, while this interaction is easier in those films with a structure dominated by tapered columnar grains separated by voids.

5.3 Conclusions

There are several important discoveries that have been described in the present chapter:

- Changes in the deposition parameters such chamber pressure and substrate temperature cause slight differences in the structure of the films (i.e. roughness and compactness). These differences in morphology are into agreement with Thorton's structural zone model and even low variations in the deposition parameters cause detectable differences in antimicrobial performance.
- Tests developed in both "dry" and "wet" conditions do not display, overall, great differences, but the evaporation of LB broth led to the crystallization of NaCl crystals and other chemicals present in the aqueous solution which influenced the deposited bacteria and the thin film. These changes were more noticeable in the "dry" tests and especially in the *E. coli* cells, making it not possible to recover any Gram negative bacteria.
- Changes in compactness were especially relevant in the 5RT films, which displayed higher antimicrobial activity in "dry" conditions. This was correlated with the higher influence of Chlorine in the surface of this film which increased

the diffusion of copper ions, thus enhancing the copper intake of bacteria deposited on the 5RT sample.

- SEM and TEM images of *S. aureus* and *E. coli* revealed limited damage to the outer membrane, more noticeable in the Gram negative cells. This lack of outer damage and the apparition of dark particles in the inside of *E. coli* cells in contact with the Cu-Zr thin film suggests that the primary mechanism of bacteria elimination for low contact times is related to the diffusion of copper ions into the cell and inner damage.

6 Summary and future directions.

Nosocomial infections are a threat to modern society with heavy human and economic consequences. To prevent pathogen colonization and reduce infections in healthcare facilities, copper has been the most extensive natural antimicrobial metal researched, but its poor mechanical properties and chemical stability render its long term use as doubtful. In contrast, we proposed the use of Cu-based metallic glasses and metallic glass composites due to their remarkable wear and corrosion resistance, but the antimicrobial properties of such materials are mostly unknown. For their use in touch surfaces, it is necessary to comprehend the parameters affecting their performance in the sort and long term. To fill this gape in knowledge we aimed to understand:

- The role of volume fraction in both wear and antimicrobial properties of Cu-based BMGCs.

- Surface finish (i.e. roughness) and oxidation influence in the biocidal capabilities of such materials.

- The possibility of developing high copper content TFMGs and tuning their properties through changes in the deposition conditions (i.e. pressure and temperature).

- Analyse the differences between “wet” and “dry” antimicrobial tests and their relation to real in site conditions.

- The mechanisms behind the contact killing of BMGCs and TFMGs in Gram Positive (i.e. *Staphylococcus aureus*) and Gram Negative (i.e. *Escherichia coli*) bacteria.

The experimental work developed in this thesis focused in this gap in knowledge, leading to several interesting findings. Our contribution to the research community can be summarized as:

- Composition and volume fraction of crystalline phases can be tuned to enhance the antimicrobial properties and wear resistance of Cu-based BMGCs, but volume fraction was more effective drastically increasing both properties when the percolation threshold (~ 50 %) is reached.

- Although greater antimicrobial performance is achieved for highly crystalline MGC, the increase in crystallinity can led to a deterioration of the material through corrosion, as the grain boundaries can act as galvanic pairs. At the same time, caution must be taken as the wear resistance of these samples can be compromised due to further wear of detached hard crystalline phases. This indicates that the percolation threshold is the optimal point to valance wear, antimicrobial and corrosion behaviour.

- Changes in roughness showed a relatively low impact in the antimicrobial behaviour of Cu-based BMGCs, in contrast to what it is reported in other works.

- The formation of CuO and Cu_2O oxides caused a substantial increase in copper ion diffusion, which coupled with the development of copper oxide needles, enhanced the antimicrobial activity of the samples.

- Deposition parameters such as chamber pressure and substrate temperature can be controlled to influence the antimicrobial properties. Variations in these parameters cause changes in the compactness of the films into agreement with Thorton's structural zone model, easing the movement of copper ions.

- Antimicrobial tests prepared in both "wet" and "dry" conditions do not display, overall, great differences. However, drying of LB broth caused the formation of NaCl crystals in the surface of the samples which lowered the number of bacteria recovered, more noticeable in GN than in GP bacteria.

- TEM and SEM images of recovered bacteria showed a limited damage to the cell envelope. Partial and total lysis was found for cells exposed to controlled dosages of $CuCl_2$, thus suggesting that this killing mechanism only plays a

significant role when the copper ion diffusion is much higher than those observed in these samples. Consequently, contact killing for the materials and timeframes analysed in this work only takes place due to the migration of copper ions into the pathogens and further damage inside the cell through mechanisms such as Femtom like reactions or DNA degradation.

The aforementioned results are of great interest to develop new high performance antimicrobial touch surfaces, but the field is relatively new and much more needs to be investigated. Using the work presented in this thesis, the natural development will entail experiments such as:

- Development of better antimicrobial tests which will emulate real hand to surface contact. To really understand the interaction between touch surfaces, bacteria and human hands, experiments using bacteria deposited on surfaces imitating human skin are currently being developed.

- Changes in superficial roughness through simple grinding did not influence the antimicrobial behaviour of these samples, however, it will be interesting to analyse if there are specific nanopatternings that could enhance this property.

- Copper ion release was shown to be affected by changes in compactness. In all BMGCs analysed, the presence of crystalline phases rich in copper increased both antimicrobial and wear performance. It is necessary to analyse if these parameters can enhance the properties of Cu-based thin films.

- Deposition of bacteria in these samples showed that the main mechanisms governing the contact killing of Cu-based surfaces involves the diffusion of copper ions and damage to the inner structures of the cell. However, the specific mechanism responsible for this is still unknown.

- In all studies GN and GP bacteria were used, however, the ability to eliminate other pathogens such as fungi or viruses and even endospore forms of GP pathogens has been disregarded. The antimicrobial activity of these novel materials and other pathogens should be analysed.

Presentations and publications

Publications

Villapún, V.M.; Dover, L.G.; Cross, A.; González, S. Antibacterial metallic touch surfaces. *Materials* **2016**, 9, 736.

Villapún, V.M.; Zhang, H.; Howden, C.; Chow, L.C.; Esat, F.; Pérez, P.; Sort, J.; Bull, S.; Stach, J.; González, S. Antimicrobial and wear performance of cu-zr-al metallic glass composites. *Materials & Design* **2017**, 115, 93-102.

Villapún, V.M.; Esat, F.; Bull, S.; Dover, L.G.; Gonzalez, S. Tuning the mechanical and antimicrobial performance of a cu-based metallic glass composite through cooling rate control and annealing. *Materials* **2017**, 10, 506.

Villapún, V.M.; Medina, J.; Pérez, P.; Esat, F.; Inam, F.; González, S. Strategy for preventing excessive wear rate at high loads in bulk metallic glass composites. *Materials & Design* **2017**, *135*, 300-308.

Presentations

Poster: Villapún, V.M; González, S “Copper based metallic glasses composites for antimicrobial touch surfaces” presented in ”Metals in biology BBSRC NIBB” hosted in Durham, 2016.

Poster: Villapún, V.M; Dover, L.G; González, S “Copper rich metallic glass composites as antimicrobial materials” Northumbria University PGR conference, 2017.

Poster: Villapún, V.M; Dover, L.G; González, S “Copper rich metallic glasses composites for antimicrobial touch surfaces” ”Metals in biology BBSRC NIBB” hosted in Durham, 2017.

Poster: Villapún, V.M; Dover, L.G; González, S “Preventing Health-care Acquired Infections through Metallic Glass Composites” presented in ”Antimicrobial coatings in healthcare: from innovation to the market” (AMiCI) hosted in Pori (Finland), 2017.

References

1. Control, E.C.f.D.P.a. Point prevalence survey of healthcare associated infections and antimicrobial use in european acute care hospitals. ECDC: Stockholm, 2013.
2. Trubiano, J.A.; Padiglione, A.A. Nosocomial infections in the intensive care unit. *Anaesthesia and Intensive Care Medicine* **2015**, *16*, 598-602.
3. Sadatsafavi, H.; Niknejad, B.; Zadeh, R.; Sadatsafavi, M. Do cost savings from reductions in nosocomial infections justify additional costs of single-bed rooms in intensive care units? A simulation case study. *Journal of Critical Care* **2015**, *31*, 194-200.
4. Lax, S.; Gilbert, J.A. Hospital associated microbiota and implications for nosocomial infections. *Cell Press* **2015**, *21*, 427-432.
5. Control, E.C.f.D.P.a. Antimicrobial resistance surveillance in europe. In *Annual Report of the European Antimicrobial Resistance Surveillance Network (EARS-Net)*, ECDC: Stockholm, 2014.
6. Stone, P.W. Economic burden of healthcare-associated infections: An american perspective. *Expert Review of Pharmacoeconomics & Outcomes Research* **2009**, *9*, 417-422.
7. Jenkins, D.R. Nosocomial infections and infection control. *Prevention and control of infection* **2017**, *45*, 629-633.
8. Khan, H.A.; Ahmad, A.; Mehboob, R. Nosocomial infections and their control strategies. *Asian Pacific Journal of Tropical Biomedicine* **2015**, *5*, 509-514.
9. Ferber, D. Superbugs on the hoof? *Science* **2000**, *288*, 792-794.
10. Sorci, G.; Cornet, S.; Faivre, B. Immunity and the emergence of virulent pathogens. *Infection, Genetics and Evolution* **2013**, *16*, 441-446.
11. Rolain, J.M.; Parola, P.; Cornaglia, G. *New delhi metallo-beta-lactamase* (ndm-1): Towards a new pandemia? *Clinical Microbiology and Infection* **2010**, *16*, 1699-1701.
12. Brink, A.J.; Coetzee, J.; Clay, C.G.; Sithole, S.; Richards, G.A.; Poirel, L.; Nordmann, P. Emergence of *new delhi metallo-beta-lactamase* (ndm-1) and *klebsiella pneumoniae carbapenemase* (kpc-2) in south africa. *Journal of clinical microbiology* **2012**, *50*, 525-527.
13. Villapún, V.M.; Esat, F.; Bull, S.; Dover, L.G.; Gonzalez, S. Tuning the mechanical and antimicrobial performance of a cu-based metallic glass composite through cooling rate control and annealing. *Materials* **2017**, *10*, 506.
14. Wright, G.D. Resisting resistance: New chemical strategies for battling superbugs. *Chemistry & Biology* **2000**, *7*, R127-R132.
15. Ghafur, A.; Mathai, D.; Muruganathan, A.; Jayalal, J.A.; Kant, R.; Chaudhary, D.; Abraham, O.C.; Gopalakrishnan, R.; Ramasubramanian, V.; Shah, S.N.*, et al.* "The chennai declaration". In *Recommendations of" A roadmap-to tackle the challenge of antimicrobial resistance"-A join meeting of medical societies of India*, 2013.
16. Dollwet, H.H.A.; Sorenson, J.R.J. Historic uses of copper-compounds in medicine. *Journal of Trace Elements in Medicine and Biology* **1985**, *2*, 80-87.
17. Khan, H.A.; Baig, F.K.; Mehboob, R. Nosocomial infections: Epidemiology, prevention, control and surveillance. *Asian Pacific Journal of Tropical Biomedicine* **2017**, *7*, 478-482.
18. Weber, D.O.; Gooch, J.J.; Wood, W.R.; Britt, E.M.; Kraft, R.O. Influence of operating room surface contamination on surgical wounds: A prospective study. *Archives of Surgery* **1976**, *111*, 484-488.
19. Maki, D.G.; Alvarado, C.J.; Hassemer, C.A.; Zilz, M.A. Relation of the inanimate hospital environment to endemic nosocomial infection. *The New England Journal of Medicine* **1982**, *307*, 1562-1566.

20. Mallison, G.F.; Haley, R.W. Microbiologic sampling of the inanimate environment in u.S. Hospitals, 1976–1977. *American Journal of Medicine* **1981**, *70*, 941-946.
21. Otter, J.A.; Yezli, S.; French, G.L. The role played by contaminated surfaces in the transmission of nosocomial pathogens. *Infection Control & Hospital Epidemiology* **2011**, *32*, 687-699.
22. Bhalla, A.; Pultz, N.J.; Gries, D.M.; Ray, A.J.; Eckstein, E.C.; Aron, D.C.; Donskey, C.J. Acquisition of nosocomial pathogens on hands after contact with environmental surfaces near hospitalized patients. *Infection Control & Hospital Epidemiology* **2004**, *25*, 164-167.
23. Boyce, J.M. Environmental contamination makes an important contribution to hospital infection. *Journal of Hospital Infection* **2007**, *65*, 50-54.
24. Weinstein, R.A. Epidemiology and control of nosocomial infections in adult intensive care units. *The American Journal of Medicine* **1991**, *91*, S179-S184.
25. Wilks, S.A.; Michels, H.; Keevil, C.W. The survival of *escherichia coli* o157 on a range of metal surfaces. *International Journal of Food Microbiology* **2005**, *105*, 445-454.
26. Kuhn, P.J. Doorknobs: A source of nosocomial infection. *Diagnostic Medicine* **1983**, *6*, 62-63.
27. Milling, A.; Kehr, R.D.; Smalla, K. Survival of bacteria on wood and plastic particles: Dependence on wood species and environmental conditions. *Holzforschung* **2005**, *59*, 72-81.
28. Kramer, A.; Schewebke, I.; Kampf, G. How long do nosocomial pathogens persist on inanimate surfaces? A systematic review. *MC Infectious Diseases* **2006**, *6*, 130.
29. Mitscherlich, E.; Marth, E.H. *Microbial survival in the environment: Bacteria and rickettsiae important in human and animal health*. Springer-Verlag: 2012.
30. Schmidt, M.G.; Attaway, H.H.; Sharpe, P.; John, J.; Sepkowitz, K.A.; Morgan, A.; Fairey, S.E.; Singh, S.; Steed, L.L.; Cantey, J.R.*, et al.* Sustained reduction of microbial burden on common hospital surfaces through introduction of copper. *Journal of clinical microbiology* **2012**, *50*, 2217–2223.
31. Dancer, S.J. How do we assess hospital cleaning? A proposal for microbiological standards for surface hygiene in hospitals. *Journal of Hospital Infection* **2004**, *56*, 10-15.
32. Griffith, C.J.; Cooper, R.A.; Gilmore, J.; Davies, C.; Lewis, M. An evaluation of hospital cleaning regimes and standards. *Journal of Hospital Infection* **2000**, *45*, 19-28.
33. Gillespie, E.; Wright, P.L.; Snook, K.; Ryan, S.; Vandergraaf, S.; Abernethy, M.; Lovegrove, A. The role of ultraviolet marker assessments in demonstrating cleaning efficacy. *American Journal of Infection Control* **2015**, *43*, 1347-1349.
34. Malik, R.E.; Cooper, R.A.; Griffith, C.J. Use of audit tools to evaluate the efficacy of cleaning systems in hospitals. *American Journal of Infection Control* **2003**, *31*, 181-187.
35. Murphy, C.L.; Macbeth, D.A.; Derrington, P.; Gerrard, J.; Faloon, J.; Kenway, K.; Lavender, S.; Leonard, S.; Orr, A.; Tobin, D. An assessment of high touch object cleaning thoroughness using a fluorescent marker in two australian hospitals. *Healthcare Infection* **2012**, *16*, 156-163.
36. Dancer, S.J. The role of environmental cleaning in the control of hospital-acquired infection. *Journal of Hospital Infection* **2009**, *73*, 378-385.
37. Dancer, S.J. Hospital cleaning in the 21st century. *European Journal of Clinical Microbiology & Infectious Diseases* **2011**, *30*, 1473-1481.
38. Weber, D.J.; Rutala, W.A.; Miller, M.B.; Huslage, K.; Sickbert-Bennett, E. Role of hospital surfaces in the transmission of emerging health care-associated pathogens: Norovirus, *clostridium difficile* and *acinetobacter species*. *American Journal of Infection Control* **2010**, *38*, S25-S33.

39. Chen, Y.C.; Lin, C.F.; Reh, Y.J.F.; Chen, J.C.; Chen, P.Y.; Chen, C.H.; Wang, T.M.; Huang, F.L. Reduced nosocomial infection rate in a neonatal intensive care unit during a 4-year surveillance period. *Journal of the Chinese Medical Association* **2017**, *8*, 427-431.
40. Iliyasu, G.; Daiyab, F.M.; Tiamiyu, A.B.; Abubakar, S.; Habib, Z.G.; Sarki, A.M.; Habib, A.G. Nosocomial infections and resistance pattern of common bacterial isolates in an intensive care unit of a tertiary hospital in nigeria: A 4-year review. *Journal of Critical Care* **2016**, *34*, 116-120.
41. Resorces, O.E. Science image library: Gram stain. http://www.scienceprofonline.com/science-image-libr/sci-image-libr-gram-stain.html (31-10-2017),
42. Beveridge, T.J. Use of the gram stain in microbiology. *Biotechnic & Histochemistry* **2001**, *76*, 111-118.
43. Bauman, R.W.; Machunis-Masuoka, E.; Tizard, I.R. *Microbiology: With diseases by taxonomy*. Benjamin Cummings: California, 2011.
44. Blog, M.B. What is a gram-negative bacteria? http://mybioblogpro.blogspot.co.uk/2015/07/what-is-gram-negative-bacteria.html (31-10-2017),
45. Stamm, W.E.; Martin, S.M.; Bennett, J.V. Epidemiology of nosocomial infections due to gram-negative bacilli: Aspects relevant to development and use of vaccines. *Journal of Infectious Diseases* **1977**, *136*, S151-S160.
46. Jarvis, W.R.; Martone, W.J. Predominant pathogens in hospital infections. *Journal of Antimicrobial Chemotherapy* **1992**, *29*, 19-24.
47. Johanson, W.G.; Pierce, A.K.; Sanford, J.P.; Thomas, G.D. Nosocomial respiratory infections with gram-negative bacilli. *Annals of Internal Medicine* **1972**, *77*, 701-706.
48. Peleg, A.Y.; Hooper, D.C. Hospital-acquired infections due to gram-negative bacteria. *New England Journal of Medicine* **2010**, *362*, 1804-1813.
49. AMiCI. Second european cost action for antimicrobial coating innovations (amici). Pori, Finland, 2017.
50. Lam, S.J.; Wong, E.H.; Boyer, C.; Qiao, G.G. Antimicrobial polymeric nanoparticles. *Progress in Polymer Science* **2017**.
51. Muñoz-Bonilla, A.; Fernández-García, M. Polymeric materials with antimicrobial activity. *Progress in Polymer Science* **2012**, *37*, 281-339.
52. Siedenbiedel, F.; Tiller, J.C. Antimicrobial polymers in solution and on surfaces: Overview and functional principles. *Polymers* **2012**, *4*, 46-71.
53. Kenawy, E.R.; Worley, S.D.; Broughton, R. The chemistry and applications of antimicrobial polymers: A state-of-the-art review. *Biomacromolecules* **2007**, *8*, 1359-1384.
54. Lemire, J.A.; Harrison, J.J.; Turner, R.J. Antimicrobial activity of metals: Mechanisms, molecular targets and applications. *Nature Reviews Microbiology* **2013**, *11*, 371.
55. Tu, M.E.; Wu, Y.H. Multiple allergies to metal alloys. *Dermatologica Sinica* **2011**, *29*, 41-43.
56. Berry, C.W.; Moore, T.J.; Safar, J.A.; Henry, C.A.; Wagner, M.J. Antibacterial activity of dental implant metals. *Implant Dentistry* **1992**, *1*, 59.
57. Luo, J.; Hein, C.; Mücklich, F.; Solioz, M. Killing of bacteria by copper, cadmium, and silver surfaces reveals relevant physicochemical parameters. *Biointerphases* **2017**, *12*, 020301.
58. Grass, G.; Rensing, C.; Solioz, M. Metallic copper as an antimicrobial surface. *Applied and Environmental Microbiology* **2011**, *77*, 1541-1547.
59. Warnes, S.L. Laboratory studies to investigate the efficacy and mechanism of action of copper alloys to kill a range of bacterial pathogens and inactive norovirus. University of Southampton, Southampton, UK, 2014.

60. Warnes, S.L.; Highmore, C.J.; Keevil, C.W. Horizontal transfer of antibiotic resistance genes on abiotic touch surfaces: Implications for public health. *mBio* **2012**, *3*, e00489.
61. Warnes, S.L.; Keevil, C.W. Inactivation of norovirus on dry copper alloy surfaces. *PLoS ONE* **2013**, *8*, e75017.
62. Borkow, G.; Gabbay, J. Copper, an ancient remedy returning to fight microbial, fungal and viral infections. *Current Chemical Biology* **2009**, *3*, 272-278.
63. Santo, C.E.; Lam, E.W.; Elowsky, C.G.; Quaranta, D.; Domaille, D.W.; Chang, C.J.; Grass, G. Bacterial killing by dry metallic copper surfaces. *Applied and Environmental Microbiology* **2011**, *77*, 794-802.
64. Meyer, T.J.; Ramlall, J.; Thu, P.; Gadura, N. Antimicrobial properties of copper in gram-negative and gram-positive bacteria. *World Academy of Science, Engineering and Technology, International Journal of Biological, Biomolecular, Agricultural, Food and Biotechnological Engineering* **2015**, *9*, 274-278.
65. Hans, M.; Mathews, S.; Mucklich, F.; Solioz, M. Physicochemical properties of copper important for its antibacterial activity and development of a unified model. *Biointerphases* **2016**, *11*, 018902.
66. Huang, L.; Fozo, E.M.; Zhang, T.; Liaw, P.K.; He, W. Antimicrobial behavior of cu-bearing zr-based bulk metallic glasses. *Materials Science and Engineering: C* **2014**, *39*, 325-329.
67. CDA. Copper development association. : http://copperalliance.org.uk (17-10-17),
68. Hans, M.; Erbe, A.; Mathews, S.; Chen, Y.; Solioz, M.; Mucklich, F. Role of copper oxides in contact killing of bacteria. *Langmuir* **2013**, *29*, 16160–16166.
69. Barillo, D.J.; Marx, D.E. Silver in medicine: A brief history bc 335 to present. *Burns* **2014**, *14*, 3–8.
70. Rebelo, R.; Manninen, N.K.; Fialho, L.; Henriques, M.; Carvalho, S. Morphology and oxygen incorporation effect on antimicrobial activity of silver thin films. *Applied Surface Science* **2016**, *371*, 1–8.
71. Kim, J.S.; Kuk, E.; Yu, K.N.; Kim, J.H.; Park, S.J.; Lee, H.J.; Kim, S.H.; Park, Y.K.; Park, Y.H.; Hwang, C.Y. Antimicrobial effects of silver nanoparticles. *Nanomedicine* **2007**, *3*, 95–101.
72. Dizaj, S.M.; Lotfipour, F.; Barzegar-Jalali, M.; Zarrintan, M.H.; Adibkia, K. Antimicrobial activity of the metals and metal oxide nanoparticles. *Materials Science and Engineering: C* **2014**, *44*, 278-284.
73. Rai, M.; Yadav, A.; Gade, A. Silver nanoparticles as a new generation of antimicrobials. *Biotechnology Advances* **2009**, *27*, 76-83.
74. Ferreri, I.; Calderon, V.S.; Galindo, R.E.; Palacio, C.; Henriques, M.; Piedade, A.P.; Carvalho, S. Silver activation on thin films of ag-zrcn coatings for antimicrobial activity. *Material Science and Engineering: C* **2015**, *55*, 547-555.
75. Pasquet, J.; Chevalier, Y.; Pelletier, J.; Couval, E.; Bouvier, D.; Bolzinger, M.A. The contribution of zinc ions to the antimicrobial activity of zinc oxide. *Colloids and Surfaces A: Physicochemical and Engineering Aspects* **2014**, *457*, 263-274.
76. Sawai, J.; Shoji, S.; Igarashi, H.; Hashimoto, A.; Kokugan, T.; Shimizu, M.; Kojima, H. Hydrogen peroxide as an antibacterial factor in zinc oxide powder slurry. *Journal of Fermentation and Bioengineering* **1998**, *86*, 521–522.
77. Zhang, L.; Li, Y.; Liu, X.; Zhao, L.; Ding, Y.; Povey, M.; Cang, D. The properties of zno nanofluids and the role of h_2o_2 in the disinfection activity against *escherichia coli*. *Water Research* **2013**, *47*, 4013-4021.
78. Dunlop, P.S.M.; Sheeran, C.P.; Byrne, J.A.; McMahon, M.A.S.; Boyle, M.A.; McGuigan, K.G. Inactivation of clinically relevant pathogens by photocatalytic coatings. *Journal of Photochemistry and Photobiology A: Chemistry* **2010**, *216*, 303-310.

79. Ercan, D.; Cossu, A.; Nitin, N.; Tikekar, R.V. Synergistic interaction of ultraviolet light and zinc oxide photosensitizer for enhanced microbial inactivation in simulated wash-water. *Innovative Food Science and Emerging Technologies* **2016**, *33*, 240–250.
80. Wöll, C. The chemistry and physics of zinc oxide surfaces. *Progress in Surface Science* **2007**, *82*, 55-120.
81. Hernández-Sierra, J.F.; Ruiz, F.; Cruz Pena, D.C.; Martínez-Gutiérrez, F.; Martínez, A.E.; de Jesús Pozos Guillén, A.; Tapia-Pérez, H.; Martínez Castañón, G. The antimicrobial sensitivity of *streptococcus mutans* to nanoparticles of silver, zinc oxide, and gold. *Nanomedicine* **2008**, *4*, 237–240.
82. Bonetta, S.; Motta, F.; Strini, A.; Carraro, E. Photocatalytic bacterial inactivation by tio_2-coated surfaces. *AMB Express* **2013**, *18*, 375709.
83. Armelao, L.; Barreca, D.; Bottaro, G.; Gasparotto, A.; Maccato, C.; Maragno, C.; Tondello, E.; Štangar, U.L.; Bergant, M.; Mahne, D. Photocatalytic and antibacterial activity of tio_2 and au/tio_2 nanosystems. *Nanotechnology* **2007**, *18*, 375709.
84. Evans, P.; Sheel, D.W. Photoactive and antibacterial tio_2 thin films on stainless steel. *Surface and Coatings Technology* **2007**, *201*, 9319-9324.
85. Yates, H.M.; Brook, L.A.; Ditta, I.B.; Evans, P.; Foster, H.A.; Sheel, D.W.; Steele, A. Photo-induced self-cleaning and biocidal behaviour of titania and copper oxide multilayers. *Journal of Photochemistry and Photobiology A: Chemistry* **2008**, *197*, 197-205.
86. Yu, J.C.; Ho, W.; Lin, J.; Yip, H.; Wong, P.K. Photocatalytic activity, antibacterial effect, and photoinduced hydrophilicity of tio_2 films coated on a stainless steel substrate. *Environmental Science & Technology* **2003**, *37*, 2296-2301.
87. Wong, M.S.; Chu, W.C.; Sun, D.S.; Huang, H.S.; Chen, J.H.; Tsai, P.J.; Lin, N.T.; Yu, M.S.; Hsu, S.F.; Wang, S.L*., et al.* Visible-light-induced bactericidal activity of a nitrogen-doped titanium photocatalyst against human pathogens. *Applied and Environmental Microbiology* **2006**, *72*, 6111-6116.
88. Chung, C.J.; Lin, H.I.; Tsou, H.K.; Shi, Z.Y.; He, J.L. An antimicrobial tio_2 coating for reducing hospital-acquired infection. *Journal of biomedical materials research Part B: Applied biomaterials* **2008**, *85*, 220-224.
89. Akhavan, O. Lasting antibacterial activities of ag-tio_2/ag/a-tio_2 nanocomposite thin film photocatalysts under solar light irradiation. *Journal of Colloid and Interface Science* **2009**, *336*, 117–124.
90. Foster, H.A.; Sheel, D.W.; Sheel, P.; Evans, P.; Varghese, S.; Rutschke, N.; Yates, H.M. Antimicrobial activity of titania/silver and titania/copper films prepared by cvd. *Journal of Photochemistry and Photobiology A: Chemistry* **2010**, *216*, 283-289.
91. Page, K.; Palgrave, R.G.; Parkin, I.P.; Wilson, M.; Savin, S.L.P.; Chadwick, A.V. Titania and silver-titania composite films on glass-potent antimicrobial coatings. *Journal of Materials Chemistry* **2007**, *17*, 95-104.
92. Yu, B.Y.; Leung, K.M.; Guo, Q.Q.; Lau, W.M.; Yang, J. Synthesis of ag-tio_2 composite nano thin film for antimicrobial application. *Nanotechnology* **2011**, *22*, 115603.
93. Reddy, M.P.; Venugopal, A.; Subrahmanyam, M. Hydroxyapatite-supported ag–tio_2 as *escherichia coli* disinfection photocatalyst. *Water Research* **2007**, *41*, 379-386.
94. de Jong, B.; Meeder, A.M.; Koekkoek, K.W.; Schouten, M.A.; Westers, P.; van Zanten, A.R. Pre–post evaluation of effects of a titanium dioxide coating on environmental contamination of an intensive care unit: The titanic study. *Journal of Hospital Infection* **2017**.
95. Wang, W.J.; Yu, J.C.; Wong, P.K. Photocatalysts for solar-induced water disinfection: New developments and opportunities. *Materials Science Forum* **2013**, *734*, 63-89.

96. Pratt, L.A.; Kolter, R. Genetic analysis of *escherichia coli* biofilm formation: Roles of flagella, motility, chemotaxis and type i pili. *Molecular Microbiology* **1998**, *30*, 285-293.
97. Dunne, W.M. Bacterial adhesion: Seen any good biofilms lately? *Clinical Microbiology Reviews* **2002**, *15*, 155-166.
98. Haiko, J.; Westerlund-Wikström, B. The role of the bacterial flagellum in adhesion and virulence. *Biology* **2013**, *2*, 1242-1267.
99. Armitage, J.P. Bacterial motility and chemotaxis. *Science Progress* **1992**, *1933-*, 451-477.
100. Katsikogianni, M.G.; Missirlis, Y.F. Concise review of mechanisms of bacterial adhesion to biomaterials and of techniques used in estimating bacteria-material interactions. *European Cells & Materials* **2004**, *8*, 37-57.
101. Krishnan, M.; Seema, S.; Tiwari, B.; Sharma, H.S.; Londhe, S.; Arora, V. Surface characterization of nickel titanium orthodontic arch wires. *Medical Journal Armed Forces India* **2015**, *71*, S340-S345.
102. Sridhar, S.; Abidi, Z.; Wilson, T.G.; Valderrama, P.; Wadhwani, C.; Palmer, K.; Rodrigues, D.C. In vitro evaluation of the effects of multiple oral factors on dental implants surfaces. *Journal of Oral Implantology* **2016**, *42*, 248–257.
103. Verardi, G.; Cenci, M.S.; Maske, T.T.; Webber, B.; Santos, L.R. Antiseptics and microcosm biofilm formation on titanium surfaces. *Brazilian Oral Research* **2016**, *30*.
104. Page, K.; Wilson, M.; Parkin, I.P. Antimicrobial surfaces and their potential in reducing the role of the inanimate environment in the incidence of hospital-acquired infections. *Journal of Materials Chemistry* **2009**, *19*, 3819-3831.
105. Aisenberg, S.; Chabot, R. Ion-beam deposition of thin films of diamondlike carbon. *Journal of Applied Physics* **1971**, *42*, 2953.
106. Wojcieszak, D.; Kaczmarek, D.; Antosiak, A.; Mazur, M.; Rybak, Z.; Rusak, A.; Osekowska, M.; Poniedzialek, A.; Gamian, A.; Szponar, B. Influence of cu-ti thin film surface properties on antimicrobial activity and viability of living cells. *Materials Science and Engineering: C* **2015**, *56*, 48-56.
107. Mathews, S.; Hans, M.; Mucklich, F.; Solioz, M. Contact killing of bacteria on copper is suppressed if bacterial-metal contact is prevented and is induced on iron by copper ions. *Applied and Environmental Microbiology* **2013**, *79*, 2605–2611.
108. Villapún, V.M.; Dover, L.G.; Cross, A.; González, S. Antibacterial metallic touch surfaces. *Materials* **2016**, *9*, 736.
109. Scheuerman, T.R.; Camper, A.K.; Hamilton, M.A. Effects of substratum topography on bacterial adhesion. *Journal of Colloid and Interface Science* **1998**, *208*, 23–33.
110. Edwards, K.J.; Rutenberg, A.D. Microbial response to surface microtopography: The role of metabolism in localized mineral dissolution. *Chemical Geology* **2001**, *180*, 19-32.
111. Hong, T.; Nagumo, M. Effect of surface roughness on early stages of pitting corrosion of type 301 stainless steel. *Corrosion Science* **1997**, *39*, 1665-1672.
112. Chu, Y.Y.; Lin, Y.S.; Chang, C.M.; Liu, J.K.; Chen, C.H.; Huang, J.C. Promising antimicrobial capability of thin film metallic glasses. *Material Science and Engineering: C* **2014**, *36*, 221–225.
113. Sharifahmadian, O.; Salimijazi, H.R.; Fathi, M.H.; Mostaghimi, J.; Pershin, L. Relationship between surface properties and antibacterial behavior of wire arc spray copper coatings. *Surface and Coatings Technology* **2013**, *233*, 74-79.
114. Chen, H.W.; Hsu, K.C.; Chan, Y.C.; Duh, J.G.; Lee, J.W.; Jang, J.S.C.; Chen, G.J. Antimicrobial properties of zr-cu-al-ag thin film metallic glass. *Thin Solid Films* **2014**, *561*, 98–101.
115. Shah, H.N.; Jayaganthan, R.; Kaur, D. Effect of sputtering pressure and temperature on dc magnetron sputtered crn films. *Surface Engineering* **2010**, *26*, 629-637.

116. Bing-Chi, L.; Kai, L.; Xiao-Li, K.; Ji-Qiang, Z.; Yu-Dan, H.; Jiang-shan, L.; Wei-Dong, W.; Yong-Jian, T. Sputtering pressure influence on growth morphology, surface roughness, and electrical resistivity for strong anisotropy beryllium film. *Chinese Physics B* **2014**, *23*, 066804.
117. Stranak, V.; Wulff, H.; Rebl, H.; Zietz, C.; Arndt, K.; Bogdanowicz, R.; Nebe, B.; Bader, R.; Podbielski, A.; Hubicka, Z. Deposition of thin titanium-copper films with antimicrobial effect by advanced magnetron sputtering methods. *Materials Science and Engineering: C* **2011**, *31*, 1512-1519.
118. Airey, P.; Verran, J. Potential use of copper as a hygienic surface; problems associated with cumulative soiling and cleaning. *Journal of Hospital Infection* **2007**, *67*, 271–277.
119. Rutala, W.A.; Weber, D.J. Uses of inorganic hypochlorite (bleach) in health-care facilities. *Clinical Microbiology Reviews* **1997**, *10*, 597-610.
120. Lalitha, A.; Ramesh, S.; Rajeswari, S. Surface protection of copper in acid medium by azoles and surfactants. *Electrochimica Acta* **2005**, *51*, 47-55.
121. Lavorgna, M.; Russo, C.; D'Abrosca, B.; Parrella, A.; Isidori, M. Toxicity and genotoxicity of the quaternary ammonium compound benzalkonium chloride (bac) using *daphnia magna* and *ceriodaphnia dubia* as model systems. *Environmental Pollution* **2016**, *210*, 34-39.
122. Wolkoff, P.; Schneider, T.; Kildeso, J.; Degerth, R.; Jaroszewski, M.; Schunk, H. Risk in cleaning: Chemical and physical exposure. *Science of the Total Environment* **1998**, *215*, 135-156.
123. Cadnum, J.L.; Mana, T.S.C.; Jencson, A.; Thota, P.; Kundrapu, S.; Donskey, C.J. Effectiveness of a hydrogen peroxide spray for decontamination of soft surfaces in hospitals. *American Journal of Infection Control* **2015**, *43*, 1357-1359.
124. Haber, F.; Weiss, J. The catalytic decomposition of hydrogen peroxide by iron salts. *In Proceedings of the Royal Society of London A: Mathematical, Physical and Engineering Sciences* **1934**, *147*, 332-351.
125. Linley, E.; Denyer, S.P.; McDonnell, G.; Simons, C.; Maillard, J.Y. Use of hydrogen peroxide as a biocide: New consideration of its mechanisms of biocidal action. *Journal of Antimicrobial Chemotherapy* **2012**, *67*, 1589-1596.
126. Flores, M.J.; Brandi, R.J.; Cassano, A.E.; Labas, M.D. Chemical disinfection with h_2o_2—the proposal of a reaction kinetic model. *Chemical Engineering Journal* **2012**, *198*, 388-396.
127. Labas, M.D.; Zalazar, C.S.; Brandi, R.J.; Cassano, A.E. Reaction kinetics of bacteria disinfection employing hydrogen peroxide. *Biochemical Engineering Journal* **2008**, *38*, 78-87.
128. Bartels, M.D.; Kristoffersen, K.; Slotsbjerg, T.; Rohde, S.M.; Lundgren, B.; Westh, H. Environmental meticillin-resistant *staphylococcus aureus* (mrsa) disinfection using dry-mist-generated hydrogen peroxide. *Journal of Hospital Infection* **2008**, *70*, 35–41.
129. Piskin, N.; Celebi, G.; Kulah, C.; Mengeloglu, Z.; Yumusak, M. Activity of a dry mist-generated hydrogen peroxide disinfection system against methicillin-resistant *staphylococcus aureus* and *acinetobacter baumannii*. *American Journal of Infection Control* **2011**, *39*, 757–762.
130. Andersen, B.M.; Rasch, M.; Hochlin, K.; Jensen, F.H.; Wismar, P.; Fredriksen, J.E. Decontamination of rooms, medical equipment and ambulances using an aerosol of hydrogen peroxide disinfectant. *Journal of Hospital Infection* **2006**, *62*, 149-155.
131. Fu, T.Y.; Gent, P.; Kumar, V. Efficacy, efficiency and safety aspects of hydrogen peroxide vapour and aerosolized hydrogen peroxide room disinfection systems. *Journal of Hospital Infection* **2012**, *80*, 199–205.
132. Thomas, E.L.; Milligan, T.W.; Joyner, R.E.; Jefferson, M.M. Antibacterial activity of hydrogen-peroxide and the lactoperoxidase-hydrogen peroxide-thiocyanate system against oral streptococci. *Infection and Immunity* **1994**, *62*, 529-535.

133. McDonnell, G. *The use of hydrogen peroxide for disinfection and sterilization applications*. JohnWiley & Sons: Hoboken, USA, 2009.
134. Int., H. http://halosil.com/halo-disinfection-system
135. DeNardis, D.; Rosales-Yeomans, D.; Borucki, L.; Philipossian, A. Characterization of copper-hydrogen peroxide film growth kinetics. *Thin Solid Films* **2006**, *513*, 311–318.
136. Armon, R.; Laot, N.; Lev, O.; Shuval, H.; Fattal, B. Controlling biofilm formation by hydrogen peroxide and silver combined disinfectant. *Water Science & Technology* **2000**, *42*, 187–192.
137. Roberge, P.R. *Engineering materials: Selection and design considerations*. McGraw Hill: New York, 2012.
138. Montes, J.C.; Hamdani, F.; Creus, J.; Touzain, S.; Correc, O. Impact of chlorinated disinfection on copper corrosion in hot water systems. *Applied Surface Science* **2014**, *314*, 686–696.
139. Cooper, I.R.; Hanlon, G.W. Resistance of *legionella pneumophila* serotype 1 biofilms to chlorine-based disinfection. *Journal of Hospital Infection* **2010**, *74*, 152-159.
140. Kim, J.; Pitts, B.; Stewart, P.S.; Camper, A.; Yoon, J. Comparison of the antimicrobial effects of chlorine, silver ion, and tobramycin on biofilm. *Antimicrobial Agents and Chemotherapy* **2008**, *52*, 1446-1453.
141. Landeen, L.K.; Yahya, M.T.; Gerba, C.P. Efficacy of copper and silver ions and reduced levels of free chlorine in inactivation of *legionella pneumophila*. *Applied and Environmental Microbiology* **1989**, *55*, 3045-3050.
142. McDonnell, G.; Russell, A.D. Antiseptics and disinfectants: Activity, action, and resistance. *Clinical Microbiology Reviews* **1999**, *12*, 147-179.
143. Kampf, G.; Rudolf, M.; Labadie, J.C.; Barrett, S.P. Spectrum of antimicrobial activity and user acceptability of the hand disinfectant agent sterillium gel. *Journal of Hospital Infection* **2002**, *52*, 141-147.
144. Brady, M.J.; Lisay, C.M.; Yurkovetskiy, A.V.; Sawan, S.P. Persistent silver disinfectant for the environmental control of pathogenic bacteria. *American Journal of Infection Control* **2003**, *31*, 208–214.
145. Guthery, E.; Seal, L.A.; Anderson, E.L. Zinc pyrithione in alcohol-based products for skin antisepsis: Persistence of antimicrobial effects. *American Journal of Infection Control* **2005**, *33*, 15-22.
146. Seal, L.A.; Rizer, R.L.; Maas-Irslinger, R. A unique water optional health care personnel handwash provides antimicrobial persistence and residual effects while decreasing the need for additional products. *American Journal of Infection Control* **2005**, *33*, 207-216.
147. Hall, T.J.; Wren, M.W.; Jeanes, A.; Gant, V.A. A comparison of the antibacterial efficacy and cytotoxicity to cultured human skin cells of 7 commercial hand rubs and xgel, a new copper-based biocidal hand rub. *American Journal of Infection Control* **2009**, *37*, 322-326.
148. McBain, A.J.; Ledder, R.G.; Moore, L.E.; Catrenich, C.E.; Gilbert, P. Effects of quaternary-ammonium-based formulations on bacterial community dynamics and antimicrobial susceptibility. *Applied and Environmental Microbiology* **2004**, *70*, 3449-3456.
149. Nakagawa, Y.; Hayashi, H.; Tawaratani, T.; Kourai, H.; Horie, T.; Shibasaki, I. Disinfection of water with quaternary ammonium salts insolubilized on a porous glass surface. *Applied and Environmental Microbiology* **1984**, *47*, 513-518.
150. Shirai, A.; Aihara, M.; Takahashi, A.; Maseda, H.; Omasa, T. Synergistic antimicrobial activity based on the combined use of a gemini-quaternary ammonium compound and ultraviolet-a light. *Journal of Photochemistry and Photobiology B: Biology* **2014**, *130*, 226–233.
151. Francavilla, C.; Low, E.; Nair, S.; Kim, B.; Shiau, T.P.; Debabov, D.; Celeri, C.; Alvarez, N.; Houchin, A.; Xu, P. Quaternary ammonium n,n-dichloroamines as topical, antimicrobial agents. *Bioorganic & Medicinal Chemistry Letters* **2009**, *19*, 2731-2734.

152. Ioannou, C.J.; Hanlon, G.W.; Denyer, S.P. Action of disinfectant quaternary ammonium compounds against *staphylococcus aureus*. *Antimicrobial Agents and Chemotherapy* **2007**, *51*, 296-306.
153. Makvandi, P.; Ghaemy, M.; Mohseni, M. Synthesis and characterization of photo-curable bis-quaternary ammonium dimethacrylate with antimicrobial activity for dental restoration materials. *European Polymer Journal* **2016**, *74*, 81–90.
154. Zaragoza Dörwald, F. *Quaternary ammonium salts*. Wiley-VCH Verlag GmbH & Co. KGaA: Weinheim, Germany, 2012.
155. Harrison, J.J.; Turner, R.J.; Joo, D.A.; Stan, M.A.; Chan, C.S.; Allan, N.D.; Vrionis, H.A.; Olson, M.E.; Ceri, H. Copper and quaternary ammonium cations exert synergistic bactericidal and antibiofilm activity against *pseudomonas aeruginosa*. *Antimicrobial Agents and Chemotherapy* **2008**, *52*, 2870-2881.
156. Hegazy, M.A.; Nazeer, A.A.; Shalabi, K. Electrochemical studies on the inhibition behavior of copper corrosion in pickling acid using quaternary ammonium salts. *Journal of Molecular Liquids* **2015**, *209*, 419-427.
157. Collins, K.J. The corrosion of metal by palmar sweat. *British Journal of Industrial Medicine* **1957**, *14*, 191–197.
158. Bond, J.W. Visualization of latent fingerprint corrosion of metallic surfaces. *Journal of Forensic Sciences* **2008**, *53*, 812-822.
159. Casey, A.L.; Adams, D.; Karpanen, T.J.; Lambert, P.A.; Cookson, B.D.; Nightingale, P.; Miruszenko, L.; Shillam, R.; Christian, P.; Elliott, T.S.J. Role of copper in reducing hospital environment contamination. *Journal of Hospital Infection* **2010**, *74*, 72-77.
160. Karpanen, T.J.; Casey, A.L.; Lambert, P.A.; Cookson, B.D.; Nightingale, P.; Miruszenko, L.; Elliott, T.S.J. The antimicrobial efficacy of copper alloy furnishing in the clinical environment: A crossover study. *Infection Control & Hospital Epidemiology* **2012**, *33*, 3-9.
161. O'Gorman, J.; Humphreys, H. Application of copper to prevent and control infection. Where are we now? *Journal of Hospital Infection* **2012**, *81*, 217–223.
162. Fredj, N.; Kolar, J.S.; Prichard, D.M.; Burleigh, T.D. Study of relative color stability and corrosion resistance of commercial copper alloys exposed to hand contact and synthetic hand sweat. *Corrosion Science* **2013**, *76*, 415-423.
163. Goodwin, F.E. *Corrosion of zinc and its alloys*. Elsevier: Oxford, 2010; Vol. Vol. 3: Corrosion and Degradation of Engineering Materials.
164. Lyon, S.B. *Corrosion of noble metals*. Elsevier: Oxford, 2010; Vol. Vol. 3: Corrosion and Degradation of Engineering Materials.
165. Tuck, C.D.S.; Powell, C.A.; Nuttall, J. *Corrosion of copper and its alloys*. Elsevier: Oxford, 2010; Vol. Vol. 3: Corrosion and Degradation of Engineering Materials.
166. Daniels, S.L.; Sprunger, P.T.; Kizilkaya, O.; Lytle, D.A.; Garno, J.C. Nanoscale surface characterization of aqueous copper corrosion: Effects of immersion interval and orthophosphate concentration. *Applied Surface Science* **2013**, *285*, 823-831.
167. Colorists, A.A.o.T.C.a. Aatcc 147 assessment of textile materials: Parallel streak method. **2004**.
168. Standardization, I.O.f. Iso 20645:2004 textile fabrics -- determination of antibacterial activity -- agar diffusion plate test. **2004**.
169. Colorists, A.A.o.T.C.a. Aatcc 100 antimicrobial test method for textile / fabrics. **1999**.
170. Committee, J.I.S. Jis l 1902 testing for antibacterial activity and efficacy on textile products. **2002**.
171. Committee, J.I.S. Jis z2801:2010 antibacterial products—test for antibacterial activity and efficacy. **2010**.

172. Standardization, I.O.f. Iso 22196:2011 measurement of antibacterial activity on plastics and other non-porous surfaces. **2011**.
173. Agency, U.S.E.P. Us epa protocol for the evaluation of bactericidal activity of hard, non-porous copper containing surface products. **2016**.
174. Tong, S.Y.; Davis, J.S.; Eichenberger, E.; Holland, T.L.; Fowler, V.G. *Staphylococcus aureus* infections: Epidemiology, pathophysiology, clinical manifestations, and management. *Clinical microbiology reviews* **2015**, *28*, 603-661.
175. Croxen, M.A.; Finlay, B.B. Molecular mechanisms of escherichia coli pathogenicity. *Nature Reviews Microbiology* **2010**, *8*, 26.
176. Driscoll, J.A.; Brody, S.L.; Kollef, M.H. The epidemiology, pathogenesis and treatment of *pseudomonas aeruginosa* infections. *Drugs* **2007**, *67*, 351-368.
177. Chu, J.H.; Lee, J.; Chang, C.C.; Chan, Y.C.; Liou, M.L.; Lee, J.W.; Jang, J.S.C.; Duh, J.G. Antimicrobial characteristics in cu-containing zr-based thin film metallic glass. *Surface and Coatings Technology* **2014**, *259*, 87-93.
178. In *Metal-related Antimicrobial Showcase Event*, Durham, 2016.
179. Villapún, V.M.; Zhang, H.; Howden, C.; Chow, L.C.; Esat, F.; Pérez, P.; Sort, J.; Bull, S.; Stach, J.; González, S. Antimicrobial and wear performance of cu-zr-al metallic glass composites. *Materials & Design* **2017**, *115*, 93-102.
180. Robine, E.; Boulangé-Petermann, L.; Derangère, D. Assessing bactericidal properties of materials: The case of metallic surfaces in contact with air. *Journal of Microbiological Methods* **2002**, *49*.
181. Lin, J.; Qiu, S.; Lewis, K.; Klibanov, A.M. Bactericidal properties of flat surfaces and nanoparticles derivatized with alkylated polyethylenimines. *Biotechnology Progress* **2002**, *18*, 1082-1086.
182. Tiller, J.C.; Liao, C.J.; Lewis, K.; Klibanov, A.M. Designing surfaces that kill bacteria on contact. *Proceedings of the National Academy of Sciences* **2001**, *98*, 5981-5985.
183. Ojeil, M.; Jermann, C.; Holah, J.; Denyer, S.P.; Maillard, J.Y. Evaluation of new in vitro efficacy test for antimicrobial surface activity reflecting uk hospital conditions. *Journal of Hospital Infection* **2013**, *85*, 274-281.
184. Santo, C.E.; Taudte, N.; Nies, D.H.; Grass, G. Contribution of copper ion resistance to survival of *escherichia coli* on metallic copper surfaces. *Applied and Environmental Microbiology* **2008**, *74*, 977-986.
185. Molteni, C.; Abicht, H.K.; Solioz, M. Killing of bacteria by copper surfaces involves dissolved copper. *Applied and Environmental Microbiology* **2010**, *76*, 4099-4101.
186. Cervantes, H.I.; Alvarez, J.A.; Munoz, J.M.; Arreguin, V.; Mosqueda, J.L.; Macias, A.E. Antimicrobial activity of copper against organisms in aqueous solution: A case for copper-based water pipelines in hospitals? *American Journal of Infection Control* **2013**, *41*, E115-E118.
187. Lin, B.; Mu, R.; Yang, L.F.; Bian, X.F. Antibacterial effect of metallic glasses. *Chinese Science Bulletin* **2012**, *57*, 1069–1072.
188. Arnell, R.D.; Kelly, P.J. Recent advances in magnetron sputtering. *Surface and Coatings Technology* **1999**, *112*, 170-176.
189. Kelly, P.J.; Arnell, R.D. Magnetron sputtering: A review of recent developments and applications. *Vacuum* **2000**, *56*, 159–172.
190. Chu, J.P.; Liu, T.Y.; Li, C.L.; Wang, C.H.; Jang, J.S.C.; Chen, M.J.; Chang, S.J.; Huang, W.C. Fabrication and characterizations of thin film metallic glasses: Antibacterial property and durability study for medical application. *Thin Solid Films* **2014**, *561*, 102-107.

191. Subramanian, B. In vitro corrosion and biocompatibility screening of sputtered $ti_{40}cu_{36}pd_{14}zr_{10}$ thin film metallic glasses on steels. *Material Science and Engineering: C* **2015**, *47*, 48-56.
192. Liu, Y.; Padmanabhan, J.; Cheung, B.; Liu, J.; Chen, Z.; Scanley, B.E.; Wesolowski, D.; Pressley, M.; Broadbridge, C.C.; Altman, S.*, et al.* Combinatorial development of antibacterial zr-cu-al-ag thin film metallic glasses. *Scientific Reports* **2016**, *6*, 26950.
193. Etiemble, A.; Der Loughian, C.; Apreutesei, M.; Langlois, C.; Cardinal, S.; Pelletier, J.M.; Pierson, J.F.; Steyer, P. Innovative zr-cu-ag thin film metallic glass deposed by magnetron pvd sputtering for antibacterial applications. *Journal of Alloys and Compounds* **2017**, *707*, 155-161.
194. Lee, J.; Liou, M.L.; Duh, J.G. The development of a zr-cu-al-ag-n thin film metallic glass coating in pursuit of improved mechanical, corrosion, and antimicrobial property for bio-medical application. *Surface and Coatings Technology* **2017**, *310*, 214-222.
195. Cai, C.N.; Zhang, C.; Sun, Y.S.; Huang, H.H.; Yang, C.; Liu, L. Zrcufealag thin film metallic glass for potential dental applications. *Intermetallics* **2017**, *86*, 80-87.
196. Chang, C.M.; Yang, C.J.; Wang, K.K.; Liu, J.K.; Hsu, J.H.; Huang, J.C. On the reflectivity and antibacterial/antifungal responses of al-ni-y optical thin film metallic glass composites. *Surface and Coatings Technology* **2017**, *327*, 75-82.
197. Faúndez, G.; Troncoso, M.; Navarrete, P.; Figueroa, G. Antimicrobial activity of copper surfaces against suspensions of *salmonella enterica* and *campylobacter jejuni*. *BMC Microbiology* **2004**, *4*, 19.
198. Nie, Y.; Kalapos, C.; Nie, X.; Murphy, M.; Hussein, R.; Zhang, J. Superhydrophilicity and antibacterial property of a cu-dotted oxide coating surface. *Annals of Clinical Microbiology and Antimicrobials* **2010**, *9*, 1-10.
199. Stranak, V.; Wulff, H.; Ksirova, P.; Zietz, C.; Drache, S.; Cada, M.; Hubicka, Z.; Bader, R.; Tichy, M.; Helm, C.A. Ionized vapor deposition of antimicrobial ti-cu films with controlled copper release. *Thin Solid Films* **2014**, *550*, 389–394.
200. Balouiri, M.; Sadiki, M.; Ibnsouda, S.K. Methods for in vitro evaluating antimicrobial activity: A review. *Journal of Pharmaceutical Analysis* **2016**, *6*, 71-79.
201. Wang, D.; Li, Y.; Sun, B.B.; Sui, M.L.; Lu, K.; Ma, E. Bulk metallic glass formation in the binary cu–zr system. *Applied Physics Letters* **2004**, *84*, 4029-4031.
202. Qiu, D.; Zhang, M.X. The nucleation crystallography and wettability of mg grains on active al_2y inoculants in an mg–10 wt % y alloy. *Journal of Alloys and Compounds* **2014**, *586*, 39-44.
203. Ashby, M.F.; Greer, A.L. Metallic glasses as structural materials. *Scripta Materialia* **2006**, *54*, 321-326.
204. Greer, A.L. Metallic glasses. *Science* **1995**, *267*, 1947.
205. Wang, Y.B.; Xie, X.H.; Li, H.F.; Wang, X.L.; Zhao, M.Z.; Zhang, E.W.; Bai, Y.J.; Y.F., Z.; Qin, L. Biodegradable camgzn bulk metallic glass for potential skeletal application. *Acta biomaterialia* **2011**, *7*, 3196-3208.
206. Liu, L.; Liu, Z.; Chan, K.C.; Luo, H.H.; Cai, Q.Z.; Zhang, S.M. Surface modification and biocompatibility of ni-free zr-based bulk metallic glass. *Scripta Materialia* **2008**, *58*, 231-234.
207. Tiller, W.A. *The science of crystallization: Microscopic interfacial phenomena*. Cambridge University Press: Great Britan, Cambridge, 1991.
208. Callister, W.D.; Rethwisch, D.G. *Material science and engineering* John Wiley & Sons: EEUU, New York, 2010.
209. Shetty, M.N. *Dislocations and mechanical behaviour of materials*. PHI Learning Pvt. Ltd: Delhi, India, 2013.

210. Dieter, G.E.; J.B., D. *Mechanical metallurgy*. McGraw-hill: New York, 1986; Vol. Vol. 3.
211. Biermann, H.; von Grossmann, B.; Ungár, T.; Mechsner, S.; Souvorov, A.; Drakopoulos, M.; Snigirev, A.; Mughrabi, H. Determination of local strains in a monocrystalline turbine blade by microbeam x-ray diffraction with synchrotron radiation. *Acta materialia* **2000**, *48*, 2221-2230.
212. Zhao, J.; Wang, A.; Green, M.A.; Ferrazza, F. 19.8% efficient "honeycomb" textured multicrystalline and 24.4% monocrystalline silicon solar cells. *Applied Physics Letters* **1998**, *73*, 1991-1993.
213. Chen, M. A brief overview of bulk metallic glasses. *NPG Asia Materials* **2011**, *3*, 82-90.
214. Grössinger, R.; Turtelli, R.S. Amorphous and nanocrystalline alloys. *IEEE transactions on magnetics* **1994**, *30*, 930860.
215. Suryanarayana, C.; Inoue, A. *Bulk metallic glasses* CRC Press: Boca Raton, 2010.
216. Wang, W.H.; Dong, C.; Shek, C.H. Bulk metallic glasses. *Materials Science and Engineering: R: Reports* **2004**, *44*, 45-89.
217. Miller, M.; Liaw, P. *Bulk metallic glasses: An overview*. Springer Science EEUU, New York, 1991.
218. Hofmann, D.C. Bulk metallic glasses and their composites: A brief history of diverging fields. *Journal of Materials* **2013**, *517904*, 1-8.
219. Wang, Z.; Li, J.; Zhang, W.; Qiao, J.; Wang, B. The self-organized critical behavior in pd-based bulk metallic glass. *Metals* **2015**, *5*, 1188-1196.
220. Eckert, J.; Das, J.; Pauly, S.; Duhamel, C. Mechanical properties of bulk metallic glasses and composites. *Journal of materials research* **2007**, *22*, 285-301.
221. Kruzic, J.J. Bulk metallic glasses as structural materials: A review. *Advanced Engineering Materials* **2016**, *18*, 1308-1331.
222. Liu, C.T.; Chisholm, M.F.; Miller, M.K. Oxygen impurity and microalloying effect in a zr-based bulk metallic glass alloy. *Intermetallics* **2002**, *10*, 1105-1112.
223. Gebert, A.; Eckert, J.; Schultz, L. Effect of oxygen on phase formation and thermal stability of slowly cooled $zr_{65}al_{7.5}cu_{17.5}ni_{10}$ metallic glass. *Acta Materialia* **1998**, *46*, 5475-5482.
224. Eckert, J.; Mattern, N.; Zinkevitch, M.; Seidel, M. Crystallization behavior and phase formation in zr–al–cu–ni metallic glass containing oxygen. *Materials Transactions* **1998**, *39*, 623-632.
225. Telford, M. The case for bulk metallic glass. *Materials today* **2004**, *7*, 36-43.
226. Axinte, E. Metallic glasses from "alchemy" to pure science: Present and future of design, processing and applications of glassy metals. *Materials & Design* **2012**, *35*, 518-556.
227. Inoue, A.; Nishiyama, N. New bulk metallic glasses for applications as magnetic-sensing, chemical, and structural materials. *Mrs Bulletin* **2007**, *32*, 651-658.
228. Li, H.F.; Zheng, Y.F. Recent advances in bulk metallic glasses for biomedical applications. *Acta biomaterialia* **2016**, *36*, 1-20.
229. Suryanarayana, C. *Non-equilibrium processing of materials*. Pergamon Amsterdam, New York, 1999; Vol. 2.
230. Chen, H.S. Metallic glasses. *Chinese Journal of Physics* **1990**, *28*, 407-425.
231. Greer, A.L. Metallic glasses… on the threshold. *Materials Today* **2009**, *12*, 14-22.
232. Klement, W.; Willens, R.H.; Duwez, P.O.L. Non-crystalline structure in solidified gold–silicon alloys. *Nature* **1960**, *187*, 869-870.
233. Duwez, P. Metallic glasses-historical background. *Glassy Metals I* **1981**, 19-23.
234. Jun, W.K.; Willens, R.H.; Duwez, P.O.L. Non-crystalline structure in solidified gold–silicon alloys. *Nature* **1960**, *187*, 869.
235. Abrosimova, G.; Aronin, A. Amorphous and nanocrystalline metallic alloys. *Progress in Metallic Alloys* **2016**.

236. Miroshnichenko, I.S. Sally iv. Device for crystallization of the alloys with high cooling rate. *Factory Lab* **1959**, *11*, 1398-1399.
237. Kramer, J. Nonconducting modifications of metals. *Annalen der Physik* **1934**, *19*, 37.
238. Drenner, A.; Couch, D.E.; Williams, E.K. Electrodeposition of alloys of phosphorus and nickel or cobalt. *Journal of Research of the National Bureau of Standards* **1950**, *44*, 109.
239. Buckel, W.; Hilsch, R. On the superconductivity of copper sulfide. *Zeitschrift für Physik* **1950**, *128*, 324.
240. Buckel, W.; Hilsch, R. Superconductivity and resistivity of tin with lattice distortion. *Zeitschrift für Physik* **1952**, *131*, 420.
241. Jones, H. A perspective on the development of rapid solidification and nonequilibrium processing and its future. *Materials Science and Engineering: A* **2001**, *304*, 11-19.
242. Turnbull, D. Under what conditions can a glass be formed? *Contemporary Physics* **1969**, *10*, 473-488.
243. Drehman, A.J.; Greer, A.L.; Turnbull, D. Bulk formation of a metallic glass: $Pd_{40}ni_{40}p_{20}$. *Applied Physics Letters* **1982**, *41*, 716-717.
244. Hays, C.C.; Kim, C.P.; Johnson, W.L. Microstructure controlled shear band pattern formation and enhanced plasticity of bulk metallic glasses containing in situ formed ductile phase dendrite dispersions. *Physical Review Letters* **2000**, *84*, 2901.
245. Inoue, A. Bulk glassy alloys: Historical development and current research. *Engineering* **2015**, *1*, 185-191.
246. Na, J.H.; Demetriou, M.D.; Floyd, M.; Hoff, A.; Garrett, G.R.; Johnson, W.L. Compositional landscape for glass formation in metal alloys. *Proceedings of the National Academy of Sciences* **2014**, *111*, 9031-9036.
247. Han, X.; Qin, Y.; Qi, K.; Li, X.; Wang, S.; Mi, J.; Song, K.; Wang, L. Glass-forming ability and early crystallization kinetics of novel cu-zr-al-co bulk metallic glasses. *Metals* **2016**, *6*, 225.
248. Egami, T. Atomistic mechanism of bulk metallic glass formation. *Journal of Non-Crystalline Solids* **2003**, *317*, 30-33.
249. Du, X.H.; Huang, J.C.; Liu, C.T.; Lu, Z.P. New criterion of glass forming ability for bulk metallic glasses. *Journal of Applied Physics* **2007**, *101*, 1-3.
250. Lu, Z.P.; Li, Y.; Ng, S.C. Reduced glass transition temperature and glass forming ability of bulk glass forming alloys. *Journal of Non-Crystalline Solids* **2000**, *270*, 103-114.
251. Hrubý, A. Evaluation of glass-forming tendency by means of dta. *Czechoslovak Journal of Physics* **1972**, *22*, 1187-1193.
252. Lu, Z.P.; Liu, C.T. A new glass-forming ability criterion for bulk metallic glasses. *Acta materialia* **2002**, *50*, 3501-3512.
253. Kozmidis-Petrovic, A.; Šesták, J. Forty years of the hrubý glass-forming coefficient via dta when comparing other criteria in relation to the glass stability and vitrification ability. *Journal of thermal analysis and calorimetry* **2011**, *110*, 997-1004.
254. Inoue, A. Stabilization of metallic supercooled liquid and bulk amorphous alloys. *Acta Materialia* **2000**, *48*, 279-306.
255. Chen, Q.; Shen, J.; Zhang, D.; Fan, H.; Sun, J.; McCartney, D.G. A new criterion for evaluating the glass-forming ability of bulk metallic glasses. *Materials Science and Engineering: A* **2006**, *433*, 155-160.
256. Johnson, W.L.; Na, J.H.; Demetriou, M.D. Quantifying the origin of metallic glass formation. *Nature communications* **2016**, *7*, 10313.
257. Wang, L.M.; Tian, Y.; Liu, R.; Wang, W. A "universal" criterion for metallic glass formation. *Applied Physics Letters* **2012**, *100*, 261913.
258. Li, Y.; Ng, S.C.; Ong, C.K.; Hng, H.H.; Goh, T.T. Glass forming ability of bulk glass forming alloys. *Scripta Materialia* **1997**, *36*, 783-787.

259. Saad, M.; Poulain, M. Glass forming ability criterion. *Materials Science Forum* **1987**, *19*, 11-18.
260. Donald, I.W.; Davies, H.A. Prediction of glass-forming ability for metallic systems. *Journal of Non-Crystalline Solids* **1978**, *30*, 77-85.
261. Egami, T.; Waseda, Y. Atomic size effect on the formability of metallic glasses. *Journal of non-crystalline solids* **1984**, *64*, 113-134.
262. Senkov, O.N.; Miracle, D.B. Effect of the atomic size distribution on glass forming ability of amorphous metallic alloys. *Materials Research Bulletin* **2001**, *36*, 2183-2198.
263. Egami, T. Universal criterion for metallic glass formation. *Materials Science and Engineering: A* **1997**, *226*, 261-267.
264. Miracle, D.B.; Senkov, O.N. Topological criterion for metallic glass formation. *Materials Science and Engineering: A* **2003**, *347*, 50-58.
265. Botta, W.J.; Pereira, F.S.; Bolfarini, C.; Kiminami, C.S.; de Oliveira, M.F. Topological instability and electronegativity effects on the glass-forming ability of metallic alloys. *Philosophical Magazine Letters* **2008**, *88*, 785-791.
266. Hafner, J.; Jaswal, S.S.; Tegze, M.; Pflugi, A.; Krieg, J.; Oelhafen, P.; Guntherodt, H.J. The atomic and electronic structure of metallic glasses: Search for a structure-induced minimum in the density of states. *Journal of Physics F: Metal Physics* **1988**, *18*, 2583.
267. de Oliveira, M.F.; Pereira, F.S.; Bolfarini, C.; Kiminami, C.S.; Botta, W.J. Topological instability, average electronegativity difference and glass forming ability of amorphous alloys. *Intermetallics* **2009**, *17*, 183-185.
268. de Oliveira, M.F. A new correlation between electronic parameters and glass forming ability of metallic alloys. *Philosophical Magazine Letters* **2011**, *91*, 418-422.
269. de Oliveira, M.F. A simple criterion to predict the glass forming ability of metallic alloys. *Journal of Applied Physics* **2012**, *111*, 023509.
270. Greer, A.L. The "confusion principle". *Nature* **1993**, *366*, 303.
271. Lu, Z.P.; Tan, H.; Li, Y.; Ng, S.C. The correlation between reduced glass transition temperature and glass forming ability of bulk glasses. *Scripta Materialia* **2000**, *22*, 667-673.
272. Park, E.S.; Kim, W.T.; Kim, D.H. A simple model for determining alloy composition with large glass forming ability in ternary alloys. *Metallurgical and Materials Transactions* **2001**, *32A*, 200-202.
273. Cohen, M.H.; Turnbull, D. Molecular transport in liquids and glasses. *The Journal of Chemical Physics* **1959**, *31*, 1164-1169.
274. Spaepen, F. A microscopic mechanism for steady state inhomogeneous flow in metallic glasses. *Acta metallurgica* **1977**, *25*, 407-415.
275. Donati, C.; Douglas, J.F.; Kob, W.; Plimpton, S.J.; Poole, P.H.; Glotzer, S.C. Stringlike cooperative motion in a supercooled liquid. *Physical review letters* **1998**, *80*, 2338.
276. Argon, A.S. Plastic deformation in metallic glasses. *Acta metallurgica* **1979**, *27*, 47-58.
277. Argon, A.S.; Kuo, H.Y. Plastic flow in a disordered bubble raft (an analog of a metallic glass). *Materials science and Engineering* **1979**, *39*, 101-109.
278. Takeuchi, S.; Edagawa, K. Atomistic simulation and modeling of localized shear deformation in metallic glasses. *Progress in Material Science* **2011**, *56*, 785–816.
279. Schuh, C.A.; Hufnagel, T.C.; Ramamurty, U. Mechanical behavior of amorphous alloys. *Acta Materialia* **2007**, *55*, 4067-4109.
280. Pampillo, C.A.; Chen, H.S. Comprehensive plastic deformation of a bulk metallic glass. *Materials Science and Engineering* **1974**, *13*, 181-188.
281. Lewandowski, J.J.; Greer, A.L. Temperature rise at shear bands in metallic glasses. *Nature Materials* **2006**, *5*, 15.

282. Fan, C.; Ott, R.T.; Hufnagel, T.C. Metallic glass matrix composite with precipitated ductile reinforcement. *Applied Physics Letters* **2002**, *81*, 1020-1022.
283. Xing, L.Q.; Li, Y.; Ramesh, K.T.; Li, J.; Hufnagel, T.C. Enhanced plastic strain in zr-based bulk amorphous alloys. *Physical Review B* **2001**, *64*, 180201.
284. Schroers, J.; William, L.J. Ductile bulk metallic glass. *Physical Review Letters* **2004**, *93*, 255506.
285. Pauly, S.; Liu, G.; Wang, G.; Kühn, U.; Mattern, N.; Eckert, J. Microstructural heterogeneities governing the deformation of $cu_{47.5}zr_{47.5}al_5$ bulk metallic glass composites. *Acta Materialia* **2009**, *57*, 5445–5453.
286. Fu, X.L.; Li, Y.; Schuh, C.A. Mechanical properties of metallic glass matrix composites: Effects of reinforcement character and connectivity. *Scripta Materialia* **2007**, *56*, 617–620.
287. Zhai, H.; Wang, H.; Liu, F. A strategy for designing bulk metallic glass composites with excellent work-hardening and large tensile ductility. *Journal of Alloys and Compounds* **2016**, *685*, 322-330.
288. Jiang, Y.; Shi, X.; Qiu, K. Numerical study of shear banding evolution in bulk metallic glass composites. *Materials & Design* **2015**, *77*, 32-40.
289. Bowden, F.P.; Tabor, D. *Friction: An introduction to tribology*. Heinemann Educational Publishers: United Kingdom, 1973.
290. Szeri, A.Z. *Tribology: Friction lubrication and wear*. McGraw-Hill: New York, 1980.
291. Spencer, N. *Engineering tribology*. Butterworth-heinemann: Boston, 2002.
292. Bhushan, B. *Principles and applications of tribology*. John Wiley & sons: New York, 2013.
293. Villapún, V.M.; Medina, J.; Pérez, P.; Esat, F.; Inam, F.; González, S. Strategy for preventing excessive wear rate at high loads in bulk metallic glass composites. *Materials & Design* **2017**, *135*, 300-308.
294. Bhushan, B. *Modern tribology handbook*. CRC Press: Boca raton, 2000.
295. Johnson, K.L. *Contact mechanics*. Cambridge university press: Cambridge, 1987.
296. Freddi, A.; Olmi, G.; Cristofolini, L. *Static stress models. In: Experimental stress analysis for materials and structures.* Springer, Cham: 2015; Vol. 4.
297. Greer, A.L. Metallic glasses. *Current Opinion in Solid State and Materials Science* **1997**, *2*, 412-416.
298. Fleury, E.; Lee, S.M.; Ahn, H.S.; Kim, W.T.; Kim, D.H. Tribological properties of bulk metallic glasses. *Materials Science and Engineering: A* **2004**, *375*, 276-279.
299. Yokoyama, Y.; Yamano, K.; Fukaura, K.; Sunada, H.; Inoue, A. Nanocrystalline zr-based bulk glassy alloys with high flexural strength. *Materials Transactions* **1999**, *40*, 1015-1018.
300. Fu, X.Y.; Kasai, T.; Falk, M.L.; Rigney, D.A. Sliding behavior of metallic glass: Part i. Experimental investigations. *Wear* **2001**, *250*, 409-419.
301. Blau, P.J. Friction and wear of a zr-based amorphous metal alloy under dry and lubricated conditions. *Wear* **2001**, *250*, 431-434.
302. Bakkal, M. Sliding tribological characteristics of zr-based bulk metallic glass under lubricated conditions. *Intermetallics* **2010**, *18*, 1251-1253.
303. Parlar, Z.; Bakkal, M.; Shih, A.J. Sliding tribological characteristics of zr-based bulk metallic glass. *Intermetallics* **2008**, *16*, 34-41.
304. Rahaman, M.L.; Zhang, L.C.; Ruan, H.H. Understanding the friction and wear mechanisms of bulk metallic glass under contact sliding. *Wear* **2013**, *304*, 43-48.
305. Tao, P.; Yang, Y.; Xie, Z.; He, Y. Research on friction and wear behavior of a bulk metallic glass under different sliding velocity. *Materials Letters* **2015**, *156*, 177-179.
306. Zhong, H.; Chen, J.; Dai, L.Y.; Yue, Y.; Wang, B.A.; Zhang, X.Y.; Ma, M.Z.; Liu, R.P. Effect of counterpart material on the tribological properties of zr-based bulk metallic glass under relatively heavy loads. *Wear* **2016**, *346*, 22-28.

307. Rahaman, M.L.; Zhang, L.; Liu, M.; Liu, W. Surface roughness effect on the friction and wear of bulk metallic glasses. *Wear* **2015**, *332*, 1231-1237.
308. Liu, Y.; Yitian, Z.; Xuekun, L.; Liu, Z. Wear behavior of a zr-based bulk metallic glass and its composites. *Journal of Alloys and Compounds* **2010**, *503*, 138-144.
309. Rahaman, M.L.; Zhang, L. On the estimation of interface temperature during contact sliding of bulk metallic glass. *Wear* **2014**, *320*, 77-80.
310. Rahaman, M.L.; Zhang, L.C.; Ruan, H.H. Effects of environmental temperature and sliding speed on the tribological behaviour of a ti-based metallic glass. *Intermetallics* **2014**, *52*, 151-158.
311. Kong, J.; Xiong, D.; Li, J.; Yuan, Q.; Tyagi, R. Effect of flash temperature on tribological properties of bulk metallic glasses. *Intermetallics* **2009**, *52*, 36-48.
312. Wu, H.; Baker, I.; Liu, Y.; Wu, X.; Munroe, P.R.; Zhang, J. Tribological studies of a zr-based bulk metallic glass. *Intermetallics* **2013**, *35*, 25-32.
313. Stachowiak, G.; Batchelor, A.W. *Engineering tribology*. Elsevier Science: New York, 2013.
314. A., A. *G171-03 "standard test method for scratch hardness of materials using a diamond stylus"* ASTM Standard: West Conshohocken, 2009; Vol. 3.
315. Adler, T.A.; Walters, R.P. Wear and scratch hardness of 304 stainless steel investigated with a single scratch test. *Wear* **1993**, *162*, 713-720.
316. Wredenberg, F.; Larsson, P.L. Scratch testing of metals and polymers: Experiments and numerics. *Wear* **2009**, *266*, 76-83.
317. Briscoe, B.J.; Sinha, S.K. Density distributions characteristics of green ceramic compacts using scratch hardness. *Tribology international* **1997**, *30*, 475-482.
318. Sinha, S.K.; Reddy, S.U.; Gupta, M. Scratch hardness and mechanical property correlation for mg/sic and mg/sic/ti metal–matrix composites. *Tribology International* **2006**, *39*, 184-189.
319. Poletti, M.G.; Fiore, G.; Gili, F.; Mangherini, D.; Battezzati, L. Development of a new high entropy alloy for wear resistance: Fecocrniw 0.3 and fecocrniw 0.3+ 5 at.% of c. *Materials & Design* **2017**, *115*, 247-254.
320. Briscoe, B.J.; Evans, P.D.; Biswas, S.K.; Sinha, S.K. The hardnesses of poly (methylmethacrylate). *Tribology international* **1996**, *29*, 93-104.
321. Leyland, A.; Matthews, A. On the significance of the h/e ratio in wear control: A nanocomposite coating approach to optimised tribological behaviour. *Wear* **2000**, *246*, 1-11.
322. Musil, J.; Kunc, F.; Zeman, H.; Polakova, H. Relationships between hardness, young's modulus and elastic recovery in hard nanocomposite coatings. *Surface and Coatings Technology* **2002**, *154*, 304-313.
323. Buschow, K.H.J. Thermal stability of amorphous zr-cu alloys. *Journal of Applied Physics* **1981**, *52*, 3319-3323.
324. Altounian, Z.; Guo-hua, T.; Strom-Olsen, J.O. Crystallization characteristics of cu-zr metallic glasses from $cu_{70}zr_{30}$ to $cu_{25}zr_{75}$. *Journal of applied physics* **1982**, *53*, 4755-4760.
325. Inoue, A.; Zhang, W.; Zhang, T.; Kurosaka, K. High-strength cu-based bulk glassy alloys in cu–zr–ti and cu–hf–ti ternary systems. *Acta Materialia* **2001**, *49*, 2645-2652.
326. Okamoto, H. Cu-zr (copper-zirconium). *Journal of phase equilibria and diffusion* **2008**, *29*, 204-204.
327. Cheung, T.L.; Shek, C.H. Thermal and mechanical properties of cu–zr–al bulk metallic glasses. *Journal of Alloys and Compounds* **2007**, *434*, 71-74.
328. Eckert, J.; Das, J.; Kim, K.B.; Baier, F.; Tang, M.B.; Wang, W.H.; Zhang, Z.F. High strength ductile cu-base metallic glass. *Intermetallics* **2006**, *14*, 876-881.

329. Dai, C.L.; Guo, H.; Shen, Y.; Li, Y.; Ma, E.; Xu, J. A new centimeter–diameter cu-based bulk metallic glass. *Scripta Materialia* **2006**, *54*, 1403-1408.
330. Inoue, A.; Zhang, W.; Zhang, T.; Kurosaka, K. Cu-based bulk glassy alloys with high tensile strength of over 2000 mpa. *Journal of non-crystalline solids* **2002**, *304*, 200-209.
331. Takeuchi, A.; Inoue, A. Classification of bulk metallic glasses by atomic size difference, heat of mixing and period of constituent elements and its application to characterization of the main alloying element. *Materials Transactions* **2005**, *46*, 2817-2829.
332. Xia, J.; Qiang, J.; Wang, Y.; Wang, Q.; Dong, C. Ternary bulk metallic glasses formed by minor alloying of cu_8zr_5 icosahedron. *Applied physics letters* **2006**, *88*, 101907.
333. Xu, D.; Duan, G.; Johnson, W.L. Unusual glass-forming ability of bulk amorphous alloys based on ordinary metal copper. *Physical review letters* **2004**, *92*, 245504.
334. Sung, D.S.; Kwon, O.J.; Fleury, E.; Kim, K.B.; Lee, J.C.; Kim, D.H.; Kim, Y.C. Enhancement of the glass forming ability of cu−zr−al alloys by ag addition. *Metals and materials International* **2004**, *10*, 575-579.
335. Qin, C.; Zhao, W.; Inoue, A. Glass formation, chemical properties and surface analysis of cu-based bulk metallic glasses. *International journal of molecular sciences* **2011**, *12*, 2275-2293.
336. Brinson, L.C. One-dimensional constitutive behavior of shape memory alloys: Thermomechanical derivation with non-constant material functions and redefined martensite internal variable. *Journal of intelligent material systems and structures* **1993**, *4*, 229-242.
337. Pauly, S.; Das, J.; Bednarcik, J.; Mattern, N.; Kim, K.B.; Kim, D.H.; Eckert, J. Deformation-induced martensitic transformation in cu–zr–(al, ti) bulk metallic glass composites. *Scripta Materialia* **2009**, *60*, 431-434.
338. Abe, T.; Shimono, M.; Ode, M.; Onodera, H. Thermodynamic modeling of the undercooled liquid in the cu–zr system. *Acta materialia* **2006**, *54*, 909-915.
339. Wu, Y.; Wang, H.; Wu, H.H.; Zhang, Z.Y.; Hui, X.D.; Chen, G.L.; Ma, D.; Wang, X.L.; Lu, Z.P. Formation of cu–zr–al bulk metallic glass composites with improved tensile properties. *Acta Materialia* **2011**, *59*, 2928-2936.
340. Zeng, K.J.; Hämäläinen, M.; Lukas, H.L. A new thermodynamic description of the cu-zr system. *Journal of phase equilibria and diffusion* **1994**, *15*, 577-586.
341. Wang, N.; Li, C.R.; Du, Z.M.; Wang, F.M.; Zhang, W.J. Calphad-comput. *Coupling Ph. Diagrams Thermochem* **2006**, *30*, 461-469.
342. Yamaguchi, K.; Song, Y.C.; Yoshida, T.; Itagaki, K. Thermodynamic investigation of the cu–zr system. *Journal of Alloys and Compounds* **2008**, *452*, 73-79.
343. Zhou, S.H.; Napolitano, R.E. Phase stability for the cu–zr system: First-principles, experiments and solution-based modeling. *Acta Materialia* **2010**, *58*, 2186-2196.
344. Kang, D.H.; Jung, I.H. Critical thermodynamic evaluation and optimization of the ag–zr, cu–zr and ag–cu–zr systems and its applications to amorphous cu–zr–ag alloys. *Intermetallics* **2010**, *18*, 815-833.
345. Effenberg, G.; Ilyenko, S. *Al–cu–zr (aluminium–copper–zirconium)*. Springer: 2005; Vol. Light Metal Systems. Part 2, 11A.
346. Raghavan, V. Al-cu-zr (aluminum-copper-zirconium). *Journal of phase equilibria and diffusion* **2011**, *32*, 452-454.
347. Wang, C.P.; Tu, S.B.; Yu, Y.; Han, J.J.; Liu, X.J. Experimental investigation of phase equilibria in the zr–cu–al system. *Intermetallics* **2012**, *31*, 1-8.
348. Pauly, S.; Das, J.; Mattern, N.; Kim, D.H.; Eckert, J. Phase formation and thermal stability in cu–zr–ti (al) metallic glasses. *Intermetallics* **2009**, *17*, 453-462.

349. Bo, H.; Wang, J.; Jin, S.; Qi, H.Y.; Yuan, X.L.; Liu, L.B.; Jin, Z.P. Thermodynamic analysis of the al–cu–zr bulk metallic glass system. *Intermetallics* **2010**, *18*, 2322-2327.
350. Zhou, C.; Guo, C.; Li, C.; Du, Z. Thermodynamic assessment of the phase equilibria and prediction of glass-forming ability of the al–cu–zr system. *Journal of Non-Crystalline Solids* **2017**, *461*, 47-60.
351. Sato, Y.; Nakai, C.; Wakeda, M.; Ogata, S. Predictive modeling of time-temperature-transformation diagram of metallic glasses based on atomistically-informed classical nucleation theory. *Scientific Reports* **2017**, *7*, 7194.
352. Peker, A.; Johnson, W.L. Time-temperature-transformation diagram of a highly processable metallic glass. *Material Science and Engineering: A* **1994**, *179-180*, 173-175.
353. Pogatscher, S.; Uggowitzer, P.J.; Löffler, J.F. In-situ probing of metallic glass formation and crystallization upon heating and cooling via fast differential scanning calorimetry. *Applied Physics Letters* **2014**, *104*, 251908.
354. Tretyachen-ko, L.A. Aluminium–copper–zirconium. *Ternary Alloys* **1992**, *5*, 113.
355. Kozieł, T.; Matusiewicz, M.; Kopyściańska, A.; Zielińska-Lipiec, A. Estimation of the cooling rate in 3 mm suction-cast rods based on the microstructural features. *Metallurgy and Foundry Engineering* **2013**, *39*, 7-14.
356. Kozieł, T. Estimation of cooling rates in suction casting and copper-mould casting processes. *Archives of Metallurgy and Materials* **2015**, *60*, 767-771.
357. Inoue, A.; Zhang, W. Formation, thermal stability and mechanical properties of cu- zr-al bulk glassy alloys. *Materials Transactions* **2002**, *43*, 2921–2925.
358. Fischer, E.R.; Hansen, B.T.; Nair, V.; Hoyt, F.H.; Dorward, D.W. Scanning electron microscopy. *Current Protocols in Microbiology* **2012**, *25:B:2B.2:2B.2.1–2B.2.47*.
359. Gonzalez, S. Role of minor additions on metallic glasses and composites. *Journal of Material Research* **2016**, *31*, 76–87.
360. Iqbal, M.; Wang, W.H. Production and properties of high strength ni free zr-based bmgs. *IOP Conference Series: Materials Science and Engineering* **2004**, *60*.
361. Boer, F.R.; Boom, R.; Matterns, W.C.M.; Miedema, A.R.; Niessen, A.K. *Cohesion in metals*. North Holland: Amsterdam, 1988.
362. González, S.; Sort, J.; Louzguine-Luzgin, D.V.; Perepezko, J.H.; Baró, M.D.; Inoue, A. Tuning the microstructure and mechanical properties of al-based amorphous/crystalline composites by addition of pd. *Intermetallics* **2010**, *18*, 2377–2384.
363. Meija, J.; Coplen, T.B.; Berglund, M.; Brand, W.A.; De Bièvre, P.; Gröning, M.; Holden, N.E.; Irrgeher, J.; Loss, R.D.; Walczyk, T.*, et al.* Atomic weights of the elements. *Pure and Applied Chemistry* **2016**, *88*, 265–291.
364. Yokoyama, Y.; Inoue, H.; Fukaura, K.; Inoue, A. Relationship between the liquidus surface and structures of zr-cu-al bulk amorphous alloys. *Materials Transactions* **2002**, *43*, 575–579.
365. Huijun, Y.; Yong, L.; Teng, Z.; Hengpen, W.; Bin, T.; Junwei, Q. Dry sliding tribological properties of a dendrite-reinforced zr-based bulk metallic glass matrix composite. *Journal of Materials Science & Technology* **2014**, *30*, 576–583.
366. Bull, S.J. Failure mode maps in the thin film scratch adhesion test. *Tribology International* **1997**, *30*, 491–498.
367. Liu, F.X.; Yang, F.Q.; Gao, Y.F.; Jiang, W.H.; Guan, Y.F.; Rack, P.D.; Sergic, O.; Liaw, P.K. Micro-scratch study of a magnetron-sputtered zr-based metallic-glass film. *Surface and Coatings Technology* **2009**, *203*, 3480–3484.
368. Zhong, H.; Chen, J.; Dai, L.; Yue, Y.; Zhang, Z.; Zhang, X.; Ma, M.; Liu, R. Tribological behaviours of zr-based bulk metallic glass versus zr-based bulk metallic glass under relative heavy loads. *Intermetallics* **2015**, *65*, 88–93.

369. Basu, J.; Nagendra, N.; Li, Y.; Ramamurty, U. Microstructure and mechanical properties of a partially crystallized la-based bulk metallic glass. *Philosophical Magazine* **2003**, *83*, 1747–1760.
370. Liu, Z.Q.; Liu, G.; Qu, R.T.; Zhang, Z.F.; Wu, S.J.; Zhang, T. Microstructural percolation assisted breakthrough of trade-off between strength and ductility in cuzr-based metallic glass composites. *Scientific Reports* **2014**, *4*, 1–6.
371. Ista, L.K.; Mendez, S.; Lopez, G.P. Attachment and detachment of bacteria on surfaces with tunable and switchable wettability. *Biofoulding* **2010**, *26*, 111–118.
372. Mathews, S.; Kumar, R.; Solioz, M.; Mathews, S.; Kumar, R.; Solioz, M. Copper reduction and contact killing of bacteria by iron surfaces. *Applied and Environmental Microbiology* **2015**, *81*, 6399–6403.
373. Ballo, M.K.; Rtimi, S.; Mancini, S.; Kiwi, J.; Pulgarin, C.; Entenza, J.M.; Bizzini, A. Bactericidal activity and mechanism of action of copper-sputtered flexible surfaces against multidrug-resistant pathogens. *Applied Microbiology and Biotechnology* **2016**, *100*, 5945–5953.
374. San, K.; Long, J.; Michels, C.A.; Gadura, N. Antimicrobial copper alloy surfaces are effective against vegetative but not sporulated cells of gram-positive *bacillus subtilis*. *Microbiologyopen* **2015**, *4*, 753–763.
375. Song , K.K.; Pauly, S.; Zhang, Y.; Gargarella, P.; Li, R.; Barekar, N.S.; Kuhn, U.; Stoica, M.; Eckertm, J. Strategy for pinpointing the formation of b2 cuzr in metastable cuzr-based shape memory alloys. *Acta Materialia* **2011**, *59*, 6620-6630
376. Kozachkov, H.; Kolodziejska, J.; Johnson, W.L.; Hofmann, D.C. Effect of cooling rate on the volume fraction of b2 phases in a cuzralco metallic glass matrix composite. *Intermetallics* **2013**, *39*, 89-93.
377. Carter, J.; Fu, E.G.; Martin, M.; Xie, G.; Zhang, X.; Wang, Y.Q.; Chu, W.-K.; Shao, L. Effects of cu ion irradiation in $cu_{50}zr_{45}ti_5$ metallic glass. *Scripta Materialia* **2009**, *61*, 265-268.
378. Biffi, C.A.; Figini, A.; Tuissi, A. Influence of compositional ratio on microstructure and martensitic transformation of cuzr shape memory alloys. *Intermetallics* **2014**, *46*, 4-11.
379. Champagne, V.K.; Helfritch, D.J. A demonstration of the antimicrobial effectiveness of various copper surfaces. *Journal of biological engineering* **2013**, *7*, 1–6.
380. Srivatsan, T.S.; Sudarshan, T.S. *Rapid solidification technology. An engineering guide*. Technomic Publishing Company Place: Lancaster, 1993.
381. Wang, Y.R.; Wei, B.C.; Sun, Y.F. Microstructure and mechanical properties of zr-cu-al bulk metallic glasses. *Transactions of Nonferrous Metals Society of China* **2007**, *17*, 929-933.
382. Wang, N.; Li, C.; Du, Z.; Wang, F.; Zhang, W. The thermodynamic re-assessment of the cu–zr system. *Calphad* **2006**, *30*, 461-469.
383. González, S.; Pellicer, E.; Suriñach, S.; Baró, M.D.; García-Lecina, E.; Sort, J. Effect of thermally-induced surface oxidation on the mechanical properties and corrosion resistance of $zr_{60}cu_{25}al_{10}fe_5$ bulk metallic glass. *Science of Advanced Materials* **2014**, *6*, 27-36.
384. Hasan, J.; Chatterjee, K. Recent advances in engineering topography mediated antibacterial surfaces. *Nanoscale* **2015**, *7*, 15568-15575.
385. Shirtcliffe, N.J.; McHale, G.; Atherton, S.; Newton, M.I. An introduction to superhydrophobicity. *Advances in colloid and interface science* **2010**, *161*, 124-138.
386. Tam, C.Y.; Shek, C.H. Oxidation behavior of $cu_{60}zr_{30}ti_{10}$ bulk metallic glass. *Journal of Material Research* **2005**, *20*, 1396-1403.
387. Tam, C.Y.; Shek, C.H.; Wang, W.H. Oxidation behaviour of a cu-zr-al bulk metallic glass. *Reviews on advanced materials science* **2008**, *18*, 107-111.
388. Asami, K.; Kikuchi, M.; Hashimoto, K. An auger electron spectroscopic study of the corrosion behavior of an amorphous $zr_{40}cu_{60}$ alloy. *Corrosion Science* **1997**, *39*, 95-106.

389. Jones, D.A. *Principles and prevention of corrosion*. Macmillan Publishing company: New York, 1992.
390. Konopka, J.F. Quantitative analysis of oxygen in metal oxides with sem/eds by direct measurement of all x-ray peaks. *AGU Fall Meeting Abstracts* **2012**.
391. Nanninga, N. Cell cycles and division, bacterial. In *The desk encyclopedia of microbiology*, Schaechter, M., Ed. Elsevier: San Diego, 2009.
392. Raffi, M.; Mehrwan, S.; Bhatti, T.M.; Akhter, J.I.; Hameed, A.; Yawar, W.; ul Hasan, M.M. Investigations into the antibacterial behavior of copper nanoparticles against *escherichia coli*. *Annals of Microbiology* **2010**, *60*, 75-80.
393. Bogdanović, U.; Lazić, V.; Vodnik, V.; Budimir, M.; Marković, Z.; Dimitrijević, S. Copper nanoparticles with high antimicrobial activity. *Materials Letters* **2014**, *128*, 75-78.
394. Ionescu, M.; Belkin, S. Overproduction of exopolysaccharides by an *escherichia coli* k-12 rpos mutant in response to osmotic stress. *Applied and Environmental Microbiology* **2009**, *75*, 483-492.
395. Haswell, E.S.; Phillips, R.; Rees, D.C. Mechanosensitive channels: What can they do and how do they do it? *Structure* **2011**, *19*, 1356-1369.
396. Mann, E.E.; Manna, D.; Mettetal, M.R.; May, R.M.; Dannemiller, E.M.; Chung, K.K.; Brennan, A.B.; Reddy, S.T. Surface micropattern limits bacterial contamination. *Antimicrobial resistance and infection control* **2014**, *28*, 1-8.
397. Copeland, M.F.; Weibel, D.B. Bacterial swarming: A model system for studying dynamic self-assembly. *Soft Matter* **2009**, *5*, 1174-1187.
398. Taubert, A.; Mano, J.F.; Rodríguez-Cabello, J.C. *Biomaterials surface science*. John Wiley & Sons: 2013.
399. Lu, H.B.; Zhang, L.C.; Gebert, A.; Schultz, L. Pitting corrosion of cu–zr metallic glasses in hydrochloric acid solutions. *Journal of Alloys and Compounds* **2008**, *462*, 60-67.
400. Sachs, F.; Morris, C.E. Mechanosensitive ion channels in nonspecialized cells. *Reviews of Physiology Biochemistry and Pharmacology* **1998**, *132*, 1-77.
401. Martinac, B.; Adler, J.; Kung, C. Mechanosensitive ion channels of *e. Coli* activated by amphipaths. *Nature* **1990**, *348*, 261.
402. Buechner, M.; Delcour, A.H.; Martinac, B.; Adler, J.; Kung, C. Ion channel activities in the *escherichia coli* outer membrane. *Biochimica et Biophysica Acta (BBA)-Biomembranes* **1990**, *1024*, 111-121.
403. Martinac, B.; Saimi, Y.; Kung, C. Ion channels in microbes. *Physiological reviews* **2008**, *88*, 1449-1490.
404. Sukharev, S.I.; Sigurdson, W.J.; Kung, C.; Sachs, F. Energetic and spatial parameters for gating of the bacterial large conductance mechanosensitive channel, mscl. *The Journal of general physiology* **1999**, *113*, 525-540.
405. Sukharev, S. Purification of the small mechanosensitive channel of *escherichia coli* (mscs): The subunit structure, conduction, and gating characteristics in liposomes. *Biophysical journal* **2002**, *83*, 290-298.
406. Peyronnet, R.; Tran, D.; Girault, T.; Frachisse, J.M. Mechanosensitive channels: Feeling tension in a world under pressure. *Frontiers in plant science* **2014**, *5*, 558.
407. Zhang, E.; Zheng, L.; Liu, J.; Bai, B.; Liu, C. Influence of cu content on the cell biocompatibility of ti–cu sintered alloys. *Material science and Engineering: C* **2015**, *46*, 148-157.
408. Aruoma, O.I.; Halliwell, B.; Gajewski, E.; Dizdaroglu, M. Copper-ion dependent damage to the bases in DNA in the presence of hydrogen-peroxide. *Biochemical Journal* **1991**, *273*, 601-604.
409. Banci, L.; Bertini, I.; Cantini, F.; Ciofi-Baffoni, S. Cellular copper distribution: A mechanistic systems biology approach. *Cellular and molecular life sciences* **2010**, *67*, 2563-2589.

410. Park, Y.J.; Song, Y.H.; An, J.H.; Song, H.J.; Anusavice, K.J. Cytocompatibility of pure metals and experimental binary titanium alloys for implant materials. *Journal of dentistry* **2013**, *41*, 1251-1258.
411. Shedle, A.; Samorapoompichit, P.; Rausch-Fan, X.H.; Franz, A.; Fureder, W.; Sperr, W.R.; Sperr, W.; Ellinger, A.; Slavicek, R.; Boltz-Nitulescu, G.*, et al.* Response of l-929 fibroblasts, human gingival fibroblasts, and human tissue mast cells to various metal cations. *Journal of dental research* **1995**, *74*, 1513-1520.
412. Yamamoto, A.; Honma, R.; Sumita, M. Cytotoxicity evaluation of 43 metal salts using murine fibroblasts and osteoblastic cells. *Journal of Biomedical Materials Research Part A* **1998**, *39*, 331-340.
413. Wayne, P.A. Clsi methods for dilution antimicrobial susceptibility tests for bacteria that grow aerobically. *CLSI document M07—A9* **2012**, *32*.
414. Santo, C.E.; Morais, P.V.; Grass, G. Isolation and characterization of bacteria resistant to metallic copper surfaces. *Applied Microbiology and Biotechnology* **2010**, *76*, 1341-1348.
415. Ruparelia, J.P.; Chatterjee, A.K.; Duttagupta, S.P.; Mukherji, S. Strain specificity in antimicrobial activity of silver and copper nanoparticles. *Acta biomaterialia* **2008**, *4*, 707-716.
416. Lu, H.B.; Li, Y.; Wang, F.H. Corrosion behavior and porous structure formation of sputtered cu–zr nanostructured films. *Journal of Alloys and Compounds* **2008**, *465*, 139-144.
417. Tang, J.; Zhu, Q.; Wang, Y.; Apreutesei, M.; Wang, H.; Steyer, P.; Chamas, M.; Billard, A. Insights on the role of copper addition in the corrosion and mechanical properties of binary zr-cu metallic glass coatings. *Coatings* **2017**, *7*, 223.
418. Little, B.; Wagner, P.; Mansfeld, F. Microbiologically influenced corrosion of metals and alloys. *International Materials Reviews* **1991**, *36*, 253-272.
419. Huang, L.; Qiao, D.; Green, B.A.; Liaw, P.K.; Wang, J.; Pang, S.; Zhang, T. Bio-corrosion study on zirconium-based bulk-metallic glasses. *Intermetallics* **2009**, *17*, 195-199.
420. Vargas, I.T.; Fischer, D.A.; Alsina, M.A.; Pavissich, J.P.; Pastén, P.A.; Pizarro, G.E. Copper corrosion and biocorrosion events in premise plumbing. *Materials* **2017**, *10*, 1036.
421. Shibata, A.; Imamura, Y.; Sone, M.; Ishiyama, C.; Higo, Y. Pd-ni-p metallic glass film fabricated by electroless alloy plating. *Thin Solid Films* **2009**, *517*, 1935-1938.
422. Guo, Q.; Noh, J.H.; Liaw, P.K.; Rack, P.D.; Li, Y.; Thompson, C.V. Density change upon crystallization of amorphous zr-cu-al thin films. *Acta Materialia* **2010**, *58*, 3633-3641.
423. Deng, Y.P.; Guan, Y.F.; Fowlkes, J.D.; Wen, S.Q.; Liu, F.X.; Pharr, G.M.; Liaw, P.K.; Liu, C.T.; Rack, P.D. A combinatorial thin film sputtering approach for synthesizing and characterizing ternary zrcual metallic glasses. *Intermetallics* **2007**, *15*, 1208-1216.
424. Xie, L.; Brault, P.; Thomann, A.-L.; Bedra, L. Molecular dynamic simulation of binary zr_xcu_{100-x} metallic glass thin film growth. *Applied Surface Science* **2013**, *274*, 164-170.
425. Chiang, P.T.; Chen, G.J.; Jian, S.R.; Shih, Y.H.; Jang, J.S.C.; Lai, C.H. Surface antimicrobial effects of $zr_{61}al_{7.5}ni_{10}cu_{17.5}si_4$ thin film metallic glasses on *escherichia coli*, *staphylococcus aureus*, *pseudomonas aeruginosa*, *acinetobacter baumannii* and *candida albicans*. *Fooyin Journal of Health Sciences* **2010**, *2*, 12-20.
426. Bouala, G.N.; Etiemble, A.; der Loughian, C.; Langlois, C.; Pierson, J.F.; Steyer, P. Silver influence on the antibacterial activity of multi-functional zr-cu based thin film metallic glasses. *Surface and Coatings Technology* **2018**, *343*, 108-114.
427. Michels, H.T.; Noyce, J.O.; Keevil, C.W. Effect of temperature and humidity on the efficacy of methicillin-resistant *staphylococus aureus* challenged antimicrobial materials containing silver and copper. *Letters in Applied Microbiology* **2009**, *49*, 191-195.
428. Clement, J.L.; Jarrett, P.S. Antibacterial silver. *Metal Based Drugs* **1994**, *1*, 467-462.

429. Depla, D. On the effective sputter yield during magnetron sputter deposition. *Nuclear Instruments and Methods in Physics Research* **2014**, *328*, 65-69.
430. Thompson, C.V.; Carel, R. Stress and grain growth in thin films. *Journal of the Mechanics and Physics of Solids* **1996**, *44*, 657-673.
431. Thompson, C.V. Grain growth in polycrystalline thin films of semiconductors. *Interface Science* **1998**, *6*, 85-93.
432. Chan, K.; Tou, T.; Teo, B. Effect of substrate temperature on electrical and structural properties of copper thin films. *Microelectronics Journal* **2006**, *37*, 930-937.
433. Thornton, J.A. High rate thick film growth. Annual review of materials science. *Annual Review of Materials Research* **1977**, *7*, 239-260.
434. Musil, J. Flexible hard nanocomposite coatings. *RSC Advances* **2015**, *5*, 60482-60495.
435. Thornton, J.A. Recent developments in sputtering--magnetron sputtering. *Metal Finishing* **1979**, *77*, 83-87.
436. Zeman, P.; Zitek, M.; Zuzjaková, S.; Čerstvý, R. Amorphous zr-cu thin-film alloys with metallic glass behavior. *Journal of Alloys and Compounds* **2017**, *696*, 1298-1306.
437. Matlaga, B.F.; Yasenchak, L.P.; Salthouse, T.N. Tissue response to implanted polymers: The significance of sample shape. *Jounal of Biomedical Materials Research A* **1976**, *10*, 391-397.
438. Kubiak, K.J.; Wilson, M.C.T.; Mathia, T.G.; Carval, P. Wettability versus roughness of engineering surfaces. *Wear* **2011**, *271*, 523-528.
439. Chu, J.H.; Jang, J.S.C.; Huang, J.C.; Chou, H.S.; Yang, Y.; Ye, J.C.; Wang, Y.C.; Lee, J.W.; Liu, F.X.; Liaw, P.K*., et al.* Thin film metallic glasses: Unique properties and potential applications. *Thin Solid Films* **2012**, *520*, 5097-5122.
440. Borkow, G.; Gabbay, J. Copper as a biocidal tool. *Current Medicinal Chemistry* **2005**, *12*, 2163-2175.
441. Knobloch, J.K.M.; Tofern, S.; Kunz, W.; Schütze, S.; Riecke, M.; Solbach, W.; Wuske, T. "Life-like" assessment of antimicrobial surfaces by a new touch transfer assay displays strong superiority of a copper alloy compared to silver containing surfaces. *PloS one* **2017**, *12*, e0187442.
442. Potts, M.; Slaughter, S.M.; Hunneke, F.U.; Garst, J.F.; Helm, R.F. Desiccation tolerance of prokaryotes: Application of principles to human cells. *Integrative and Comparative Biology* **2005**, *45*, 800-809.
443. Louis, P.; Trüper, H.G.; Galinski, E.A. Survival of *escherichia coli* during drying and storage in the presence of compatible solutes. *Applied Microbiology and Biotechnology* **1994**, *28*, 390-402.
444. Baird-Parker, A.C.; Davenport, E. The effect of recovery medium on the isolation of *staphylococcus aureus* after heat treatment and after the storage of frozen or dried cells. *Journal of Applied Microbiology* **1965**, *28*, 390-402.
445. Umeda, A.; Ueki, Y.; Amako, K. Structure of the *staphylococcus aureus* cell wall determined by the freeze-substitution method. *Journal of Bacteriology* **1987**, *169*, 2482-2487.
446. Hajmeer, M.; Ceylan, E.; Marsden, J.L.; Fung, D.Y. Impact of sodium chloride on *escherichia coli* o157: H7 and *staphylococcus aureus* analysed using transmission electron microscopy. *Food Microbiology* **2006**, *23*, 446-452.
447. Sun, D.; Xu, D.; Yang, C.; Shahzad, M.B.; Sun, Z.; Xia, J.; Zhao, J.; Gu, T.; Yang, K.; Wang, G. An investigation of the antibacterial ability and cytotoxicity of a novel cu-bearing 317l stainless steel. *Scientific Reports* **2016**, *6*, 29244.
448. Subramanian, B.; Maruthamuthu, S.; Rajan, S.T. Biocompatibility evaluation of sputtered zirconium-based thin film metallic glass-coated steels. *International Journal of Nanomedicine* **2015**, *10*, 17.
449. Hayat, M.E. *Fixation for electron microscopy*. Academic Press: London, 1981.

450. Khalaj, M.; Kamali, M.; Khodaparast, Z.; Jahanshahi, A. Copper-based nanomaterials for environmental decontamination–an overview on technical and toxicological aspects. *Ecotoxicology and Environmental Safety* **2018**, *148*, 813-824.
451. Liu, R.; Memarzadeh, K.; Chang, B.; Zhang, Y.; Ma, Z.; Allaker, R.P.; Ren, L.; Yang, K. Antibacterial effect of copper-bearing titanium alloy (ti-cu) against *streptococcus mutans* and *porphyromonas gingivalis*. *Sicentific Reports* **2016**, *6*, 29985.
452. Noyce, J.O.; Michels, H.; Keevil, C.W. Potential use of copper surfaces to reduce survival of epidemic meticillin-resistant *staphylococcus aureus* in the healthcare environment. *Journal of Hospital Infection* **2006**, *63*, 289-297.
453. Chatterjee, A.K.; Sarkar, R.K.; Chattopadhyay, A.P.; Aich, P.; Chakraborty, R.; Basu, J. A simple robust method for synthesis of metallic copper nanoparticles of high antibacterial potency against *e. Coli*. *Nanotechnology* **2012**, *23*, 085103.
454. Baker, J.; Sitthisak, S.; Sengupta, M.; Johnson, M.; Jayaswal, R.K.; Morrissey, J.A. Copper stress induces a global stress response in *staphylococcus aureus* and represses sae and agr expression and biofilm formation. *Applied and Environmental Microbiology* **2010**, *76*, 150-160.
455. Lu, H.B.; Li, Y.; Wang, F.H. Influence of composition on corrosion behavior of as-cast cu–zr alloys in hcl solution. *Electrochimica Acta* **2006**, *52*, 474-480.